Probing the Rapid Transient Gamma-ray Sky

Studies of FRBs, Mergers, and Flares

Matthew W.A. Lundy

Department of Physics
McGill University, Montreal
December 15, 2025

A thesis submitted to McGill University in partial fulfillment of the requirements of the degree of Doctor of Philosophy

"This whole field is a minefield"

- Trevor Weekes

founder of ground based gamma-ray astronomy

Contents

List of Figures

List of Tables

Abstract

Studying the shortest observable timescales of astrophysical transients is key for understanding the origin and emission mechanisms of these sources. In this thesis, we intend to probe the question: What are the fastest transients at TeV (tera-electron volt) energies? We attempt to investigate this question from two directions. Firstly, we explore transients at other wavelengths and leverage the concept of temporal coincidence to search for sub-threshold transients, particularly looking for coincident emission from fast radio bursts (FRBs). Secondly, we investigate known systems like Active Galactic Nuclei (AGN), to explore if new observations and dedicated analyses can show variability on sub-minute timescales.

We focus on the VERITAS non-detection of TeV counterparts to 13 FRB repeaters and two non-repeaters. These non-detections provide constraints on FRB emission models, and a discussion of the implications of these results will be presented. Additionally, we will present a search for rapid variability using VERITAS observations of BL Lacertae in its 2024 flaring state. In BL Lacertae, we find a hint ($> 2\sigma$) of sub-minute variability during the flare, which would be, if confirmed, the most rapid blazar variability detected at TeV timescales. We will discuss the context of previous studies on rapid phenomena and where this work sits in relation to current and next-generation studies.

Résumé

L'étude des plus courtes échelles de temps observables des transitoires astrophysiques est essentielle pour comprendre l'origine et les mécanismes d'émission de ces sources. Dans cette thèse, nous cherchons à explorer la question suivante : quels sont les transitoires les plus rapides à des énergies de l'ordre du TeV (téraélectronvolt) ? Nous tentons d'aborder cette question sous deux angles. Premièrement, nous explorons les transitoires à d'autres longueurs d'onde et exploitons le concept de coïncidence temporelle pour rechercher des transitoires sous-seuil, en particulier l'émission coïncidente des sursauts radio rapides (FRB). Deuxièmement, nous étudions des systèmes connus comme les noyaux actifs de galaxies (AGN), afin de déterminer si de nouvelles observations et analyses spécifiques peuvent montrer une variabilité à des échelles de temps inférieures à la minute.

Nous nous concentrons sur la non-détection par VERITAS des homologues TeV de 13 répéteurs de FRB et de deux non-répéteurs. Ces non-détections imposent des contraintes aux modèles d'émission de FRB, et une discussion des implications de ces résultats sera présentée. De plus, nous présenterons une recherche de variabilité rapide à l'aide des observations VERITAS de BL Lacertae dans son état d'éruption de 2024. Dans BL Lacertae, nous trouvons un indice ($> 2\sigma$) de variabilité sub-minute pendant l'éruption, ce qui serait, si confirmé, la variabilité de blazar la plus rapide détectée à l'échelle de temps du TeV. Nous discuterons du contexte des études antérieures sur les phénomènes rapides et de la place de ces travaux par rapport aux études actuelles et futures.

Acknowledgments

There are numerous people I would like to thank that made this work possible. This will be an incomplete list and so I apologize in advance if you have been excluded. The first, and most obvious person I need to thank is Kenneth Ragan. Ken has been my supervisor since 2018 and I have now worked with him professionally for more time than any other individual in my life. It has been an incredibly rewarding experience with so many opportunities and I am very grateful that he took a chance, and accepted me into this program. Ken has made my time here some of the most important in my life, and it is something I will always appreciate.

I would also like to thank Jamie Holder, for both some inspiration and guidance. Jamie was always there to provide a permission structure for having wild ideas. FRBs at VERITAS owe a lot to Jamie's continued effort and expertise. Ralph Bird, Tarek Hassan, Juniper Foote, and Michael Daniel also provided key insights at the beginning of this project that steered it in the right direction.

I would also like to thank the leads of the VERITAS working groups: David Williams, Marcos Santander, Ruo Yu Shang, Qi Feng, Reshmi Mukherjee, Deivid Ribeiro, and Sajan Kumar. I would also like to thank the entirety of the ACG and OAWG working groups. Lucy Fortson, Jodi Christiansen, and Amy Furniss in particular helped get me interested blazars which now compose an exciting chapter of this thesis.

There have also been mentors that have provided me stern guidance when needed. David Hanna has eternally burned lessons into my brain

and he has also raised the standard of what I consider acceptable. Jim Cline also provided some crucial motivation and a humbling experience during my early work.

The technical staff at the VERITAS basecamp that existed through my time, Jack, Emmet, Bill, Alisha, Gareth, and (again) Michael deserve more thanks than they get. The whole of the VERITAS experiment relies on instruments that, without them, would have surely broken down.

I would like to thank Lana, and the whole of the FST Science Pod 1, for I'm absolutely sure that I've provided the worst expense reports with the longest delays of perhaps any graduate student. I'm pretty sure this thesis will be finished long before my expense reports are done. The McGill administrative staff also deserve my thanks; Carolina, Maxime, Eddie, Louise, Lauren, Joanna, and Diane. The McGill lab staff as well made working on parts of this project both fun and easy; Robert, Robert, Brandon, and Philip. Juan as well for powering the cluster that I overworked for this thesis and for guiding me through my first experience with huge computational power.

I would like to thank all the postdocs and graduate students in the McGill astroparticle group who worked with me during this time. Thomas was a great friend and I am still sad that he did not decide to do his PhD and instead chose to make money and get married. Julia, and Sreela who were here right at the very beginning. Natalia, and Leo for being there right at the end. Tony provided a framework and a model for what success looked like for a VERITAS student. Ste, Ben, Jonathan, and Sajan all provided support when needed and I hope that come the fall I will be able to follow in their successful footsteps.

I also have many previous people in my educational journey who I need to thank. Vicky Kaspi for driving FRBs at McGill and being a joy to assist in her class. Lorne Nelson for giving me my first chance at research. C.R. Magwaza for really showing me what a love of teaching looks like and Jon Sievers for always being there for bouncing an idea off of.

Finally, on generally personal notes, I would like to thank Sam for being there to support me during my highs and my lows. From the first time she got here to now, it has dramatically improved what this PhD experience became. Gordon also deserves thanks for making sure I do not take myself so seriously. I would also like to thank my family; my brother Nick, my sister Caity, and nana Marilyn (who still wishes I went to UofT). I would also like to thank Grandma Tina who always supported me and was proud even when she was going through some tough times. Finally, the most important people are my parents Peter and Marlene, who gave me the permission and support to do this really hard thing and without them I might have been forced to be lawyer or worse an engineer.

This research was undertaken thanks in part to funding through the Arthur B. McDonald Canadian Astroparticle Physics Research Institute. This research is supported by grants from the U.S. Department of Energy Office of Science, the U.S. National Science Foundation and the Smithsonian Institution, by NSERC in Canada, and by the Helmholtz Association in Germany. This research used resources provided by the Open Science Grid, which is supported by the National Science Foundation and the U.S. Department of Energy's Office of Science, and resources of the National Energy Research Scientific Computing Center (NERSC), a U.S. Department of Energy Office of Science User Facility operated under Contract No. DE-AC02-05CH11231. I acknowledge the excellent work of the technical support staff at the Fred Lawrence Whipple Observatory and at the collaborating institutions in the construction and operation of the instrument. I acknowledge use of the CHIME/FRB Public Database, provided at https://www.chime-frb.ca/ by the CHIME/FRB Collaboration.

Author's Contributions

The author is a member of the VERITAS collaboration. This means that although the work in this thesis is primarily the author's, there was feedback and guidance from many members of the collaboration that contributed to the results. In a similar way, the author also contributed to many other VERITAS projects that are not directly a part of the work in this thesis. These efforts, that are required to maintain VERITAS and as such are critical for the results in this thesis, are included in a small section towards the end of the listed contributions.

Chapter 1: Introduction & Chapter 2: Gamma-ray Astronomy

- Literature Review

  Collation of sources, summary of information, and updates to seminal figures are all the thesis author's original work.

Chapter 3: VERITAS

- Calibrations

  The author was responsible for taking and processing numerous calibrations, including but not limited to: photostatistic gain, telescope pointing, reflectivity, and bias curves.

- Validation

  Validation of IRFs were the responsibility of the author. This included measuring the systematics between analysis techniques and characterizing the seasonal systematic errors in the standard gamma-ray analysis.

Chapter 4: Transient Landscape

- Implementation of Techniques

  The implementation of the theoretical statistical techniques into gamma-ray data analysis was the author's original work.

- Interpretation and Collection

  The collection of minimum timescale transients across all source classes and connecting their contexts were the author's own work.

Chapter 5: Observations of Fast Radio Bursts

- Analysis

  The author was the lead on all FRB analyses included in this thesis and was responsible for writing all of the high-level analysis processing scripts.

- Organizing Observations

  The author was responsible for the scheduling of FRB observations, the selection of FRB sources, and the maintenance of the relevant sections of the VERITAS long term plan.

- Publication

  A subset of the non-repeater results are submitted for publication, and the author is the corresponding author responsible for preparing that manuscript.

Chapter 6: Observations of Rapid Blazars

- Trigger/Proposal
  The author was responsible for drafting and submitting the TOO request that resulted in the observations taken for this thesis.

- Analysis
  The author was responsible for the initial analysis, and producing the rapid variability results. The author also was responsible for drafting the initial VERITAS alert to the public.

Chapter 7: Conclusion

- Summary and Discussion
  The discussion of the contents of the thesis and its implications is the author's original work.

- Gammapy Point-like Validation
  The validation, code modifications, and the proposal to the VERITAS science board for approval of the use of *Gammapy* and VEGAS was the author's original contribution.

Other contributions to VERITAS

- Observing Shifts
  The author traveled to the VERITAS site, leading data taking for projects including those in this thesis and acted as senior observer, or "czar" starting in 2019.

- Data Quality Monitoring
  Contributed to nightly assessment and flagging of data from VERITAS.

- Software Maintenance and Updates
  Contributed both bug fixes, and improvements to the VEGAS software analysis package, V2DL3, and *Loggen*.

- Paper Committees and Secondary Analysis

  Confirmed VERITAS results with an independent analysis, and formal review of VERITAS publications.

- Enhanced Current Monitor

  The calibration, and monitoring of the quality of the ECM, was the author's responsibility from 2020-2025.

CHAPTER 1

Introduction

Bald heads forgetful of their sins,
Old, learned, respectable bald heads
Edit and annotate the lines
That young men, tossing on their beds,
Rhymed out in love's despair
To flatter beauty's ignorant ear.

William Butler Yeats, 1865-1939

1.1 The Fundamental Questions

Gamma-ray astronomy is still a topic that remains full of uncertainty and mystery. Over a third of the known gamma-ray sources remain unidentified, some of which are the brightest sources known. In most sources it is still not known how the gamma-rays are even being produced and what is the connection between the particle accelerator and gamma-ray source. Every time a new detector has been commissioned, new complicated results that have challenged most of the fundamental assumptions that were held, have emerged. The field is still limited by

low statistics; often O(10) counts make a significant difference. The systematics are challenging; often it is required to characterize the propagation of hundreds of thousands of relativistic particles through 10 km of turbulent atmosphere. In addition to all of this, the angular resolution is poor, the worst in the photon field and second only to neutrinos and gravitational waves, making even the most significant results difficult to interpret. All of this together creates one of the most complex fields in astronomy today.

Why then would somebody choose to study gamma-ray astronomy? Although the work is challenging, the questions that it seeks to answer have major implications for some of the longest open questions in astronomy, like the mystery of cosmic rays and the origins of astrophysical neutrinos. In addition, the field promises the ability to probe for physics beyond the Standard Model, at energies beyond what can be produced on Earth. Authors sometimes pedantically discuss the distinction between astroparticle physics, and particle astrophysics. Separating the name of these fields is logical. However, gamma-ray astronomy ends up in an awkward in-between position. Since gamma-ray astronomy uses photons (i.e. particles) to study both fundamental physics and astrophysical sources which term describes us? Astroparticle astrophysics? This awkwardness shows the interesting intersectional position that gamma-ray astronomy occupies; with the same techniques we can probe axions and weakly interacting massive particles (WIMPs), intergalactic magnetic fields and Lorenz invariance violation, the structure of active galactic nuclei (AGNs) jets and the acceleration in supernova remnants (SNRs). It is for this diversity of both source classes, particle and astrophysical techniques, and the big questions that people are drawn to gamma-ray astronomy.

This thesis will seek to tackle the questions; **are fast radio bursts (FRBs) associated with a gamma-ray counterpart, and what is the minimum duration of blazar emission?** Why we tackle pseudo questions though is because their implications drive a bigger holistic picture. So in this introduction we will begin with the broad scope and hopefully narrow in to a point where this pseudo-question not only makes sense but in a broader context is understood to contribute to some more fundamental questions.

Cosmic Rays

Ever since the early work at the turn of the 20th century regarding the source of a mysterious radiation, the origin of cosmic rays has been one of the largest open questions in astrophysics. Cosmic rays are charged particles mostly made up of protons although there is a non-negligible contribution of higher mass nuclei and fundamental particles like electrons and positrons (Particle Data Group et al. 2022). Although Viktor Hess was able to show in the landmark balloon flight that the origin of the radiation was astrophysical (V. F. Hess 1912; V. Hess 2018), locating the galactic and extragalactic sources capable of producing these particles has evaded simple explanation. Detailed observations of the spectrum of cosmic rays across over 6 decades of energy can be seen in Figure 1.1. The spectrum has been measured to an remarkable precision, following an energy dependent power law ($E^{-\gamma}$ with index of approximately 2.7 across most of the energy range, with "solar modulation" dominating below 30 GeV (Angüner 2023). Above that energy there are a couple of notable changes in spectral index known as the "knee" and the "ankle" which potentially correspond to leakage due to the limits of magnetic containment, and the transition between the dominance of different source classes. A full discussion of the interpretation of the cosmic ray spectrum is beyond the scope of this work and can be seen in the review by (Gabici et al. 2019).

The first place one might search for the origin of cosmic rays is by looking at their spatial distribution. There is strong evidence of anisotropy at the lowest and highest energies which one could naively think is dominated by the location of the source of cosmic rays (Abdul Halim et al. 2024). However, due to the charged nature of the particles, this is in fact dominated by effects created by the Galactic magnetic field (Blasi 2013). At lower energies, the Galactic magnetic field will deflect these particles as they travel through the halo for tens of millions of years, and at higher energies the uncertainties in the modeling of the field means that deflection is very difficult to correctly remove making it difficult to reconstruct their origin (Blasi 2013). This is where gamma-rays can play a significant role. As gamma-rays are uncharged particles, they can be localized directly to the location of particle acceleration. However, gamma rays can be produced in processes that do not necessitate hadronic acceleration, so gamma-ray production is a necessary but not sufficient condition for identifying a location of cosmic-ray acceleration.

To further complicate things, there could be a significant offset between the time of the cosmic ray acceleration and the observation of the gamma-rays. Thousands of years may pass and the accelerators that are able to be studied today may not be representative of the average population of sources that are contributing. Therefore, we need to understand not only the gamma-ray sources in the present day, but also understand how they evolve so that we can calculate the sum of their total contributions. This makes characterizing these known sources, spatially, spectrally, and temporally a critical priority and ongoing task.

The topic of this thesis, very high energy transients, is of particular interest. As many persistent galactic source classes struggle to explain every component of the spectrum of cosmic rays, it is possible that a significant contribution of particle acceleration occurs in short, sporadic, and rare injection events (Cristofari 2021). The contribution of magnetar transients in particular may also play a significant role in the observed galactic component of the cosmic ray spectrum (Patel et al. 2025). At the time of writing, there exist few constraints on rapid gamma-ray transients and so there may exist a large population of unresolved sources that have remained hidden beyond the edge of the currently measured temporal domain. Therefore, both in the case of detections and non-detections the work that is presented here will allow for a deeper understanding of the effect of these transient sources on the cosmic ray spectrum.

The extragalactic cosmic-ray spectrum has a similar ambiguity from the unknown contribution of transient sources. It does appear though, with the current integrated cosmic-ray sky maps, that the extragalactic accelerator population may be dominated by transients (Telescope Array Collaboration et al. 2023). Only very few point sources are able to potentially explain some of the highest energy events, so building a better understanding of what are the limits to transients is critical to understand if these events fall within the limits of various source classes. The most promising source class to explain the extragalactic portion of the spectrum is blazars, which are discussed in detail in Chapter 6. In this chapter we study one of the most well known members of the source class in what is potentially the most extreme state the source has ever been measured. Observations of the extreme members of the blazar class is critical to understand what could be the most energetic contributions from blazars to the extremely high energy end of the

cosmic-ray spectrum.

Neutrinos

Neutrinos are often distinguished from cosmic rays since like gamma-rays they are neutral messengers. This means that unlike cosmic rays they do point back to their region of acceleration. Unlike photons, neutrinos are far more difficult to detect. Only kilometer scale detectors like IceCube and KM3Net have the effective area to probe the astrophysical neutrino sky (Aartsen et al. 2017; KM3NeT Collaboration et al. 2024). Although IceCube, currently the most sensitive neutrino observatory in the world, has been in operation for over a decade, most neutrino alerts released by the telescope cannot be associated directly with an astrophysical object. A strong correlation between neutrinos and gamma rays would be direct evidence of hadronic acceleration. This direct correlation has remained elusive. This means that much of the neutrino sky is still consistent with multiple different explanations involving multiple different source classes. Understanding the origin of the diffuse neutrino background and its connection to diffuse cosmic rays and gamma rays is one of the largest outstanding questions in astroparticle physics.

Although there has been a detection of significant persistent excess around some Seyfert galaxies, and a similar correlation with excesses and the Galactic plane, much of the neutrino background cannot be explained without invoking transient sources (IceCube Collaboration et al. 2022; Icecube Collaboration et al. 2023). To date, only one source, TXS 0506+056, has been identified as undergoing both a gamma-ray and neutrino flare, but at a marginal level of significance; $\sim 3\sigma$ (IceCube Collaboration et al. 2018). Although the last decade has increased our knowledge of the neutrino sky and provided many hints as to the astrophysical origin, the detection of astrophysical neutrinos themselves due to the high rates of atmospheric neutrinos and low rate of astronomical neutrinos, making it difficult to see progress without a wider multi-messenger picture. Figure 1.2 shows the measured candidate astrophysical IceCube neutrino events, overlaid with the known gamma-ray sources.

Both transient sources included in this thesis, fast radio bursts and BL Lac type galaxies, have been proposed as sources of neutrino emission (Righi et al. 2017;

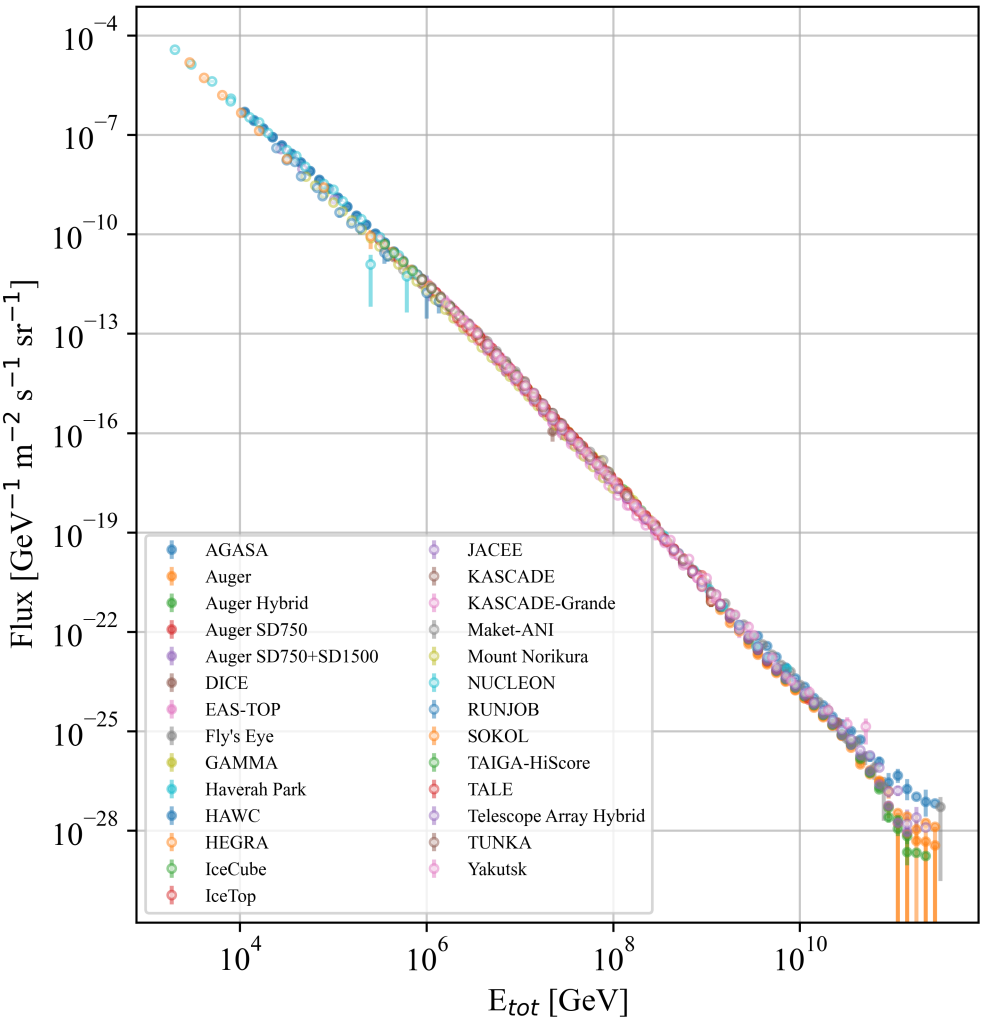

Figure 1.1 The integrated all-particle cosmic ray spectrum as a function of the total energy using data collated from the Cosmic Ray Database (Maurin et al. 2023). Across over 6 decades of energy and 27 experiments the spectrum appears to follow an almost featureless power-law of index ∼2.7 (Takeda et al. 2003; Swordy et al. 2000; EAS-Top Collaboration et al. 1999; Bird et al. 1994; Ter-Antonyan 2014; Garyaka et al. 2008; Ave et al. 2003; Alfaro et al. 2017; Morales-Soto et al. 2022; Rawlins et al. 2015; Aartsen et al. 2019; Aartsen et al. 2013; Aartsen et al. 2020; Takahashi 1998; Antoni et al. 2005; Schoo et al. 2015; KASCADE-Grande Collaboration et al. 2009; Arteaga-Velázquez et al. 2017; Apel et al. 2011; Apel et al. 2013; Chilingarian et al. 2007; Ito et al. 1997; Grebenyuk et al. 2019; Abraham et al. 2008; Abraham et al. 2010; The Pierre Auger Collaboration et al. 2015; Fenu et al. 2017; Abreu et al. 2021; Apanasenko et al. 2001; Derbina et al. 2005; Ivanenko et al. 1993; Astapov et al. 2022; R. U. Abbasi et al. 2018; D. Ivanov 2015; Prosin et al. 2014; A. A. Ivanov et al. 2009).

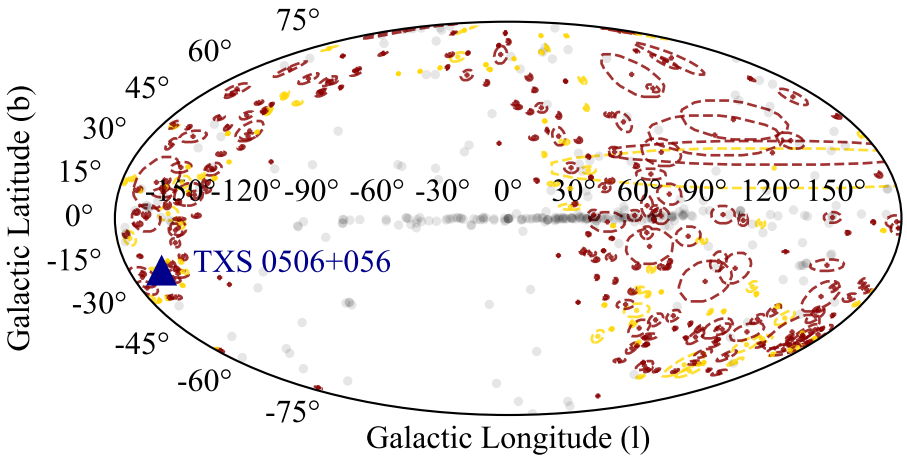

Figure 1.2 Neutrino alerts from IceCube's ICECAT-1 (R. Abbasi et al. 2023). Symmetrized 90% error regions are also shown. Highlighted is the location of TXS 0506+056, the one high significant flaring blazar coincidence. The large gap in the center is due to the lack of sensitivity of IceCube to southern hemisphere sources. "Gold" quality alerts are shown in yellow, and "Bronze" alerts are shown in red. In gray are the known TeV sources. No clear visual correlation is evident.

Qu et al. 2022). Using the intermediate signal of gamma-rays may provide more insight on the acceleration mechanisms in these sources so their relative contributions can be better constrained. As such, this thesis can be viewed as an indirect step towards a holistic understanding of the diffuse neutrino sky.

Understanding Powerful Accelerators

One of the great promises of astroparticle physics is the ability to leverage accelerators in the universe much more powerful than those we can create on Earth to probe physics beyond the Standard Model. There has already been much work done in the high energy field as a whole, and the TeV community in particular, on this topic (Cristofari 2021). Historically, we see this reflected in the Hulse-Taylor pulsar tests of general relativity, the discovery of the positron, and the detection of neutrino oscillations (Taylor et al. 1982; Anderson 1933; Ahmad et al. 2002). All three of these Nobel Prize winning discoveries were only made possible by an understanding of powerful astrophysical environments and by leveraging that knowledge to probe beyond what could easily be measured experimentally on Earth.

The use of astrophysical probes has not stopped in recent years, and the gamma-ray field has been leading in many of these efforts. The current highest center of mass energy that can be produced on Earth is $\sim$13 TeV at the Large Hadron Collider (LHCb collaboration 2025). Gamma-ray experiments regularly probe systems capable of accelerating particles well above a PeV (Aharonian et al. 2021). This allows for the gamma-ray field to probe for new particles that cannot be measured at the LHC, such as what is done with indirect dark matter searches including searches for WIMPs and axions (Acharyya et al. 2024a; Batković et al. 2021). The field also produces studies of fundamental forces, like searches for Lorentz Invariance Violation, and measurements of the photon cross-section (Zitzer et al. 2013; Lin 2020).

One of the limits to these studies is the large systematics introduced by uncertainties in source intrinsic effects. Since most of these studies rely on measuring deviations from underlying source properties (time evolution, spectra, morphology) one requires a thorough understanding and characterization of the gamma-ray sources in order to minimize uncertainties. Work like this thesis, where we probe the limits of transients, is a critical foundation that future fundamental searches can build on.

1.2 The Specific Question Addressed In This Work

The specific question that this thesis is seeking to answer is "What is the nature of the GeV/TeV sky at the shortest timescales"? This question is interesting due to its connections to the larger questions above, and remains an understudied question due to the low statistics and rarity of bright events. As will be seen, the timescale of emission is directly connected to the potential acceleration mechanisms and so by probing for the minimum timescale we are naturally testing for the validity of certain acceleration models. Additionally, as new transient source classes have emerged at other wavelengths, it has allowed us to study the TeV properties of previously unknown objects. Without these external inputs, the low-statistics of gamma-ray astronomy would make such a search very difficult or impossible.

The first way we will approach this question is by taking the brightest flare from a source that is known to experience some of the most rapid variability in the TeV sky and see if there is evidence for sub-minute variability. The source chosen is BL Lacertae (hereafter BL Lac) and the thesis will use data from the VERITAS instrument collected during the major 2024 flare. This would be the first detection of sub-minute variability from this source by any TeV instrument and would confirm earlier tentative measures of sub-minute variability in sources like Mrk 501.

The second way we will approach this is by searching for TeV counterparts to rapid transients in other wavelength bands. We will focus on fast radio bursts (FRBs), a class of rapid millisecond radio transients. Although there have been numerous claimed hints or detections of multi-wavelength counterparts to FRBs, there remains no clear progenitor. No emission has been detected at TeV energies but there exist numerous theories that predict that some fraction of FRBs may produce observable GeV/TeV emission. If detected, this would not only aid in clarifying the origin of FRBs but also their contribution to the diffuse cosmic ray and neutrino background and provide a powerful tool in studying fundamental physics.

1.3 Thesis Overview

This thesis seeks to review the basics of the VHE field before focusing on the transient sky and presenting novel VERITAS results. Chapter 2 covers the basics of the gamma-ray field, summarizing the current source classes, and the relevant theories of particle acceleration and radiation. A brief overview of the instrumentation of the field will also be presented. Chapter 3 will go into the details of the VERITAS instrument, describing the methods of analysis and operation. A focus will be placed on certain aspects of the pipeline that the author participated in. Chapter 4 will then review the most rapid VHE transients currently known and the techniques that are being used to study them.

After the literature review, we will present the results of two searches for rapid transients starting with Chapter 5. In this chapter, a summary of the VERITAS fast radio burst program and the results of the deepest VHE study of fast radio bursts to date will be presented. It will be followed by Chapter 6 where the results of the study of a rapid flare from BL Lac will be presented.

Finally the prospects for future analysis and upgrades to the software/hardware and the summary of the results will be presented in Chapter 7.

CHAPTER 2

Gamma-ray Astronomy

I can feel the gamma rays like a turbulence at the center of my soul!

Bill Mantlo, 1951-

Gamma-ray astronomy, as it is normally defined, covers the study of astrophysical photons from 1 MeV to over 1000 TeV. As this is over 9 decades of photon energies, which is a larger change than that from radio to X-ray, it is often useful to subdivide the energy ranges into those managed by different observational techniques. High energy gamma-ray astronomy covers the energy range from 100 MeV to 100 GeV. This is measured by pair production telescopes like *Fermi*-LAT that will be described in Section 3.1. The next energy range is the very high energy (VHE) range, which spans from ∼100 GeV to ∼100 TeV. This is observed by imaging atmospheric cherenkov telescopes like VERITAS, which will be described in Chapter 3. Since the boundary between VHE and high energy is mostly deter-

mined by the sensitivity range of VHE instruments, which continue to push their thresholds lower, this definition continues to evolve (Cortina et al. 2023). Finally, the ultra high energy (UHE) covers all photons above 100 TeV. This is detected with particle detector telescopes, like LHAASO. The focus of this thesis will remain on the VHE band and studying the transients that exist within it.

When trying to find the most rapidly-varying VHE sources, we first need to understand what processes can produce gamma rays at TeV energies. We will begin by listing several classes of sources that are well known gamma-ray emitters and then describe how the particles in these systems gain their energy. In other words, we will describe the *acceleration processes* in these systems. We will then describe the processes by which these particles convert that kinetic energy into radiation, or the *radiative processes*. Additionally, many of these processes will govern not only the emission but also how these sources are observed on Earth. We will also briefly discuss the physics governing *air showers* induced by these high energy particles.

2.1 Sources in the Field

The VHE sky is composed of a large number of different sources and source classes. The number of sources that are known in the VHE range at the time of writing, as reported by TeVCat (Wakely et al. 2008), is 315. In this catalog, and the field in general, sources are broadly categorized as follows:

Extragalactic Sources

- Blazars: Active galactic nuclei (AGN) with the jetted emission directed along the line of sight
  - BL Lac (HBL/IBL/LBL): A subtype of AGN characterized by a featureless non-thermal spectrum, based on the prototypical object BL Lac. The class is further divided by the peak location in the spectral energy distribution with high peak BL Lacs (HBLs), intermediate peak BL Lacs (IBLs), and low peaked BL Lacs (LBLs) all of which are detected at VHE.

- GRB: Gamma-ray burst, a powerful gamma-ray transient often associated with a supernova.
- Globular Cluster: A dense cluster of old stars. The VHE emission is thought to arise from some of the evolved degenerate systems that are found in these regions.
- Starburst galaxy : A galaxy undergoing a large amount of star formation. It is currently unclear if stellar winds or some other process dominate the emission.
- FSRQ: Flat spectrum radio quasar, thought to be off axis emission of a AGN.

Galactic Sources

- Supernova remnants (large nebula formed after a supernova) and other nebulae powered by pulsars:
  - Shell supernova remnants: Young/Middle aged supernova remnants with a prominent radio shock creating a shell like appearance.
  - PWN: Pulsar wind nebula. A bright region of synchrotron emission created by interactions of the pulsar wind with surround material.
  - TeV Halo: Large extended emission surrounding a pulsar. Thought to be the final stage of pulsar evolution with free electrons streaming into the interstellar medium.
- Nova: Thermonuclear eruptions due to accretion from a star onto a white dwarf.
- Binaries: Systems including an orbiting compact object gravitationally bound with a stellar companion or another compact object.
  - Microquasar: A subtype of binary systems composed of an evolved star and a black hole, launching jets into the surrounding medium.
- Superbubble: A compact cluster of stars powering a large very luminous HII region (a nebula of ionized hydrogen).

- Molecular Cloud: Hadronic interactions in a dense molecular environment leading to an over-density of diffuse emission that appears like a point source.
- Pulsar: Pulsed periodic emission tied to the rotation of a central neutron star.
- Massive Star Cluster: A cluster of massive O/B stars where the interactions between stellar winds are thought to be regions of acceleration.

Other Sources

- Unidentified (UNID): Sources with no known, or multiple counterparts leading to no unambiguous identification.
- Dark: Sources with constraining upper limits in the GeV energy range and no known multi-wavelength counterpart.

These source classes are not evenly distributed in number; the vast majority of TeVCat sources are blazars and the majority of those sources are HBLs. A distribution of these sources can be seen in Figure 2.1. From this figure the structure of the galactic plane and the different spatial distribution of source classes are apparent.

The number and types of sources have changed significantly as instruments have evolved; this can be seen in Figure 2.2. Early in the development of VHE telescopes, source identification was successful only for a handful of sources focusing primarily on very close SNR and blazars. The current generation of imaging atmospheric Cherenkov telescopes dramatically increases both the number and types of sources due to their superior sensitivity and angular resolution. Finally, in the last several years, all-sky survey telescopes with poor angular resolution have again increased the number of sources. However, many of these sources have not been associated with a multi wavelength counterpart leading to many more dark or unknown source.

Even though there is a wide diversity of sources, many of the underlying physics of the gamma-ray production are thought to be the same. Microquasars, accretion driven jets launched from black holes, are thought to be galactic counterparts to blazars. Massive star clusters are similarly thought to be counterparts

to starburst galaxies. In Chapter 4 we will focus on the transient sources of this list and describe their durations and properties. Of this list only AGN, GRBs, pulsars and nova are known to exhibit rapid variability. Some sources are thought to undergo slow flux changes over decades but that will not be the focus of this work.

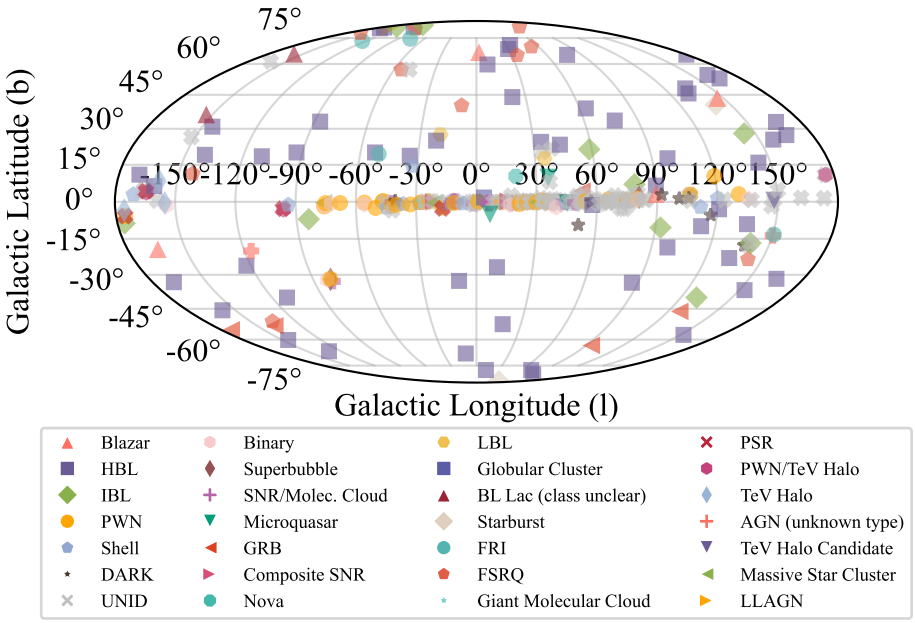

Figure 2.1 Galactic projection of the TeVCat Catalog (updated: March 2025) of known TeV sources plotted in a Mollweide projection (Wakely et al. 2008). Overlapping source definitions are separated to follow the distinctions made in the individual papers.

2.2 Acceleration

In order to produce TeV emission, charged particles must be accelerated to multi-TeV energies. This process of providing particles this required energy is known as **acceleration**. We will discuss some of the relevant acceleration processes but it is

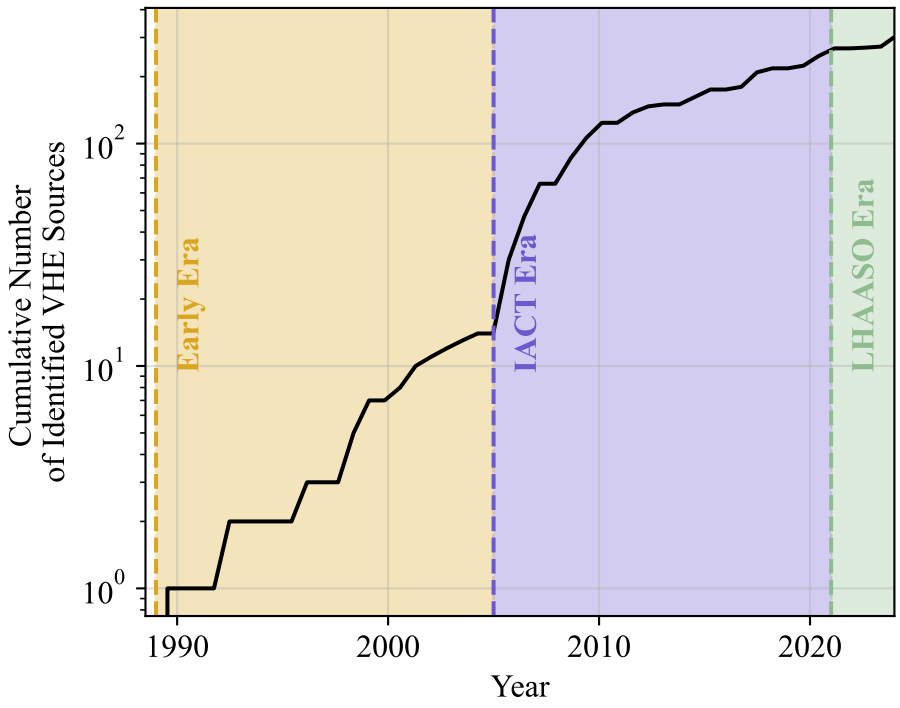

Figure 2.2 "Kifune" plot of the TeVCat Catalog (updated: March 2025) (Kifune 1996; Wakely et al. 2008). Three eras are highlighted; the "Early Era" with various small gamma-ray detectors operating simultaneously, the "IACT Era" where the three major operating IACTs (such as VERITAS) dominated the source detection rate, and finally the current LHAASO epoch where most new VHE sources are found by the LHAASO observatory.

still an open question as to which acceleration process dominates in most gamma-ray emitting systems.

Since magnetic fields do no work, one requires either an electric field or some local variation in the electric field creating small electric fields over a large area to accelerate charged particles. Although both are relevant we will start with the stochastic case, where the average electric field is quite small but the variation in the electric field drives the momentum changes in the particles. These are more ubiquitous in astrophysical environments because of the difficulty that comes from

maintaining a strong electric field.

Fermi Acceleration

The first and simplest acceleration process is a stochastic process originally proposed in the work by Fermi (1949), with a modernized derivation in Longair (2011), which will be summarized in the following section. Consider the case of a series of randomly moving infinitely massive "magnetic mirrors" which can be clouds or some other system. Take these mirrors to be moving with velocity V, with $V << c$. Take a test particle traveling with initial angle, θ, to the normal of the surface of a mirror. A sketch of this with the mirrors depicted as clouds can be seen in Figure 2.3. Now, it would seem that random reflection would lead to both acceleration and deceleration in equal measure, but this is not the case.

To see how much a particle is accelerated, as with any collision, we can simply apply conservation of the energy and momentum. A simple choice of frame is the center of momentum frame, which, given the infinite mass and therefore the unchanging velocity of the mirror, is the frame with the mirror moving at velocity V. In this frame the energy of the particle is given by:

$$E^{mom} = \left(1 - \frac{V^2}{c^2}\right)^{-\frac{1}{2}} (E + Vp\cos\theta) \tag{2.1}$$

with E being the initial energy of the particle, c being the speed of light, V being the velocity of the cloud, θ being the angle between the particle and the mirror, and E^{mom} being the energy of the particle. We can simplify by introducing $\gamma_V = 1/\sqrt{1 - \frac{V^2}{c^2}}$ to get:

$$E^{mom} = \gamma_V (E + Vp\cos\theta). \tag{2.2}$$

Now, since the change in momentum only lies in the x direction we can consider just the x component of the momentum (see Figure 2.3). In the same center of momentum frame this is given as:

$$p^{mom} = \gamma_V (p\cos\theta + \frac{VE}{c^2}), \tag{2.3}$$

with p_{mom} being the original momentum of the particle. Recalling that the energy is the same for the particle before and after the collision in the cloud frame and the

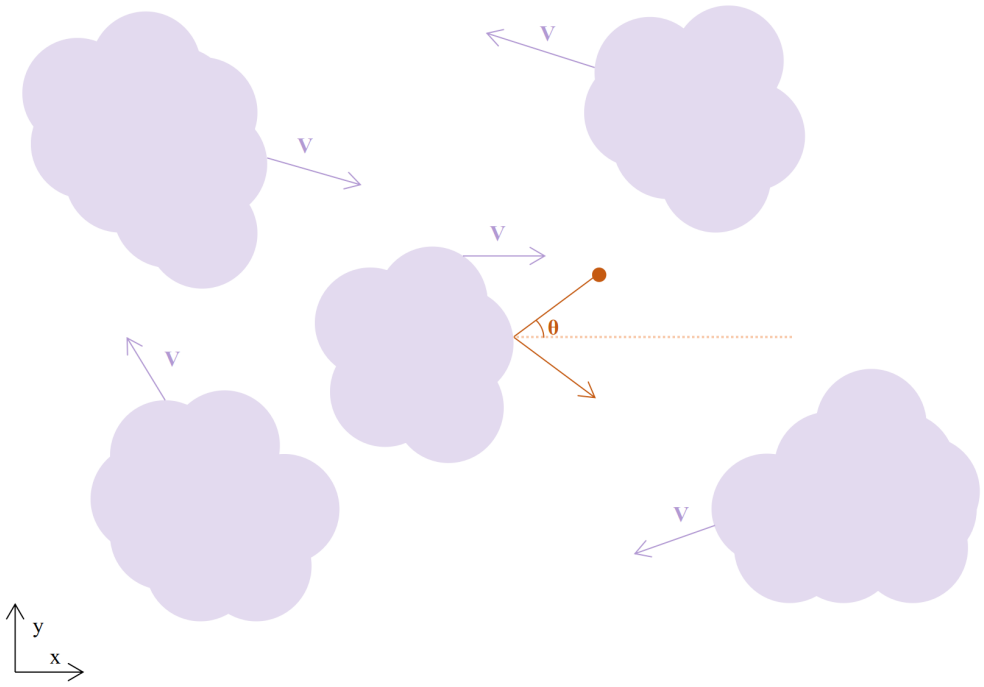

Figure 2.3 Visualization of the configuration used to derive the energy gained by a test particle due to second order Fermi acceleration. Clouds, shown in purple, are traveling with characteristic velocity V. A collision of a test particle, is shown aligned such that the change in momentum lies only along the x direction. The arbitrary angle θ is shown between the cloud and the particle trajectory.

only change is the sign of the momentum we can convert back into the observer's frame to find:

$$E^{obs} = \gamma_V (E^{mom} + V p^{mom}). \tag{2.4}$$

Taking the previous equations we can simplify to find:

$$E^{obs} = \gamma_V (\gamma_V (E + V p \cos\theta) + V \gamma_V (p \cos\theta + \frac{VE}{c^2})), \tag{2.5}$$

$$E^{obs} = \gamma_V^2 E (1 + 2V p \cos\theta + \frac{V^2}{c^2})). \tag{2.6}$$

Since $p/E = \frac{v \cos\theta}{c^2}$, we can also find the relative change in energy of the particle for a single collision. This is:

$$\frac{E^{obs}}{E} = \gamma_V^2(\frac{2Vv\cos\theta}{c^2} + \frac{V^2}{c^2}). \tag{2.7}$$

This change can be both positive and negative depending on v and the angle θ. Expanding to the second order results in:

$$\frac{E^{obs} - E}{E} = (\frac{2Vv\cos\theta}{c^2} + 2\left(\frac{V^2}{c^2}\right)). \tag{2.8}$$

We now want to find the average over many collisions, regardless of the incoming angle. But not all collision angles are equally probable. In the relativistic limit, where $v \to c$, the probability of a collision at an angle θ is proportional to $\gamma_V(1 + (V/c)\cos\theta)$. Thus, we get the following for the expected value for the change in energy in a collision:

$$\langle\frac{E^{obs} - E}{E}\rangle = \frac{2V}{c}\left(\frac{\int_0^\pi \cos\theta[(1 + (V/c)\cos\theta)]\sin\theta d\theta}{\int_0^\pi [(1 + (V/c)\cos\theta)]\sin\theta d\theta} + 2\left(\frac{V^2}{c^2}\right)\right), \tag{2.9}$$

$$\langle\frac{E^{obs} - E}{E}\rangle = \frac{2V}{c}\left(\frac{V}{3c}\right) + 2\left(\frac{V}{c}\right) = \frac{8}{3}\left(\frac{V}{c}\right)^2. \tag{2.10}$$

This shows that to second-order in (V/c), we are gaining a fraction of the initial energy every time, so there will be an exponential increase in the energy of particles involved in these collisions. Consider many collisions occurring over time, along with some probability that the particle leaves the collision region, denoted by P. Ignoring the leading constant, this means that after k collisions, the number of particles N with respective energies E still in the acceleration region is:

$$N = N_0 P^k, \tag{2.11}$$

$$E = E_0\left(\left(\frac{V}{c}\right)^2\right)^k. \tag{2.12}$$

Rearranging the equations to eliminate k and simplifying gives,

$$\frac{\ln(N/N_0)}{\ln(E/E_0)} = \frac{\ln P}{\ln\left(\frac{V}{c}\right)^2}, \tag{2.13}$$

$$\frac{N}{N_0} = \left(\frac{E}{E_0}\right)^{\ln P/\ln\left(\frac{V}{c}\right)^2}. \tag{2.14}$$

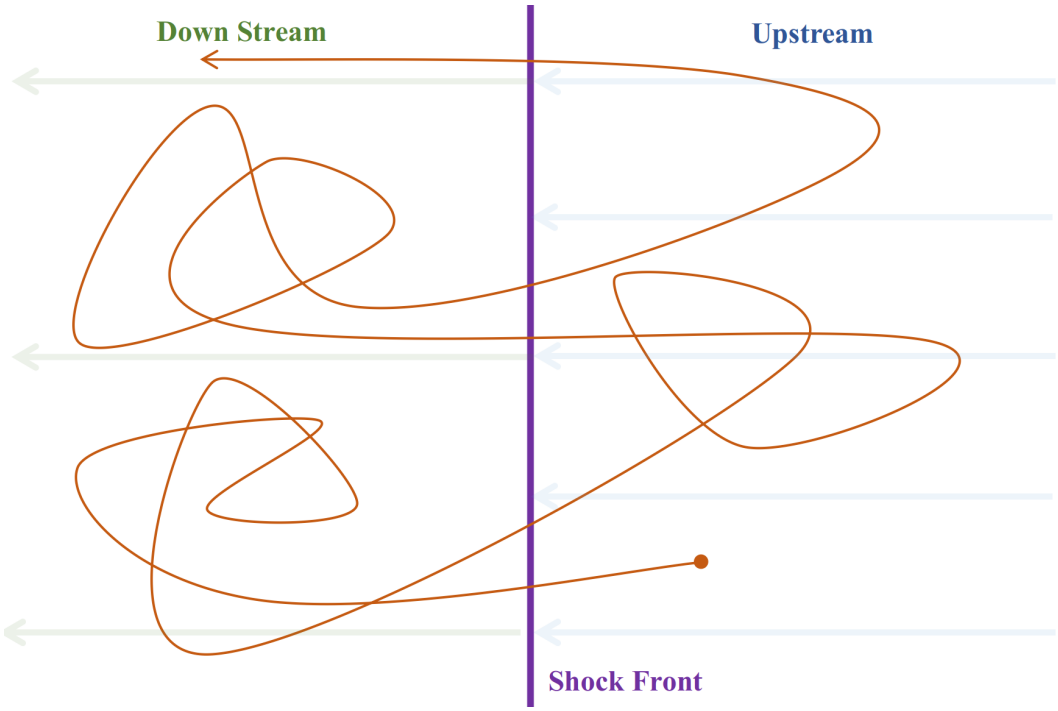

Figure 2.4 Visualization of a test particle trajectory in diffusive shock acceleration. The scattering occurs in the turbulent environments, and the acceleration occurs during the crossing of the shock front. Instead of scattering off multiple different moving clouds, acceleration occurs during multiple upstream and downstream crossings of the shock front. An illustrative direction and speed of the flow of the material is shown through faded arrows.

This is the power-law distribution of the energy spectrum of the accelerated particles. The index on $(V/c)^x$, $x = 2$, defines this process as *second-order* Fermi acceleration. A similar derivation can be made for particles crossing a turbulent shock front. Particles encountering the shock front multiple times effectively create a series of head-on collisions leading to *first-order* acceleration, dependent on V/c. This process, known as diffuse shock acceleration, is illustrated in Figure 2.4. The theory of diffuse shock acceleration was originally reported by several groups (Axford et al. 1977; Krymskii 1977; Bell 1978; Blandford et al. 1978).

We now have an acceleration process that can occur in a variety of environments with no strong net magnetic field, and it is well understood from first prin-

ciples. This theory has dominated the models for a large number of persistent gamma-ray sources as the expected primary form of acceleration. However, it is unable to fully describe some phenomena as seen in transient gamma-ray sources. Therefore, we will also consider alternative acceleration mechanisms.

Magnetic Reconnection

Magnetic reconnection is another potential acceleration mechanism. Magnetic reconnection occurs when magnetic field lines of opposite polarity rejoin and break multiple times in a plasma. Figure 2.5 illustrates the basic process. This process converts the energy stored in the magnetic field into the kinetic energy of a particle. Although used to explain solar flares, the phenomenon is still imperfectly understood theoretically. Currently, studies of magnetic reconnection involve sophisticated particle-in-cell and magnetohydrodynamics simulations. It is useful to consider the two basic models of reconnection, one of which was developed by Sweet (1958) and Parker (1957), and the other by Petschek (1964).

Both of these models are reviewed in Longair (2011); here it is sufficient to highlight that early theoretical progress in this field has been driven by decreasing the duration of the acceleration to match the short timescales seen in astrophysical phenomena like solar flares It was found that the geometry of the problem could be reduced by the "Sweet–Parker" mechanism (Longair 2011). This process notes that as two current regions are brought together, reconnection occurs not in the full plasma but in a narrow region of the colliding fields where a neutral line will form (the neutral current sheet). If this system is considered to behave analogously to a hydrodynamic process, then the region that is formed dictates the speed of the ohmic energy loss, which can be found to be much smaller than diffusion ($\sim 10^4$ seconds). This, however, is still much larger than the timescales seen in nature and does not consider three-dimensional effects that are present in the problem. The model also ignores much of the non-reconnection, potentially turbulent behavior of the gas. The Petschek (1964) model found that the timescales can be further reduced if standing waves around the region are considered, but it was still not sufficient to explain hourly timescales.

Although no model currently exists that is able to analytically describe all of

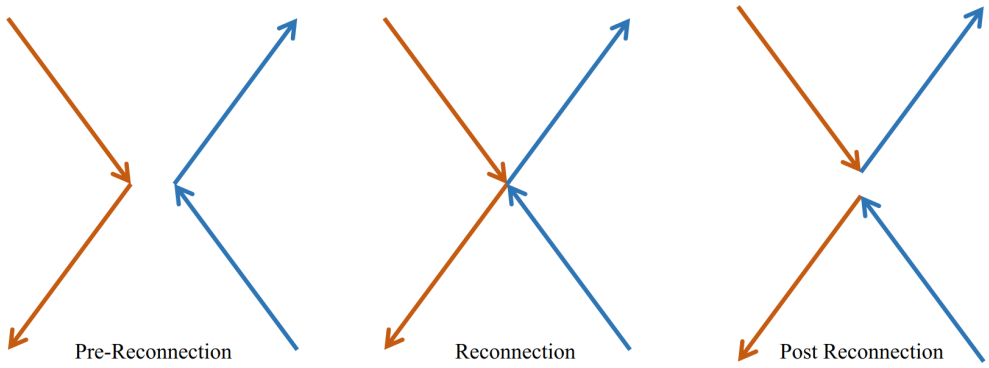

Figure 2.5 Illustration of magnetic field lines of opposite polarity undergoing reconnection. Colors are used to illustrate the initial field lines. and to track the reconnection.

the behavior in reconnection processes, it is a process that appears to occur in local environments and has been reproduced in laboratories. Much like other hydrodynamic processes, even though we cannot describe it analytically, we can still use some of the high-level properties that seem to emerge in order to group potential phenomena that may be explained by this process. One of those high-level emergent behaviors is the ability to produce much more rapid phenomena than emission, requiring large regions of acceleration.

2.3 Radiative Processes

There are a variety of radiative processes necessary to understand both the detection techniques and the source emission of high energy photons. A *radiative* process in this sense is anything that can either produce or impart energy onto

photons. Some basic properties, like absorption and ionization, that do not play a major role in either the detector technology or source spectrum will not be discussed.

Bremsstrahlung

Bremsstrahlung, German for *braking radiation*, is a radiation process that occurs when particles are decelerated in an electric field. Here we will consider the Larmor formula:

$$P = \frac{2q^2}{3c^3}a^2 \tag{2.15}$$

where radiation, of power P, will be produced when charge q is decelerated in the Coulomb field. Although this is commonly seen in thermal systems, the radiation frequency of that emission is far below what is normally relevant in high-energy astrophysics. The far more important process, as will be seen in later discussion of air showers, is the relativistic non-thermal bremsstrahlung emission.

Pair Production

Electron pair production, the process of converting a photon to an electron and a positron, is one of the most common processes due to the low mass threshold of the combined rest mass of the electron and the positron. The pair production process can be described as

$$\gamma + Z = e^+ + e^- + Z, \tag{2.16}$$

with Z being a mediator nuclei present for the conservation of momentum. The Feynman diagram of this process is shown in Figure 2.6. Pair production is also possible with just two photons instead of the mediator nucleus. Based on conservation of energy, it is clear that this process has a cut-off below $2m_ec^2$ (as there will not be sufficient energy to create the mass of the two particles), but above that energy, it becomes a dominant process for the passage of photons through matter. In the limit of high energies (above ~ 1 GeV), the cross section for this process is

$$\sigma = \frac{28A^2\alpha^3}{9m_e^2}\left(\log\left(\frac{183}{A^{1/3}}\right) - \frac{1}{42}\right), \tag{2.17}$$

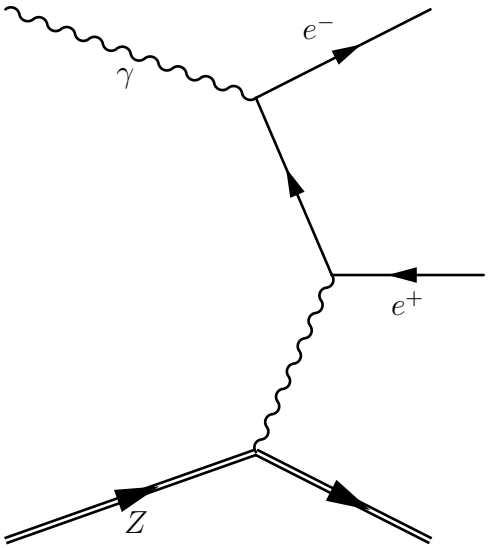

Figure 2.6 Feynman diagram for pair production with a mediator nucleus.

with A being the atomic number of the nucleus, m_e representing the mass of the electron, and α being the fine structure constant (Bethe et al. 1934). At very high incident photon energies, the recoil energy/momentum of the nucleus is small and the resulting e^+/e^- are highly relativistic. For very high-energy photons, this will typically produce electrons traveling at relativistic speeds, as only a small fraction of energy is lost during the production process.

Synchrotron Radiation

Synchrotron radiation is one of the largest sources of low-energy photon emission. As particles move through magnetic fields, the particles may spiral around the magnetic field's lines. This process releases energy in the form of radiation. The characteristic spectrum of synchrotron radiation requires a detailed discussion of beaming, and the precise geometry of the problem (Rybicki et al. 1979). For our discussion, we will start from the given result that in the relativistic case, the power emitted by a single charged particle per unit frequency can be given by

$$P(\omega) = \frac{\sqrt{3}}{2\pi} \frac{q^3 B \sin\alpha}{mc^2} N\left(\frac{\omega}{\omega_c}\right), \tag{2.18}$$

for mass m with charge q moving in magnetic field of strength B, with angle α between the field and velocity. ω is the frequency of the emission. There is also a normalization factor, N, dependent on the ratio of the frequency to the critical frequency ω_c. The frequency $\omega \propto E^2 B_\perp$, with the electric field strength E. For a single electron, the emission will not only get more powerful, but also will peak toward more energetic values as the magnetic field increases. Although it is technically possible for synchrotron emission to produce radiation above 100 GeV, the magnetic field strengths required are far above what is seen in astrophysical sources. Instead, in an average energetic astrophysical source, synchrotron radiation is produced at keV energies. These keV photons do provide the ideal seed population for further acceleration processes as we will see. It is also important to note that the above power is for a single charged particle.

For the true spectral energy distribution (SED) of an astrophysical source, we have to consider the summed synchrotron emission from a distribution of charged particles. It is often natural to assume a power-law for the underlying distribution of electrons, although it is sometimes the case that a more complicated function is required. An illustration SED arising from a power-law distribution of electrons is shown in Section 2.3.

Inverse Compton Scattering

Inverse Compton scattering, or Compton scattering in general, is the most important process for understanding astrophysical VHE spectra (Compton 1923). The process is a simple collision between high-energy photons and electrons, where the momentum of the photon is transferred between the electron and the photon. Inverse Compton scattering is used to describe when the photon increases in momentum after the collision, as opposed to the electron. Since the energy of a photon is proportional to wavelength, this means that the process shifts the spectrum of the seed photons to shorter wavelengths, up-scattering them eventually to gamma rays. A Feynman diagram showing this interaction can be seen in Figure 2.7. At low energies for an electron, this interaction occurs at a rate given by the Thomson Cross section (Richard Fitzpatrick 2014), with $\hbar$ being the reduced Planck constant:

$$\sigma_T = \frac{8\pi}{3}\left(\frac{\alpha\hbar c}{m_e c^2}\right)^2 \approx 0.665\ \text{b} \tag{2.19}$$

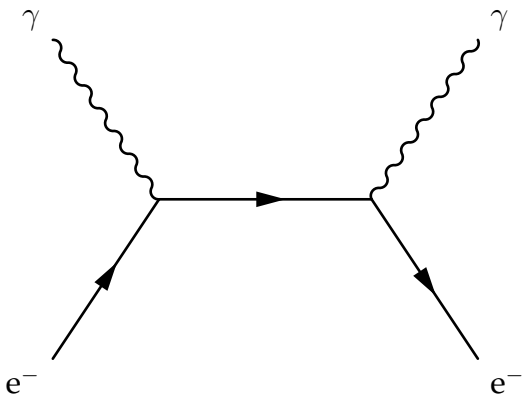

Figure 2.7 Feynman diagram for Compton scattering.

in units of Barns (10^{-28} m^2). A typical scatter process of a single photon with a low-energy electron, with Lorentz factor γ, will typically lead to an increase in energy of the photon by a factor γ^2. This means that when a photon is upscattered with an electron following a power-law distribution of index δ, the resulting spectrum of photons will follow $(\delta - 1)/2$. The effect of typical inverse Compton emission in processes is to convert the energy in a population of electrons into a much higher energy of radiation. For the most energetic regime, the so-called Klein-Nishina regime, the Thomson cross section is suppressed by a factor that is proportional to the inverse of their energy.

Synchrotron Self-Compton/External Compton

Synchrotron self-Compton (SSC) is tying together synchrotron emission and inverse Compton scattering and is a description that explains the characteristic dual peak structure that is seen in many high-energy sources. An illustration of a typical SED can be seen in Figure 2.8. Synchrotron self-Compton involves the inverse Compton scattering of synchrotron radiation (Condon et al. 2016). The same population of electrons is used both in the production of the synchrotron photons and the inverse Compton scattering of those photons. Self-interactions will dominate in environments with dense photon emission. In some regimes, other seed photons will dominate the high-energy emission in what is referred to as external inverse Compton.

Since there is a connection between the low-energy and the high-energy spectrum part of a SSC spectrum, joint modeling of the entire SED allows for constraining multiple physics parameters relating to the environment. Factors like magnetic field strength, Lorentz factor, radius of the emission region, and the particle spectrum in the source environment are all probed when studying the spectral energy distribution of sources with SSC emission.

Pion Decay

Pion decay is a deviation from our previous processes because this process is known as a *hadronic* process. This is opposed to what is known as a *leptonic* process, which covers all of the previous radiative processes. Although protons and other hadronic particles can be accelerated and radiate via synchrotron or scattering processes, often these are subdominant components to the observed emission due to the mass suppression term in their cross-sections. Pion decay is a common process for systems with a high density of accelerated protons when there is also sufficient density of target material, and it contains unique signatures not present in any other emission process. This means that observing pion decay signatures in the spectrum of a source is one way to confirm if a source is a hadron accelerator as opposed to a lepton accelerator. Identifying these systems remains one of the highest priorities in VHE astronomy because of the implications for understanding cosmic rays and neutrinos.

The first step in the production of pions is the scattering of protons. In a proton-proton collision, the threshold for the creation of π^0 is 290 MeV in kinetic energy in the center of mass. Although charged pions, $\pi^{+/-}$, are important to understand the full dynamics of some high-energy processes, for gamma-ray astronomy the most important particle is the neutral pion. The neutral pion (π^0), is a short-lived particle, and the largest branching ratio for its decay is the creation of two photons. To write out the processes for π^0 creation and decay, respectively:

$$p + p = p + p + \pi^0, \tag{2.20}$$

$$\pi^0 = \gamma + \gamma. \tag{2.21}$$

Thus, a cosmic-ray proton flux impinging on material will generate a gamma-ray flux from the decays of these pions. The exact shape of the resulting gamma-ray

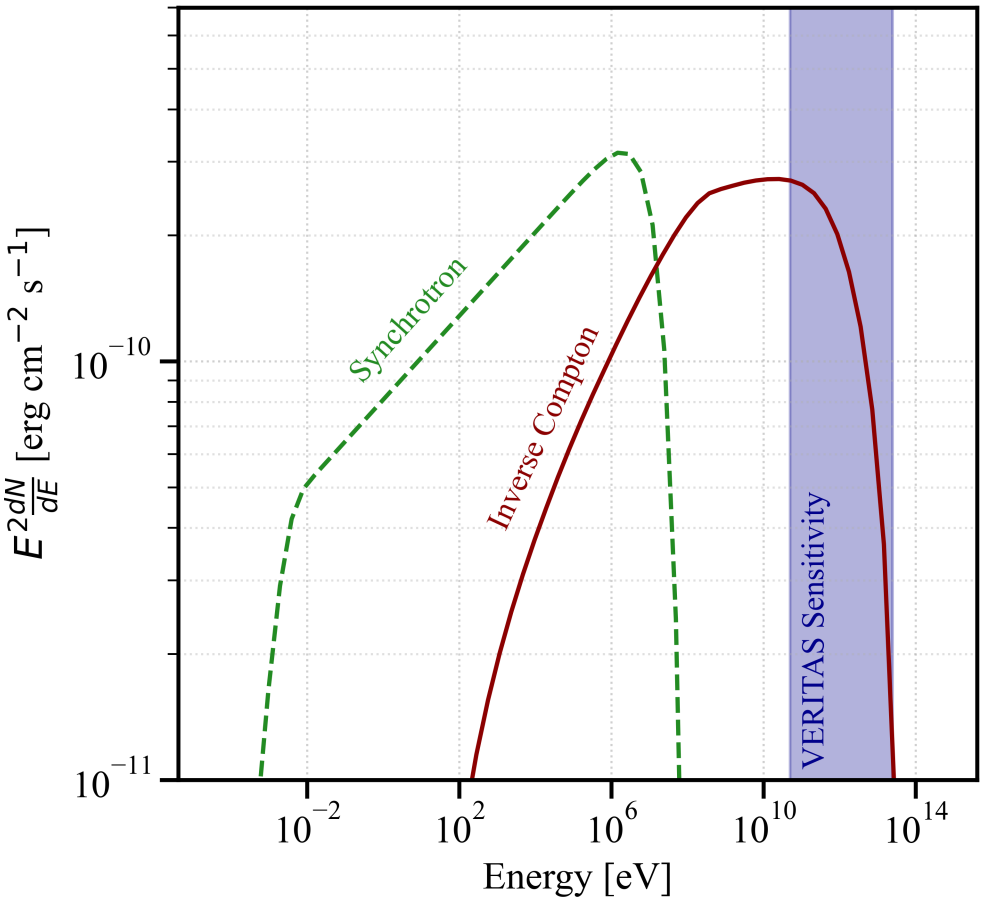

Figure 2.8 A simple example synchrotron self-Compton spectrum generated for a single zone system using *agnpy* (C. Nigro et al. 2022). The emission region has an electron population following a power-law of index 2.8. The range of VERITAS sensitivity is overplotted. As can be seen, in this prototypical case, inverse Compton emission is the dominant contribution to the observed VERITAS data.

spectrum depends on the index of the spectrum of the accelerated protons. When the proton-proton interactions from a power-law proton spectrum are viewed in the observer's frame, they typically result in a "pion bump". A very common analysis in gamma-ray astronomy is determining whether a pion-like spectrum or a SSC spectrum is preferred.

Cherenkov Radiation

One of the key signatures for detecting particles in air is Cherenkov radiation. Unlike the previous radiation mechanisms, whose importance is mostly critical for understanding how emission is produced, Cherenkov radiation is key for understanding how we detect these particles in Earth's atmosphere. Cherenkov radiation occurs when a particle's phase velocity exceeds the speed of light in a given medium. The Cherenkov energy lost for a given incremental distance dx is governed by the Frank-Tamm equation:

$$\frac{dE}{dx} = \frac{(ze)^2}{c^2} \int_{\epsilon(\omega)>(1-\beta^2)} \omega \left(1 - \frac{1}{\beta^2 \epsilon(\omega)}\right) d\omega, \tag{2.22}$$

with ω being the frequency of the emission, and ϵ representing the emissivity of the medium, with z being the number of charges, e being the elementary charge, c being the speed of light, and $\beta = \frac{v}{c}$ with particle velocity v (Frank et al. 1937; Jackson 1998). As can be seen, once integrated assuming $\epsilon(\omega)$ is constant, the photon intensity is proportional to ω^2, and since the higher frequency emission is absorbed by the atmosphere, atmospheric Cherenkov radiation is dominated by blue/UV emission peaking around 340 nm (Holder 2015). This is what makes Cherenkov radiation an ideal means of detecting high-energy particles in air. It takes high-energy emission, which is difficult to directly measure, and produces optical light where there already exist many sensitive detector technologies.

Another feature of Cherenkov radiation is the characteristic angle of emission. A diagram of this angle, θ, can be seen in Figure 2.9. The Cherenkov angle is given by

$$\cos\theta = \frac{c}{v n_{med}}, \tag{2.23}$$

with n_{med} being the refractive index of the medium, and v being the velocity of the particle. Since the speed of light in a medium is c/n_{med}, the property of the

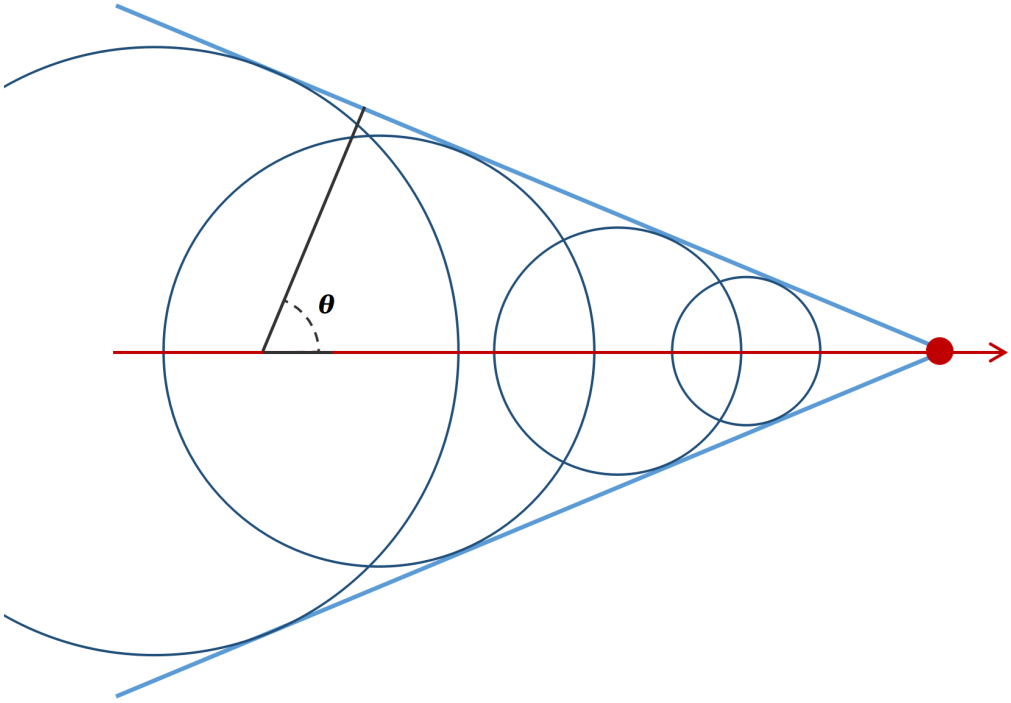

Figure 2.9 A diagram of the geometry of Cherenkov emission. The path of a charged particle can be seen in red, along with the emitted Cherenkov radiation from the particle in light blue. The Cherenkov angle is shown as θ along with the two-dimensional slice of the spherical wavelets used to model the emission in dark blue.

emission only occurring above the speed of light can also be seen as the only values for which there is a non-zero opening angle. A common analogy for understanding Cherenkov emission is as a form of "shock" front, like a sonic boom. As can be seen in Figure 2.9, you can view the emission as being the interference of many individual wavlets producing a shock front in the wake of the particle.

2.4 Air Showers

Now we will consider the results of interactions in the atmosphere of multiple energetic cosmic particles. Air showers are the combination of many individual particle interactions that can be treated as a single statistical whole. A particle shower

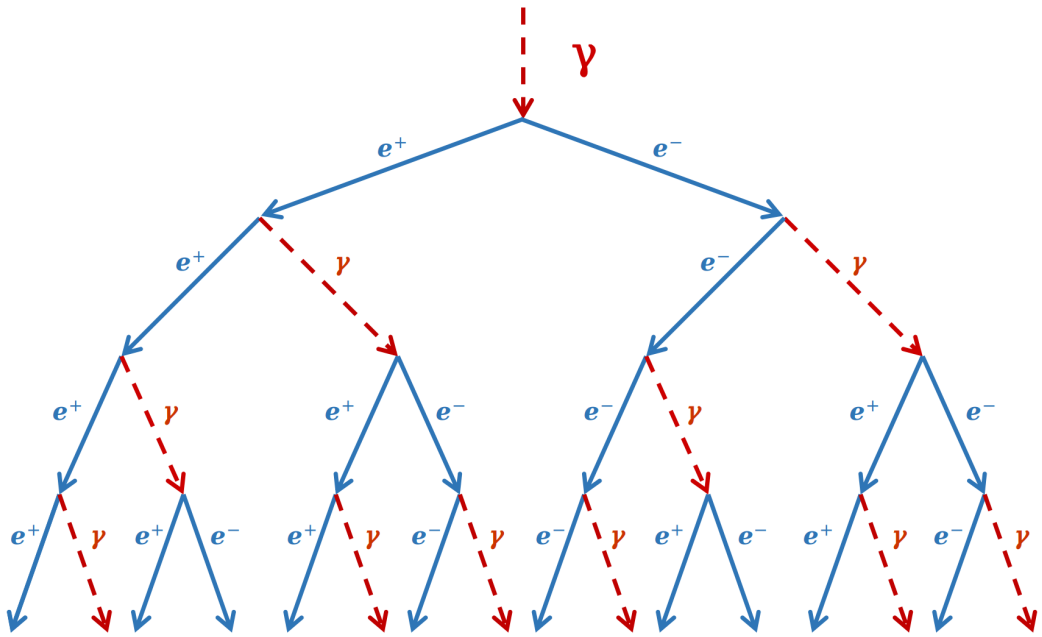

Figure 2.10 A simplified model of an electromagnetic shower arising from an initial high-energy photon. The dashed red lines correspond to photons, and the blue solid lines correspond to electrons and positrons. At each stage of depth, there is a doubling of the total population via either bremsstrahlung or pair creation.

will occur when a sufficiently energetic particle interacts with a dense medium, as occurs frequently for cosmic rays and air, which we refer to as an "air shower".

This statistical whole can be understood with a simple scaling model (Heitler 1944; Carlson et al. 1937). Air showers regularly occur for particles of sufficiently large energy, where a single particle interaction's fractional energy loss due to radiation is very small. The simplest form of air shower is a purely electromagnetic shower. A toy model of electromagnetic shower development can be seen in Figure 2.10. These showers can begin with a single photon pair-producing into an electron and a positron. The momentum will be shared among the particles, but with sufficient initial energy, these particles go on to produce new high-energy photons via bremsstrahlung. These photons, with sufficient energy, will then proceed to

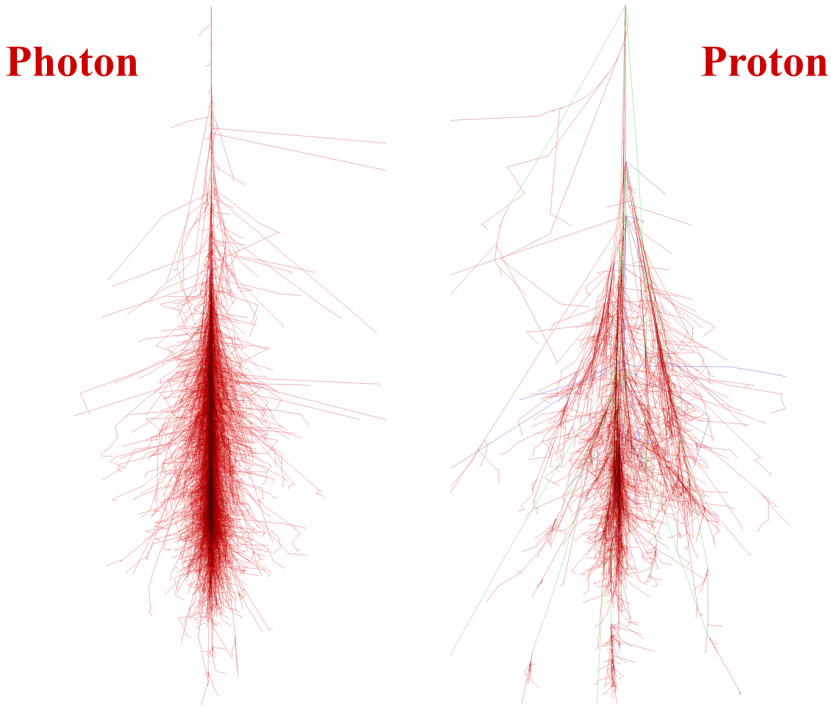

Figure 2.11 Simulations of airshowers initiated by a 100 GeV photon (left) and a 100 GeV proton (right) produced with the CORSIKA simulation package (D. Heck et al. 1998; Schmidt et al. 2005). The first interaction occurs at 30 km, with the plot showing 30.1 km vertically and 10 km horizontally. Red lines show the track of electrons, positrons, and gamma rays. Green shows the path of muons, and blue shows the path of hadrons. There is a clear difference in the morphology of the two showers due to the presence of hadronic interactions in the proton-induced shower.

produce their own electron/positron pairs, and the process will repeat for each individual photon in turn. As the original energy is shared amongst more and more photons and electron/positron pairs, the average energy of these particles drops, and other processes like ionization become dominant; the shower ceases to develop.

More formally, consider the original particle energy as E_0. We will also define the lengths X and λ_e as the depth of the shower and the length of one interaction (the radiation length), respectively. These can be related if we know the number of stages of particle production the shower has undergone, which will be denoted by n, as $X = n\lambda_e$. At each stage, the original particle's energy is split between two particles. Since on average the total number of particles doubles, at each stage the total number of particles as a function of depth is $N(X) = 2^n = 2^{X/\lambda_e}$, and the energy of individual particles at each depth is $E(X) = \frac{E_0}{2^{X/\lambda_e}}$. This should infinitely grow, but as mentioned before, the maximum will occur near the critical energy where ionization begins to dominate and particles no longer strongly radiate. It can be shown, as in Engel et al. (2011), that this occurs at,

$$X_{max}(E_0) \approx \lambda_e \ln\left(\frac{E_0}{E_c}\right). \tag{2.24}$$

So, the depth of any particular air shower (X_{max} is related to the primary energy of the initial particle. This is useful as the properties of the showers can be used to infer information about the original particle. For typical energies of showers detected by ground-based detectors, this *shower maximum* will occur at roughly 10 km. Although one could directly measure the particles produced in the shower, this is not the only way to gain information about the particles produced. Since they are traveling relativistically in air, there is also an accompanying Cherenkov light that travels with the shower front. This Cherenkov "flash" is typically a few nanoseconds long.

To expand this simple model to hadronic showers, which are more complicated due to the diversity of hadronic interaction processes, is beyond the scope of this work. Hadronic showers contain many particles with complicated potential products, including muons and pions. The diversity of interactions and outcomes, along with the large transverse momenta of the secondary, leads to larger shower-to-shower variations and more asymmetry in many of the resulting sub-showers.

An illustration of the differences between leptonic and hadronic air showers can be seen in Figure 2.11. In general terms, hadronic showers have significant substructure with many distinct sub-showers initiated by secondary products, whereas electromagnetic showers are mostly governed by Compton scattering and pair production as explained in the above section, leading to higher symmetry and smaller lateral extent (Holder 2015).

CHAPTER 3

VERITAS

In veritas vino

Pliny the Elder, 23-79 A.D.
(modified)

The Very Energetic Radiation Imaging Telescope Array System (VERITAS) is one of four major operating IACTs. Here we will summarize the extensive process of converting measured Cherenkov light into the four high-level products that we obtain from an event: the two-dimensional position on the sky, the energy, and

whether to consider it as a gamma ray or a background event. We will then summarize how we convert lists of events into high-level data products like spectra, sky maps, and light curves.

The VERITAS array is located in Tucson, Arizona (+31° 40′ 30.21″, -110° 57′ 7.77″, 1268 m) at the Fred Lawrence Whipple Observatory. It is composed of four nearly identical imaging atmospheric cherenkov telescope (IACTs), labeled T1-4. Each contains a camera composed of 499 photomultiplier tubes and a mirror made of 350 individual hexagonal facets arranged in a Davies-Cotton optical design (Davies et al. 1957; Krennrich et al. 2007). Each total mirror has a diameter of 12 m, and the field of view of the instrument is $> 3.5°$. The telescopes are sensitive to the energy range from 85 GeV[1] to >30 TeV (Park et al. 2015). A recent photograph of the array can be seen in Figure 3.1.

VERITAS has been in operation for over 15 years with first light in 2007 (Maier et al. 2008). Since then, VERITAS has collected approximately 1,000 hours of science observations a year. VERITAS has undergone two major upgrades, which have created three epochs of sensitivity denoted as V4, V5, and V6 (D. Kieda 2011; D. B. Kieda 2013). V4 was the original configuration of the telescopes. V5 solved some of the issues with the initial placement of the telescopes that led to a high muon rate between T1 and T4 by moving T1. V6 upgraded the photomultiplier tubes in the VERITAS camera, significantly improving the sensitivity of the detector and lowering the energy threshold.

Although the sensitivity of the VERITAS observatory changes yearly with age, there have been no major changes to the hardware since 2012. The data included in this thesis is composed entirely of V6 data.

3.1 Types of Detectors

Although VERITAS is an IACT, it is helpful to understand the three primary types of gamma-ray detectors in order to contextualize the advantages of IACTs when

[1]This was the most sensitive instrument across its entire energy range and only recently has the first of many of the Cherenkov Telescope Array Observatory (CTAO) telescopes come online and become more sensitive below ∼200 GeV (H. Abe et al. 2023)

Figure 3.1 Photograph of the VERITAS array. The red telescope is the pSCT, which currently does not operate with VERITAS and will be described in Chapter 7. Credit: Center for Astrophysics | Harvard & Smithsonian.

compared to other detectors, and to understand how IACTs uniquely contribute to our understanding of the gamma-ray sky.

Pair Production Telescopes

Pair production telescopes are a conceptually simple detector technology. The largest gamma-ray observatory that uses the pair-production technique is *Fermi*-LAT, the Large Area Telescope. When describing a "typical" detector, we will mostly be referring to *Fermi*-LAT specific details (Atwood et al. 2009). A schematic of the components of a pair-production detector can be seen in Figure 3.2. It is composed primarily of three parts: an anti-coincident shield, a converter tracker,

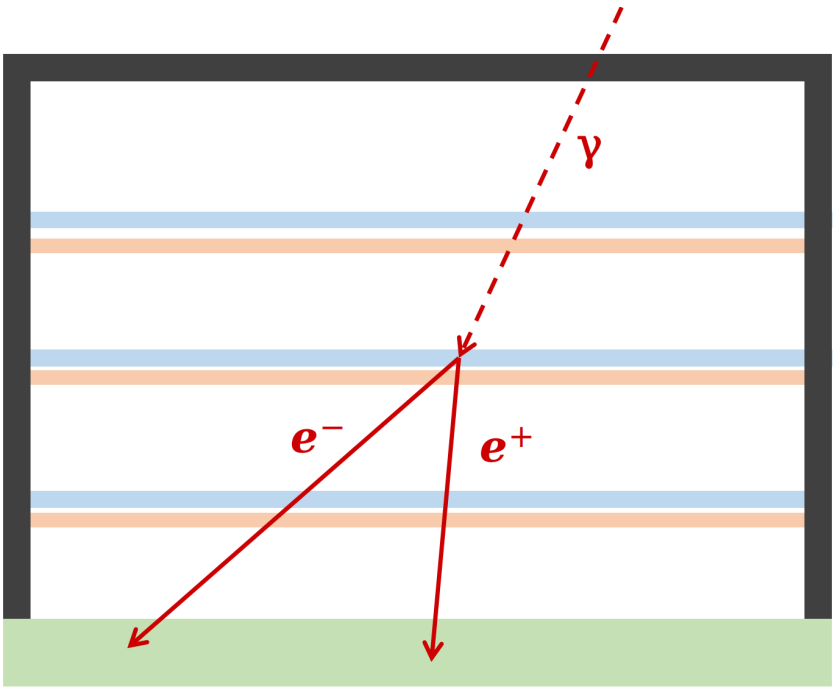

Figure 3.2 Schematic of a pair production telescope. Anti-coincident shields are shown in black, the calorimeter is shown in green, the particle trackers are shown in orange, and the conversion foils are shown in blue. An incoming photon, in red, converts into an electron and a positron that travel through the detector. Adapted from the Fermi-LAT Collaboration (2021).

and a calorimeter.

Recall, for every gamma-ray detector we will be seeking to determine three physical quantities: direction, particle type, and energy. The tracker is responsible for the direction of the particle. As incoming gamma rays pass through the detector, they interact with the high-Z material to produce an e^+/e^- pair. The position of the charged particles is then recorded as they pass through the multiple layers of interspersed position-sensitive detectors (ex., silicon strip detectors). Since the gamma rays detected typically have energies far above the rest mass of the electron, the direction that can be reconstructed from the recorded tracks of the particles can be used to determine the origin of the original gamma-ray.

However, other charged particles are equally likely to be detected as they pass

through the tracker, and since the rate of cosmic rays is far higher than gamma-rays, these detectors need a method of vetoing charged particles not produced inside the detector. This component, which can be used to reject particles that are not gamma-rays, is called an anti-coincident detector. This is a high-efficiency detector built around the tracker, designed to record the initial entry of any external charged particle, allowing them to be vetoed from the sample (Moiseev et al. 2005). They are typically made of some scintillator and photo-detector combination, and can have efficiencies of over 0.9997 (Moiseev et al. 2005). With an efficient anti-coincidence detector, it is assured with a high degree of significance that all detected particles that do not trigger the vetoes are gamma rays.

Energy in these systems can be measured with a calorimeter. The calorimeters are typically placed after the particle has passed through the tracker, since the accurate pointing measurement of the e^+/e^- must be made before the degradation in the calorimeter showering (Atwood et al. 2009). In the case of *Fermi*-LAT, this is performed using an array of CsI crystals. The high-energy limit of the detector's ability to reconstruct the energy is when there is significant leakage, and a shower cannot be fully contained. This occurs for *Fermi*-LAT above ~ 1 GeV.

The main weakness of the technology is apparent when scaling the detector to higher energies. The technique requires gamma-rays to impinge on the detector, so the instrument must be located above the atmosphere. This means that size becomes a technical challenge due to the issues of weight in spacecraft launches. Since the effective area (a concept discussed in Section 3.7) directly scales with the size of the tracker, the limit to the size of the detector will be driven by the maximum weight and volume that can be launched. A similar argument can be made about calorimeter depth and weight. Although there are proposals for future missions that could increase the sensitivity by an order of magnitude, they are still in very early stages (Buckley et al. 2022).

The benefits of this technique are that it has a very large field of view ($\sim$2.4 sr), since particles passing through anywhere in the tracker can be reconstructed (Atwood et al. 2009). Additionally, since these detectors have to be outside the atmosphere, they normally have a high livetime. In this work, we will leverage this strength and use *Fermi*-LAT as an external trigger for our VERITAS observations and also as a complementary comparison for our observations of rapid blazars in

Section 6.

Particle Detector Arrays

Particle detector arrays are a class of detectors where the particles from an air shower directly interact with the detector. The most common form of these detectors is a water Cherenkov detector, where the particles from the air shower pass through some enclosed tank of water, producing Cherenkov light that is measured by some internal photodetector. Building an array of these means that the shape of the shower on the ground can be reconstructed by the individual deposition in the individual detectors.

Examples of current and future entirely water Cherenkov particle detectors include HAWC and SWGO (Abeysekara et al. 2023; Huentemeyer et al. 2019). Other detector technology supplements the water Cherenkov with particle detectors like plastic scintillators spread over a large area. This is the case for the LHAASO-KM2A experiment (Aharonian et al. 2021). Finally, there is sometimes a mixture of shielded and unshielded detectors used in an array in order to reject air-showers containing penetrating muons, which would imply that the shower is initiated by a hadronic particle. A sketch of a HAWC-like detector can be seen in Figure 3.3.

The advantages of this technique come from the expected gamma-ray purity and large effective area. Since the detector technology is relatively simple, there can be cost effective large arrays spread over hundreds of meters, effectively creating an instrument with an effective area of $\sim 10^5 \mathrm{m}^2$. However, this area is usually coarsely instrumented, making the precision of the angular localization difficult. These detectors often additionally have very high thresholds, making it difficult for them to reconstruct showers below $\sim$ 1 TeV. Like the pair-production technique, these detectors have a large field of view and little deadtime. This makes them an ideal trigger for gamma-ray transients, but only for the rare events with emission about 1 TeV.

Imaging Atmospheric Cherenkov Technique

The Imaging Atmospheric Cherenkov Technique/telescope is a detector technology that utilizes the Cherenkov light generated by air showers in the atmosphere

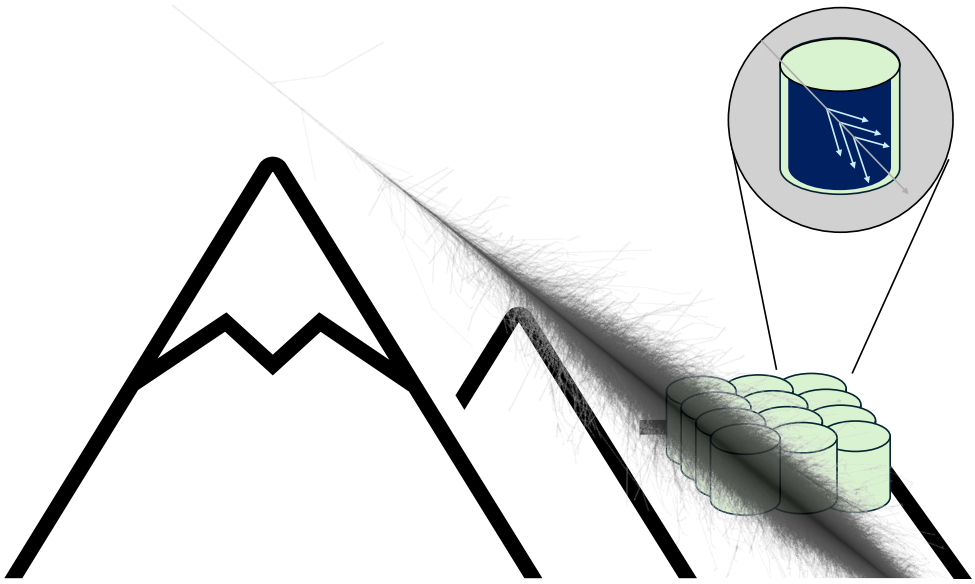

Figure 3.3 Sketch of a particle detector array, not to scale. The illustration shows a series of tanks at high elevations with an electromagnetic air-shower (1 TeV air shower) directly passing through the detector. The inset shows an individual particle passing through the water contained in one tank, producing Cherenkov light through the passage. Based on a figure and with images from Fabian Schmidt and A. Albert et al. (2019).

to study gamma-rays. The technique was pioneered at the Fred Lawrence Whipple observatory by the Smithsonian Astrophysical Observatory group with the Whipple telescope (Weekes et al. 1989). Unlike the other detector technologies, Cherenkov telescopes utilize the Earth's atmosphere as the main detector volume. A sketch of the IACT technique can be seen in Figure 3.4. Air showers are generated whenever a particle of sufficient energy passes through the atmosphere, and the resulting secondary particles also produce Cherenkov light that can be collected by instruments on the ground. The flash of blue light lasts only $\sim$10 ns, but is spread over a large area, meaning multiple telescopes can image the same shower. When they do, since they are viewing the same shower stereoscopically, they can accurately reconstruct the original of the shower without any degeneracy.

Unlike other techniques, where a large area needs to be instrumented to increase the sensitivity of the detector, air showers deposit a light pool over hun-

dreds of meters, meaning even a relatively compact detector can still have a large effective area, $>10^4$ m^2 (Park et al. 2015). Additionally, due to the stereoscopic technique and the improved resolution of the shower image, Cherenkov telescopes have the highest angular resolution of the three techniques, with a 68% containment less than 0.1° (Park et al. 2015).

The major limitations of Cherenkov telescopes are a limited field of view and more observing restrictions. Photomultiplier tubes, as are typically used on current-generation instruments, cannot be used in bright conditions, and so Cherenkov telescopes only operate under moonless nights. The limited field of view means that Cherenkov telescopes need to select their targets for long exposures and cannot simply survey the sky like the others. This means that Cherenkov telescopes are best suited as follow-up instruments that can study known sources and provide a higher resolution spectro-morphological study of the object.

3.2 VERITAS Trigger

This section begins the detailed description of the step-by-step process that is used in reconstructing the data for this work. The first step of the VERITAS data collection is the trigger. Triggers are implemented into physics instruments when there are large data rates, or the ratio of useful data to noise is very small, or recording data comes with a large deadtime. In VERITAS's case, all of this is true, and so triggering is a must. A key principle in designing a good trigger is to balance data rate with signal acceptance. In VERITAS, the system is designed such that the trigger strongly prefers to accept signal over background or noise events. The trigger is incorporated at the hardware level and determines when an event is created and 24 nanoseconds of photomultiplier tube trace data is stored into a VERITAS bank format (VBF) file for later processing. The trigger comes in three levels, denoted as L[1-3], and will be summarized here from the work of Weinstein (2008).

L1 - Constant Fraction Discriminator

The initial step in the trigger is a Constant Fraction Discriminator (CFD). These are the initial triggers in every pixel of the VERITAS camera that trigger at the same

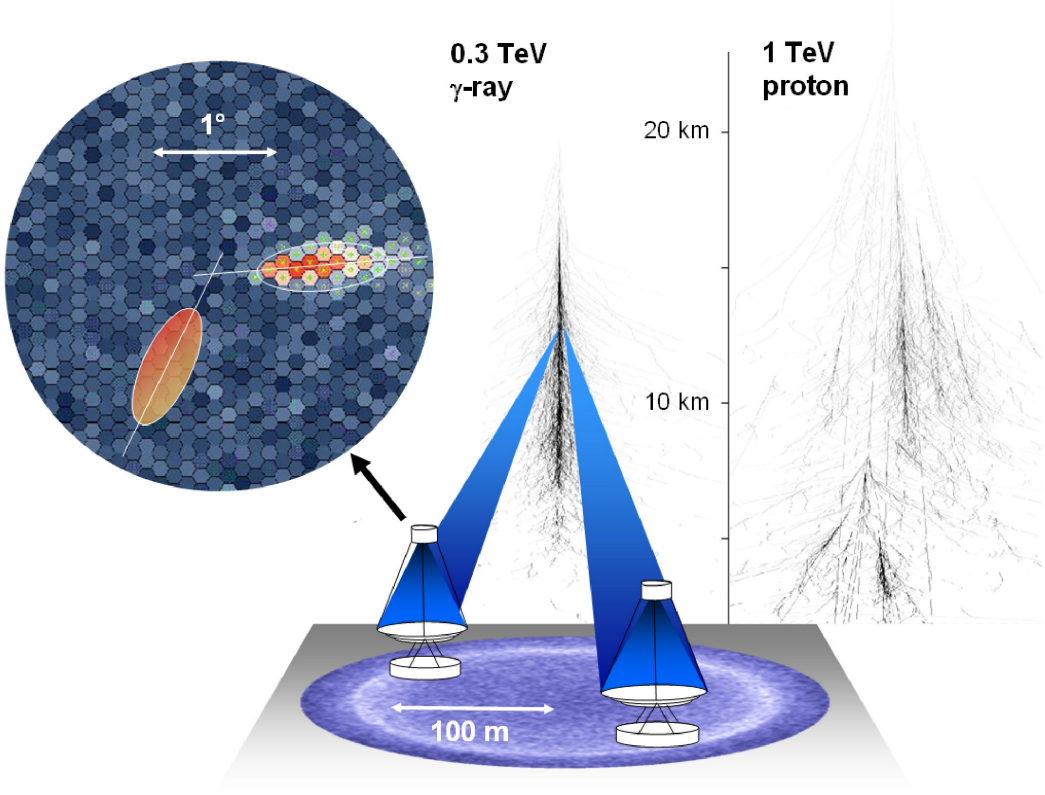

Figure 3.4 Illustration of the IACT technique, showing a 300 GeV gamma-ray producing Cherenkov light and being imaged by ground based telescopes. The camera image shows both the idealized image and one with noise and pixelization for illustration. A proton and gamma-ray shower are shown along with their energies, and the typical scale of the shower images in the camera plane (∼1 degree) is also shown. Figure from Hinton et al. (2009)

point in the rising amplitude of a signal. The CFDs threshold is a key parameter in selecting the VERITAS trigger threshold. The threshold is decided by balancing the rate of night sky background (NSB) and the acceptance rate of the signal. A typical calibration that is used in VERITAS to determine this quantity is known as a *bias curve*. Observations are taken with a steadily increasing threshold, and at each level, the level 2 and level 3 trigger rates are measured. The NSB based triggers are seen empirically to follow a power-law distribution ($A_{NSB}^{-\gamma_1 x}$), and the cosmic ray and gamma-ray triggers also follow a power law ($B_{NSB}^{-\gamma_2 x}$). Since the two indices γ_1 and γ_2 are not equal, with $\gamma_1 > \gamma_2$, we can get a purer signal by increasing this threshold. The maximization of the retained signal while not entering the noise-dominated regime is taken as the inflection point of the total rate with an additional small buffer. An example of a bias curve can be seen in Figure 3.5, where the rates shown are the L2 and L3 rates. Once the threshold has been set, the CFD returns a binary decision, "triggered/not-triggered" for every photomultiplier tube and passes this to the next stage, L2.

L2 - Pattern trigger

The next level trigger is the level two, pattern trigger (Weinstein 2008). Since a Cherenkov light pool from a shower is expected to be both compact and smooth, it is expected that for real events, multiple contiguous pixels should be triggered. A signal splitter redirects the binary-triggered output of the CFD signals into pattern-selection trigger modules, which are pre-programmed to trigger if three adjacent pixels within a subsection trigger within $\sim$6 ns. This dramatically reduces the number of triggers to approximately ~ 5 KHz for nominal operations.

L3 - Array trigger

The level three, and final trigger, checks for simultaneity between telescopes (Weinstein 2008). Although real Cherenkov showers could trigger only a single telescope, reconstruction quality dramatically improves when stereoscopic techniques can be implemented. This requires a minimum of two telescopes to be involved. When a L2 trigger is achieved in a telescope, a signal is transmitted to a pair of digital asynchronous transceiver modules. The signals are then delayed with a pulse

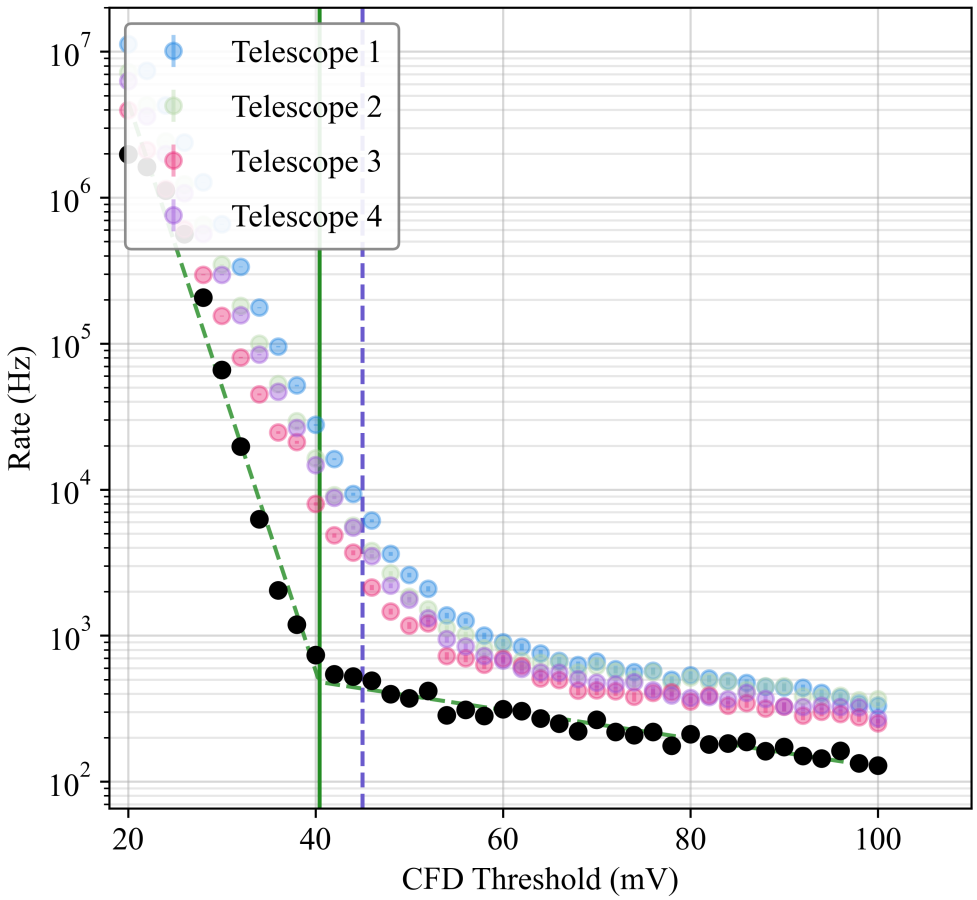

Figure 3.5 A bias curve for the VERITAS observatory taken on 2013-10-28. Shown in color are the telescopes' L2 rates, and in black the arrays' L3 rates. The typical threshold of 45 mV is shown as a dashed blue line, along with a fit to the data producing a measured inflection point at ~ 40 mV is shown in green. The NSB regime begins to dominate at the inflection point for CFD thresholds below ~35 mV.

delay module to search for coincidences between any of the six telescope combinations. Delays need to be implemented to account for arrival time differences due to the cable/fiber length and the differences between the arrival times of the Cherenkov light on the telescopes due to non-vertical pointing. The L3 trigger reduces the rate of events to ~ 400 Hz for a typical run in the year 2025. At this point, a VME GPS timestamp is given and the event is saved to eventually be packaged in the proprietary VBF format. The VBF format typically contains a series of events, each of which contains the FADC traces of every pixel in the camera during the time of the event, as well as pedestal events (triggered events with no light), and some other event-level flags.

3.3 Cleaning and Calibration

All of the subsequent sections have to do with offline analysis. Due to the complexity of the analysis, numerous techniques have been developed to properly analyze IACT data, and often different techniques are chosen for different analyses. Currently VERITAS utilizes two primary low-level analysis packages: ED and VEGAS (Maier et al. 2017; Cogan 2008). Although there are some significant differences in the analysis packages, their performance converges to approximately the same sensitivity. Every published result requires that high-level physical results be verified with an independent secondary analysis in the opposing package. In this thesis, we will use both packages, performing the FRB analysis with VEGAS and the blazar results with ED.

Data cleaning and calibration are the first steps, and this requires removing pixels without significant Cherenkov light and then converting the measured charge into a number of physical photons. The gain differs pixel by pixel and changes nightly due to variations in the performance of the photomultiplier tubes. To account for these variations, a nightly "flasher" run is taken. These runs are ~ 2 minute observations with an external trigger running at $\sim$300 Hz with an external light flashing at 15 different light levels and fully illuminating the camera (Hanna et al. 2010). This light, and its fixed known levels of brightness, allows for a gain to be calculated for every run taken that night. This process is applied to every image, along with other minor corrections, flagging problematic pixels, and collecting

database information.

After calibration, the pixels involved in the event are selected; the rest are removed or "cleaned". One cleaning algorithm that is commonly used relies on first identifying "islands" of contiguous pixels above a fixed threshold. This threshold is lower than what was required to initially trigger the event. This allows for the rejection of pixels outside of the patch of light in the image that could be elevated due to random fluctuation in the night sky background or internal issues like after-pulsing or arcing, creating artificial charge in the camera. Then, an additional buffer radius of 1-2 pixels is added around every island to make sure that even the faint tails of the events are used in the later analysis. More complicated analyses, such as those involving techniques like "nearest neighbors" clustering, are currently under development and are used in some more advanced analyses.

3.4 Directional Reconstruction and Event Parameterization

Once an event has been recorded by the instrument and calibrated, there are numerous approaches to convert the image into useful information about the original shower. This process is known as image parameterization. Additionally, at this stage, we use the stereoscopic technique of aligning the axes of the showers to obtain a direction of origin. There are three different techniques that have been implemented in VERITAS data analysis. The primary technique used in this thesis is "template reconstruction", but this method is seeded by Hillas reconstruction and could be further improved with the Neural Network techniques so we outline them for completeness.

Hillas Reconstruction

The first analysis is known as the "Hillas" reconstruction. Hillas reconstruction can be viewed initially as a moment analysis (Hillas 1985). This derivation of the Hillas parameters follows the internal memo of Vladimir Vassiliev and Stephen

Fegan (2005)[2]. Take a series of telescopes, where i shows the telescope index, j is pixel index, n^{ij} is the photoelectrons in pixel j of telescope i. $\overrightarrow{p}^{ij}$ is the vector of the location from the center of the field of view of the respective telescope i of pixel j. With these definitions the zeroth moment of the image (N), which is called "size", is defined as:

$$N^i = \sum_j n^{ij}. \tag{3.1}$$

Size, i.e. N^i is the sum of the number of photoelectrons in telescope i, will be correlated with the total energy of the event. The first moment (or the image centroid vector) is given by:

$$V^i_\alpha = \frac{1}{N_i} \sum_j n^{ij} p^{ij}_\alpha. \tag{3.2}$$

Now there are two vectors that compose V, indicated by the index α. The primary one is often denoted as the "length", and the second as the "width". The length vector is critical for directional reconstruction. The intersection of the individual length vectors of images involved in the event can be transformed to the origin point of the original gamma-ray. This method of reconstruction through intersection has been the primary means of reconstruction for the current generation of telescopes. Since all four telescopes will not intersect perfectly for every event, the size-weighted center is often selected.

These Hillas moments are used for the energy and direction of reconstruction, but have also been found to be useful in distinguishing signal from background (i.e., in gamma/hadron separation). To do this, it is often the convention to average the scaled values of these image parameters across telescopes. From this, we obtain the mean scaled width/length (respectively MSCW, MSCL). The higher-order quadrupole moments are also occasionally used for this purpose.

Higher level parameters of the reconstructed event position and low-level minimum thresholds are also used in conjunction. These include the distance from the center of the camera in the camera plane (distance), the reconstructed altitude of maximum particle density (Shower Max Height), the number of photomultiplier tubes in an image (N_{tubes}, and the squared distance from the source position to the reconstructed coordinate of the event (θ^2).

[2]Internal VERITAS Memo

Template Reconstruction

Template-based reconstruction relies on finding the best-fit template to the data, instead of relying on pure geometric quantities. With VERITAS, this technique is called Shower Image Template Method (ITM), which is currently only implemented in VEGAS (Christiansen et al. 2017). A similar method is used in H.E.S.S. called ImPACT (Parsons et al. 2014). These methods rely on building templates based on large numbers of shower simulations to generate templates for different energies, depth of first interaction, zenith and azimuthal angles, and various core locations. Then, with an initial seed from the standard Hillas reconstruction, a best-fit template can be found for the data. In cases where there are missing pixels (like the edge of the camera or with broken photomultiplier tubes), these methods are less biased. This technique faces challenges due to simulation mismatch with the data and is prone to biases with small events. ITM does increase the sensitivity by $\sim 40\%$ compared to a standard Hillas analysis, making it the default choice for standard VEGAS analyses.

Reconstruction Uncertainty

All reconstruction techniques carry with them some uncertainty in the reconstruction. This is normally quantified at a very high level by the measurement of the spread of point sources or from the spread in the uncertainty of simulations. This is then averaged for certain configurations of zenith, azimuth, and energy and called the point spread function, or PSF. PSF is defined in several ways, although it is often nearly Gaussian, it is typically quoted as a containment radius, for example 68%, instead of a width, since there can be minor deviations from a Gaussian distribution. PSF is a quantity that is dependent on the instrument, the method of reconstruction, the quality of the particular event, and the size of the event. Since the size of the event is correlated with energy, PSF is also an energy-dependent quantity. For VERITAS at 200 GeV, it is approximately 0.16 degrees, but can be as low as 0.08 degrees.

For a standard analysis, only one source region is assessed regardless of energy. This circular region scales depending on the size of the PSF in order to maximize signal-to-noise. As the background in the on-region is roughly uniform as a func-

tion of area, and the PSF is roughly Gaussian, there is an ideal radius of integration beyond which you integrate a much higher fraction of background relative to signal. Thus, the performance of the reconstruction directly scales the sensitivity of the analysis as smaller PSFs allow for smaller source regions and therefore less integration of background. More advanced techniques have the ability to change the integration region as a function of energy to account for the variations in the PSF.

3.5 Gamma/Hadron Separation

Our next step, once our events have been parametrized, is rejecting the largest source of background, hadronic air showers. This process is known as *gamma/hadron separation*. As seen in Section 2.4, hadronic showers exhibit distinct physical characteristics due to the presence of various phenomena, such as pion decay. These differences are imprinted onto the Hillas parameters, resulting in an observed difference between hadronic and gamma-ray showers. For this discussion, when referring to gamma-rays as the initial particle, we also mean any purely electromagnetic air shower. In practice, gamma-ray-like events will be contaminated with an irreducible background of electrons, since electrons will produce a photon via bremsstrahlung and then be effectively indistinguishable from a photon-induced air shower. We refer to gamma/hadron separation instead of electromagnetic/hadronic since protons and photons dominate their respective samples.

There is a balance in gamma-hadron separation to be struck between the purity of the sample and the amount of the signal rejected. This balance has many names in different fields; in statistics, this is known as *type I/II errors* or false positives and false negatives. In the case of gamma-ray astronomy, we do not need to know if an individual event is a gamma ray; rather, we just would like to make a statistical argument about the ensemble. In most cases, the limit for the sensitivity of the analysis is the rate of photons detected, and it is acceptable to have a higher fraction of background as long as the statistical fluctuations in the background do not exceed the signal strength. In other words, for gamma-ray astronomy, we want to optimize for the *statistical significance of a source* rather than the purity of the sample. The T.-P. Li et al. (1983) function used for the statistical significance is discussed in

Section 4.1.

There are other reasonable choices of optimizations that could be chosen. VERITAS could optimize on reducing the error on the estimation of the spectral parameters, which in principle may be better for certain analyses where the source is far above the threshold of detection and the characterization of the source is the most important. Alternatively, we could optimize gamma-ray purity, enabling statistical studies of clustering to identify new transients and increasing the likelihood that they are astrophysical. The choice of significance is justified since most of the interesting VERITAS sources sit very close to the threshold, and having a standard method of gamma-hadron separation simplifies later steps of the analysis.

A final general note is that gamma/hadron separation also acts as a quality cut. Gamma-rays are expected to occupy a relatively narrow region of the Hillas parameters due to the symmetry of purely electromagnetic showers; poorly reconstructed events can have parameters that span a much larger region, see Figure 3.6. So these showers, where energy estimation or directional reconstruction may be poor, will also be rejected at a higher rate than well-reconstructed events.

Box Cuts

The simplest gamma/hadron rejection algorithm, known as *GEO* or *box cuts*, takes six Hillas Parameters and simply iterates through different combinations of accepted values until one finds the maximum of the significance function. All sources that pass cuts are considered gamma-rays, and all sources that fall outside are rejected.

To choose the cut parameters and values, a large sample of bright gamma-ray source data is selected, and different cuts are applied to the sample until a maximum of significance is reached. Often, the source counts that are passed into the significance calculation are downsampled to become $\sim 1-10\%$ of the original flux to allow optimization for different source brightnesses. It is also found that sources with different spectra require different cuts. As such, three sets of cuts are used for sources that are soft (power-law index $\sim$4), medium ($\sim$ 2), and hard ($<$2). The Hillas parameters used, along with the values for soft, medium, and hard cuts in VEGAS v2_5_10 are shown in Table 3.1. A parameter that also has to be

simultaneously optimized is θ or the size of the *ON* region. Typical distributions for two box cuts, for a gamma-ray dense part of the sky and for a background region, are shown in Figure 3.6.

Hillas Parameter	**Soft Cuts**	**Medium Cuts**	**Hard Cuts**
Mean Scaled Width	0.05/1.1	0.05/1.1	0.05/1.1
Mean Scaled Length	0.05/1.3	0.05/1.3	0.05/1.4
Distance [deg]	0/1.43	0/1.43	0/1.43
Shower Max Height [km]	$7/\infty$	$7/\infty$	$0/\infty$
Size [d.c.]	$400/\infty$	$700/\infty$	$1200/\infty$
N_{tubes}	5/499	5/499	5/499
θ^2 [deg^2]	0.03	0.01	0.01

Table 3.1 Cuts used for the VEGAS work in this thesis. The values are shown for three different spectral indices of sources, and shown as the $minimum/maximum$ value for the source to be accepted as a gamma-ray-like event.

Boosted decision trees

Boosted decision trees (BDTs) are a common form of machine learning that is often applied to discriminate between two samples. In VERITAS, an implementation of a BDT is used regularly by ED for gamma/hadron separation (Krause 2017). A BDT is a multivariate technique that can combine multiple parameters into a single discriminating variable. Like other machine learning techniques, the power comes from applying a generic non-linear functional form that can be used to leverage non-linear correlations between parameters and also weight parameters by their relative importance. BDTs show significant improvement over box cuts, with $\sim 15\%$ improvement to the sensitivity of analysis. BDTs are currently being implemented in VEGAS as well, but those results are not included in this work.

3.6 Background Estimation

Current analysis techniques after gamma-hadron separation do not assign a probability to each event of being a gamma-ray, but instead just create a list of gamma-

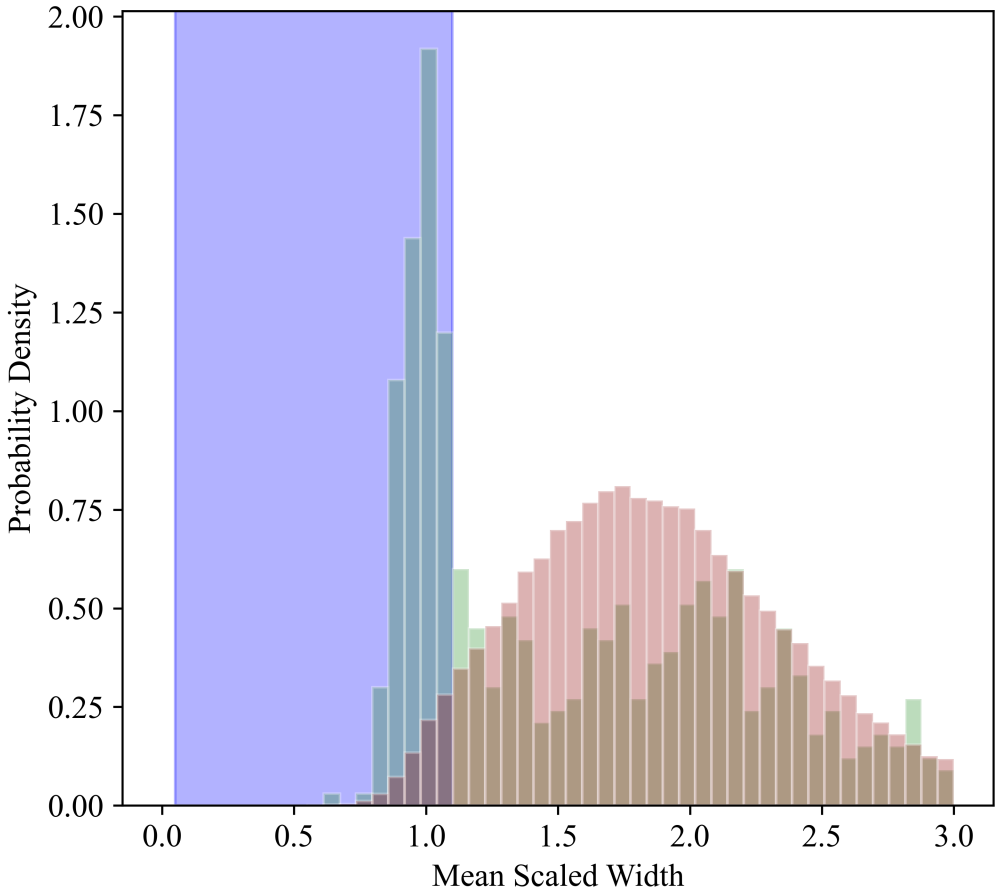

Figure 3.6 The blue region shows the events labeled as gamma-rays in VERITAS analysis. Two distributions are shown; the green shows the mean scaled width (MSCW) for events in a region of the sky with the Crab Nebula, which is the brightest persistent gamma-ray source in the Northern Hemisphere. In red is the distribution of MSCW for events in a background region with no known TeV source. The red distribution can be seen as reflective of a purely hadronic background, and the green can be seen as a mixture between gamma-rays and hadrons. A clear peak in the mixed distribution is seen in the region identified as gamma-rays in the analysis. Only reconstruction cuts have been applied.

like events. This list may still contain non-gamma-ray events (i.e., background), as well as the signal we seek, and these numbers must be quantified. That is, we seek to understand if the number of selected events is consistent with our estimate of the non-gamma-ray background, or if there is an excess that would represent a gamma-ray signal. Although the expected number of background events could be estimated entirely from simulations, it is desirable in analyses to estimate this from the observations. This allows for the effects of the unique conditions to be quantified from the observations, thus implicitly taking account of unique observation conditions such as elevation angle, night sky background levels, photomultiplier tube noise.

One important consideration for IACTs compared to other techniques is the non-uniform *acceptance*. Acceptance in this sense is defined as the relative sensitivity to gamma rays as a function of a parameter of interest. A high acceptance means a higher rate of detected gamma rays for the same signal strength. Considering acceptance is important because IACTs have a strong acceptance dependence as a function of the radial distance from the camera center.

On-Off Background Estimation

Historically, the most common form of background estimation was the use of *On/Off* observations. *On/Off* observations take one set of observations of a field with no known gamma-ray sources, followed by another observation of a field with a putative source. The total counts in a location in the source field are given as N_{on}, and the number of counts in the background region is given as N_{off}. Now, if the exposures are the same in both the *ON* and *OFF* observations, then regions in the same part of the FoV can be directly compared. However, if the exposures of one of the observations differ, then a scaling factor, $\alpha = \frac{t_{on}}{t_{off}}$, needs to be introduced. A discussion of how these three values are properly handled to convert to an unbiased statistic will be discussed in Section 4.1. Here, it is sufficient to observe that values of α less than 1 mean that we are considering more background (*Off*) time, leading to more statistical precision on the determination of the background since given a constant rate, the precision by which that rate can be experimentally determined increases with the duration of the observation.

The major advantage to *On/Off* observations is that they allow you to measure

the significance in the whole FoV. For sources where there are no regions where backgrounds can be estimated simultaneously then the on/off technique is still used (i.e. highly extended sources). The major disadvantage is that it is costly in terms of exposure time to collect data without sources, and as will be seen later, in order to approach similar α values to other techniques it requires a factor of 5 increase in the total exposure. Due to the limited potential observing time of IACTs and the already huge exposures required, this is not a viable method for most sources.

Wobble Background Estimation

The next estimation technique is *wobble* or *reflected regions*. The basic principle relies on first displacing the object from the center of the FoV to a position moderately offset, or to *wobble* your observations. IACT acceptance is maximum at the center of the FoV, and declines further out in the camera. To first order, the acceptance is azimuthally symmetric, although there are significant second-order effects caused by camera imperfections and the geometry of the array. If we ignore these effects and only consider the background as symmetric, then it's clear that we can estimate the background for a "wobbled" observation by comparing the source region to any region that is at the same radial distance from the camera center as the wobbled region. In fact, we could consider *every* region that is at the same radial distance and decrease our α by increasing the area of the observations instead of the exposure time. This allows for a minimization of α while not needing many observations. An illustration of the geometry can be seen in Figure 3.7.

The choice of the radial distance of the wobble affects the result both by increasing the number of potential off regions, but also by decreasing the acceptance. As such, a balance between the two is often chosen, with 0.5° observations being typical for VERITAS point sources. The second order effects of the lack of symmetry of the observations are also mitigated by not only wobbling in a single direction. Instead, VERITAS observations are typically wobbled in the four cardinal directions (in celestial coordinates) in roughly equal proportion. Although it is often the case that our observations are targeted at a source, sometimes that source position is not well known or the object is very extended. In those cases the radial separation

is increased to a value of 0.7°. This method does rely on having at least one region that is non-overlapping and located at the same radial distance from the center of the FoV as the putative source. For sources that overlap with the center of the camera, such a region does not exist, and so other methods must be used to estimate the background. This affects sources with uncertain positions and sources that are very extended.

Ring Background Estimation

Ring background is a method developed to help with some of the problems of wobble, while still not requiring dedicated *Off* observations. It takes an annulus around the test region, usually 0.7-1.0° for VERITAS, and then measures the background in that region. An example annulus can be seen in Figure 3.7. The difficulty comes from the estimation of α, which, unlike the previous methods, requires some knowledge or estimate of the shape of the acceptance. When assuming azimuthal symmetry, this is what is known as the *acceptance*. The acceptance can be measured by stacking all of the observations taken for a given source and, excluding the source, fitting a smoothly-varying function to the radial distribution (typically a low order spline). This acceptance can then be used to weight the size of the *Off* region by the relative ratio of the average acceptance, resulting in a correct scaling of the estimated background. The measurement of the radial acceptance is an imperfect process and does introduce a large systematic error, especially when performed with low statistics runlists. A second issue is that the radial acceptance is not constant with energy, meaning that often, unless one measures this acceptance at every energy, thereby re-entering the low statistics estimation regime where there are issues, one has an inaccurate estimate at higher energies. Because of this, ring background methods are normally only used to assess the overall significance at a sky location and not to measure the energy dependent background that may be needed to construct a spectrum.

FoV Background Method

FoV background is a more recent development for background estimation, and it seeks to correct for the second-order effects of asymmetries in the background.

It leverages a better prior on the distribution of the background to estimate the rate at a test location, by relying on the prior construction of a background model, which reflects the distribution of the background in the data. This can be driven by data when available, but can also be constructed using Monte-Carlo simulations. Backgrounds can be energy dependent and symmetric, in what is known as a 2D background, or non-symmetric, which is known as a 3D background. Whatever the style of the background, it is then re-normalized to the particular observations under study, excluding the source location. Even more sophisticated techniques involve the joint fitting of the source and background counts using this model. Unlike other methods, the field of view background technique does leverage every part of the observation in its background estimation, so it has the potential to have the lowest uncertainty. What is less clear is how to estimate this uncertainty on the background estimation. The error does not scale with, α as α is undefined. This will be discussed further in Section 4.1. The major issue with FoV background comes from overconfidence in the estimator due to model mismatch. This method is only as powerful as the reliability of the background model, which can often have issues due to simulations mismatching with data, or changes in the background rates between the observations that construct the models and the data that uses them. Thus the technique, although powerful, does require a careful estimation of the systematic biases.

Other Techniques

There are other methods for estimating background that try to improve on individual use cases but are not generally used for sources due to their degradation of sensitivity. The most common use case that requires a specialized estimate is for largely extended faint sources. One sophisticated technique is the matrix decomposition method (Acharyya et al. 2024b). Instead of directly constructing a background estimate using the average of the gamma-ray-like events in a background observation, it instead finds the principal eigenvectors of the moments of the reconstructed Cherenkov images. This allows the data background to be constructed from events not included in the final analysis (i.e. rejected events). The background of gamma-ray like events is then estimated from the background of non-gamma-

ray like events, because this ratio is the same for all observations taken in similar configurations.

3.7 Instrument Response Functions

Instrument response functions (IRFs) are maps that take instrument-measured quantities and convert them into physical units (like count rate to a flux). VERITAS currently implements 3 forms of IRF; an energy look-up table, an effective area, and a migration matrix. These are all produced in approximately the same way. Simulations are generated in *CORSIKA* covering the range of observed parameters of azimuth, zenith, noise, and offset (Dieter Heck et al. 2012). These are also processed through *GrOptics* (for simulating the optics of the VERITAS telescope) and *CARE*, which is used for simulating the camera electronics, including the trigger. A table summarizing the simulation's parameter space can be seen in Table 3.2. Once these simulations have been produced and passed through the trigger, the remaining events are analyzed through the typical cleaning and image analysis steps. These analyzed simulated events still contain the true values corresponding to their energy and flux, which we can use to reconstruct our efficiency and to quantify the error in our methods of converting to physical quantities like energy and direction.

Observing Parameter	**Simulation Values**
Azimuth (deg)	0,180
Zenith (deg)	0,20,30,35,40,50,55,60
Offset (deg)	0,0.25,0.5,0.75,1.0,1.25,1.5,1.75,2.0
Noise (MHz)	50,75,100,130,160,200,250,300,350,400,450

Table 3.2 Summary of the values of the simulation parameters used for the construction of VERITAS IRFs. Although the full range of noises and offsets are presented here, for some IRFs only a subset are used when appropriate.

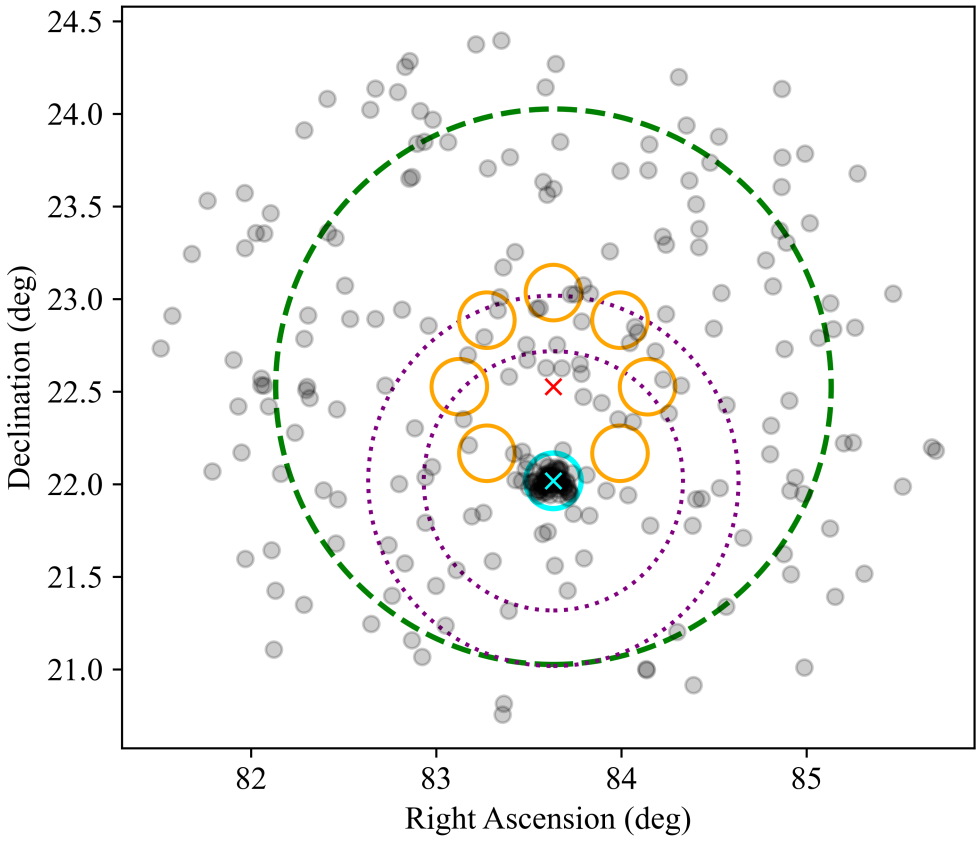

Figure 3.7 The gamma-ray locations for a typical observation of the Crab Nebula with three common background estimation regions over-plotted. The center of the telescope point is marked with a red cross. The location of the Crab Nebula is shown in cyan along with a typical integration radius. In orange, equally sized regions equidistant from the center are overplotted; these are *wobble* background regions. The field of view used to fit a template background in the *FoV* background method, is shown in green. Finally, in purple, the concentric rings of the *ring* background method are shown.

Energy Look-up Tables

A look-up table is a series of precalculated values for the combination of two or more values that encodes a complicated non-linear function. The first IRF is the energy look-up table, which takes the quantity of *size*, and the distance of the reconstruct event position from the array to estimate an event's energy. For values that fall between bins, energies are interpolated from the look-up table. Look-up tables have many of the same advantages that are resolved in modern problems with machine learning. They allow for a broad range of flexible transfer functions, and they offload much of the initial computational work to the generation of the table; when used, they require very little time per event.

Effective Areas

The effective area of a detector is a measure of the area over which a particle could arrive and be detected by the instrument, convoluted with the efficiency of detection. For a IACT, the typical area corresponds to a region on the ground where shower cores still produce detectable light at the location of the telescopes. An example of a VERITAS effective area can be seen in Figure 3.8. Initially, there is a rising efficiency as the showers increase in brightness and are also detectable across a larger region, before flattening out to approximately a constant value across all energies. Effective areas like the one presented here are often calculated for a fixed source integration radius (as how much of the PSF is integrated affects the function), but more modern effective areas do not include any fixed integration radii and instead pair themselves with the measured PSFs in order to be generically used for any integration radii. These are known as "full-enclosure" effective areas, and are currently used by some IACT's but not VERITAS.

3.8 Spectral Reconstruction

The final stage in the analysis is spectral reconstruction. Although spectral reconstruction may seem simple, there is an interesting divergence in the philosophy of reconstruction that appears. The simplest way that reconstruction can be performed, and the way VERITAS has traditionally reconstructed spectra, is by *un-*

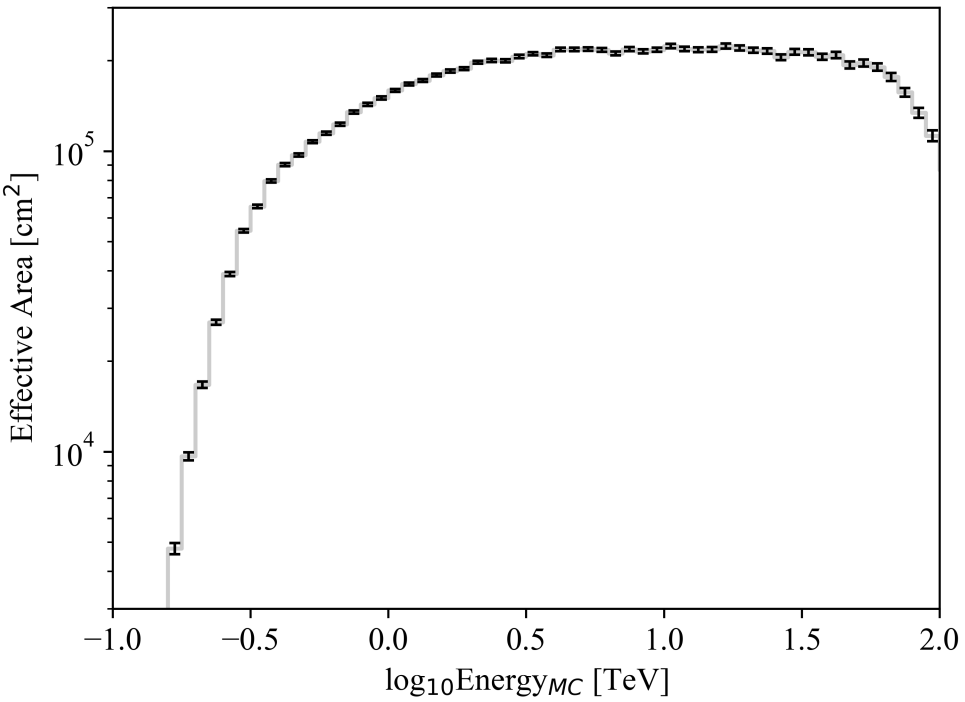

Figure 3.8 The typical VERITAS effective area for a given observation as a function of the true energy from the injected simulations. Errors emerge from the limited number of showers used to construct the effective area. A sharp cut-off appears at low energy before remaining relatively flat between 1-100 TeV. Note the vertical scale at the plateau, which is approximately the size of the Cherenkov light pool on the ground.

folding. Unfolding takes the effective area, as described in Section 3.7, and takes an energy range and divides the excess counts by the effective area. This unfolded data can then be compared to theoretical predictions or other physical values. The other method is *forward-folding*, where the effective area is instead applied to a model, which is then directly compared to the reconstructed data. While these two processes may seem equivalent, the binning effects and other details sometimes cause these two methods to have different results. The benefits of unfolding are that the results are model independent, meaning that others can use these points easily without additional information about the model that was used for the recon-

struction. We will use unfolding for our FRB results, as we do not have a strong model prior, and we will use forward folding when characterizing the details of blazars.

3.9 Validation

Validation is a critical process to ensure that a data analysis package is working effectively. Validation is simply ensuring that the instrument and analysis pipeline are producing reliable results and quantifying the systematic errors that cause deviations. Often, validation requires taking unique calibration data or even generating synthetic data. The simplest validation scenario would be if data taken with the instrument could be compared to an absolute prior on what the instrument should measure. In this case, one could simply investigate that data and quantify the differences. However, with most physics experiments, there is no reference source that can be readily used for a perfect validation. As we will see, we can still use some sources to test for consistency and some simulations to estimate absolute error; together, these can provide an incomplete but sufficient picture of the systematics.

In order to validate the VERITAS analysis, we perform several tests. The first test involves comparing the output of a standard analysis of the Crab Nebula across instruments and with previous observations. Any deviations from those historic values are used to estimate our "energy scale" systematic. The Crab Nebula is used because the source is bright at VHE and non-variable. This corresponds to the average error in the spectra reconstructed by VERITAS in each energy bin. An illustration of this energy scale validation can be seen in Figure 3.9. There are some issues with this validation, and it would not be sufficient to completely validate our IRF even if the agreement of the curves shown in Figure 3.9 was excellent. The first issue is that this validation relies on instruments that also cross-validate with VERITAS, so there is some lack of true independence of the reference measurements. Secondly, this test does not actually confirm that what the other instruments and VERITAS have measured is correct, but simply that the measurements are consistent. There are also some assumptions that are necessary about the stability of the VHE Crab nebula flux, although these appear to be well justified (C. B.

Adams et al. 2022). Typical values for the VERITAS energy-scaled systematic error are $\pm 20\%$.

Another validation that is performed is the construction of the "migration matrix". This is a measure of bias and error in reconstructing the energy of photons. It works by taking simulations at known energies, passing them through the analysis pipeline, and then producing a matrix comparing the reconstructed values to the generated values. For a VERITAS analysis, we define the "safe" energy range as the region where the bias (or average difference between the reconstructed and true energy) is below 5% and the precision (the scatter in the distribution of the reconstructed energy) is below 10%. A slice of the "migration matrix" can be seen in Figure 3.10.

An additional validation that is performed is to measure the distribution of significances in blank fields, i.e., fields where we believe there are no bright gamma-ray sources. This tests both our ability to properly measure background and whether we are in a valid regime for our statistical assumptions. The distribution of the statistic is normally measured to ensure that it is consistent with a mean of zero, and a standard deviation of one (i.e. normally distributed).

Many other parts of the VERITAS pipeline have been extensively studied, and other validations exist for many different parts. The validations described here are the regular validations that are performed every season, along with the generation of new IRFs.

Gammapy

Gammapy is a Python package that reads in a DL3 file, as defined in the *Data formats for gamma-ray astronomy* (Cosimo Nigro et al. 2021), and performs general high-level analysis, including background estimation, spectral reconstruction, and model fitting. A DL3 contains a list of parameterized events after gamma-hadron separation. This effectively can act as a replacement or substitute for various methods implemented in *VEGAS*. One of the major benefits of *Gammapy* is that, due to its adoption as the high-level analysis for the future CTAO instrument, there is a much larger set of tools and techniques that have been combined from the current generation of IACTs. Finally, using a consistent package between various IACT

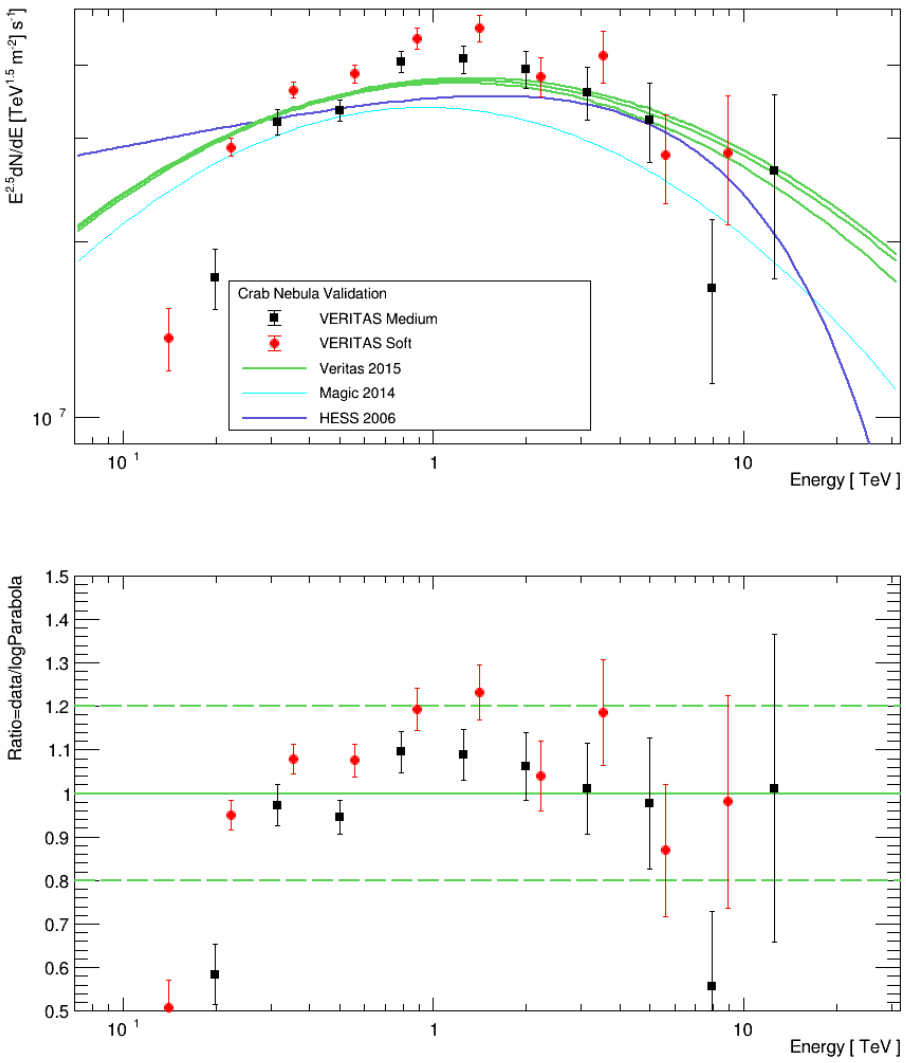

Figure 3.9 2024-2025 Winter validation of the VERITAS IRFs. The top figure shows the energy spectrum of the Crab Nebula reconstructed by VERITAS with two different sets of cuts: Medium and Soft, shown in black and red, respectively. Comparison spectra from Aharonian et al. (2006), Aleksić et al. (2016), and Park et al. (2015) are also shown. The bottom figure shows the residuals between the spectrum in Park et al. (2015) and the reconstructed points.

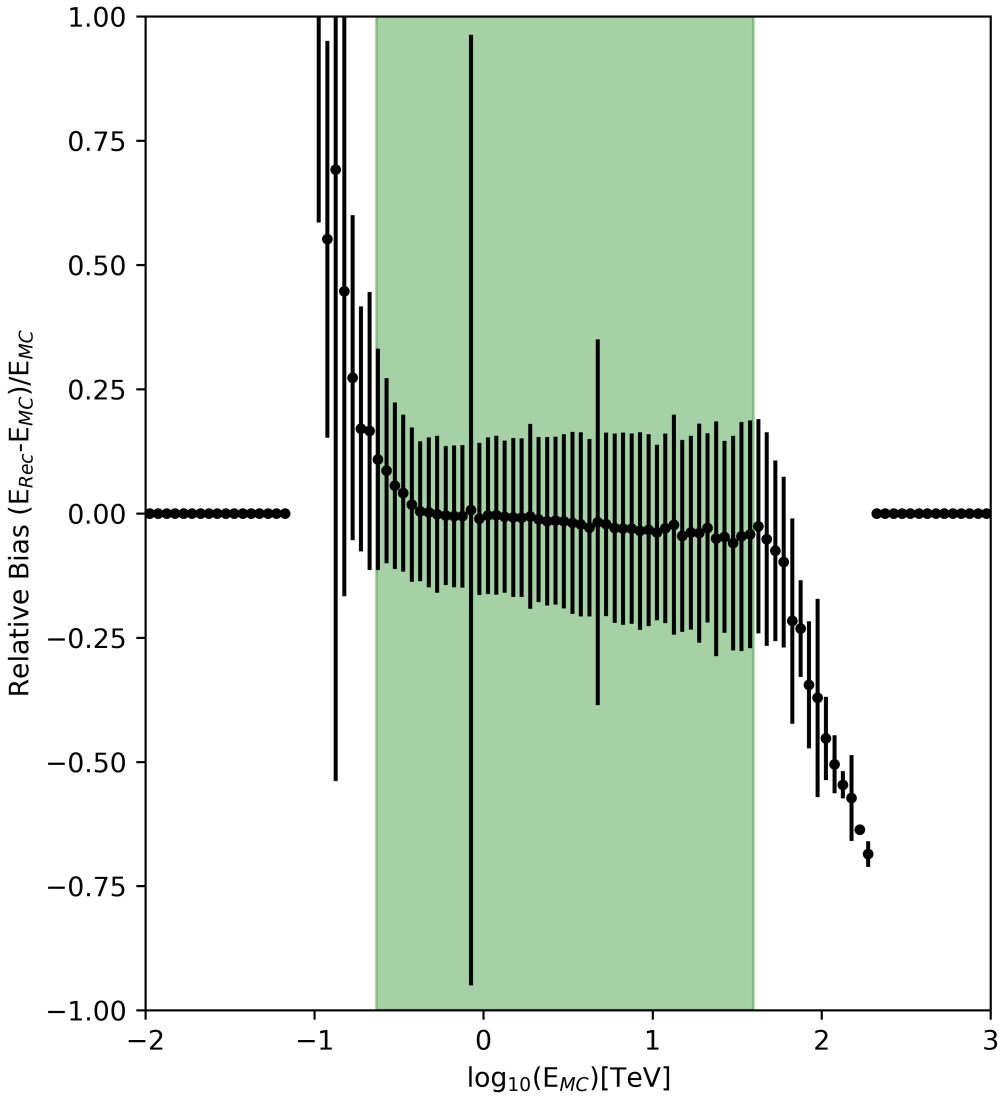

Figure 3.10 A typical slice of the migration matrix of VERITAS for the Image Template Method. Shown in green is the section selected for valid spectral reconstruction. Outside of this range is where a large bias appears or where events fail to reconstruct altogether. The uncertainty on each point represents the spread of the reconstructed energy (E_{rec}) from simulations at that Monte-Carlo energy (E_{mc}). The mean and standard deviation in the inset are calculated for the valid spectral region and can be viewed as an overall estimate of the bias. Outside the safe energy range, the bias is set to zero, as is convention.

instruments allows for simpler comparisons and combinations of the data from various instruments. Combining data allows us to reduce the effect of individual instrumental systematics and also increases the total exposure and coverage on various interesting sources.

Point Source V2DL3 Validation

Here we present a brief comparison between the validation for VEGAS as a low-level reconstruction technique, and *gammapy* is presented here for point sources. The work that these plots originate from[3] is the most complete cross-validation performed between these two high-level packages, and demonstrates that they produce consistent results within a small margin of error.

We produce six plots for validation; firstly, we compare the spectrum (dN/dE) for the Crab Nebula, reconstructed with VEGAS and *gammapy* (Figure 3.11). Next, we compare the number of *ON* events and the significances (Figure 3.12). Finally, we compare the results of the reconstructed Crab spectrum with previously published VERITAS results in $E^{2.5}\frac{\mathrm{d}N}{\mathrm{d}E}$ space. Comparisons with the spectrum of the Crab Nebula from M. Collaboration et al. (2015) and Aharonian et al. (2006) are also overlayed (Figure 3.13).

3.10 Determination of Sensitivity

One of the largest challenges of IACTs is the determination of sensitivity. Typical IACT observations between tens and hundreds of hours on a single source. Due to the time investments required, having a good understanding of the sensitivity of these instruments is desirable. Determination of sensitivity is also important when comparing significances across instruments and across analysis packages in order to determine when differences in results are expected.

To be clear, we discuss two types of sensitivity for IACTs, *differential sensitivity* and *integral sensitivity*. The integral sensitivity is a measure of how sensitive the instrument is to a detection, specifically how long it would take, in observations of a source at a specific flux level, to exclude the null hypothesis (i.e., that there is

[3] Internal Memo: Lundy 2024

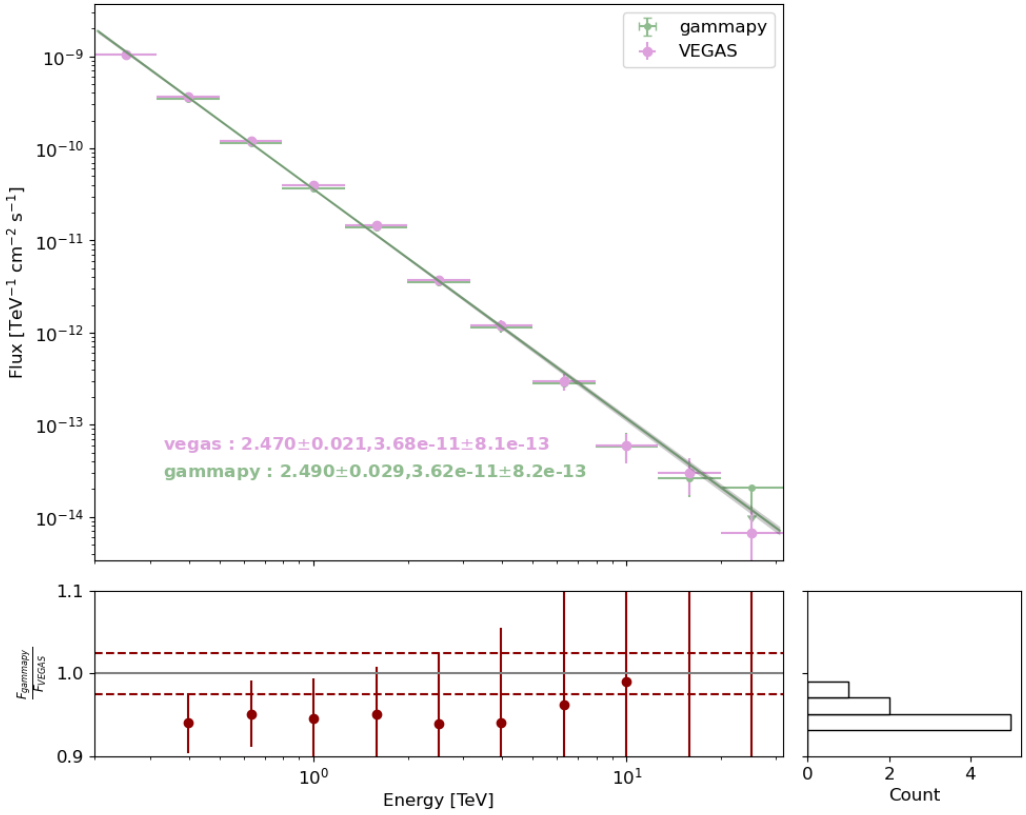

Figure 3.11 Comparison between the spectra of VEGAS and *gammapy* on the Crab Nebula. The top panel shows the two spectra with their best-fit power laws. The best fit spectral indices and normalization in units of $\mathrm{cm}^{-2}\mathrm{s}^{-1}\mathrm{TeV}^{-1}$ is shown. In the lower panel, the ratio between the two is shown, with a histogram of their distributions to the right.

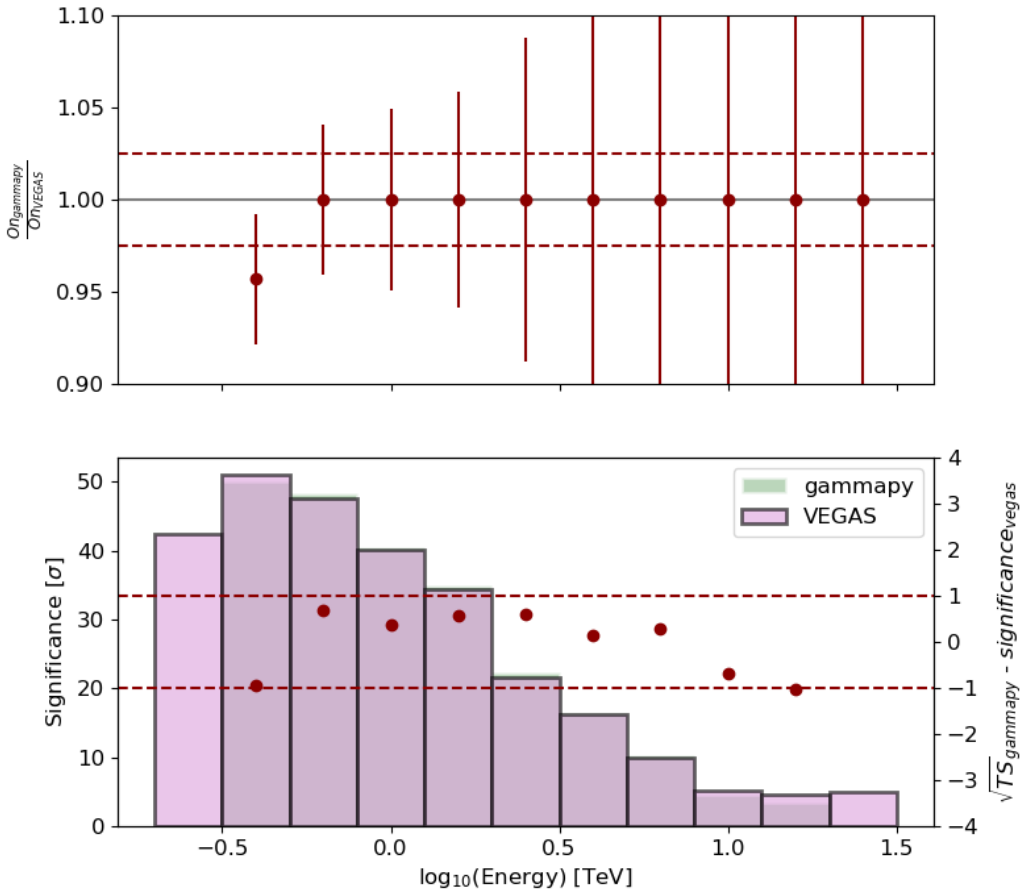

Figure 3.12 Comparison between the *On* events in *gammapy* and VEGAS from an analysis of the Crab Nebula. The top panel shows the comparison of the *On* events. Plots are taken from an internal memo where On is equivalent to ON in this text. At low energies, there are some differences due to how the packages handle thresholds, but the values are generally consistent. The bottom panel shows the significance of the excess for both packages as a function of energy. The small differences are overplotted as red markers (right scale). They all fall between $\pm 1\sigma$, consistent with small changes in the overall estimates of the background counts. The $\sqrt{TS}$, the square root of the test statistic, is shown and is equivalent to the T.-P. Li et al. (1983) significance for the statistic used.

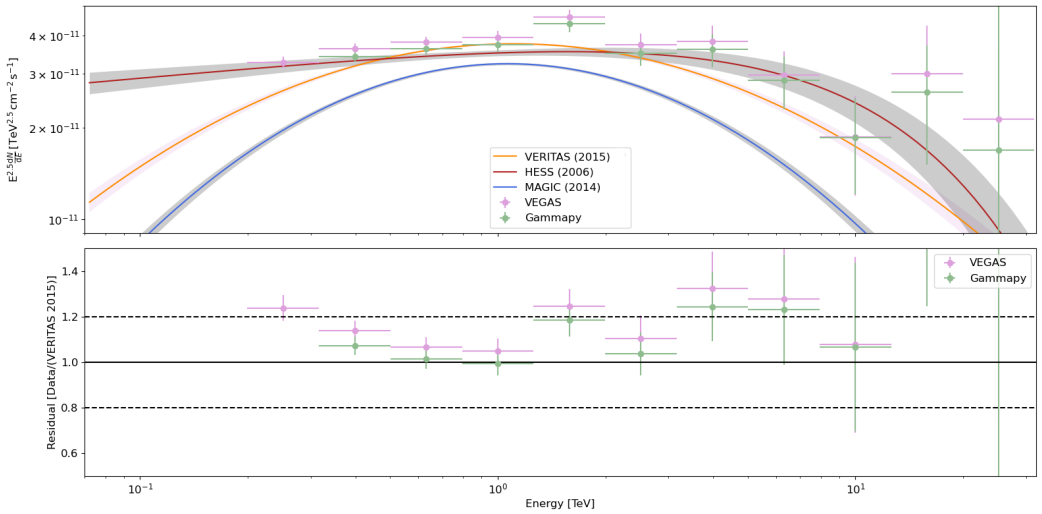

Figure 3.13 Similar to Figure 3.9 but for the validation of *gammapy* with the Crab Nebula. A smaller runlist is selected for this comparison, and instead of different cuts, different packages are compared to the same reference values. The differences between the packages are constrained by the overall systematic uncertainty.

no source emission) at the 5 σ level. The differential sensitivity is defined as the minimum flux that is required to obtain a significant spectral bin. Often, sensitivity values are quoted as what is required for a 2σ detection in a spectral bin. A plot of the VERITAS differential sensitivity is shown in Figure 3.14. However, the difference between the postulated spectral index and a specific source's index may result in sources above the nominal flux limit still being undetectable. Sensitivity can be calculated either by using simulations or data. The integral sensitivities are typically measured using the Crab Nebula or a similar bright persistent source.

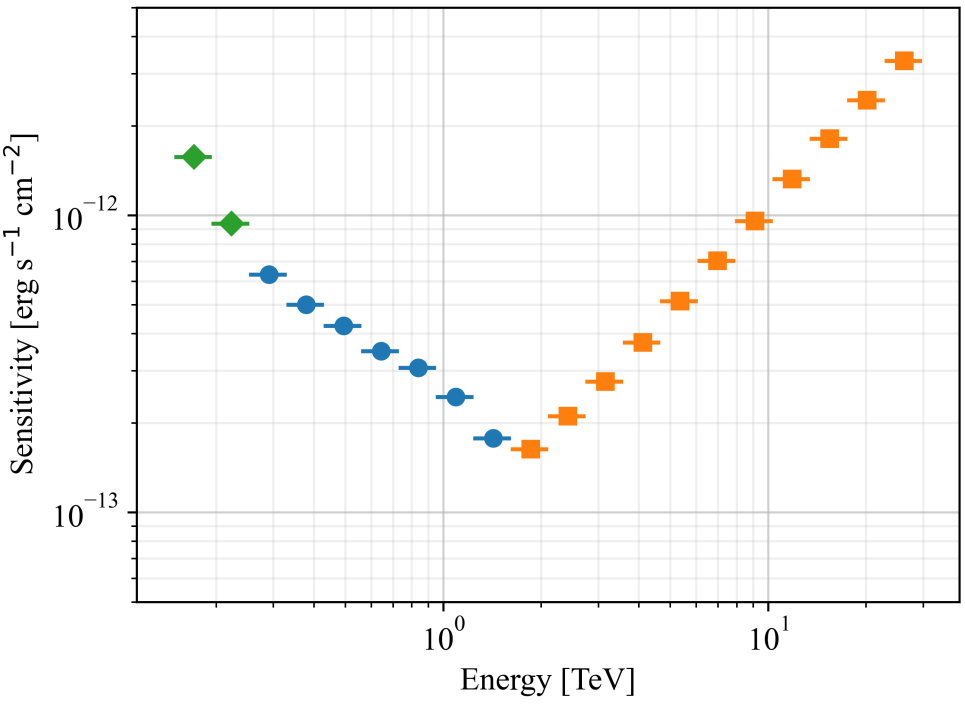

Figure 3.14 VERITAS 50 hour sensitivities calculated using *gammapy* for typical low zenith high quality observations. Three regimes limit the VERITAS differential sensitivity. In green diamonds, the background systematic fraction exceeds 15%; in blue circles, the significance is $< 2\sigma$, and in orange squares, the number of ON counts is less than three. The points show the minimum flux in each bin where VERITAS would still reconstruct a significant spectral point.

CHAPTER 4

The Transient Landscape

> [Courage] to me meant ploughing through that dull gray mist that comes down on life ... [a] sort of insistence on the value of life and the worth of transient things.
>
> F. Scott Fitzgerald, The Offshore Pirate

In the previous chapters, our instrument and the basic theoretical concepts of gamma-ray astronomy were presented. In this section, we highlight some key results of the field that are relevant to the search for rapid transients. We will also demonstrate some of the fundamental statistical processes employed in gamma-

ray astronomy, as the work presented here differs in some minor ways from other results reported in the literature. We will also discuss the overall strategies that have been used to measure variability in gamma-ray astronomy and examine some of their strengths and shortcomings to justify the choices made in the subsequent section.

4.1 Gamma-ray Astronomy Statistics

In gamma-ray astronomy, prominent issues include systematic uncertainties and low statistics, which means that a proper accounting of statistics plays a crucial role in avoiding overconfidence in results (Archambault et al. 2013). Traditionally, we have quoted a limit in VERITAS of a 5σ result (excluding the null hypothesis) to constitute a discovery. It is often implied that we will be using the (T.-P. Li et al. 1983) formulation of the significance[1] which is as follows:

$$\begin{aligned} S_{LiMa} = &\sqrt{2}\Big\{ N_{on} \ln \left[\frac{1+\alpha}{\alpha} \left(\frac{N_{on}}{N_{on}+N_{off}} \right) \right] \\ &+ N_{off} \ln \left[(1+\alpha) \left(\frac{N_{off}}{N_{on}+N_{off}} \right) \right] \Big\}^{1/2}, \end{aligned} \tag{4.1}$$

with N_{on} being the number of counts in the region selected for testing the null hypothesis, N_{off} being the measured number of counts in a region dominated by background, and α being a scaling value between the exposures of the two regions. The significance is quoted in a scale where it is roughly equivalent to the standard deviation of the normal distribution. This well-known equation is defined under the assumption of a Poisson-distributed signal and a Poisson-distributed background. Often in gamma-ray astronomy, our signals are Poisson-distributed because we are counting individual events at a constant and low rate. The background assumption is more complex and depends on the method used to estimate the number of expected background counts in the ON region. The three traditional background methods used by VERITAS, ON/OFF, wobble, and ring background,

[1] For all significances, it is conventional to include a positive or negative sign depending on the sign of $N_{on} - \alpha N_{off}$. Here, we assume this is the case for all significances throughout this work.

all count events in a background region, allowing these uncertainties to be well described as Poissonian.

Other newer background techniques can estimate the background without directly counting events. The most common of these techniques is *FoVBackground*, where the estimated background model is fit using a minimizer to the events in the field of view. The *FoVBackground* method scales and fits the template of the background to the observed count rate in the field. Two sources of uncertainty in the *FoVBackground* model come from the construction of the templates and the fitting of the templates. Normally, these background templates are either fit to the data using a minimizer like minuit, scipy, or sherpa, or they are scaled based on the total number of counts in the ON/OFF region, with uncertainty as follows:

$$M = \frac{(N_{counts} - N_{pred} + N_{bkg})}{N_{bkg}}, \tag{4.2}$$

$$E = \frac{\sqrt{(N_{counts} - N_{pred} + N_{bkg})}}{N_{bkg}}, \tag{4.3}$$

with M and E being the scale and the uncertainty of the normalization. It appears from these formulas, although it is not clear, that there is an assumption here of some Poisson uncertainty on the background. We have seen that for well-constructed backgrounds, this uncertainty is on the order of 3-5% in VERITAS data.

The significances reported using the *FoVBackground* method are normally reported using the Cash statistic (Cash 1979)[2] which ignores uncertainty on the background and a Poisson uncertainty on the signal. The significance of a signal using the Cash statistic can be formulated as:

$$S_{Cash} = \sqrt{2}\Big\{N_{on}\left[\ln\left(\frac{N_{on}}{N_{bkg}}\right) - 1\right] + N_{bkg}\Big\}^{1/2}. \tag{4.4}$$

If we take into account the uncertainty on the background, we can construct a conditional probability just as was done to derive Li & Ma in the case of a Poisson background. In the case of a Gaussian background, we then have a slightly different formulation that was previously derived in (Vianello 2018);

[2]It is worth mentioning here that *gammapy* also uses a statistic they refer to as "cstat". Cstat stands for Cash statistic and is simply a different formulation of the Cash statistic, depending on whether or not it is the background-subtracted number of counts inputted.

$$S_{Vian} = \sqrt{2}\left(N_{on}\ln\left(\frac{N_{on}}{B_0^{mle}}\right) + \frac{(N_{bkg} - B_0^{mle})^2}{2\sigma^2} + B_0^{mle} - N_{on}\right)^{1/2}, \tag{4.5}$$

with

$$B_0^{mle} = \frac{1}{2}\left(N_{bkg} - \sigma^2 + \sqrt{N_{bkg}^2 - 2N_{bkg}\sigma^2 + 4N_{on}\sigma^2 + \sigma^4}\right), \tag{4.6}$$

with σ being the variance of the normally distributed background. But, the statistics from Vianello (2018), T.-P. Li et al. (1983), and Cash (1979) all fail in the case of low background and signal statistics producing a non-normal distribution and overestimating or underestimating the confidence of the result. They all rely on the assumption that the signal is Gaussian in nature. It has been shown in T.-P. Li et al. (1983) that this is a poor estimator when $N_{bkg}, N_{on} < 10$. For many of the rapid transients under study here, it is essential to introduce a new statistic that accurately describes their behavior at low event rates. Such a statistic was derived in the work of Knoetig (2014), as we will refer to it as the Knoetig significance. The formulation is as follows:

$$S_{Knoe} = \sqrt{2}\,\mathrm{erf}^{-1}\left(1 - \frac{\gamma}{\gamma + \phi\delta}\right), \tag{4.7}$$

with erf^{-1}, referring to the inverse of the error function. γ, δ, ϕ are defined as:

$$\gamma = (1 + 2N_{bkg})\alpha^{1/2+N_{on}+N_{bkg}}\Gamma(1/2 + N_{on} + N_{bkg}), \tag{4.8}$$

$$\begin{aligned}\delta = {} & 2(1+\alpha)^{N_{on}+N_{off}}\,\Gamma(1 + N_{on} + N_{bkg}) \\ & \times\ {}_2F_1\left(\tfrac{1}{2} + N_{bkg}, 1 + N_{on} + N_{bkg}; \tfrac{3}{2} + N_{bkg}; -\tfrac{1}{\alpha}\right),\end{aligned} \tag{4.9}$$

$$\phi = \frac{\sqrt{\pi}}{2\arctan(1/\sqrt{\alpha})}. \tag{4.10}$$

Here, Γ is a gamma function and ${}_2F_1$ is a hypergeometric function. Although the equation encounters some practical implementation issues due to overflow with the Γ function, it remains valid for both large and small number of counts. Additionally, this Bayesian significance is well-defined around zero, making negative excesses unphysical, rather than adopting the negative significance convention of the other significances. This makes the handling of significance, but also the placement of upper limits, more precise.

Look-Elsewhere Effect/Trials

When investigating a gamma-ray observation, multiple tests are often conducted. These tests are referred to as trials, and due to the preferential selection of high-significance results, the true probability of obtaining at least one result above a certain significance level is sometimes significantly lower than the probability suggested by that level. The number of trials is often difficult to quantify. In the cases presented in this work, we consider the use of different cuts, temporal regions, or spatial regions; each represents a distinct trial. We do not treat each point in a sky map as a different trial, since we are not considering any uncertainty in the source position. If there were an excess in a different region of the map, we would not consider it. Instead, those maps are used purely for illustrating the overall systematic accuracy in background modeling, not for distinct statistical tests.

To apply the correction for this trials effect, sometimes known as the look-elsewhere effect, we apply a so-called "trials factor". This factor can be defined using Monte Carlo simulations, but in our case it is often sufficient to ask what the probability is of obtaining one value with at least probability p out of N trials. This gives the formula for a binomial trials factor of:

$$p_{post} = 1 - (1 - p)^N. \tag{4.11}$$

This conservative factor provides an estimate of the global probability of obtaining at least one p-value at that level. For the rest of this work, the post-trial significance should be considered as the more accurate measure of the true probability of any excess.

4.2 Techniques to Constrain Variability Timescales

In addition to the statistical tools for assessing excess, there are also similar tools that can be used to identify and quantify temporal variability. The challenge for these methods is not to overinterpret natural random clustering while accurately reconstructing the underlying properties of the flux distribution. Because of the

low statistics of our gamma-ray observations, this is a non-trivial determination. Broadly, the field has converged on several standard methods, including binned methods, Bayesian Block, Fourier Analysis, Unbinned Clustering Methods, and likelihood-based modeling.

Binned Methods

Binned methods are the simplest way of measuring temporal variability and are often used as a preliminary tool of investigation before a more detailed analysis can be applied. Binned methods use bins that are uniform in either the number of counts or in time duration. Then either the bin size is incremented until there is no significance in a majority of bins, or a prior bin choice well below the expected variability is selected. Suppose there is still variability between the bins (either by comparison to a constant model or some other evaluation). In that case, the bin duration is taken as the minimum duration of the variability. When the bin size can be reduced well below the variability timescale observed in the data, another technique for determining minimum variability is to take the minimum temporal distance between two bins in the light curve where the flux difference is a factor of two different.

Both of these simple methods have potential shortcomings. For example, the bin edges may not be ideally placed, resulting in rapid phenomena smeared between multiple bins. Additionally, if there is rapid variability, but it does not result in a flux doubling, instead producing some rapid fluctuation or oscillation, this will not be captured by these methods. These methods, though, are fairly robust and, for bright signals, should be consistent with the more detailed procedures explained below.

Bayesian Blocks

One of the most well-established techniques for characterizing variability when the number of events is sufficiently large is Bayesian Blocks (Scargle 1998; Scargle et al. 2013). There are many different variants and forms of Bayesian blocks, each sensitive to different time scales of variability. The problem that the Bayesian Blocks

approach initially seeks to solve is to subdivide the data into piecewise constant intervals with a variable number of change points. That is:

$$F(t) = \begin{cases} X_0 & -\infty < t < t_1 \\ X_1 & t_1 \leq t < t_2 \\ .. & \\ X_{N_{blocks}} & t_{N_{blocks}} < t < \infty \end{cases}, \tag{4.12}$$

where $F(t)$ is the flux as a function of time, and X_n is the amplitude of the flux after each change point n. The problem is determining the location of the change points and the number of blocks. Clearly, a best-fit model to any data set would be a separate time block for each data point, but this is not very useful. New segments should only be added when they significantly improve the global likelihood. It is also the case that we should prefer simpler models to more complex models. As such, it is natural to introduce a *prior* where the number of change points is much less than the number of individual data points. A geometric prior is often defined for this, where:

$$P(N_{blocks}) = \frac{1-\gamma}{1-\gamma^{N+1}}\gamma^{N_{blocks}}, \tag{4.13}$$

with γ being a parameter that dictates, by constant likelihood, the probability of finding more blocks, and N is the total number of data points (either time-tagged events or binned events). This geometric prior is an arbitrary but well-behaved choice, and other priors may be useful for other problems. Often, though, it is assumed that one is performing a Bayesian Blocks routine with this prior. The choice of γ is dependent on the probability for fake bins to emerge, and therefore the significance of any change point. However, determining this exact relationship is dependent on the number of data points and the type of signal. From simulations of noise-free Poissonian rates, an approximate formula for relating these quantities (with the probability of fake bins being p_0) is:

$$-\log\gamma = 4 - 73.53 p_0 N^{-0.478}, \tag{4.14}$$

with $-\log\gamma$ being what is referred to as **ncp_prior** in many Bayesian block implementations (Scargle et al. 2013). For values typical of VERITAS data, with between 10 and 50 counts, **ncp_prior** will vary from 2.9 to 3.4 (assuming a p_0 for 2σ). Although Bayesian blocks can be applied to binned data, binning removes some of

the detailed information about the arrival time of events and also sets a minimum timescale to the precision of the data. Therefore, if you assume a constant background rate, one can examine the events in a region directly and apply the analysis to them.

The Bayesian block algorithm is an iterative algorithm that iterates through the most optimal partition of N events. Let R denote the iteration, so for a given iteration, we calculate the optimal segmentation of R cells. The first iteration is trivial since it encompasses all data. At each stage, it can be demonstrated that the optimal segmentation at that stage must be the previous segmentation with only one additional partition, which can be calculated by iterating through all evaluated changepoints (usually occurring at fix values between data points) and evaluating the fitness function (a function that determines the likelihood, including the prior), and selecting the point that maximizes it. When using Bayesian Blocks, we will employ a modified implementation of the work by VanderPlas (2012).

Fourier Methods

Fourier methods are techniques that involve analyzing the power spectral density, or scaled Fourier transform, of the data. For many stochastic processes, such as those observed in the long-term evolution of blazars, one common way to assess the variability timescales is by analyzing the power spectral density. The key search criterion is for changes in the overall slope of the power spectral density, also known as a break. The breaks are thought to correspond to characteristic timescales intrinsic to the system (McHardy et al. 2006). This technique has long been employed in X-ray astronomy and also holds a prominent place in the study of blazar flares and long-term monitoring (McHardy et al. 2006). The problems with this method stem from unevenly sampled event-level data, which often lacks sufficient density to display a power spectral density with adequate resolution for a robust determination of the break timescale. As such, proper determinations of the uncertainty in the power spectral density functions often require careful consideration and construction of synthetic light curves (Emmanoulopoulos et al. 2013).

The method is robust when the statistics in the dataset are extensive. Unlike

Bayesian blocks, Fourier methods can also increase the significance of variations that have persistent characteristic timescales but may be fairly faint (as opposed to bright flares) even if they are non-periodic. The technique can also be easily extended to multiple datasets where the expected behaviour in frequency space is similar, but individual flaring events may not be.

Unbinned Clustering Methods

Unbinned clustering methods have been rarely used for blazar flares but are employed in other rapid transient searches, such as those for primordial black holes (Archambault et al. 2017). Unbinned clustering examines the relative distance between the arrival times and the spatial locations of events to search for excesses above an expected background. In some cases, the locations are also considered as flexible, and for other analyses, only temporal clustering is analyzed. The main issue is determining what the background is expected to be. To do this, event times are often scrambled with rejected hadronic events, assigning the time of a background event to an event that passes selection cuts. This effectively breaks any temporal correlations that exist and provides a random sample to determine the chance coincidences while preserving total counts and the relative temporal changes in background event rate. Then, different timescales are grouped together (i.e., all clusters 0.1 to 1 second in duration) so that a rate of background events can be measured for each timescale evaluated.

Unbinned clustering, although applicable to any timescale, is not as sensitive as methods that allow for a prior on the shape of the evolution. The flux of sources also needs to be high enough to produce a sufficient number of events within a window where the correlations can be detected above the background. Trials accounting is especially challenging with this method, often requiring a pessimistic number of trials due to the exhaustive search of all effective event arrival time combinations.

Lightcurve Model Methods

Lightcurve model methods are a series of likelihood-based methods where one assumes a model of the source and then determines the likelihood of the properties

of the emission based on the likelihood of a particular model. Like the previous methods, depending on how the analysis is carried out — prior to or post-binning — there can be some effects on the minimum timescale of the emission measured, which must be above the minimum binning scale. For determining the variability timescale, a temporal model is compared to a baseline evolution, and the best-fit duration of that model is quoted as the variability timescale. Standard models include exponentials or Gaussians with an underlying constant, persistent emission.

If the true temporal evolution of the sources matches the model that is being fit to the data exactly, then this prior on the shape adds additional information that the other methods ignore. However, if the model is incorrect, then it may still show a high significance but an unrealistic result. Since the significance of the result depends on the null hypothesis against which the model is compared, this method requires an exceptionally detailed understanding of the baseline evolution; otherwise, it may be prone to overconfidence in the results. It also fails if the underlying model is too complex for the data being fitted, as the underlying data may not contain sufficient information to span the degrees of freedom adequately.

4.3 Blazar Flares

Blazar flares are one of the most common phenomena observed by IACTs. Blazars are thought to be systems powered by a supermassive black hole ($\sim 10^{8-9} M_{\odot}$), which powers relativistic jets through the accretion of material (Event Horizon Telescope Collaboration et al. 2019; Cerruti 2020). They are the brightest persistent sources in the universe. In VHE, the emission that is seen is thought to be dominated by the jet. The relativistic beaming of this jet is also believed to cause many of the important signatures, such as the rapid variability seen in these sources (Wagner et al. 1995). There is still much we do not know about the structure of jets or where even the observed high-energy emission occurs. For a relatively modern review, see Böttcher (2019).

Blazars exhibit variations on a variety of timescales from minutes to years, with rapid changes in flux occurring on short timescales. These are often referred to as flares. A summary of the most rapid VHE flares observed to date can be seen in Table 4.1. One example of a rapid flare is the observation of PKS 2155-304 by

H.E.S.S. in 2006 (Aharonian et al. 2007), shown in Figure 4.1. At the time, this was the most rapid VHE variability observed for any VHE source, and due to the remarkable brightness of the flare, it still remains one of the most significant detections of minute-scale variability.

Observing more sources with similar or shorter minimum timescales has been a challenge. Although early work by MAGIC revealed a shorter timescale of variability in Mrk 501, no other blazar has been observed to vary at sub-minute timescales (J. Albert et al. 2007). Other types of blazars like flat spectrum radio quasars and radio galaxy systems, such as PKS 1222+21 and IC 310 have been added to the overall sample of rapidly varying sources since the MAGIC observations of Mrk 501, but they both are only seen to vary on a timescale of minutes (Aleksić et al. 2011; Aleksić et al. 2014). Still, the question remains whether the minimum timescale measured by MAGIC is a fundamental intrinsic property of blazars or whether this is still limited by the quality and number of observations of rapid blazar flares.

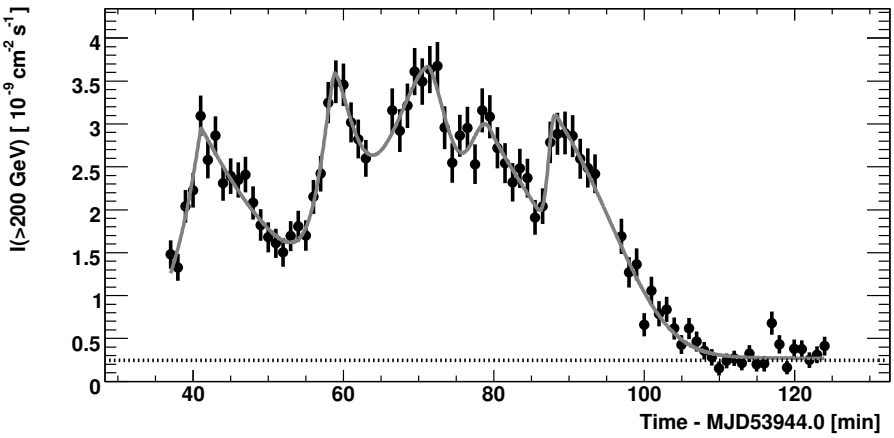

Figure 4.1 H.E.S.S. data for the VHE flux above 200 GeV for the 2006 flare of PKS 2155-304. Data is shown with one-minute binning. The dashed line shows the flux of the Crab Nebula, and the curve is a fit to the five bursts. Figure is taken from Aharonian et al. (2007).

Source Name	Year of Flare	Minimum Variability Timescale (s)	Method	Observatory
		BL Lacs		
1ES 1959+650	2012	~ 900	Binning	VERITAS
BL Lac	2011	780 ± 240	Model Fit	VERITAS
	2017	2160^{+480}_{-420}	Model Fit	VERITAS
Mrk 421	1996	$\sim$900	Binning	Whipple
	2010	1680^{+1200}_{-564}	Model Fit	VERITAS
Mrk 501	2007	50 ± 23	Model Fit	MAGIC
PKS 2155-304	2006	224 ± 60	Binning/Fourier	H.E.S.S.
		FSRQs		
PKS 1222+21	2010	516^{+66}_{-54}	Model Fit	MAGIC
		Other		
IC 310	2012	$\sim$294	Model Fit	MAGIC

Table 4.1 Summary table of detected minimum variability timescales of active galactic nuclei. Variability timescales are shown as the doubling/halving time or equivalent (Aliu et al. 2014; Aleksić et al. 2011; Aharonian et al. 2007; J. Albert et al. 2007; Abeysekara et al. 2020; Gaidos et al. 1996; Abeysekara et al. 2018; Arlen et al. 2013; Aleksić et al. 2014).

4.4 Pulsars and Magnetar Flares

Pulsars are the most rapid VHE phenomena currently measured, but only the periodic emission has been detected from these sources, and only from a relatively small sample. Only three pulsars are currently seen at VHE; their parameters are presented in Table 4.2.

Pulsed emission being detected at VHE suggests that there are emission processes capable of emitting rapid VHE emission. However, pulsars are not detected in single pulses by VHE; instead, it is the long integration of many periods before a statistical excess is recovered. In other wavelength bands, pulsars exhibit a range of transients at different timescales and fluxes (like giant pulses or flares), and detecting individual pulses is common. In the VHE though, due to their low flux, it may not be expected that current generation instruments could detect any of those normal pulsar transients. Indeed, no explosive pulsar transients have been seen by ground-based detectors. However, *Fermi*-LAT has reported the detection, based on a photon clustering analysis, of GeV emission from GRB 200415A and associated this emission with a magnetar giant flare in the Sculptor galaxy (Fermi-LAT Collaboration et al. 2021). Magnetar giant flares are bright flaring phenomena associated with highly magnetized neutron stars, and are the most energetic non-catalytic phenomena associated with stellar objects, with power thought to be originating from their magnetic energy reservoirs (Beniamini et al. 2025). Here non-cataclysmic means that the progenitor continues to persist after the event, unlike in the case of GRBs or similar cataclysmic events.

Extracting a spectrum for GRB 200415A, assuming a power-law, gives a flux of $(4.1 \pm 2.2)\ 10^{-6} \times \mathrm{cm}^{-2}\ \mathrm{s}^{-1}$ with an index of 1.7 ± 0.3 (Fermi-LAT Collaboration et al. 2021). This hard index and high flux would make this source detectable to current generation detectors like VERITAS. This, however, relies on the assumption that there exists no spectral change between the GeV and TeV emission, which has yet to be verified.

Source Name	Maximum Energy [GeV]	Variability Timescale	Observatory
		Pulsars	
Crab	1500	~ 0.7 ms	LAT, MAGIC, VERITAS, LST-1
Vela	20,000	~ 2 ms	LAT, H.E.S.S.
Geminga	75	~ 11 ms	LAT, MAGIC, LST-1
		Magnetar Flare	
GRB 200415A	1.7	~ 300 s	LAT

Table 4.2 Summary table of time scales and fluxes of pulsar processes in the VHE. Timescales are shown as 50% of the pulse or on-phase duration, which can be viewed as an upper limit of the duration of the rise/fall time. For the magnetar flare, the time scale is the duration of significant emission from *Fermi*-LAT.
References; Crab: VERITAS Collaboration et al. (2011), Ansoldi et al. (2016), and K. Abe et al. (2024); Vela: **h˙e˙s˙s˙collaboration˙discovery˙2023**; Geminga: MAGIC Collaboration et al. (2020) and K. Abe et al. (2025); GRB 200415A: Fermi-LAT Collaboration et al. (2021).

4.5 Fast Radio Bursts

To date, there has been no VHE emission detected from FRBs, although there have been numerous hints from nearby multi-messenger/wavelength bands. The most relevant search is Xing et al. (2024), which claims a GeV gamma-ray flare lasting 15.6 seconds in spatial coincidence with FRB 20240114A. The highest energy photon of this 6.1σ flare has an energy of 1.01 GeV. The measurement gives an implied index of 2.4$\pm$0.7 and a photon flux of 8.3×10^{-6} cm^{-2}s^{-1} (0.1–500 GeV). This would be well above the sensitivity of current IACT detectors, assuming no energetic cut-off. However, similar searches have evaluated the same data set and come to opposing conclusions (Principe et al. 2023; Principe et al. 2024). To date, this remains an intriguing excess that suggests the possibility of TeV emission from these sources.

Currently, the only X-ray or gamma-ray emission associated with an FRB-like burst originates from SGR 1935+2154. This source experienced an outburst in 2020, with X-ray emission observed by several instruments, including Insight-HMXT

(C. K. Li et al. 2021), INTEGRAL (Mereghetti et al. 2020), and Konus-Wind (Ridnaia et al. 2021). The burst was in temporal coincidence with a radio burst that was extremely luminous, as seen by CHIME (CHIME/FRB Collaboration et al. 2020b) and STARE2 (Bochenek et al. 2020), and if a similar luminosity burst occurred in a nearby galaxy, it would have also been bright enough to be detectable. This is the most robust detection of higher-energy transients from an FRB, as the burst occurred in both spatial and temporal coincidence with the bright radio emission. With the assumption that the emission is a synchrotron maser, one can scale the expected high-energy emission for the more luminous FRBs to predict the peak flux of the expected FRB counterparts (Margalit et al. 2020). These models predict that for the most luminous FRBs, one could have short-lived (millisecond) emission above 100 GeV. So, both from the theoretical extrapolation from galactic transients and from the observations of FRBs at ∼GeV energies, there is motivation for FRBs to be detectable by IACTs.

4.6 Gamma-ray Bursts and Other Transients

There exist two other classes of explosive transients seen by IACTs, namely novae and GRBs. Gamma-ray bursts are rare at VHE energies. Because of the high sensitivity of IACT, one might expect a high rate; however, to date, only five have been measured (Noda et al. 2022). Most gamma-ray bursts are undetectable at VHE, due to absorption from the extragalactic background light. There has been no VERITAS detection of a GRB yet. This appears to be largely due to poor weather and observing conditions on the few occasions that an IACT-observable GRB occurred.

No prompt emission has been seen from a GRB at VHE energies. Instead, what is measured is the fading afterglow. Although only 5 GRBs have VHE measured afterglows, and of those only 2 have resolvable light curves, it appears to be the case that the evolution of the light curves follows a fading power-law distribution parameterized as:

$$F(t) = At^{-\beta}, \tag{4.15}$$

with β being the characteristic index of the fading/brightening, A being the amplitude of the flux at time zero, and t being the time. Since GRBs follow a power-law,

they do not have a defined t_{50}. So when comparing to the exponential decay seen in blazar flares, we take the estimated timescale to be the time from the highest flux point to the next point that is less than 50%.

In cases where no resolvable evolution can be observed, a coarse limit on the variability timescale can be placed by considering the time between the last significant observation and the first non-significant detection. As an example, if the GRB is observed on the first night of observations but not on the second night, then we can place a rough estimate of the variability timescale of one day.

As can be seen in Table 4.3, these sources are relatively slow transients at VHE energies - much slower than blazar flares or pulsars. Although no short GRBs have been seen at VHE, there does exist the hint of a signal from GRB 160821B (Acciari et al. 2021). Although this was only detected at 3σ, it supports the hypothesis that other similar sources may be detectable.

Novae follow a generally similar behavior to GRBs in the VHE band. Novae are rare, bright thermonuclear bursts observed on white dwarfs. Although Fermi-LAT has seen over a dozen novae, IACTs have only detected a single eruption[3]. Like with the GRBs, what is seen is not a prompt event but instead a steadily fading afterglow following a power-law index. As such, even though novae are rapid transients at X-ray energies, it is not the case that they are rapid transient candidates in VHE.

[3] LAT Nova Catalog

Source Name	**Time of First Detection After Trigger (s)**	T_{50}/T_{200} **(s)**	**Observatory**
	Long Gamma-ray Bursts		
GRB 180720B	606	$< 1.1 \times 10^6$	H.E.S.S.
GRB 190114C	57	94	MAGIC
GRB 190829A	258	$< 9.3 \times 10^4$	H.E.S.S.
GRB 201216C	56	~ 800 s	MAGIC
GRB 221009A	0/230	~ 3 s	LHAASO
	Short Gamma-ray Bursts		
GRB 160821B	24	-	MAGIC
	Nova		
RS Oph	~ 86400	$1.7{\times}10^5$	H.E.S.S. + others

Table 4.3 Summary table of minimum variability timescales of tentative and detected gamma-ray bursts and shock-powered transients detected in VHE. For GRB 221009A, the observed timescale for the observations after 230s, when the source was detected by LHAASO. We take the H.E.S.S. parameters for RS Oph, as they present the most reliable variability.
References; GRB 180720B: Abdalla et al. (2019); GRB 190114C: Acciari et al. (2021); GRB 190829A: **h˙e˙s˙s˙collaboration˙revealing˙2021**; GRB 201216C: (H. Abe et al. 2024); GRB 221009A: Cao et al. (2023); RS Oph **h˙e˙s˙s˙collaboration˙time-resolved˙2022**.

CHAPTER 5

Observations of Fast Radio Bursts

> There is no folly of the beast of the earth which is not infinitely outdone by the madness of man.
>
> Herman Melville, Moby Dick

In this chapter, we will discuss the VERITAS observing program surrounding FRBs and present results of the analysis targeting these sources. Since there are different kinds of FRBs - those that repeat, those that are periodic, and even one-offs - we describe here in detail the target selection and the evolution of the observing program. This will include a discussion of the radio telescopes that observed the FRBs simultaneously with the VERITAS observations. We will then briefly summarize the results from the search through the targeted observations, which are dominated by repeating FRB (or "repeaters"). This will include a search for per-

sistent emission, a search for bursts targeted at the location of known FRBs, and finally a blind search for gamma-ray excesses. After this, an analysis of a coincident non-repeater burst in the FoV of VERITAS will be presented. This will be followed by a brief discussion of the implications of these results when compared to previous analyses of these sources.

Throughout the work on this thesis, naming conventions for FRBs have changed in the literature at least 3 times. The original naming convention for an FRB was just the date in the form of FRB YYMMDD, with FRB 121102 being a prototypical example. The naming convention then switched to include coordinates in the form FRB YYMMDD.JHHMM+DD, with FRB 180814.J0422+73 being an example. Finally, the Transient Name Server (TNS) names were agreed upon, in the form FRB YYYYMMDDi, where i is an alphabetical increment. This addresses two challenges with the previous naming schemes: for days with multiple detected bursts, the first naming scheme becomes confusing, and for FRBs where localizations improve with refined observations, having the coordinates be those of the first observation is often confusing. Repeaters are referred to by the first detected burst from the source. Hereafter, we will use the TNS names to refer to all sources, even though the source may not be referred to by that name in the cited publications.

5.1 Radio Triggers

VERITAS uses external radio observations to motivate and select targets to observe. These telescopes are used both to identify repeating sources and as references for determining if an FRB occurred during the observation. Although VERITAS monitors alerts through ATels of most major radio observatories, only two telescopes have a notable contribution to this work, due to their geographic position.

CHIME

The Canadian Hydrogen Intensity Mapping Experiment (CHIME) is a large FoV drift scan telescope located at the Dominion Astrophysical Radio Observatory

Figure 5.1 Image of one of the four CHIME radio dishes. Author included for scale (183 cm).

(CHIME Collaboration et al. 2022). The position of CHIME (49.32°, -119.62°, 545 m) relative to VERITAS allows for potential monitoring of any region of the instantaneous CHIME FoV at any time. CHIME is composed of four 100 m $\times$ 20 m semicylindrical dishes oriented North-South. An image of one of the four CHIME dishes can be seen in Figure 5.1. CHIME monitors the 400-800 MHz band, covering a sky area of over 200 deg^2. The combination of this FoV with a high sensitivity and powerful correlator makes CHIME one of the most powerful detectors for identifying new FRBs.

Green Bank Telescope

The Robert C. Byrd Green Bank Telescope (GBT) is a 100-m single dish radio telescope and is used in conjunction with VERITAS for early repeater observations (GBT Support Staff 2025). GBT operates in Pocahontas County, WV, United States, in a radio quiet zone (38.433121°, -79.839835°). The dedicated observations presented here were processed externally and communicated to VERITAS. The observations used in this text were taken with the Green Bank Ultimate Pulsar Processing Instrument (DuPlain et al. 2008). The data used to identify the burst for this work was taken with a bandwidth of 800 MHz centered at a frequency of 2000 MHz. The details of all GBT detections will be presented in a future publication and have been communicated to the author privately.

5.2 Summary of VERITAS Targeted Observing Program

VERITAS has collected over 200 hours of dedicated FRB observations. Most of these observations are strictly simultaneous with the time that the CHIME telescopes are monitoring the source. Scheduling is performed nightly to ensure that observations are only taken during CHIME transits. A breakdown of the exposures by source and by year is shown in Figure 5.2.

Early observations were taken in a mixture of wobble and non-wobble observations. Although not discussed in this work, VERITAS has a parasitic optical backend that is used to monitor the optical brightness of sources in selected pixels. To maximize the sampling rate, the number of pixels used must be minimized. Since VERITAS operates with altitude/azimuth mounts, there is field rotation present in the observations. In other words, objects rotate around the center of the camera during long observations. Therefore, to minimize the number of necessary pixels, the only place in the camera where a source can be placed is the center. This comes with the natural disadvantage of higher systematics due to acceptance corrections being necessary for background rejection, but it benefits from higher sensitivity and rapid optical coverage. This causes the sensitivity and systematics of VERITAS observations to change in the later exposures compared to early observations,

where the optical backend was not regularly used.

Another impact on the VERITAS observations is the change in pointing direction due to better source localization. The early VERITAS observations were originally targeted at the CHIME locations of highest probability. Early CHIME results, prior to ~ 2020 or online results, can have large error regions extending to ~ 3 degrees if one includes the small probability that the bursts occur in a sidelobe of the CHIME beam. Fortunately for VERITAS, even the average poor localization is smaller than the field of view of VERITAS, meaning that when a burst from the source has improved localization, it is very likely that the archival VERITAS exposures will/did have overlap with the improved localization region. Whenever an improved localization is provided, VERITAS updates the pointings used to ensure overlapping optical coverage, with the central pixel being monitored. So even though the optical is not the focus of the work, it has significant impacts on our VHE observations due to the constraints of the system, causing us to adapt our pointing strategy around it. A complete list of the final FRB coordinates and DMs used is shown in Table 5.2.

See below for a description of the particular details of the individual sources, why they were selected, and if there are unique considerations about their observing strategy. Since little was initially known about which FRB repeaters would be of interest, there was a dynamic evolution of the observing program in conjunction with the growing knowledge about the FRB population. The program quickly centered around targeted observations of CHIME observing windows, which continue to this day.

Initially, the VERITAS program was attempting to obtain the longest exposures at repeater locations. Thus, we observed every known repeater for the longest duration allowed by the observing schedule. We did not coordinate observations with the radio observatory for most of the follow-up, and we also did not focus on overlap with CHIME. This later changed to a focus on simultaneous bursts, which meant selecting repeaters with the most total bursts and observing them only when the source was transiting through the CHIME field of view. This decreases the overall exposure on the source but increases the overall rate of confirmed radio bursts during VERITAS observations. Currently, the VERITAS program operates in a triggered mode, only observing repeaters when they are in a hyperactive state.

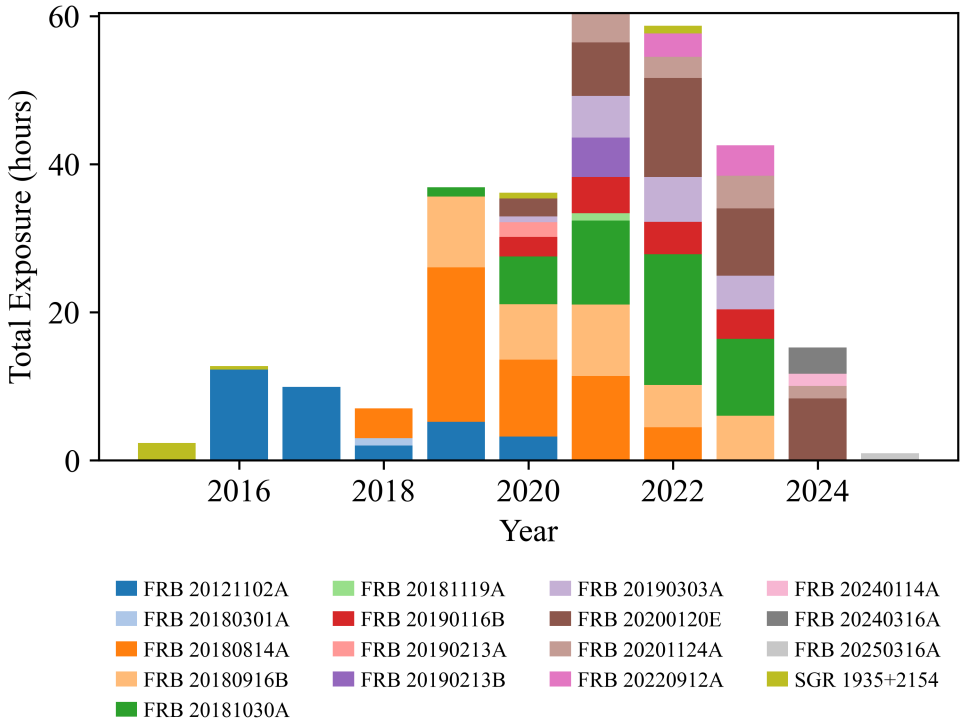

Figure 5.2 Summary of dedicated VERITAS observations of FRB repeaters and FRB-like sources. Colors are used to distinguish between different sources. Exposures are shown before quality selection.

This increases the density of overlapping bursts while minimizing the blank exposures. Currently, VERITAS attempts to observe FRBs which satisfy any of the following criteria:

- If any CHIME FRB has over three bursts detected in 2 minutes;
- If any CHIME FRB has over ten bursts in less than 10 days;
- If any FRB has over one hundred bursts detected by any instrument in less than 10 days;
- If any FRB has a counterpart candidate detection from another instrument.

This strategy has been in place since July 2024, and has resulted in the last three FRB sources observed by VERITAS, including the first non-repeater targeted since

FRB Name	**Right Ascension** (ICRS)	**Declination** (ICRS)	**Dispersion Measure** (pc cm^{-3})
		Non-repeaters	
20250316A	12h09m44.3s±0.1s	+58d50m56.7s±0.1s	161.3±0.4
		Repeaters	
20180301A	06h12m54.44s±0.63s	+04d40m15.8s ±0.61	536^{+8}_{-13}
20121102A	05h31m58.70s±0.1s	+33d08m52.5s±0.1s	558.1±3.3
20180814A	04h22m40.94s±23s	+73d39m16.20s±27s	190.8±1.5
20180916B	01h58m00.75017s±2.3mas	+65d43m00.3152s±2.3mas	348.76±0.10
20181030A	10h34m20.1s±30.6s	+73d45m05s±47s	103.5±0.3
20181119A	12h41m52s±36s	+65d07m02s±29s	364.05±0.09
20190116B	12h49m04s±66s	+27d09m50s±88s	444.99±0.5
20190213B	18h25m02s±20s	+81d24m05s±26s	302±1
20190213A*	02h14m00s±16m	+20d04m00±20m	651.45±0.05
	02h07m00s±16m	+20d05m00±20m	
20190303A	13h51m59s±11s	+48d07m16s±12s	222.4±0.7
20200120E	09h57m54.69935s±1.2mas	+68d49m00.8529s±1.3mas	87.7527±0.0003
20201124A	05h08m03.54s±0.05s	+26d03m38.4s±0.9s	414±3
20220912A	23h09m04.9s±2s	+48d42m25.4s±1s	219.46±0.04
20240114A	21h27m39.86s±1.4s	+ 04d19m45.01s±1.4s	527.65±0.01
20240316A	23h38m16.8s±36s	+32d19m48s±36s	351±1

Table 5.1 Summary of the FRB properties used in the VERITAS analysis. Errors are provided when quoted in the original work. Although there are minor DM changes for repeaters, the DM with the smallest localization error is selected for timing corrections.
*: No well-defined central R.A. for analysis, the first coordinates are used.

Sources: FRB 20180301A, FRB 20181030A, FRB 20190116B: CHIME/FRB Collaboration et al. (2024); FRB 20121102A: Chatterjee et al. (2017); FRB 20180814A: CHIME/FRB Collaboration et al. (2019a); FRB 20180916B: Marcote et al. (2020); FRB 20181030A: M. Bhardwaj et al. (2021b); FRB 20181119A, 20190303A, 20190213B: Michilli et al. (2023); FRB 20190213A: Fonseca et al. (2020); FRB 20200120E:Kirsten et al. (2022); FRB 20201124A: Fong et al. (2021); FRB 20220912A: Ravi et al. (2023) and McKinven et al. (2022); FRB 20240114A: Tian et al. (2024); FRB 20240316A: Curtin et al. (2024); FRB 20250316A Andrew et al. (2025) and Ng et al. (2025).

2018. In the following section, we will go through the notable FRBs that VERITAS has observed, and give a brief description when appropriate.

FRB 20180301A

FRB 180301 was the first targeted follow-up observation of an FRB by VERITAS. When the FRB was announced, VERITAS took a series of dedicated prompt exposures that were targeted at the location of the FRB. At the time, many automated alert systems were not equipped to distribute real-time alerts automatically, and so observations were substantially delayed from the time of measured radio emission. The initial detection was published in an ATel using Breakthrough Listen observations from the CSIRO Parkes radio telescope, with further details published in a subsequent analysis (Danny C. Price et al. 2018; D. C. Price et al. 2019). The burst was initially detected on 2018-03-01 at 07:34:19.76 UTC, with the ATel released with a ∼17-hour delay. VERITAS observations began approximately 5 days after the radio burst. In a subsequent analysis, due to the presence of a geosynchronous satellite, the authors could not rule out an anthropogenic origin (D. C. Price et al. 2019) or contamination resulting from sidelobe detection. Subsequent bursts detected by other instruments were able to confirm that this was indeed a repeating FRB (Luo et al. 2020). It was also localized to a star-forming galaxy at a distance of z = 0.3304 (Bhandari et al. 2022).

FRB 20121102A

FRB 20121102A was the first ever repeating FRB discovered, which allowed for the first time dedicated follow-up with both VERITAS and other instruments to attempt to preemptively observe the location of a FRB to anticipate future coincident bursts (L. G. Spitler et al. 2016; Josephy et al. 2019). FRB 20121102A shows evidence of periodicity with a 159.3 ± 0.8 day period in the L band (1-2 GHz). This is one of only two known periodic FRBs and has the longer period of the two (Cruces et al. 2021; CHIME/FRB Collaboration et al. 2020a). FRB 20121102A has also been well-localized by the VLA (Chatterjee et al. 2017; Tendulkar et al. 2017). This precise localization also means it is one of only 2 FRB at the time of writing with a persistent radio source (PRS). This compact emission region ($<$0.7 pc) is a constant, faint radio source in spatial coincidence with the location of the FRB repeater, and it is often thought to be directly connected to the progenitor of the FRB. FRB 20121102A is also likely the best-studied FRB in terms of both total radio hours and duration

of monitoring. All of these properties make FRB 20121102A an interesting source to observe, since its behavior and environment appear to make it unique.

FRB 20180814A

The second repeating FRB was the first repeating FRB identified by CHIME and was discovered during the commissioning of the instrument (CHIME/FRB Collaboration et al. 2019a). Also known as FRB 180814.J0422+73, this source was the first evidence of a broader class of repeating FRBs. It is also one of many repeating FRBs that are not significantly detected by other radio instruments. This is in contrast to FRB 20121102A, which to date has only been detected a single time by CHIME. The differing activity levels in different frequency bands could be indicative of distinct intrinsic source properties in the class of CHIME-detected sources compared to the general FRB population.

FRB 20180916B

FRB 20180916B is also one of the most well-studied FRBs as it is the only other periodic repeating FRB (CHIME/FRB Collaboration et al. 2020a). Also known as FRB 180916.J0158+65, it was originally discovered by CHIME but has been subsequently detected by many radio telescopes (CHIME/FRB Collaboration et al. 2019b). The source was localized to a spiral galaxy at a redshift of 0.0337 ± 0.0002 (Marcote et al. 2020). The period of the source is significantly lower than that of FRB 20121102A, with a best-fit period of 16.35 ± 0.15 days. The confirmed proximity of the source and the periodic behavior make it an interesting source for multi-wavelength follow-up, as the interactions with a potential binary system (which is suggested based on the duration of the orbital period) may lead to emission mechanisms that are not possible in isolated environments.

FRB 20181030A

Originally discovered by CHIME, this source was promising for follow-up due to its low DM (CHIME/FRB Collaboration et al. 2019b). The source was later localized to a nearby host galaxy, NGC 3252 (M. Bhardwaj et al. 2021b). This is a

star-forming galaxy, as opposed to some of the other hosts, such as dwarfs or spirals, where some later FRBs were localized. This is the first of the nearby FRB repeaters targeted by VERITAS, and they pose an interesting tension: since they are very close, we expect little absorption, so the resulting gamma-ray signal should be quite bright. But we may expect more energetic counterparts from more distant FRBs. Nearby sources have much lower energies for the detected bursts ($< 10^{35}$ erg) compared to more distant sources, which can reach energies above 10^{40} erg (M. Bhardwaj et al. 2021b). This effect happens when less luminous sources are more common than more luminous source so that searches that probe more distantly (integrating more volume), are more likely to detect the rarer more luminous sample. This is seen in many systems and is exemplified in nearby systems like FRB 20181030A.

FRB 20200120E

FRB 20200120E was first discovered by CHIME and, like FRB 20181030A, is primarily notable because of its small distance (M. Bhardwaj et al. 2021a). The localization was initially identified in the vicinity of M 81, with a distance of 3.63±0.34 Mpc (Karachentsev et al. 2002). This source has the lowest DM of any FRB, implying that it is the nearest FRB. Like FRB 20181030A, the bursts are not remarkably energetic and are well below the energies achievable by known magnetar bursts (M. Bhardwaj et al. 2021a). This means that magnetars are capable of producing bursts in the range of energies that overlap with this repeater. Improved localization of the FRB was not only found to be in M 81, but also in a nearby globular cluster (Kirsten et al. 2022). This tension of being both one of the systems that resembles a magnetar in terms of energetics, yet unlike Galactic magnetars in terms of its location, makes this a unique source that merits dedicated VERITAS observations.

FRB 20201124A

FRB 20201124A is a source originally announced by CHIME due to its high activity and was also seen by multiple radio instruments, including ASKAP, FAST, VLA, Effelsberg, uGMRT, and Stockert (Chime/Frb Collabortion 2021; Kumar et al. 2021; Xu et al. 2021; Law et al. 2021; L. Spitler et al. 2021; Wharton et al. 2021; Herrmann

2021). The source was localized to host galaxy SDSS J050803.48+260338.0 located at redshift 0.098±0.002 and the progenitor was further localized to a starforming region within the galaxy (Kilpatrick et al. 2021; Piro et al. 2021). Within the Milky Way, star-forming regions are locations where significant magnetar populations are found. Thus, the magnetar-driven model aligns well with this localization. Unlike previously discussed systems, there is no need to invoke alternative formation channels to explain this source with a magnetar model. This, combined with its high activity, makes this FRB an ideal source for follow-up.

FRB 20240114A

As briefly discussed in the last section, FRB 20240114A is the only FRB with emission observed above 1 GeV (Xing et al. 2024). The source was originally identified by CHIME and announced via ATel in Shin et al. (2024). Three bursts were initially detected by CHIME within approximately ten days, which, due to the low declination of the source of ~ 4 degrees implied and the extreme rate of bursts since the CHIME window in which the source was observed was very small. This was later confirmed with over 500 bursts seen by FAST (J. Zhang et al. 2024). The source was localized to a dwarf galaxy at a redshift of z = 0.13 (Mohit Bhardwaj et al. 2024).

The tentative GeV gamma-ray emission from this source makes it an interesting source to follow up with VERITAS (Xing et al. 2024). In Xing et al. (2024), the source emission appears to be significantly brighter for multiple weeks, with some of the significant emission being composed in part by at least one ~ 16 second flare. If confirmed, this would be an extremely unusual activity cycle that is not seen in any other currently known source. The results in Xing et al. (2024) do still need to be reconciled with other analyses on the same datasets yielding null results (Xing et al. 2024; Principe et al. 2024).

FRB 20250316A

This is the only recent targeted non-repeater observation by VERITAS. The high peak flux of the source (1.6 ± 0.1 kJy) led to the source being well localized to the nearby galaxy NGC 4141 with the CHIME baseband localization (Ng et al. 2025). The arcminute localization on its own would not be enough to merit targeted ob-

servations; however, a candidate Einstein Probe transient, EP J120944.2+585060, was observed in spatial coincidence with the FRB (Sun et al. 2025). A relatively bright X-ray luminosity (3×10^{39}erg/s) signalled a potential counterpart with higher energy emission. However, with further improved localization of the radio transient from 1 arcminute to approximately 150 milliarcseconds showed the overlap to be insignificant (CHIME/FRB Collaboration et al. 2025). The analysis of persistent emission is still presented in this work; however, the likelihood of detecting any potential counterpart has been significantly reduced.

SGR 1935+2154

SGR 1935+2154 is a Galactic magnetar and differs from the other objects under study in that it is primarily observed through its multi-wavelength emission, rather than in radio wavelengths. Since the source was discovered in 2014 by *Swift*-BAT, it has undergone numerous burst storms (Stamatikos et al. 2014; Younes et al. 2017). In the 2020 burst storm, a millisecond bright radio outburst referred to as FRB 2000428 was detected by CHIME and STARE2 in spatial coincidence with the magnetar and in temporal coincidence with a millisecond X-ray burst seen by multiple instruments (CHIME/FRB Collaboration et al. 2020b; Bochenek et al. 2020; C. K. Li et al. 2021; Mereghetti et al. 2020; Ridnaia et al. 2021). The burst was significantly less energetic than all bursts seen from cosmological FRBs at the time, leading to this being classfied as an "FRB-like" burst instead of an FRB. Since then, other nearby sources like FRB 20200120E, with low burst luminosities, have been detected, leading SGR 1935+2154 to appear more like a member of the class of low-lumosity FRB than a unique event (Margalit et al. 2020; Pearlman et al. 2025). For this work, we will assume the original X-ray localization: 19h 34m 55.68s +21d 53' 48.2" (Cummmings et al. 2014).

Other FRBs

FRB 20181119A, FRB 20190116B, FRB 20190213B, FRB 20190213A, FRB 20190303A, FRB 20220912A, FRB 20240316A are all additional sources selected for VERITAS observing. They were all selected based on their CHIME activity as reported through the CHIME/FRB Public Database and ATels (McKinven et al. 2022; T. Ab-

bott et al. 2024). After approximately a year or two of VERITAS observations, if the activity level is no longer high, observations tend to be terminated. For many of these sources, initial CHIME localizations were used before a refined "baseband" localization could be provided (Michilli et al. 2023; CHIME/FRB Collaboration et al. 2024). Baseband localizations from the offline analysis of CHIME significantly reduce the localization error, which is critical for our studies. The density of bursts occasionally allows for improved localizations from groups like MeerKAT or ASKAP, which we then use (Fong et al. 2021; Tian et al. 2024). For the final best-fit localization, refer to Table 5.1 and the corresponding citations.

5.3 Targeted Results

To search for emission from fast radio bursts, we assess three distinct emission schemes: persistent, prompt, and non-simultaneous. To account for a broad range of different models and to constrain as much information as possible about the emission. These analysis plans were defined a priori and were not optimized on the data. All VERITAS observations are processed with VEGAS v2_6_2 with CARE IRFs valid up to 2024. Gamma/hadron cuts are optimized for soft sources; since most FRBs are extragalactic, regardless of their intrinsic spectrum, significant extragalactic absorption will result in a softer measured spectrum.

Persistent Emission

The first analysis that is performed is for persistent emissions. This is a search for a continuous signal in the entire data set. Persistent emission imposes constraints on the average rate of excess emission from the region of the fast radio burst. This can place constraints on features such as a nebular component or a relationship to another bright, persistent source of gamma-ray emission. For the search for persistent emission, we impose higher run-quality selection criteria than for the search for prompt emission, so the exposure is smaller and may not overlap with the observations used in the later sections. The persistent analysis takes the entire exposure and stacks the events spatially to search for an excess above the expected background rate, assuming that the source is a point source at the most

probable region of the FRB. This analysis is performed for every source, with the background estimation coming from a ring-background estimator. The results of the persistent emission analysis can be seen in Figure 5.2.

For all sources in Table 5.1, no significant emission is detected; therefore, we apply the average effective area to determine a flux upper limit for the source, using the Feldman et al. (1998) method. Additionally, a stacked analysis is performed that takes into account the spatial significance of all sources, using the exposure-weighted α and effective area. These upper limits are presented in Table 5.2. In addition, the individual spatial significance maps of all regions surrounding the location of the source (the "sky maps") are presented in Appendix A. The observed count excesses in the sky maps are approximately normally distributed, so there is no evidence of significant systematics. In addition, an unweighted stacking analysis is performed, summing the on counts and off counts of all the repeaters using the average α.

Name	**On Counts**	**Off Counts**	α	**Significance** [σ]	**Exposure** [min]	**Flux Upper Limit** [10^{-13}cm^{-2} s^{-1}]	**Energy Range [TeV]**
Non-repeaters							
20250316A	17	433	0.037	0.26	31.11	89	0.263-30
Repeaters							
20180301A	42	1004	0.039	0.36	51.90	60	0.219-30
20121102A	725	15974	0.042	2.4	1005.52	28	0.219-30
20180814A	764	20578	0.038	-0.25	1869.58	26	0.457-30
20180916B	781	21994	0.037	-1.1	1522.1	5.0	0.316-30
20181030A	745	19236	0.042	-0.81	2182.0	11	0.457-30
20181119A	19	509	0.037	0.0	38.84	88	0.316-30
20190116B	536	12038	0.044	0.11	714.27	23	0.166-30
20190213B	47	1587	0.035	-1.08	244.79	6.6	0.661-30
20190213A	57	1527	0.041	-0.74	72.59	44	0.182-30
20190303A	509	14605	0.036	-1.01	828.10	13	0.200-30
20200120E	883	24364	0.037	-0.80	1886.04	5.8	0.316-30
20201124A	380	11421	0.037	-1.36	489.67	10	0.166-30
20220912A	197	4344	0.042	1.09	259.73	43	0.219-30
20240114A	45	1428	0.036	-0.83	78.49	22	0.263-30
20240316A	136	3465	0.037	0.59	156.92	59	0.166-30
SGR 1935+2154	69	1590	0.040	0.65	108.99	75	0.182-30
Stacked	5878	154137	0.039	-1.74	11436.94	2.2	0.116-30

Table 5.2 Summary of the persistent VHE emission limits from all targeted FRB observations by VERITAS. Due to the poor localization of FRB 20190213A it is not included in the stacking analysis, nor is the non-repeating FRB 20250316A.

Burst Search

Here we identify all FRB repeater bursts that are known to have occurred during or near simultaneous observations of VERITAS using the CHIME/FRB Public Database[1] and internal communications with GBT. We additionally searched for other bursts in the literature but did not find any bursts that were not included in the list compiled using CHIME and GBT. We first perform an analysis to find any bursts that overlap within 12 hours of a VERITAS observation.

Since VERITAS observations are scheduled to overlap with the whole of the CHIME window, you may expect that every burst that CHIME observes on a day with a VERITAS observation must have overlapping data. Several factors contribute to this not being strictly true, as the VERITAS telescope slew time, other scheduling priorities, and observer error often result in slight differences between the time of the VERITAS observation and the true transit of the source through the CHIME window. An additional factor to consider was that the "CHIME Transit Calculator" was used to estimate the width of the CHIME beam as a function of elevation[2] for early observations. The reported transit duration from the tool was closer to an effective exposure rather than a true temporal width. This led to an underestimation of the true width of the beam; therefore, a corrective factor of 1.3 was applied to increase the duration of subsequent observations to account for this underestimation. This results in many near-simultaneous VERITAS observations in the early exposures that are displaced by a few minutes from true simultaneity with CHIME.

A full summary is presented in Table 5.3 with all bursts that occurred on the same UTC day as a VERITAS observation. Those that occurred overlapping with a VERITAS observation are marked as "Simultaneous". The bursts are labelled with an internal incremental burst number that will be used to reference which of the VERITAS near or simultaneous bursts is being evaluated. The time of the burst is also presented. The times are given as measured by CHIME and GBT, with no barycentering or DM corrections applied. We find 73 bursts that match our criteria. Of those bursts, 56 are strictly simultaneous and are subsequently evaluated in more detail for excess emission. An additional column is present to identify the

[1] CHIME/FRB Public Database
[2] Transit Calculator

Number	Time of Burst	Detector	Optical	Simultaneous
	FRB 20121102A			
1	2017-11-25 10:21:21.988599803	GBT	✓	✓
2	2017-11-25 10:25:16.950316331	GBT		
3	2017-11-25 10:41:39.369934830	GBT	✓	✓
4	2017-11-25 10:52:56.631575148	GBT	✓	✓
5	2017-11-25 10:57:05.670177327	GBT		
6	2017-11-25 11:03:47.031237097	GBT	✓	✓
7	2017-11-25 11:04:43.337883884	GBT	✓	✓
8	2017-11-25 11:10:24.966647825	GBT	✓	✓
9	2017-11-25 11:19:37.994478238	GBT	✓	✓
10	2017-11-25 11:21:27.494566385	GBT	✓	✓
11	2017-11-25 11:22:06.061929110	GBT	✓	✓
12	2017-11-25 11:26:22.842135220	GBT	✓	✓
13	2017-11-25 11:26:55.133115021	GBT	✓	✓
14	2017-11-25 11:27:05.952617289	GBT	✓	✓
15	2017-11-25 11:28:20.245947344	GBT	✓	✓
16	2017-11-25 11:31:16.394918351	GBT	✓	✓
17	2017-11-25 11:45:54.152398976	GBT	✓	✓
18	2017-11-25 11:55:09.810515866	GBT		
	FRB 20180814A			
19	2019-09-29 11:58:34.000000	CHIME		
20	2019-10-29 09:41:58.675691	CHIME		✓
	FRB 20180916B			
21	2019-10-30 07:41:52.755579	CHIME		
22	2019-10-30 07:33:56.995676	CHIME		
23	2019-12-18 04:09:27.633710	CHIME		✓
24	2020-01-20 01:49:14.068615	CHIME		
25	2021-11-01 07:17:54.613657	CHIME		✓
26	2021-11-01 07:18:45.857564	CHIME		✓
27	2021-11-01 07:25:05.059348	CHIME		✓
28	2021-11-03 06:55:44.361963	CHIME		✓
29	2023-11-08 06:58:16.835878	CHIME		
30	2023-12-08 04:54:21.78998	CHIME	✓	✓
	FRB 20190303A			
31	2021-05-14 06:27:09.535040	CHIME		
32	2021-06-06 04:42:02.997504	CHIME		

Table 5.3 Summary of simultaneous FRBs observed during VERITAS observations.
Sources: GBT: Lynch (private communication, 2017); CHIME: T. C. Abbott et al. (2025)

Number	Time of Burst	Detector	Optical	Simultaneous
	FRB 20220912A			
33	2022-10-18 05:26:30.030315	CHIME	✓	✓
34	2022-10-20 05:23:14.433671	CHIME		
35	2022-10-21 05:07:29.149286	CHIME	✓	✓
36	2022-10-21 05:10:29.816309	CHIME	✓	✓
37	2022-10-25 04:54:08.848560	CHIME	✓	✓
38	2022-10-25 04:54:36.342223	CHIME	✓	✓
39	2022-10-25 04:56:56.783250	CHIME	✓	✓
40	2022-10-25 04:57:00.353651	CHIME	✓	✓
41	2022-10-25 04:58:31.398881	CHIME	✓	✓
42	2022-10-25 04:59:01.794478	CHIME	✓	✓
43	2022-11-17 03:24:16.880507	CHIME	✓	✓
44	2022-11-17 03:24:55.124695	CHIME	✓	✓
45	2022-11-17 03:25:44.646318	CHIME	✓	✓
46	2022-11-17 03:25:47.335913	CHIME	✓	✓
47	2022-11-17 03:25:56.773097	CHIME	✓	✓
48	2022-11-17 03:28:10.466539	CHIME	✓	✓
49	2022-11-18 03:19:57.600757	CHIME	✓	✓
50	2022-11-18 03:21:28.756091	CHIME	✓	✓
51	2022-11-19 03:18:14.042409	CHIME	✓	✓
52	2023-09-20 07:05:59.421058	CHIME		
53	2023-09-20 07:07:50.315835	CHIME		
54	2023-09-20 07:11:03.723056	CHIME	✓	✓
55	2023-09-20 07:16:05.917417	CHIME	✓	✓
56	2023-09-21 07:09:57.048366	CHIME	✓	✓
57	2023-09-21 07:12:40.012807	CHIME	✓	✓
58	2023-09-21 07:16:12.766254	CHIME		
59	2023-09-21 07:16:51.364339	CHIME		
60	2023-09-23 06:58:28.367900	CHIME	✓	✓
61	2023-09-23 06:59:16.819973	CHIME	✓	✓
62	2023-09-23 07:00:13.435215	CHIME	✓	✓
63	2023-09-23 07:11:13.802165	CHIME		
64	2023-10-11 05:49:01.990755	CHIME	✓	✓
65	2023-10-14 05:39:52.208924	CHIME	✓	✓
66	2023-10-15 05:28:49.607523	CHIME		
67	2023-10-16 05:31:01.286715	CHIME	✓	✓
68	2023-10-17 05:28:02.671296	CHIME	✓	✓
69	2023-10-18 05:22:19.112601	CHIME	✓	✓
70	2023-10-18 05:22:19.773204	CHIME	✓	✓
71	2023-10-18 05:25:12.017541	CHIME	✓	✓
72	2023-10-19 05:16:35.283548	CHIME	✓	✓
73	2023-11-07 04:02:25.915730	CHIME	✓	✓

Table 5.3 (continued)

radio observatory that detected the emission, and a final column labels whether the source is monitored by the VERITAS optical backend. The results of the parasitic optical backend are not included in this work; however, if there is a mark, it also indicates that the source is centered in the VERITAS observations. We further reduce this list by eight bursts due to exposures taken with only three VERITAS telescopes, causing higher systematics, reduced sensitivity, and challenges in flux reconstruction.

After identifying 48 bursts of interest, we take those arrival times and remove the time delay due to dispersion based on the frequency of the reported emission (ν), following:

$$t_{DM} = \frac{DM}{\nu} \frac{e^2}{2\pi m_e c}, \tag{5.1}$$

with e being the electric charge, m_e being the electron mass, and c the speed of light (Condon et al. 2016). Once this initial timing correction has been applied to the FRB time, there is also a correction to the solar system barycenter to avoid minor timing issues due to the different geographic positions of the radio observatory and the VERITAS instrument. These barycentering corrections are applied using the JPL ephemeris implemented in *Astropy* (Rhodes 2011; Astropy Collaboration et al. 2013; Astropy Collaboration et al. 2018; Astropy Collaboration et al. 2022). The same correction is then applied to the VERITAS events that fall into a region 0.1 degrees around the best fit FRB location in five temporal windows: $\pm 10^{-3}$,$\pm 10^{-2}$,$\pm 10^{-1}$,$\pm 10^{0}$,$\pm 10^{1}$ seconds.

The gamma-ray background is then estimated using the entire run and a ring background analysis with a 0.6-0.8 degree annulus. This assumes that the background rate is stable over 30 minutes, which is true of most high-quality VERITAS observations. Since the entire duration of the run is used, the value of α is very small, and the background count rate used to estimate the background is on the order of hundreds of counts; therefore, using numerically unstable significance estimators produces unreliable results. Instead, initial results are presented using the estimation from T.-P. Li et al. (1983). This also facilitates easy comparison with other results in the literature; however, it should not be interpreted as a reliable measure of significance. Also presented is a stacked analysis using the average α, the sum of the off-counts, and the sum of the on-counts. No weighting is applied to the individual FRBs, in order to avoid bias due to a model-dependent prior.

In the 48x5 bins, find only one bin with a hint of significant emission ($> 3\sigma$), which corresponds to burst 67 in the 1-second window. For this burst, we apply a more rigorous statistical treatment using the significance as described in Knoetig (2014). This results in a pre-trial significance of 3.8σ. We then apply a trials factor for 240 trials, resulting in a final significance of 2.1σ. Since there are no significant detections, integral upper limits are then calculated using the average effective area and dead time throughout the run, as described in Feldman et al. (1998).

Blind Search

Since no emission was observed in either the persistent case or the burst case, a search was conducted "blindly" to look for narrow (temporally) emission occurring at any time in the observations at the spatial location of the repeater. There are multiple techniques that can be used to search for excess without prior knowledge of the burst time. The simplest method one could consider is to evaluate all time bins in a run. However, this comes with a statistical penalty of the trials factor as described in Section 4.1, as well as being inefficient and computationally expensive. Most runs can be rejected outright due to having insufficient counts to be statistically significant, even if those events were clustered tightly temporally.

Consider a typical VERITAS run that lasts 500 seconds, with a typical background rate of 0.01 counts/s and an $\alpha = 0.1$. If we are searching for 0.001-second transients, then we require six counts in a bin to achieve a 5σ result pre-trials. However, there are 5×10^5 trials; for a post-trial significance of 5 σ, 12 counts are required. That 12-count excess, when considered over the entire 500-second run with 50 background events, leads to a 3 σ excess. Thus, we can start by identifying runs with a run-wise 3 σ excess, before moving to smaller windows. We present the results of this run-by-run significance in Appendix C.

A single VERITAS run of interest is identified on FRB 20121102A, which exhibits a run-wise excess at a statistical significance of 3.8σ. This run was taken during the early stages of VERITAS exposures in wobble, allowing for both a ring background and a wobble background to be calculated for cross-validation of the background estimation. Detailed information about this VERITAS exposure is presented in Table 5.4. A spatial significance distribution can be seen in Figure 5.3.

In the next step, the run was then subdivided into the same bin sizes used for the targeted burst search. In all bins below 10^0 s, no bins contained more than two events. In the 10^1 s bins, the most significant bin contained 3 On counts, which does not result in a significant detection when considering the $> 90,000$ trials present in the search through this single run. This lack of significance, when considering the statistical selection effects properly, is reinforced by an independent analysis performed on this observation using EventDisplay, which yielded no significant excess throughout the duration of the exposure. Interpreting this single excess as a normal statistical excursion, we find no significant excess in the blind search through all of the VERITAS exposures.

Parameter	**Value**
Run Information	
Start Time	2017-09-27 10:24:30.13
Duration [s]	1800.4
Mean Elevation [deg]	65.9
Mean Right Ascension	05:35:32.2
Mean Declination	+33:08:39.8
Wobble Background	
On Counts	38
Off Counts	222
α	0.077
Pre-trial Significance [σ]	4.14
Ring Background	
On Counts	39
Off Counts	420
α	0.046
Pre-trial Significance [σ]	3.83

Table 5.4 Information for the one VERITAS run (Run Number: 87120) above the excess threshold for a refined blind analysis. The duration and configuration of the observations are reported, along with the two significances.

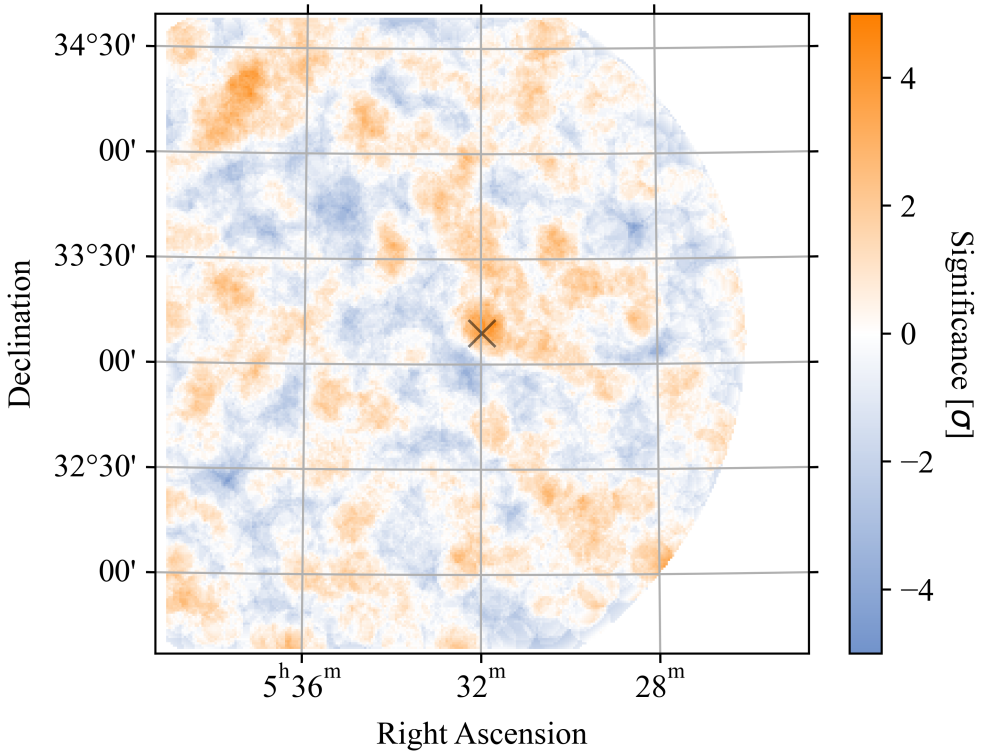

Figure 5.3 Spatial significance of the excess in a single run VERITAS exposure on 2017-09-27 on FRB 20121102A. The statistical excess observed at the source location is a pre-trial value, and a proper treatment of the trial factor reduces the overall magnitude of the significance across the map.

5.4 Coincident Non-Repeaters

Since no emission was found for any targeted repeating FRB, the parameter space of non-repeaters was explored. These observations are more difficult to obtain and are mostly due to chance coincidence. To place prompt limits on a non-repeater, even with the fastest telescope, observations cannot be triggered by radio detections of fast radio bursts, as the delays in propagation time between radio and high-energy bands result in prompt gamma-ray emission occurring prior to the detection time of radio emission. Therefore, obtaining these observations relies on a triple coincidence; an FRB must occur, be visible in the CHIME file of view, and

be within the VERITAS field of view. The rate of these can be increased by increasing the VERITAS overlap with CHIME, and there were early attempts to increase the overlap by planning VERITAS observations to occur 30 minutes past culmination where the VERITAS field of view overlaps with the CHIME field of view[3]. This practice was only in place for several months and was found to add too much complexity to an already complex VERITAS observing schedule; therefore, the coincident overlaps are now less frequent.

Instead, VERITAS now passively monitors alerts from CHIME through VOEvents, an alert system that provides initial FRB position and times (T. C. Abbott et al. 2025). This search can be used to identify candidate events for later refinement and analysis. It is also used to prompt extended observations of certain fields when high-significance events overlap with the VERITAS field of view.

An initial search was performed for any FRB event, not labelled as a repeater, where the 95% error region of the event overlapped with the typical VERITAS 1.75 degree radius of the pointing direction. The VERITAS run also needed to occur within 10 hours of the burst arrival time. The sample was reduced further by removing any source with an error region with a radius larger than 5 degrees, or if it was later retracted. The VERITAS runs were also inspected, with any associations with problematic or calibration runs removed. The results of this search can be seen in Table 5.5, with seven overlapping runs and six bursts. One burst was of particular interest: FRB 20240509A, which occurred during the VERITAS exposure. This source was selected for an independent analysis, which is presented below.

FRB 20240509A

FRB 20240509A is a likely non-repeating FRB identified by CHIME, with detailed information presented in Table 5.6. The dynamic burst spectra, or "waterfall" plot, is shown in Figure 5.6. Refined quantities from the offline baseband analysis are included and used as the default for the location of the spatial analysis and the timing corrections when available.

[3]VERITAS normally observes sources near culmination, but this is a fairly flexible requirement. The main benefit is a decreased threshold, which increases sensitivity for most sources. However, for some especially hard sources, targeted observations may be taken as low as possible to maximize the effective area above 1 TeV.

Since it is important for the implications of the search whether the source is a repeater or non-repeater, we apply a new technique based on the work in Pleunis et al. (2021) to assign a likelihood that the source is a repeater or non-repeater based on a Gaussian process classifier (GPC) and the morphology of the burst. Gaussian process classifiers model the underlying non-linear function that maps a series of features into a binary classification (Pedregosa et al. 2011). The advantage over other classifiers is that, in addition to a label, they also provide a confidence. We supplied our classifier with a series of labelled repeaters and non-repeaters from the first CHIME catalog (CHIME/FRB Collaboration et al. 2021). Although this naturally contains contamination of some non-repeaters that may later be identified as repeaters, it gives an initial estimate of the likelihood. The GPC used here was based on a *scikit-learn* implementation (Pedregosa et al. 2011). This analysis revealed that FRB 20240509A has a probability of being a non-repeater of greater than 99%. This is not surprising as the visible narrow and broadband features are characteristic of other sources that have not been seen to repeat.

Search for Excess VHE Emission from FRB 20240509A

Similar to the targeted observations, we apply multiple searches for excess emission from this source. In Figure 5.5 we show a spatial sky map for the duration of the total VERITAS observation. No excess emission is observed at the source location, so we reduce the number of temporal windows to three. All events are barycentered and dispersion corrected as was performed with the non-repeaters. Slightly different windows were selected due to the null results of the repeaters and to reduce the number of trials in this analysis; the narrowest window used in the repeater analysis was excluded. The trials factor is more important here than in the repeater analysis, since any excess seen with repeaters should be able to be replicated with subsequent follow-up; this cannot be done with non-repeaters. We also change the duration of the 10-second window to cover the entire duration of the run, and it can be viewed closer to a persistent limit or an afterglow-like limit. The results of these window searches can be seen in Table 5.7. This is presented along with upper limits in the case of null detections. To illustrate the window search and demonstrate the stability of the background rate, a temporal histogram

is displayed in Figure 5.6. Background estimation is more robust with the non-repeaters, as the Wobble background can be used instead of the ring-background method.

Referring to Table 5.7, no excesses are seen in any of the windows evaluated, and as such, upper limits are placed using the standard (Rolke et al. 2001) method.

PATH, and the PAN-STAARS catalog were used to search for a host to FRB 20240509A (Aggarwal et al. 2021). Finding no potential hosts, we estimate distance using *Fruitbat* along with the YMW16 galactic free electron model (Batten 2019; Yao et al. 2017). This gives an estimated distance of z$\sim$ 0.87. This rough estimate enables the placement of constraints on the intrinsic emission, allowing for cross-comparison of our results to other observations of localized sources. Our constraints can be seen in Figure 5.7.

FRB TNS Name	Spatial Separation (°)	Localization Error (°)	Temporal Separation (s)
FRB 20211103F	2.23	0.82	+886
FRB 20211112C	0.54	0.24	-4751
FRB 20211112C	1.46	0.24	-2919
FRB 20220105C	2.63	1.63	-2173
FRB 20230920A	2.01	0.73	+180
FRB 20240507A	1.54	0.50	-4057
FRB 20240509A	1.52	0.49	0

Table 5.5 List of non-repeating candidate FRBs that occurred near VERITAS observations. Spatial and temporal separation are from the time and location of the FRB to the central pointing and beginning/end of the nearest VERITAS observations.

5.5 Discussion

Currently, there exist only weak constraints on the GeV/TeV emission from most known repeaters. In 2016-2017, MAGIC observed FRB 121102 during five radio bursts. This allowed for an average upper limit on the persistent above 100 GeV of 6.6×10^{-12} photons per cm^{-2}. H.E.S.S. has also recently published observations

Parameter	Value
Time of Detection (UTC)	2024-05-09 07:39:12.834127
Baseband Right Ascension (ICRS)	222.369 $\pm$0.014°
Baseband Declination (ICRS)	26.404 $\pm$0.013°
VOEvent Right Ascension (ICRS)	222.56 $\pm$0.49°
VOEvent Declination (ICRS)	26.32 $\pm$0.49°
Dispersion Measure (pc cm^{-3})	1129.274 $\pm$ 0.015
Flux (Jy)	3.55 $\pm$ 0.44
Fluence (Jy ms)	3.37 $\pm$ 0.48
Fitburst 1-Sided Width (1σ, ms)	0.209
Fitburst 1-Sided Scattering Timescale (1σ, ms)	0.435
VOEvent Signal to Noise	15.25

Table 5.6 FRB 20240509A Radio Properties.

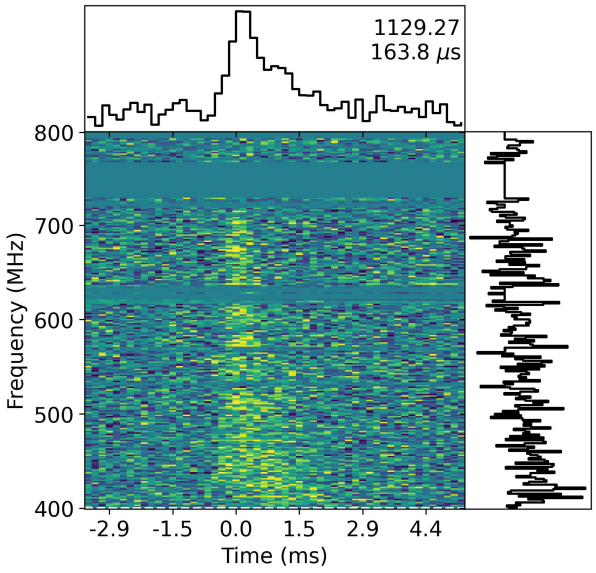

Figure 5.4 De-dispersed dynamic spectra for FRB 20240509 from CHIME (a "waterfall" plot). The band-average flux is shown above with the dispersion measure (in units of cm^{-3}) inset. The spectrum is shown in the right panel (averaged over time).

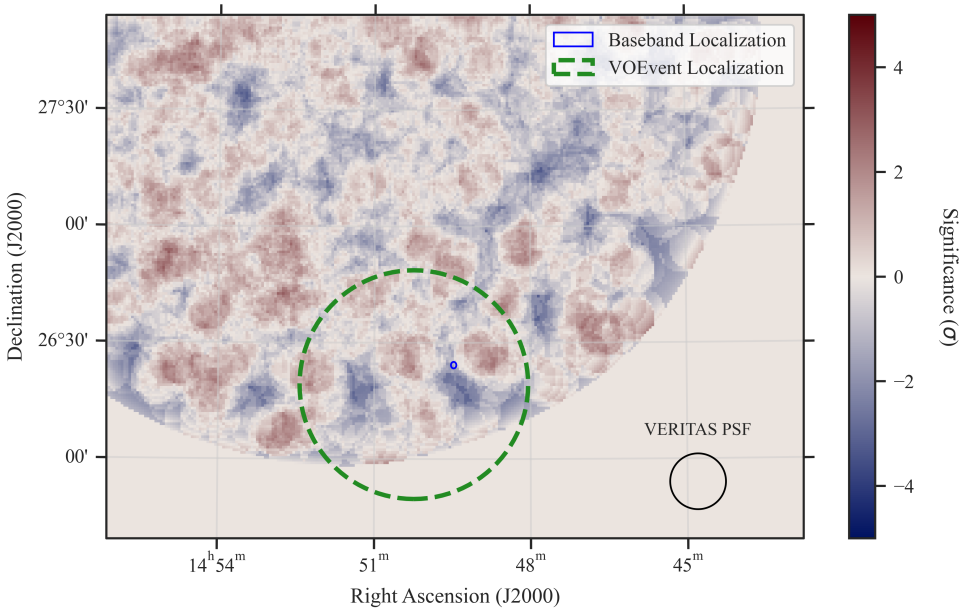

Figure 5.5 FRB 20240509 spatial excess map. The two 95% error regions from the CHIME localization are overplotted. They show the VOEvent and the baseband localization in green dashed and blue solid, respectively. All points outside of 1.75 degrees from the VERITAS pointing direction are marked with a null detection. The VERITAS PSF is also shown (defined as $\frac{5}{3}R_{68\%}$, where R_{68} is the 68% containment radius).

Time Window (s)	**On Events**	**Off Events**	**Significance(σ)**	**Integral Flux Upper Limit ($>$ 200 GeV, cm^{-2} s^{-1})**
-0.005-0.005	0	0.0021	-0.01	1.8×10^{-6}
-0.05-0.05	0	0.021	-0.03	1.8×10^{-7}
-0.5-0.5	0	0.21	-0.11	1.8×10^{-8}
-216-1591	6	372	-1.29	1.01×10^{-11}

Table 5.7 Summary of the burst analysis for FRB 20240509A.

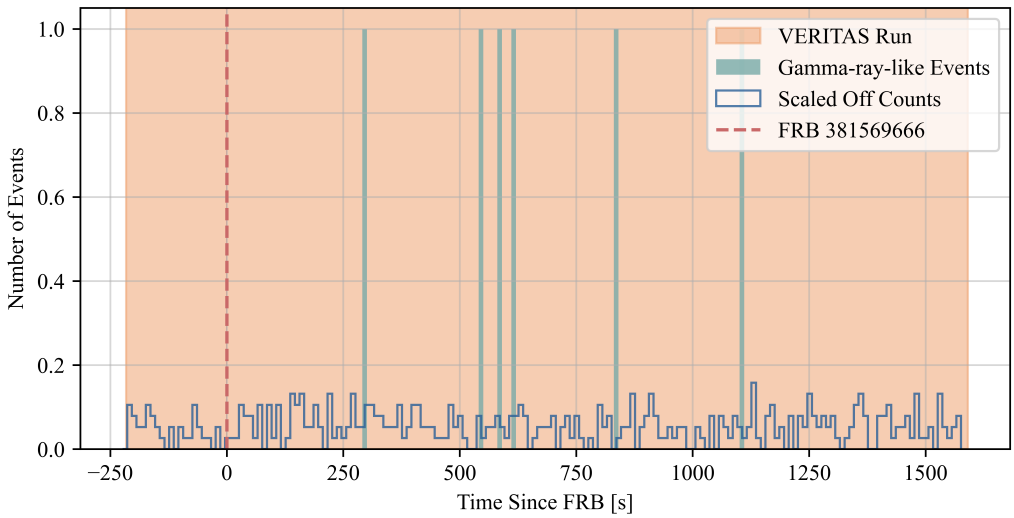

Figure 5.6 Temporal histogram of gamma-ray like events in the FRB 20240509A's *On* region (filled green bars). The background rate is shown by a blue, unfilled histogram. The bins have a 10-second width and start at the first event measured in the VERITAS exposure. The background histogram is scaled to represent the expected rate at the integration location.

conducted on 11 non-repeater follow-ups in the southern hemisphere (Aharonian et al. 2025). They placed various 99% luminosity upper limits of 10^{44-48}erg s^{-1}.

In both cases, we find that our persistent limits are far more sensitive, for example, FRB 20200120E, at a distance of 3.6 Mpc (Freedman et al. 1994), assuming a power law index of -2, provides a luminosity upper limit of $\sim 4\times10^{39}$ erg/s. This is interestingly near the theoretically predicted value of a persistent wind bubble gamma-ray emission, $\sim 10^{39}$ erg/s at 1 TeV, which is noted in the H.E.S.S. paper and is unconstrained by their previous follow-up (Murase et al. 2016; Murase et al. 2017). This demonstrates the power of our observations to constrain new theoretical models and highlights the advantages of radio coverage in the Northern Hemisphere, since more repeaters can be studied with much deeper observations than in previous studies in the South, where monitoring is sparser.

When looking at constraints on non-repeaters, there are no limits on the ratio of gamma-ray to radio emission from ground-based instruments in the prompt

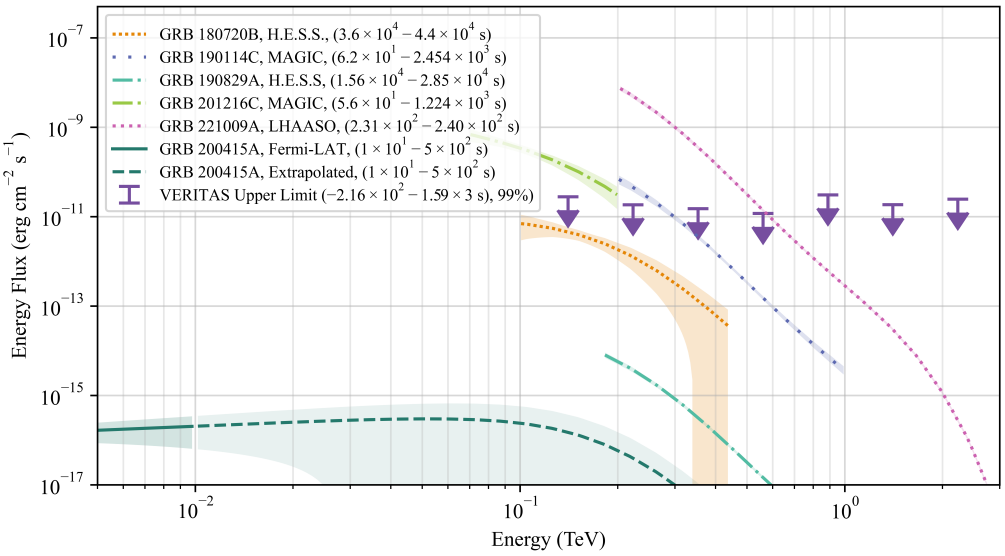

Figure 5.7 Spectral energy distribution and comparison between all VHE detected GRBs, and the VERITAS FRB 20240509A non-detection. VERITAS limits are presented at the 99% confidence level. All comparisons are scaled to the putative distance of the FRB (z = 0.87) and adjusted for total brightness and extinction. The *Fermi*-LAT measurement of GRB 200415A, a magnetar detected by *Fermi*-LAT, is also shown with a power-law extrapolation to higher energies. The times of the observations used are shown in the legend.

time windows investigated in this work. There is, however, an opposite approach. Consider the ratio of fluences $\eta^F_{r\gamma}$, which is defined as:

$$\eta^F_{r\gamma} = \frac{F_{radio}(400 - 800\ \mathrm{MHz})}{F_\gamma(200\ \mathrm{GeV}\text{ - }30\ \mathrm{TeV})} \tag{5.2}$$

with the gamma-ray fluence (F_γ) derived from a window that is four times one-sided width of the radio burst, with fluence (F_{radio}). Taking this into account, we find a fluence ratio $\eta^F_{r\gamma} > 3.3 \times 10^{-10}$ for FRB 20240509. This can be compared to the previous non-detection of radio emission coincident with gamma-ray bursts, $\eta^F_{rX} < 5 \times 10^{-10}$ (Curtin et al. 2024). Thus, if one makes the assumption that the X-ray emission has the same fluence as the gamma-ray emission during an event, then the allowed range of emission ratios is quite small.

We also consider a more generic comparison to known gamma-ray bursts. This is presented in Figure 5.7 with data from GRB 180720B, GRB 190114C, GRB 190829A, GRB 200415A, GRB 221009A, and GRB 201216C (**h˙e˙s˙s˙collaboration˙revealing˙2021**; Acciari et al. 2019; Abdalla et al. 2019; Blanch 2020; LHAASO Collaboration et al. 2023; Fermi-LAT Collaboration et al. 2021). It is seen that for all gamma-ray bursts that were detected promptly (<1 hour) by VHE instruments, the flux falls above the sensitivity of our observations. This means that we can significantly constrain the emissions that follow these GRBs. For magnetar-like emission, we have only ever detected gamma-rays from a single nearby source. Due to the distance to this source, when scaled to the distance of this distant FRB we do not significantly contain any prompt emission by several orders of magnitude.

The results of the analysis presented in this work indicate no strong evidence of VHE emission, either prompt or persistent, from any of the most active FRB repeaters and from non-repeaters. This is consistent with the previous non-detections by the other two VHE instruments, allowing for the placement of tight constraints on the most energetic emission from this broad class of sources. Due to the ability of VERITAS to monitor the CHIME field of view, not only are the limits of this work the deepest persistent limits to date, but they also span the broadest range of source subclasses and include the first prompt limits on a range of repeaters and non-repeaters.

CHAPTER 6

Observations of Rapidly Varying Blazars

> What a [Lac]-brain is this! By the Lord, our plot is a good plot as ever was laid ... and full of expectation
>
> William Shakespeare, Hamlet

6.1 Introduction of BL Lacertae

In this chapter, we will summarize the study of rapid flaring in BL Lacertae during 2024. BL Lacertae (hereafter BL Lac) is a source observed by VERITAS, MAGIC, H.E.S.S., and *Fermi*-LAT and is located at redshift z=0.069 (Miller et al. 1978). We will summarize previous work on this source and discuss the implications of the

studies of rapid variability present in BL Lac. When investigating this extreme flaring, three key questions were considered:

- Is this the brightest this source has ever been measured?
- Is there evidence for extreme spectral evolution?
- Is there evidence for sub-minute variability?

For all of these questions, we find the answer is yes. In this chapter, we will expound on these questions, addressing them individually with dedicated analyses. We will begin with a brief overview of the previously measured states in this system. The mechanism by which the VERITAS observations were triggered will then be discussed. The observations themselves will then be described, followed by sections describing the excess detection and spectral reconstruction. This will end with the detection of rapid variability in the source, followed by a brief discussion on the implications for the size of the emission region.

Flares from the object are numerous at VHE, with the first detection at VHE coming from the Crimean Observatory (Neshpor et al. 2001); and the most recent detection of enhanced emission occurred in 2021, as detected by LST-1 and MAGIC (MAGIC Collaboration et al. 2019; Nozaki et al. 2023). Currently, the most rapid variability from BL Lac that has been measured is from the VERITAS collaboration with a decay constant of 13±4 minutes. Hints of similar timescale decays have been reported by LST-1 (Nozaki et al. 2023; Abeysekara et al. 2018).

Trigger for Observations

The VERITAS observations were triggered in 2024 by a FlaapLUC (Fermi- LAT automatic aperture photometry Light CUrve) alert (Lenain 2018). FlaapLUC is an automated Fermi-LAT pipeline for producing alerts when there is a signficant flux increase from a gamma-ray blazar. Previously, VERITAS has responded to numerous Fermi-LAT triggers, utilizing various techniques to determine if a blazar is visible to VERITAS and if the source is of interest. These include searching for excesses of high-energy ($\gtrapprox$ 1 GeV) photons at known source locations and looking at lightcurves generated by tools like the Fermi-LAT light curve repository (Abdollahi et al. 2023). These traditional methods have led to significant delays: often,

by the time the observations are conducted by the ground-based experiments, the flare has already subsided. More sophisticated tools, like the light curve repository, use three-day bins with a complete unbinned analysis. FLaapLUC performs coarse aperture photometry around a list of predefined sources, assuming no significant background contributions. If a source passes above 3σ above the long-term flux average, then a likelihood analysis is performed. This two-step process enables updates to occur more frequently, typically updating multiple times a day. This, paired with reported spectral extrapolation, has enabled VERITAS to have more confidence in the flares it observes and to observe them more quickly.

The rapidity of the FlaapLUC alert compared to an ATel alert is shown in Figure 6.1. As can be seen from the figure, the details of which will be described in the next section, the FLaapLUC alert appears approximately two full days before the significant excess is reported to the community through an ATel (Zyl et al. 2024). Thus, if VERITAS had waited for another VHE instrument to report an excess, the flare would have already ended. From this, it is evident that the new updates to the VERITAS trigger for flares have made the instrument more responsive to these interesting events.

6.2 Summary of Observations

A summary of the VERITAS observations on the 2024 BL Lac data set can be seen in Table 6.1. Due to the nature of blazar flares being exceptionally soft, the threshold is more critical for these sources than for galactic or harder-spectrum sources. As such, observing conditions such as elevation and weather make a significant difference in the reliability and significance of detections. The first night featured four runs conducted in mostly good conditions, with only minor rate issues (often due to increased light levels) occurring during the first 30 seconds of each run and some minor effects resulting from low elevations, which caused fluctuations in the measured sky brightness stability in the infrared.

The second night proved more problematic, with only a single run obtained at a 41-degree elevation. This low elevation will increase the threshold by hundreds of GeV when compared to exposures taken above 55 degrees elevation. On other nights, observations could begin earlier and capture BL Lac setting before it fell too

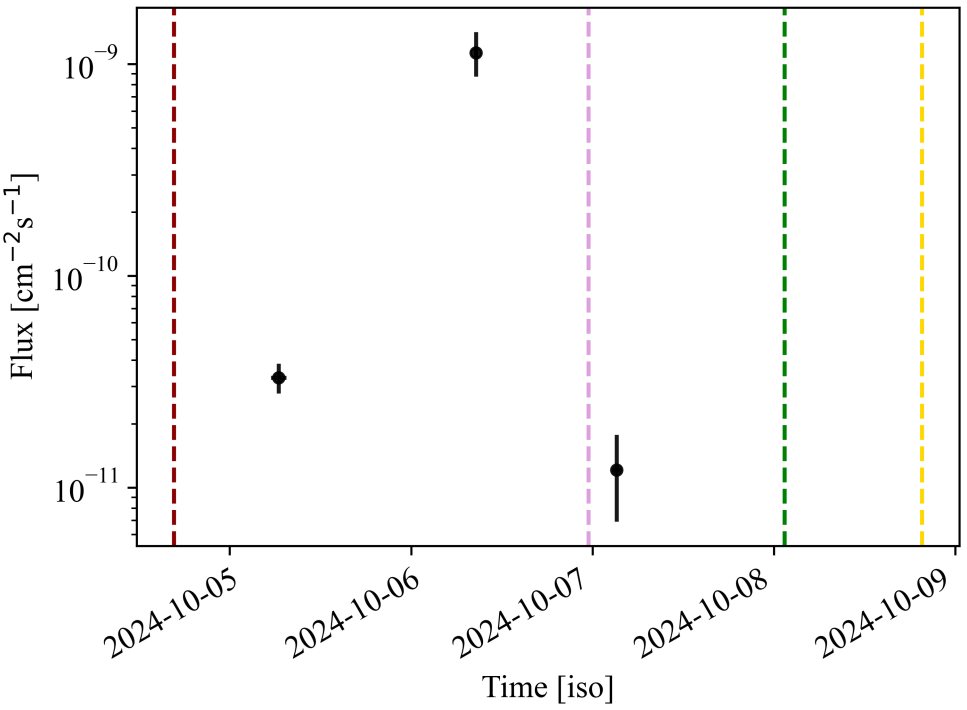

Figure 6.1 Daily binned lightcurve of the VERITAS observations of the 2024 BL Lac flare along with alerts and trigger time denoted by dashed lines. In red, the FlaapLUC alert (Lenain 2018). In pink, the ATel from Fermi-LAT (Zyl et al. 2024). In green, the VERITAS ATel, and in yellow the ATel from LHAASO (A. F. V. Collaboration 2024; Xiang et al. 2024).

low. Still, the high temperatures (30 degrees Celsius) caused delays to ensure the safety of the instrument. VERITAS uses a coarse online analysis to monitor data taking and to measure significance in real-time. This allows for the ToO observations to be contingent on brightness. For extreme events, VERITAS can continue to observe at low zenith angle but only when prompted by the online analysis. This source did not meet this criterion on this night, and so only one run was taken.

The final night had three exposures taken, but the first had significant issues due to clouds. Clouds cause an uncertain, rapidly changing effective area, resulting in a reduced trigger rate. Therefore, all portions of VERITAS runs with significant variability in the measured trigger rate are removed.

Date	Run Number	Duration (min)	Usable Time (min)	Mode	FIR	Elevation (deg)	Azimuth (deg)	L3 Rate (Hz)	NSB (μA)
20241005	109390	30	27	0.5N	0.1 (A)	72	314	416	9.4 (d)
20241005	109391	30	30	0.5S	0.1 (A)	67	305	360	9.0 (d)
20241005	109392	30	30	0.5E	0.1 (A)	62	303	347	9.2 (d)
20241005	109393	30	30	0.5W	0.2 (B)	55	301	331	9.2 (d)
20241006	109408	30	20	0.5N	0.3 (C)	41	303	514	10.7 (d)
20241007	109418	16	10	0.5S	0.5 (D)	68	55	437	9.7 (m)
20241007	109419	12	11	0.5S	0.1 (A)	71	52	424	9.4 (m)
20241007	109420	30	29	0.5E	0.1 (A)	74	43	393	9.2 (d)

Table 6.1 Summary Table of BL Lac 2024 Observations. Date shows the UTC date of the observation, and Run Number is the internal VERITAS ID for the observation. Duration is the total integrated exposure of the run. The usable time is the total time after manually removing periods with problems due to weather, hardware, or software issues. Mode is the observing pointing strategy used during the observation. The format is the angular distance of the wobble in degrees, followed by the cardinal direction of the wobble in celestial coordinates. The elevation and azimuth are the average pointing for the entire run. L3 rate is the average trigger rate for the run. Night sky background (NSB) corresponds to the average current value in the telescopes. The influence of the sun and moon on this brightness level is presented next to this value with *m*, meaning moderate influence, and *d*, meaning dark (little to no influence). Far infrared (FIR) is a measurement of the standard deviation of the sky temperature measured in arbitrary units using an infrared radiation thermometer.

6.3 Results

All analysis was performed using EventDisplay v490.7. At the time of writing, this is the second latest version of EventDisplay, with v491 being the most recent. However, v491, which includes adaptations to improve performance above 10 TeV, degrades performance near the threshold. This causes the analysis to perform worse in the newer version, with lowered significance and unphysical event rates that do not agree with independent secondary results from VEGAS. The gamma/hadron separation is performed with cuts optimized for sources with soft spectral indices. All high-level analysis is performed using point-like IRFs and Gammapy v1.3 (Acero et al. 2024).

Detection and Spectral Variability

The results of the statistical analysis are shown in Table 6.2. The significances are reported as test statistics [1], based on a wobble background and following the method of T.-P. Li et al. (1983). The first and second nights both have independent significant detections, and the third night shows evidence for persistent emission contingent on the prior of elevated emission from the first two nights. The spectra also appear to vary from the first night to the second, with the first night being softer, and the subsequent night appearing much brighter and harder. Compared to the previous spectral index value of 3.28 seen by VERITAS in 2016, the first night appears much softer than the system has been measured previously when in an elevated state (Abeysekara et al. 2018).

Minimum Timescale Variability

Due to the high significance of the detection on the first night in particular, a search for minimum timescale variability using an unbinned Bayesian block method was conducted. An unbinned Bayesian block with events extracted from a 0.1-degree radius around the source was applied to find the optimal binning for the data. The prior level for the bins was set such that the false positive rate is below what

[1] The test statistics presented in this chapter follow the Gammapy convention but are equivalent to the significance presented previously

Date	$\sqrt{TS}$ [σ]	Normalization $\mathbf{TeV^{-1}s^{-1}cm^{-2}}$	Index
2024-10-05	7.8	$1.7\pm1.2 \times 10^{-13}$	5.2 ± 0.5
2024-10-06	6.4	$1.1\pm0.2 \times 10^{-11}$	3.9 ± 0.5
2024-10-07	3.0	-	-

Table 6.2 Nightly significance and spectral parameters reported by VERITAS for the BL Lac flare of 2024. For the final night, no spectra are reported due to insufficient significance. The normalization and index are reported for a power-law with reference energy of 1 TeV.

would equate to $\sim 2\sigma$ significance. The underlying assumption is that the background is not variable over the course of the run, which was verified by applying a Bayesian block to the background data. Although variability was observed on hour timescales, no rapid changes were detected in the background that might have biased the results.

The results of the optimal Bayesian blocks for the first night can be seen in Figure 6.2. The values and detection significances of the individual bins in the first run can be seen in Table 6.3. A slow, persistent decay can be observed; however, an individual bin, the third bin in the table starting at 968 seconds after the start of data taking, is notably short and bright, doubling the flux compared to the two surrounding bins. This bin is well contained within the first run and does not occur at a run transition. Bins overlapping with run transitions may be subject to more variability, and the discontinuity in the data may cause it to resemble a change in rate. Still, these effects do not impact the bin with rapid variability seen in these observations.

To assess the robustness of this signal to binning, we use a similar bin-width for the deadtime-corrected bin, 30 seconds, and apply uniform binning throughout the run to determine if the bin still emerges as a significant excess. The result can be seen in Figure 6.3. The bin that overlaps with the ideally selected Bayesian block is the highest in the entire dataset (7 counts, compared to an average of 1.14 counts). This leads to a significance of $\sim 4\sigma$ above the average count rate of the run.

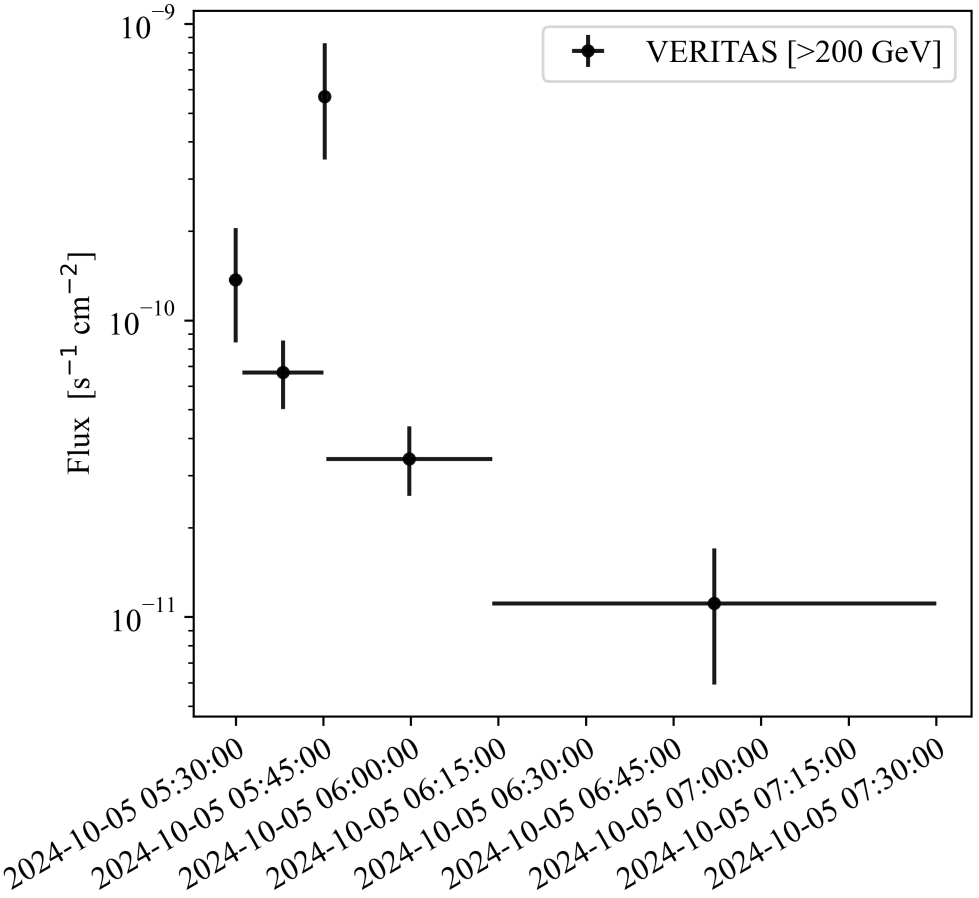

Figure 6.2 Bayesian block binning of the 2024-10-05 BL Lac lightcurve above 200 GeV. A clear fading can be seen, with one superimposed bin of rapid variability.

Start Time	Duration [s]	$\sqrt{TS}$ [σ]	On Counts	Off Counts
0.0	138.3707	4.01	7	0.75
138.3707	830.0172	5.88	22	4
968.3879	30.4568	5.02	6	0.125
998.8447	756.1099	3.78	13	3.375

Table 6.3 Rebinning results for the run number 109390. The start time is defined from the beginning of the run. Duration is given as the elapsed time and not the livetime. The number of bins here differs from Figure 6.2, as only bins from the first run are shown, whereas the other plot shows bins for the entire night.

Individual Photon Distributions

To validate the signal, we examined the distribution and quality of the events that comprise the signal, ensuring that there were no apparent issues with reconstruction that could have introduced bias during the rapid flare. In Figure 6.4, the spatial and temporal event distribution can be seen. The location of the excess in the lower center shows both a statistical increase in rate in the spatiotemporal area where the rapid variability appears to be located. Although six events occur in the light curve, there are actually seven events that contribute to the statistical power of the bin, as it was constructed with a larger on-region and no threshold, which differs from the method used to determine significance and spectra. These events were all manually extracted, and the raw events were analyzed to ensure there was no significant noise signature. All of the events that compose the excess have $E \sim 200$ GeV; they all appear as relatively small events that are well-behaved, elliptical events with no clear electronic noise domination or non-physical event parameterization.

Further, we investigated the multiplicity of the events. Most events that VERITAS sees are two-telescope events that are composed of a higher noise fraction when compared to gamma-rays. Looking at the multiplicity of the events composing the flare, we have:

- 3/7 four telescope events
- 3/7 three telescope events

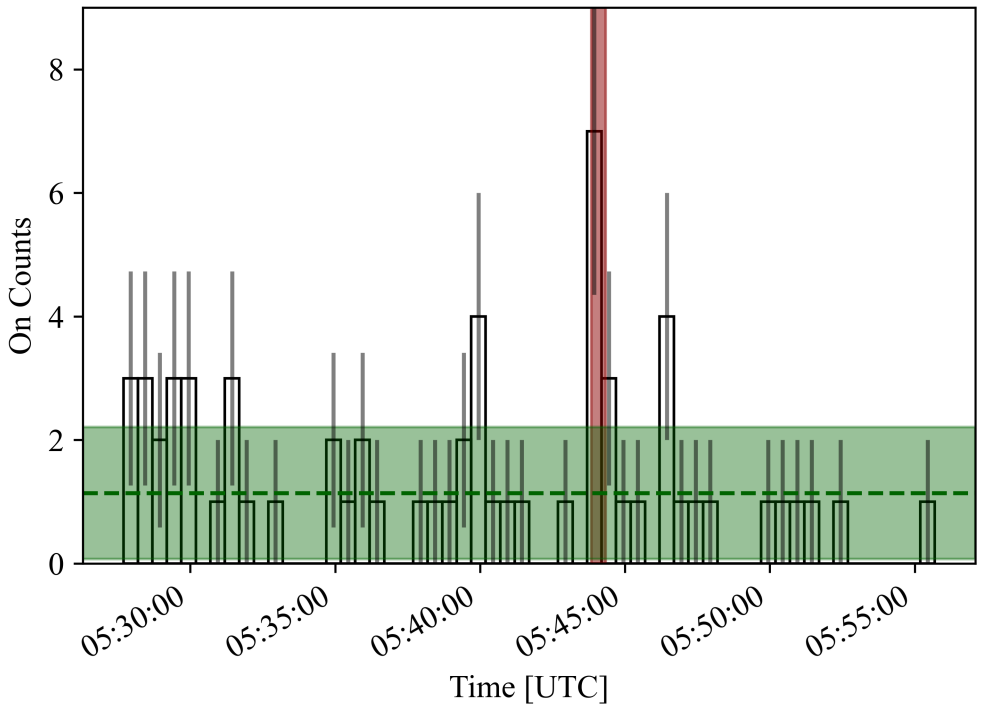

Figure 6.3 30 second uniform binning On count event histogram for the 2024-10-05 BL Lac flare. The red-shaded area indicates the region selected by the Bayesian block as a significant region of excess emission. The green dashed line and the shaded area show the average and standard deviation of the expected counts through the run, taking the mean value of the histogram bins.

- 1/7 Two telescope events

Although four telescope events are more likely to be astrophysical, this is not taken into account in either the gamma/hadron separation or the statistical weighting of noise and signal events for background estimation. Because VERITAS assigns a binary gamma-ray classification instead of a probabilistic likelihood, it's challenging to translate this multiplicity into a quantitative statement about the true probability distribution that the cluster is both physical and significant.

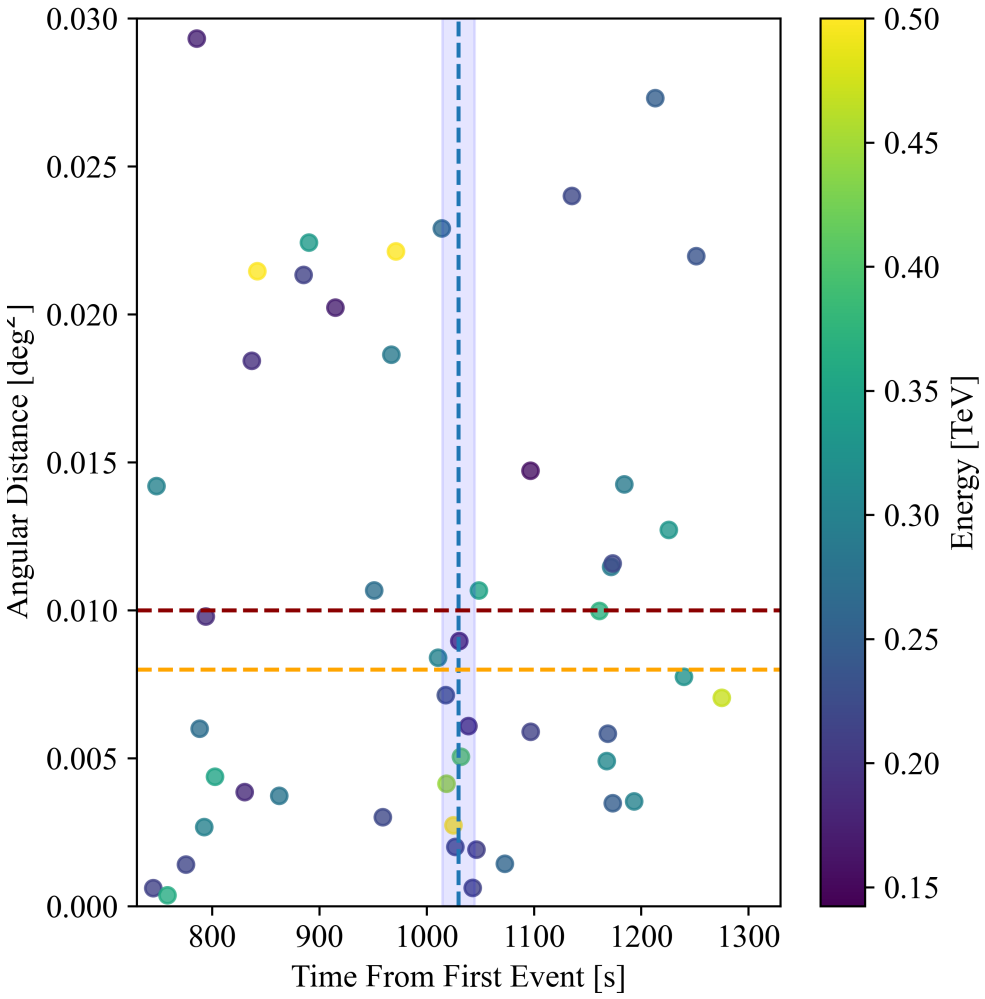

Figure 6.4 The spatial and temporal distribution of the events, unbinned. The energy of the event is shown as the color of the point (with all values above 0.5 TeV set to the color of 0.5 TeV). The orange dashed line shows the on region of the spectral analysis, and the red line shows the region of the Bayesian block. In blue, the location and width of the rapid bin are shown. A slightly wider range is selected for the Bayesian blocks, as background has a less significant effect on determining variability, so integrating a higher rate of signal increases the method's sensitivity. This also aligns with the same radius size that was chosen for the VEGAS cross-check.

6.4 Discussion

These results present evidence, at the same level of significance as previous similar analyses, of rapid-subminute variability from BL Lac (Pandey et al. 2022). These can be used to place constraints on the size of the emission region, which can be defined as:

$$R < \frac{ct_{var}\delta}{1+z} \tag{6.1}$$

with R being the size of the emitting region, c the speed of light, and t_{var} being the timescale of variability (Abeysekara et al. 2018). The distance z can be determined from optical observations, and δ is the Doppler factor. The Doppler factor can be estimated from the motion of radio knots in the jet to be $\sim$23.8 (Hervet et al. 2016). Taking these values and the minimum half bin duration as an estimate of the variability timescale t_{var}, we have an upper limit on the size of the emission region of approximately $\sim 1.1 \times 10^{11}\mathrm{M}_{\odot}$, which is approximately 10% of the Schwarzschild radius of the black hole, assuming a mass of $1.1{\times}10^{12}\mathrm{M}_{\odot}$ (Abeysekara et al. 2018). If confirmed, this would be the first reported VHE emission that falls below the black hole event horizon for BL Lac. However, uncertainties in the calculation of the black hole mass may still be an important consideration, which we leave for future work. A similar discussion of these details can be found in Gupta et al. (2012). This is not the first detection of sub-horizon variability seen at VHE (Aleksić et al. 2014), but it is the first time this has been observed in BL Lac at VHE. Multiple theories invoking mini-jet structures, jet cloud interactions, and magnetospheric models can be used to explain sub-horizon variability, and for a discussion of the implications of the sub-horizon scale variability, please see Aleksić et al. (2014).

CHAPTER 7

Conclusions

The woods are lovely, dark and deep.
But I have promises to keep,
And miles to go before I sleep,
And miles to go before I sleep.

Robert Frost, 1874-1963

7.1 Summary of Results

In this work, we described two key searches, the search for FRBs gamma-ray signals and the search for VHE sub-minute flares from blazars. We find the following:

- There is no evidence for VHE GRB-like emission from FRB 20240509A, a likely non-repeating FRB, disfavoring cataclysmic gamma-ray burst models for the radio progenitor.

- There is no evidence for persistent, prompt, or rapid VHE emission from many of the most promising multi-wavelength fast radio burst repeater candidates. New limits are placed in these windows that improve previous observations by orders of magnitude and probe previously unconstrained models.

- There is potential evidence for sub-minute variability in the blazar BL Lacertae, suggesting smaller emission regions (below the Schwarzschild horizon radius), which is far smaller than in previous observations.

- The BL Lacertae flare in 2024 was an exceptional flare in many regards, with both the brightest and softest VHE emission detected from the source, suggesting a broader range of potential emission states is possible from the source.

Our conclusion to the larger open question about the rapid transient VHE sky is that blazars occupy a unique space, characterized by the brightest second-scale emission. Although some galactic compact objects at VHE are suggestive of the presence of powerful and smaller emission regions, there is currently no evidence of transient sub-second VHE emission from fast radio bursts, which are potentially the highest fluence form of emission associated with stellar mass compact objects.

There are still numerous open questions and further analyses to be performed. Continuing to monitor for closer and brighter FRBs could improve the probability of detecting a high-energy counterpart. A secondary confirmation of the rapid variability of BL Lacertae, either from subsequent prompt follow-up from VERITAS or another IACT, would help to improve the modest significance of the detection presented here and confirm the size of the emission region.

Figure 7.1 A photograph of the pSCT. Credit: Amy Oliver, Fred Lawrence Whipple Observatory, Center for Astrophysics — Harvard & Smithsonian.

7.2 Future Work

The two last major upgrades to the VERITAS observatory were the camera upgrade in 2012 and the instrumentation of the ECM in 2018. The Fred Lawrence Whipple Observatory has two major upgrades planned for 2025-2026, which have been in development for over five years. These two upgrades have direct impacts on the FRB work included in this thesis.

Prototype Schwarzschild-Couder Telescope

One of the largest upgrades to the Fred Lawrence Observatory will be the addition of the prototype Schwarzschild-Couder Telescope, or pSCT (Colin B. Adams et

al. 2022). This a large single mirror design with a focal length between 1.2-1.4, like VERITAS. The pSCT uses Schwarzschild-Couder design, which allows for a much higher angular resolution and field of view (Colin B. Adams et al. 2022). The optical design of most currently active and planned IACTs is based on the Davies-Cotton optical configuration.

Because of the use of Hillas parameters, an improved angular resolution in a VHE camera does not necessarily directly lead to improvements in gamma-ray angular reconstruction. Currently, the development of dedicated pSCT simulations and new reconstruction algorithms is underway to leverage the additional details provided by the increased angular resolution, to improve both sensitivity and angular resolution. For blazars, there is often suppression due to the extragalactic background light absorption, suppressing > 10 TeV showers for any source located at a moderate distance ($\sim$z$>$0.1). Since this is the region where the pSCT is expected to be most sensitive, there is likely no improvement expected in the study of rapid blazar flares that comes from the inclusion of the pSCT into the VERITAS array.

The pSCT's field of view, however, is an improvement that should increase the rate of observed non-repeating FRBs. Exact predictions for the rate require some assumptions about the pSCT observing program that may differ significantly from that of VERITAS. Making the assumption that the pSCT will have roughly a similar temporal overlap with CHIME as VERITAS has had in the past 4 years, and that the rate of CHIME detected FRBs remains the same, we would expect a rate of coincident non-repeating FRB of approximately 0.9 per year. This rate may allow us to better probe a range of sources to confirm within a few years that FRB 20240509A is not a uniquely misaligned or faint source, but that faint VHE emission is a property of most non-repeating sources.

Optical Backend Upgrade

The next upgrade to VERITAS is to the parasitic optical backend. Although not discussed in great detail in this thesis, VERITAS is one of the most sensitive optical telescopes for millisecond transients. An upgrade is planned to enhance sensitivity to sub-millisecond transients and increase the field of view of the optical mon-

itoring to the entire camera. The planned upgrade will replace the current flash analog-to-digital converter with one that splits the PMT signals to the gamma-ray and optical recording backend. For the brightest blazars, this may enable simultaneous monitoring of optical variations, facilitating correlation of any measured variability. For the fast radio bursts, this would enable simultaneous optical monitoring of non-repeaters, allowing for millisecond limits down to approximately 13th magnitude in the B-band.

New IACTs

On the horizon are several major IACTs that will increase the overall understanding of the VHE sky. The largest project is the Chenrenkov Telescope Array Observatory (CTAO). CTAO is expected to have an increase in sensitivity of approximately a factor of 10 over current-generation instruments and is being constructed as two independent systems, with one located in the northern hemisphere in La Palma and the other in the Atacama Desert in the south (Cherenkov Telescope Array Consortium et al. 2019). Additionally, the future development of the Large Array of imaging atmospheric Cherenkov Telescopes (LACT) in China on the LHAASO site may lead to enhanced performance and also increases the likelihood of coincidences with Chinese observatories like FAST, which are not accessible to the current generation of IACTs (Z. Zhang et al. 2025). However, neither of these instruments can observe simultaneously with CHIME, and the level of chance coincidence with any known radio observatory is expected to be quite low. Therefore, the non-coincident observation presented here may remain the most sensitive observation for many years.

APPENDIX A

Search for Persistent Emission

In this appendix, we present the individual spatial significance searches for persistent emission around targeted VERITAS FRB observations. We present the sky maps, which are assessments of the spatial significance at all locations with significant VERITAS sensitivity, using the Li and Ma estimation of significance (T.-P. Li et al. 1983). We assess significance out to 1.7 degrees from the telescopes' pointing direction; above this radius and to about 2.5 degrees, sources can still be detected, but sensitivity is degraded and systematic biases are larger. For null detections, because of the definition of the significance, each point should be randomly distributed and follow a normal distribution. The significance is assessed in a 0.1-degree radius circle with background estimated using an annulus between radii 0.6 and 0.8. This means that the sky maps will be correlated with a 0.1 degree radius, which corresponds roughly to the point spread function of VERITAS (introducing another similar correlation scale to the sky maps).

Figures A.1 through A.16 show sky maps for the FRBs listed in Table 5.2. There is no significant excess seen in any of the sky maps.

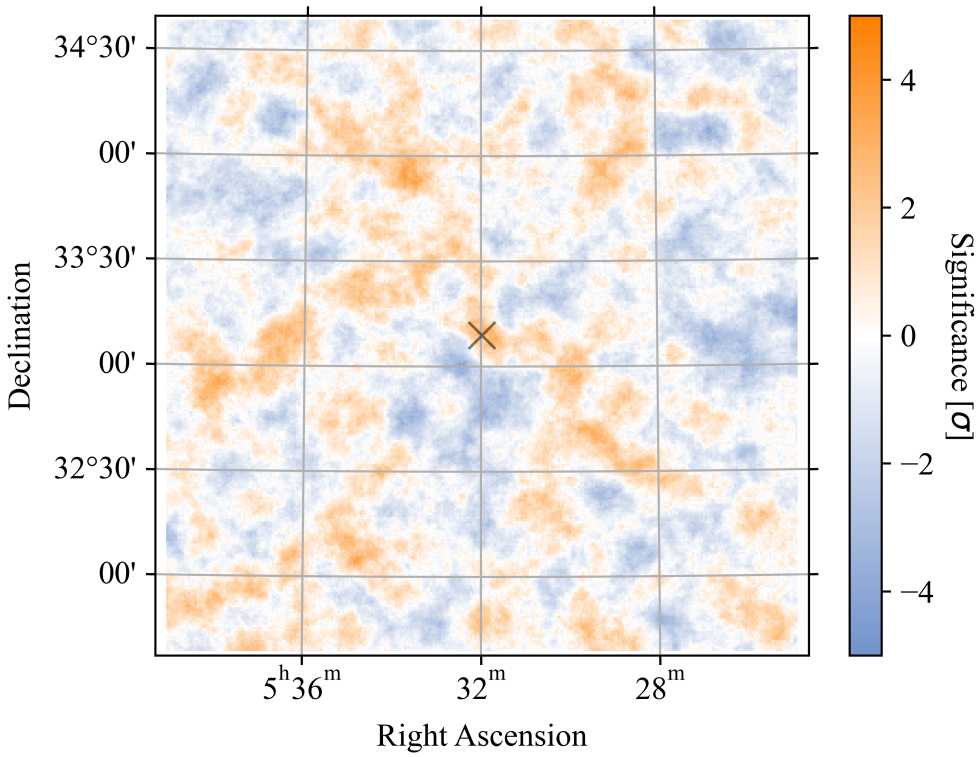

Figure A.1 Spatial significance of excess VERITAS emission for the region around FRB 20121102A. The location of the FRB localization is shown as a black cross.

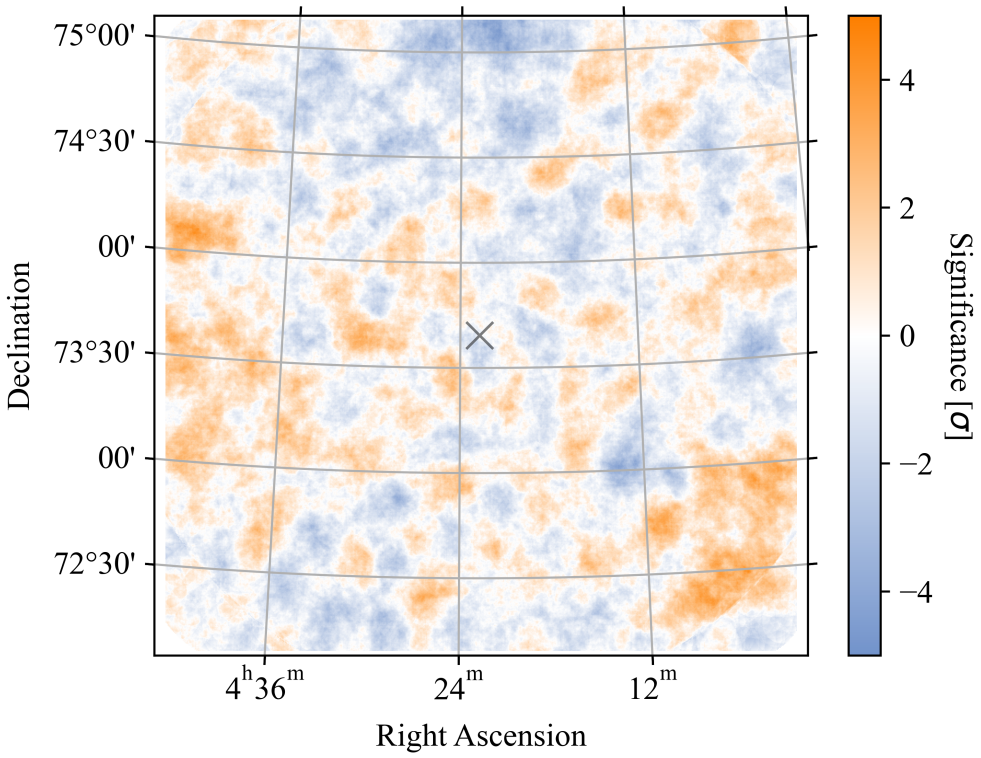

Figure A.2 Same as Figure A.1 for FRB 20180814A.

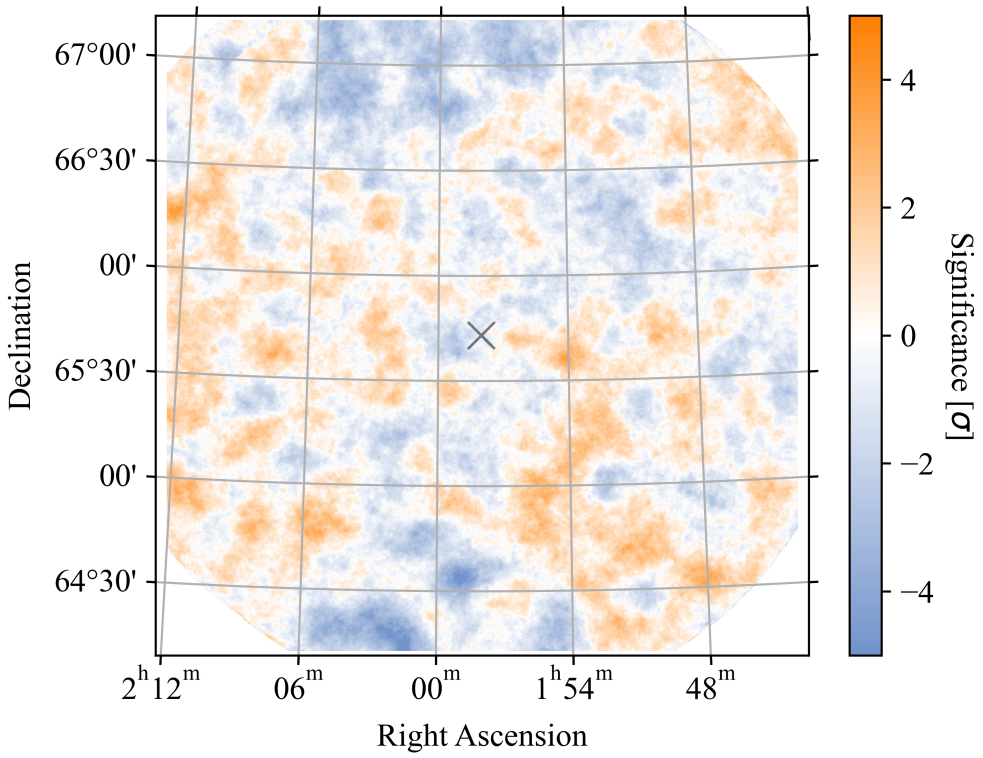

Figure A.3 Same as Figure A.1 for FRB 20180916B.

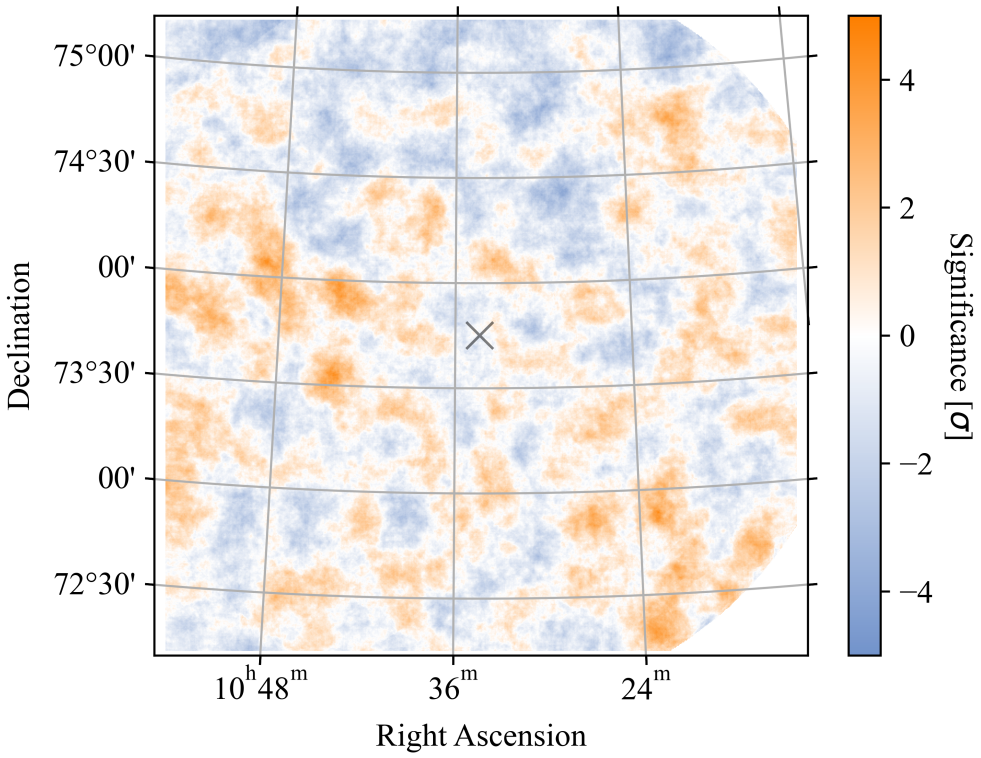

Figure A.4 Same as Figure A.1 for FRB 20181030A.

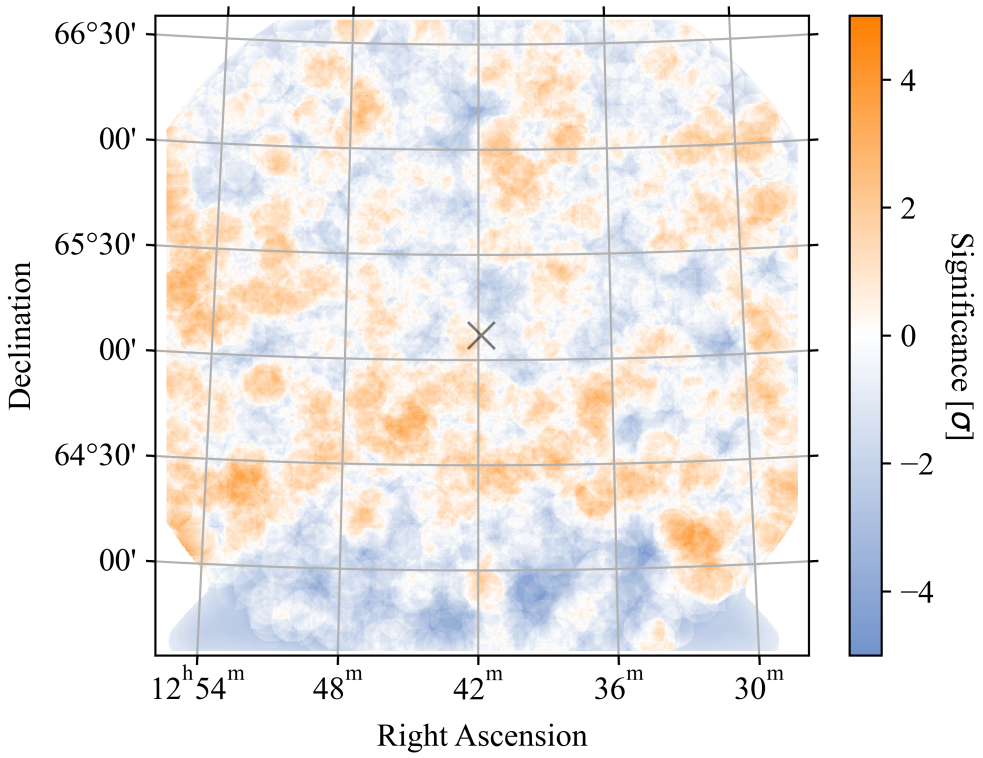

Figure A.5 Same as Figure A.1 for FRB 20181119A.

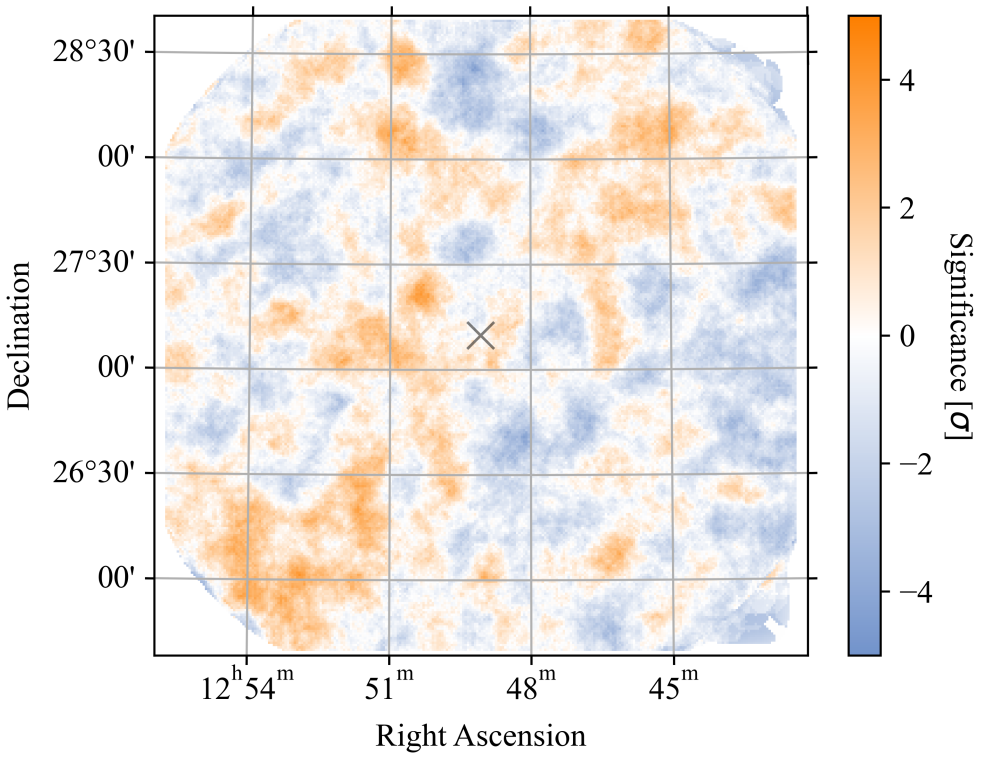

Figure A.6 Same as Figure A.1 for FRB 20190116B.

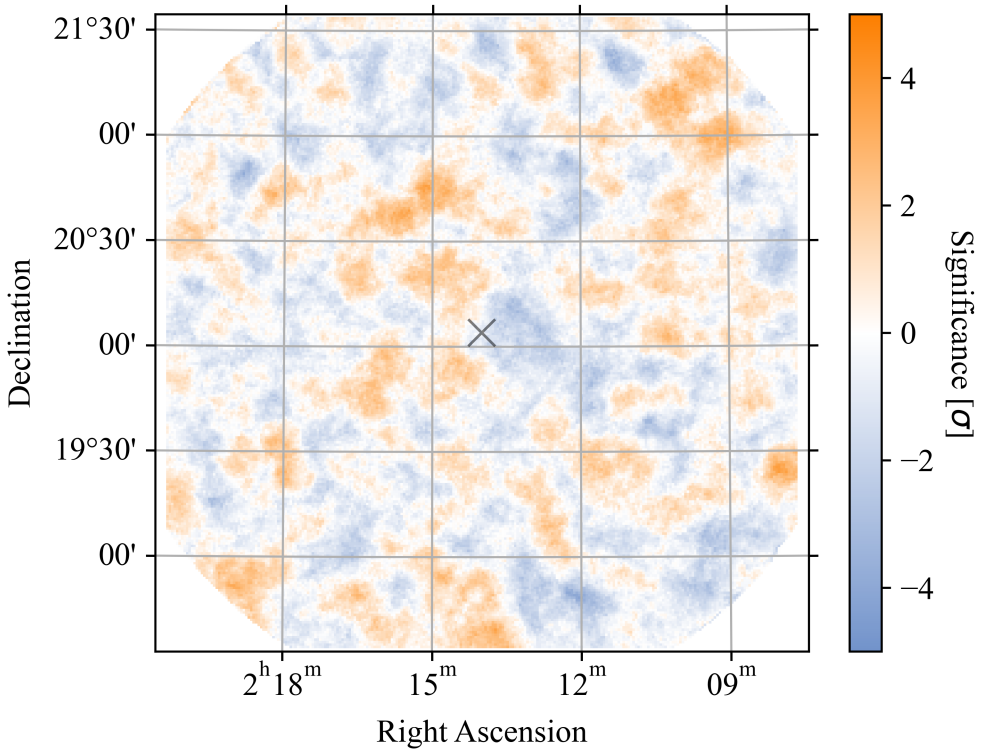

Figure A.7 Same as Figure A.1 for FRB 20190213A.

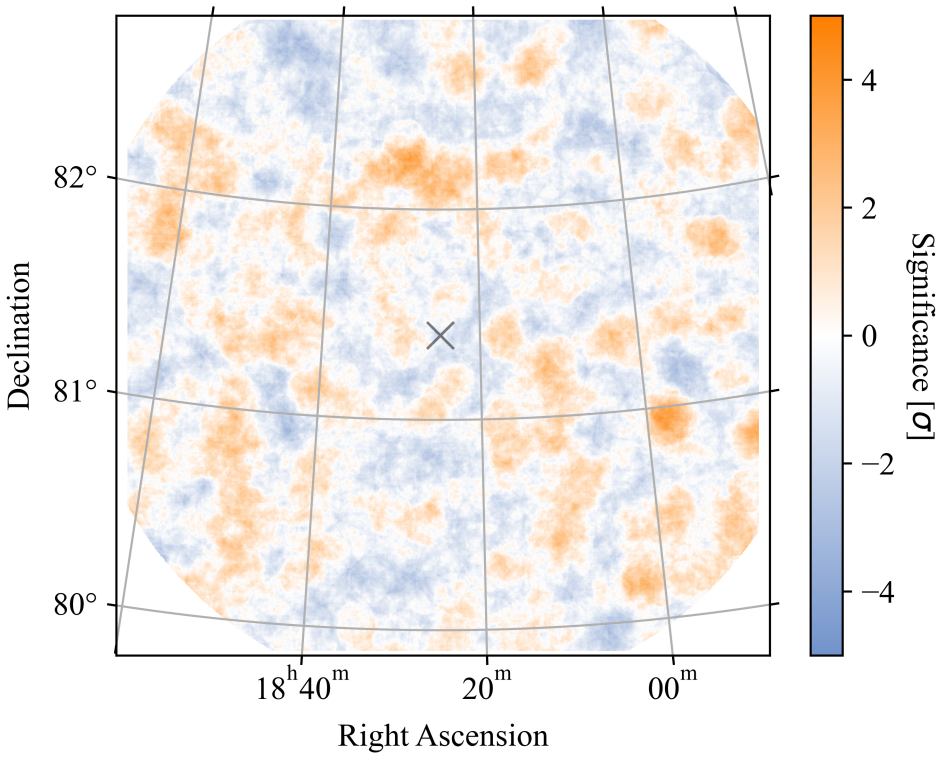

Figure A.8 Same as Figure A.1 for FRB 20190213B.

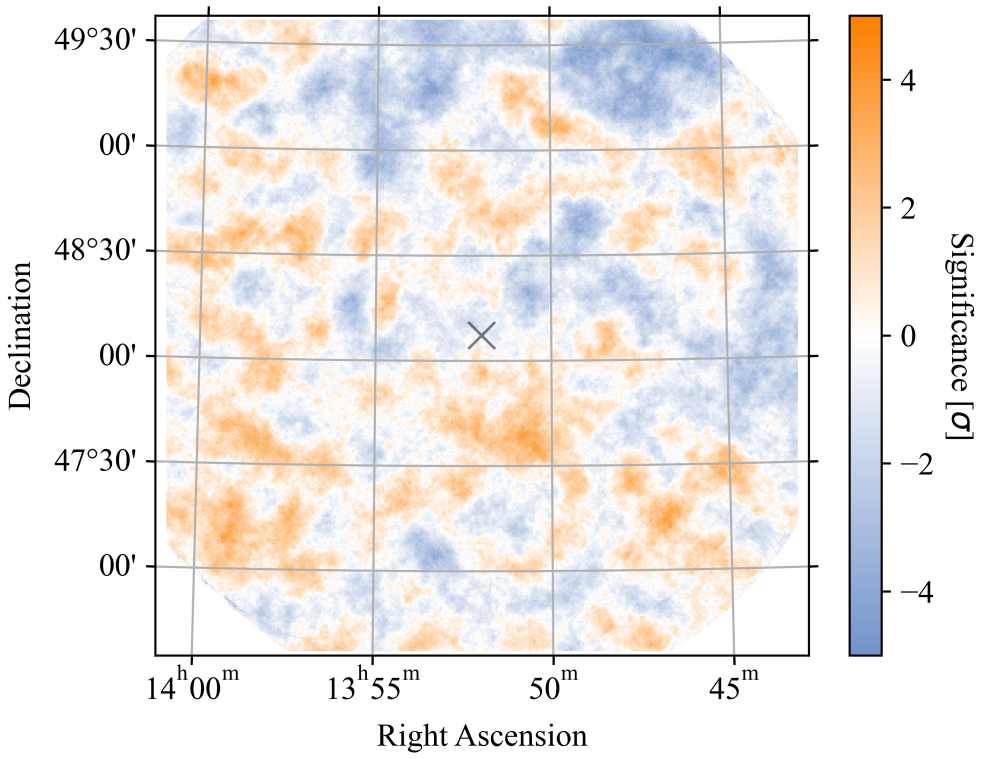

Figure A.9 Same as Figure A.1 for FRB 20190303A.

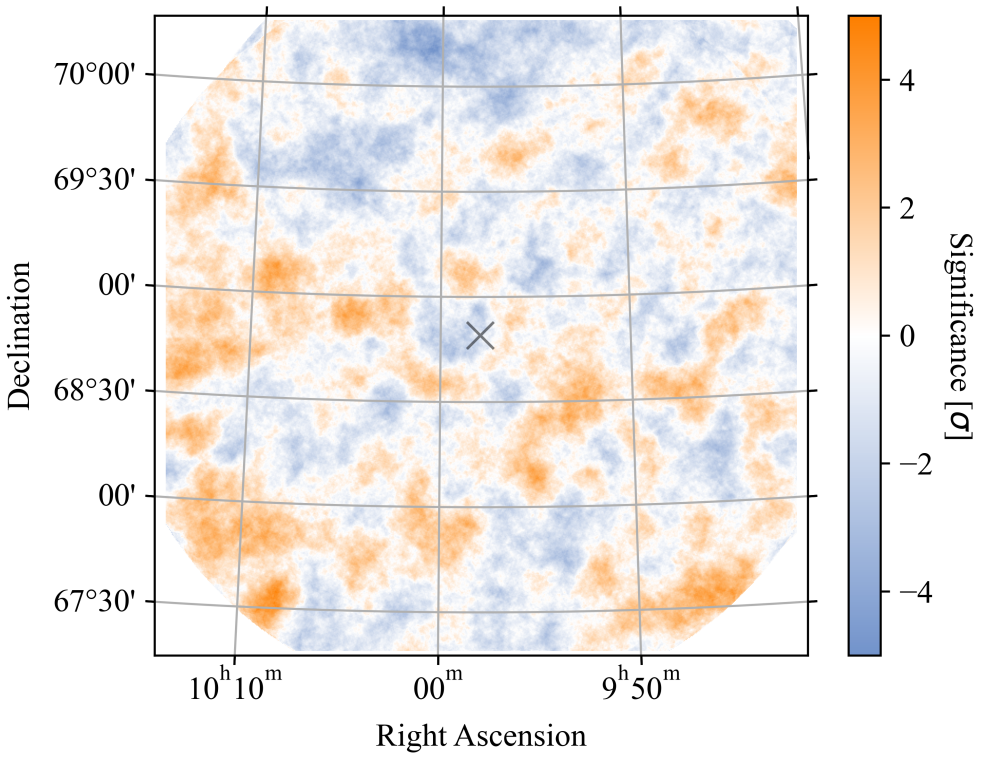

Figure A.10 Same as Figure A.10 for FRB 20201124A.

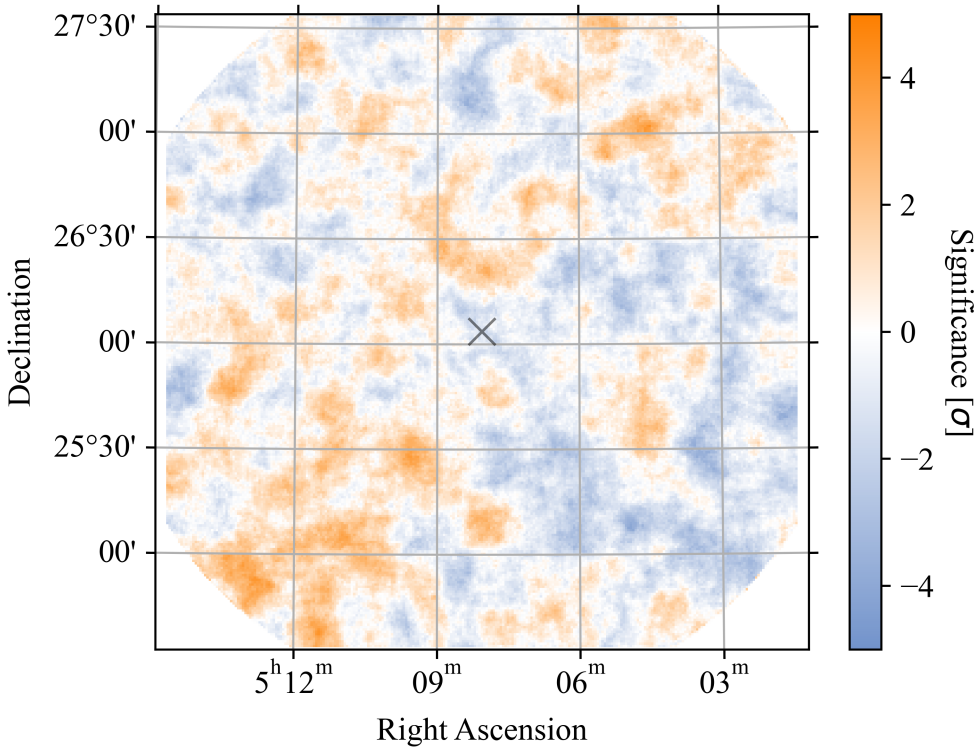

Figure A.11 Same as Figure A.1 for FRB 20201124A.

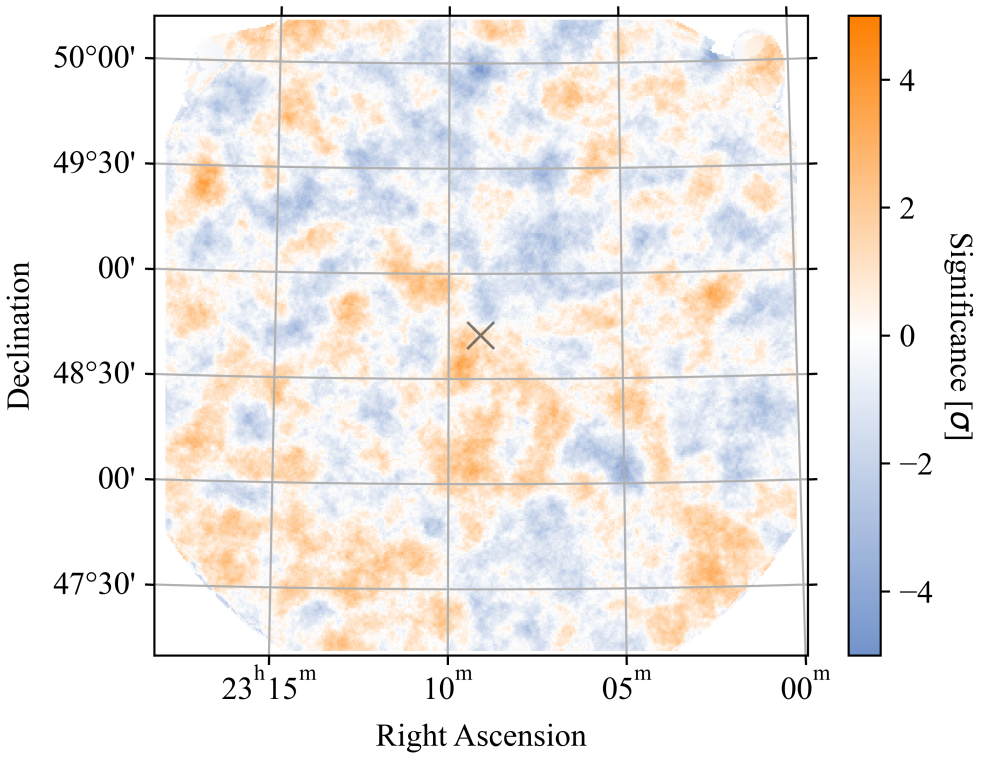

Figure A.12 Same as Figure A.1 for FRB 20220912A.

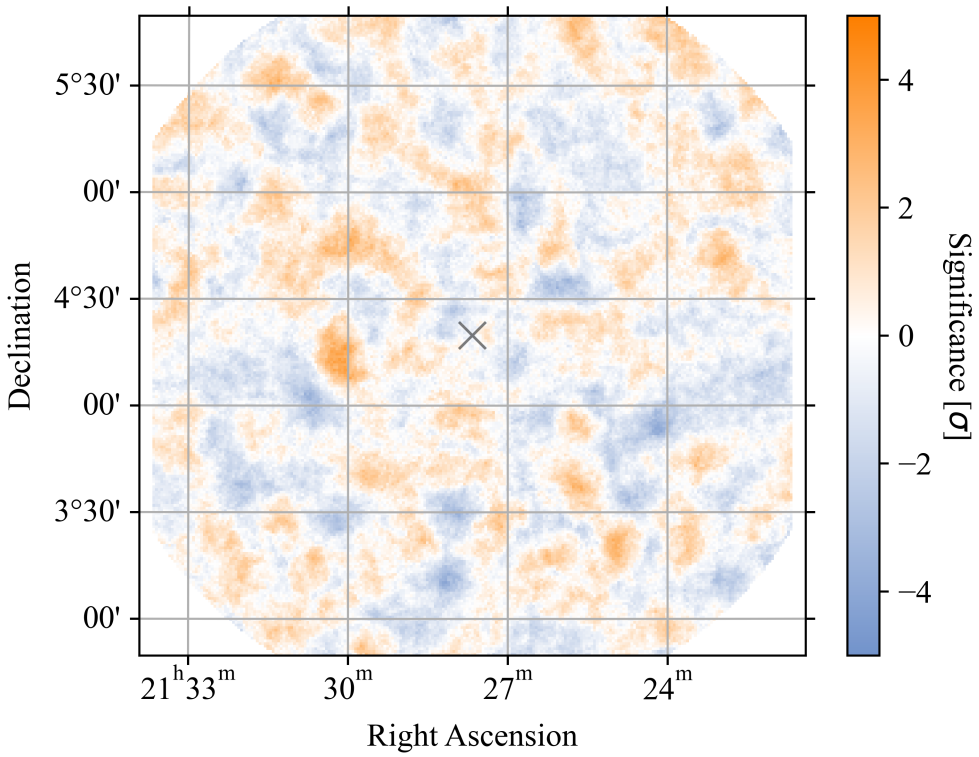

Figure A.13 Same as Figure A.1 for FRB 20240114A.

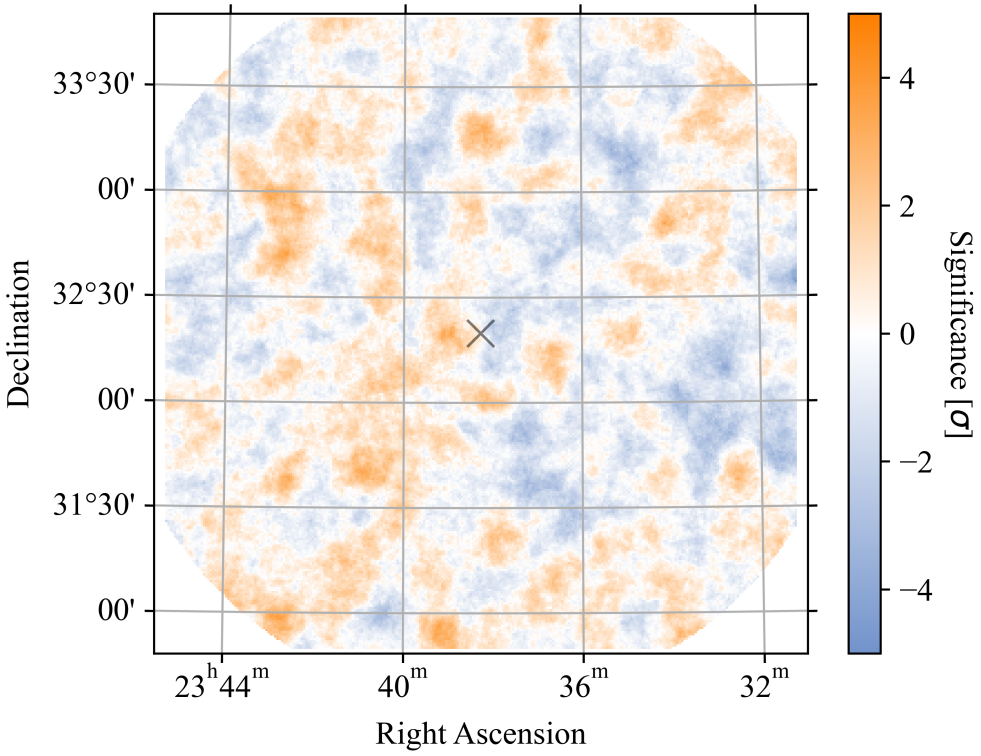

Figure A.14 Same as Figure A.1 for FRB 20240316A.

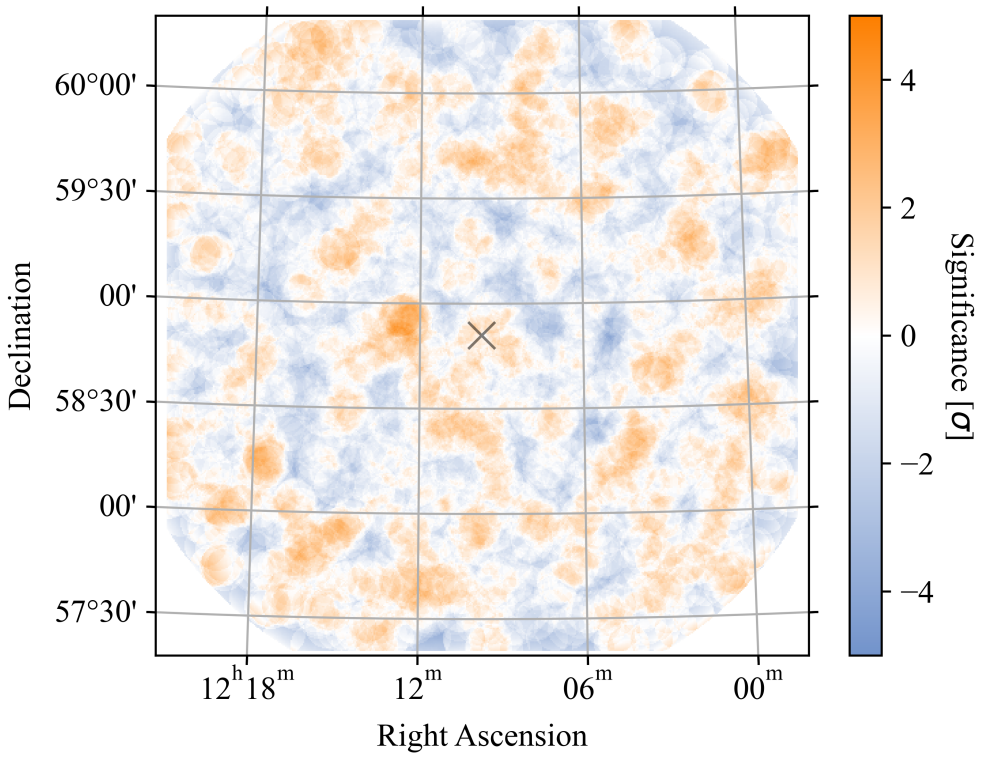

Figure A.15 Same as Figure A.1 for FRB 20250316A.

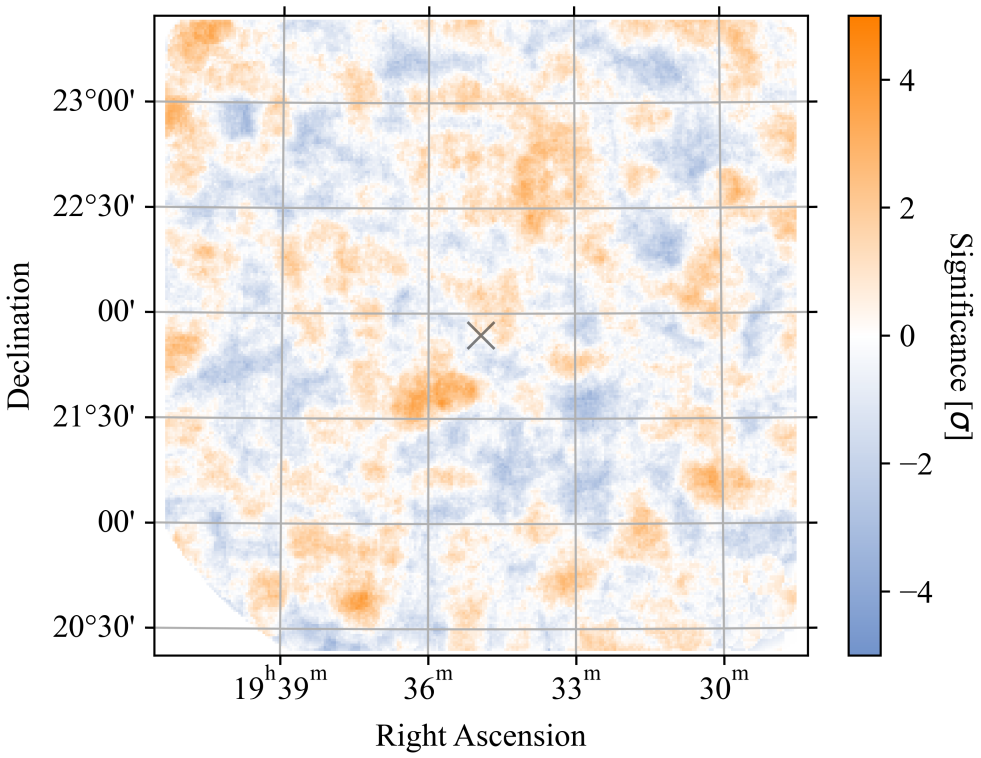

Figure A.16 Same as Figure A.1 for SGR 1935+2154.

APPENDIX B

Burst Analysis

Table B.1: VERTIAS VHE results of the targeted analysis around known FRB times. Windows are defined such that any bursts within the $\pm window$ are counted. *On* counts are counts within 0.1 degree of the FRB during the window, whereas *Off* are values determined from the whole run and scaled to the duration of the event. α is the ratio of the area of the On and the Off region. $Significance_{LiMa}$ is the significance as defined in T.-P. Li et al. (1983). Stacked results represent the total of all events and are displayed at the bottom. More information about the individual bursts, including the associated repeater, can be found in Table 5.3.

Burst Number	**Window [s]**	**On Counts**	**Off Counts**	α	**Significance**$_{LiMa}$ [σ]
1	0.001	0	5.1×10^2	2.7×10^{-8}	-0.0053
	0.01	0	5.1×10^2	2.7×10^{-7}	-0.017
	0.1	0	5.1×10^2	2.7×10^{-6}	-0.053
	1	0	5.1×10^2	2.7×10^{-5}	-0.17
	10	1	5.1×10^2	0.00027	1.5

Continued on next page

Burst Number	Window [s]	On Counts	Off Counts	α	Significance$_{LiMa}$ [σ]
3	0.001	0	5.2×10^{2}	2.3×10^{-8}	-0.0049
	0.01	0	5.2×10^{2}	2.3×10^{-7}	-0.015
	0.1	0	5.2×10^{2}	2.3×10^{-6}	-0.049
	1	0	5.2×10^{2}	2.3×10^{-5}	-0.15
	10	0	5.2×10^{2}	0.00023	-0.49
4	0.001	0	5.2×10^{2}	2.3×10^{-8}	-0.0049
	0.01	0	5.2×10^{2}	2.3×10^{-7}	-0.015
	0.1	0	5.2×10^{2}	2.3×10^{-6}	-0.049
	1	0	5.2×10^{2}	2.3×10^{-5}	-0.15
	10	0	5.2×10^{2}	0.00023	-0.49
6	0.001	0	4.8×10^{2}	2.4×10^{-8}	-0.0048
	0.01	0	4.8×10^{2}	2.4×10^{-7}	-0.015
	0.1	0	4.8×10^{2}	2.4×10^{-6}	-0.048
	1	0	4.8×10^{2}	2.4×10^{-5}	-0.15
	10	0	4.8×10^{2}	0.00024	-0.48
7	0.001	0	4.8×10^{2}	2.4×10^{-8}	-0.0048
	0.01	0	4.8×10^{2}	2.4×10^{-7}	-0.015
	0.1	0	4.8×10^{2}	2.4×10^{-6}	-0.048
	1	0	4.8×10^{2}	2.4×10^{-5}	-0.15
	10	0	4.8×10^{2}	0.00024	-0.48
8	0.001	0	4.8×10^{2}	2.4×10^{-8}	-0.0048
	0.01	0	4.8×10^{2}	2.4×10^{-7}	-0.015
	0.1	0	4.8×10^{2}	2.4×10^{-6}	-0.048
	1	0	4.8×10^{2}	2.4×10^{-5}	-0.15
	10	0	4.8×10^{2}	0.00024	-0.48
9	0.001	0	4.8×10^{2}	2.4×10^{-8}	-0.0048
	0.01	0	4.8×10^{2}	2.4×10^{-7}	-0.015
	0.1	0	4.8×10^{2}	2.4×10^{-6}	-0.048
	1	0	4.8×10^{2}	2.4×10^{-5}	-0.15

Continued on next page

Burst Number	Window [s]	On Counts	Off Counts	α	Significance$_{LiMa}$ [σ]
	10	0	4.8×10^{2}	0.00024	-0.48
10	0.001	0	4.8×10^{2}	2.4×10^{-8}	-0.0048
	0.01	0	4.8×10^{2}	2.4×10^{-7}	-0.015
	0.1	0	4.8×10^{2}	2.4×10^{-6}	-0.048
	1	0	4.8×10^{2}	2.4×10^{-5}	-0.15
	10	0	4.8×10^{2}	0.00024	-0.48
11	0.001	0	4.8×10^{2}	2.4×10^{-8}	-0.0048
	0.01	0	4.8×10^{2}	2.4×10^{-7}	-0.015
	0.1	0	4.8×10^{2}	2.4×10^{-6}	-0.048
	1	0	4.8×10^{2}	2.4×10^{-5}	-0.15
	10	0	4.8×10^{2}	0.00024	-0.48
12	0.001	0	4.8×10^{2}	2.4×10^{-8}	-0.0048
	0.01	0	4.8×10^{2}	2.4×10^{-7}	-0.015
	0.1	0	4.8×10^{2}	2.4×10^{-6}	-0.048
	1	0	4.8×10^{2}	2.4×10^{-5}	-0.15
	10	0	4.8×10^{2}	0.00024	-0.48
13	0.001	0	4.8×10^{2}	2.4×10^{-8}	-0.0048
	0.01	0	4.8×10^{2}	2.4×10^{-7}	-0.015
	0.1	0	4.8×10^{2}	2.4×10^{-6}	-0.048
	1	0	4.8×10^{2}	2.4×10^{-5}	-0.15
	10	0	4.8×10^{2}	0.00024	-0.48
14	0.001	0	4.8×10^{2}	2.4×10^{-8}	-0.0048
	0.01	0	4.8×10^{2}	2.4×10^{-7}	-0.015
	0.1	0	4.8×10^{2}	2.4×10^{-6}	-0.048
	1	0	4.8×10^{2}	2.4×10^{-5}	-0.15
	10	0	4.8×10^{2}	0.00024	-0.48
15	0.001	0	3.4×10^{2}	2.9×10^{-8}	-0.0045
	0.01	0	3.4×10^{2}	2.9×10^{-7}	-0.014
	0.1	0	3.4×10^{2}	2.9×10^{-6}	-0.045

Continued on next page

Burst Number	Window [s]	On Counts	Off Counts	α	Significance$_{LiMa}$ [σ]
	1	0	3.4×10^2	2.9×10^{-5}	-0.14
	10	0	3.4×10^2	0.00029	-0.45
16	0.001	0	3.4×10^2	2.9×10^{-8}	-0.0045
	0.01	0	3.4×10^2	2.9×10^{-7}	-0.014
	0.1	0	3.4×10^2	2.9×10^{-6}	-0.045
	1	0	3.4×10^2	2.9×10^{-5}	-0.14
	10	0	3.4×10^2	0.00029	-0.45
17	0.001	0	3.4×10^2	2.9×10^{-8}	-0.0045
	0.01	0	3.4×10^2	2.9×10^{-7}	-0.014
	0.1	0	3.4×10^2	2.9×10^{-6}	-0.045
	1	0	3.4×10^2	2.9×10^{-5}	-0.14
	10	0	3.4×10^2	0.00029	-0.45
20	0.001	0	2.1×10^2	2.3×10^{-8}	-0.0031
	0.01	0	2.1×10^2	2.3×10^{-7}	-0.0099
	0.1	0	2.1×10^2	2.3×10^{-6}	-0.031
	1	0	2.1×10^2	2.3×10^{-5}	-0.099
	10	0	2.1×10^2	0.00023	-0.31
23	0.001	0	2.5×10^2	4.3×10^{-8}	-0.0046
	0.01	0	2.5×10^2	4.3×10^{-7}	-0.015
	0.1	0	2.5×10^2	4.3×10^{-6}	-0.046
	1	0	2.5×10^2	4.3×10^{-5}	-0.15
	10	0	2.5×10^2	0.00043	-0.46
25	0.001	0	4×10^2	2.4×10^{-8}	-0.0044
	0.01	0	4×10^2	2.4×10^{-7}	-0.014
	0.1	0	4×10^2	2.4×10^{-6}	-0.044
	1	0	4×10^2	2.4×10^{-5}	-0.14
	10	0	4×10^2	0.00024	-0.44
26	0.001	0	4×10^2	2.4×10^{-8}	-0.0044
	0.01	0	4×10^2	2.4×10^{-7}	-0.014

Continued on next page

Burst Number	Window [s]	On Counts	Off Counts	α	Significance$_{LiMa}$ [σ]
	0.1	0	4×10^2	2.4×10^{-6}	-0.044
	1	0	4×10^2	2.4×10^{-5}	-0.14
	10	0	4×10^2	0.00024	-0.44
27	0.001	0	4×10^2	2.4×10^{-8}	-0.0044
	0.01	0	4×10^2	2.4×10^{-7}	-0.014
	0.1	0	4×10^2	2.4×10^{-6}	-0.044
	1	0	4×10^2	2.4×10^{-5}	-0.14
	10	0	4×10^2	0.00024	-0.44
28	0.001	0	3.4×10^2	2.7×10^{-8}	-0.0043
	0.01	0	3.4×10^2	2.7×10^{-7}	-0.014
	0.1	0	3.4×10^2	2.7×10^{-6}	-0.043
	1	0	3.4×10^2	2.7×10^{-5}	-0.14
	10	0	3.4×10^2	0.00027	-0.43
30	0.001	0	1.7×10^2	5.4×10^{-8}	-0.0043
	0.01	0	1.7×10^2	5.4×10^{-7}	-0.014
	0.1	0	1.7×10^2	5.4×10^{-6}	-0.043
	1	0	1.7×10^2	5.4×10^{-5}	-0.14
	10	0	1.7×10^2	0.00054	-0.43
33	0.001	0	1.3×10^2	7.4×10^{-8}	-0.0044
	0.01	0	1.3×10^2	7.4×10^{-7}	-0.014
	0.1	0	1.3×10^2	7.4×10^{-6}	-0.044
	1	0	1.3×10^2	7.4×10^{-5}	-0.14
	10	0	1.3×10^2	0.00074	-0.44
35	0.001	0	1.1×10^2	9.2×10^{-8}	-0.0045
	0.01	0	1.1×10^2	9.2×10^{-7}	-0.014
	0.1	0	1.1×10^2	9.2×10^{-6}	-0.045
	1	0	1.1×10^2	9.2×10^{-5}	-0.14
	10	0	1.1×10^2	0.00092	-0.45
36	0.001	0	1.1×10^2	9.2×10^{-8}	-0.0045

Continued on next page

Burst Number	Window [s]	On Counts	Off Counts	α	Significance$_{LiMa}$ [σ]
	0.01	0	1.1×10^{2}	9.2×10^{-7}	-0.014
	0.1	0	1.1×10^{2}	9.2×10^{-6}	-0.045
	1	0	1.1×10^{2}	9.2×10^{-5}	-0.14
	10	0	1.1×10^{2}	0.00092	-0.45
37	0.001	0	1.6×10^{2}	9.4×10^{-8}	-0.0055
	0.01	0	1.6×10^{2}	9.4×10^{-7}	-0.017
	0.1	0	1.6×10^{2}	9.4×10^{-6}	-0.055
	1	0	1.6×10^{2}	9.4×10^{-5}	-0.17
	10	0	1.6×10^{2}	0.00094	-0.55
38	0.001	0	1.6×10^{2}	9.4×10^{-8}	-0.0055
	0.01	0	1.6×10^{2}	9.4×10^{-7}	-0.017
	0.1	0	1.6×10^{2}	9.4×10^{-6}	-0.055
	1	0	1.6×10^{2}	9.4×10^{-5}	-0.17
	10	1	1.6×10^{2}	0.00094	1.4
39	0.001	0	1.6×10^{2}	9.4×10^{-8}	-0.0055
	0.01	0	1.6×10^{2}	9.4×10^{-7}	-0.017
	0.1	0	1.6×10^{2}	9.4×10^{-6}	-0.055
	1	0	1.6×10^{2}	9.4×10^{-5}	-0.17
	10	0	1.6×10^{2}	0.00094	-0.55
40	0.001	0	1.6×10^{2}	9.4×10^{-8}	-0.0055
	0.01	0	1.6×10^{2}	9.4×10^{-7}	-0.017
	0.1	0	1.6×10^{2}	9.4×10^{-6}	-0.055
	1	0	1.6×10^{2}	9.4×10^{-5}	-0.17
	10	0	1.6×10^{2}	0.00094	-0.55
41	0.001	0	1.6×10^{2}	9.4×10^{-8}	-0.0055
	0.01	0	1.6×10^{2}	9.4×10^{-7}	-0.017
	0.1	0	1.6×10^{2}	9.4×10^{-6}	-0.055
	1	0	1.6×10^{2}	9.4×10^{-5}	-0.17
	10	1	1.6×10^{2}	0.00094	1.4

Continued on next page

Burst Number	Window [s]	On Counts	Off Counts	α	Significance$_{LiMa}$ [σ]
42	0.001	0	1.6×10^{2}	9.4×10^{-8}	-0.0055
	0.01	0	1.6×10^{2}	9.4×10^{-7}	-0.017
	0.1	0	1.6×10^{2}	9.4×10^{-6}	-0.055
	1	0	1.6×10^{2}	9.4×10^{-5}	-0.17
	10	1	1.6×10^{2}	0.00094	1.4
43	0.001	0	1.2×10^{2}	8×10^{-8}	-0.0044
	0.01	0	1.2×10^{2}	8×10^{-7}	-0.014
	0.1	0	1.2×10^{2}	8×10^{-6}	-0.044
	1	0	1.2×10^{2}	8×10^{-5}	-0.14
	10	1	1.2×10^{2}	0.0008	1.7
44	0.001	0	1.2×10^{2}	8×10^{-8}	-0.0044
	0.01	0	1.2×10^{2}	8×10^{-7}	-0.014
	0.1	0	1.2×10^{2}	8×10^{-6}	-0.044
	1	0	1.2×10^{2}	8×10^{-5}	-0.14
	10	0	1.2×10^{2}	0.0008	-0.44
45	0.001	0	1.2×10^{2}	8×10^{-8}	-0.0044
	0.01	0	1.2×10^{2}	8×10^{-7}	-0.014
	0.1	0	1.2×10^{2}	8×10^{-6}	-0.044
	1	0	1.2×10^{2}	8×10^{-5}	-0.14
	10	0	1.2×10^{2}	0.0008	-0.44
46	0.001	0	1.2×10^{2}	8×10^{-8}	-0.0044
	0.01	0	1.2×10^{2}	8×10^{-7}	-0.014
	0.1	0	1.2×10^{2}	8×10^{-6}	-0.044
	1	0	1.2×10^{2}	8×10^{-5}	-0.14
	10	0	1.2×10^{2}	0.0008	-0.44
47	0.001	0	1.2×10^{2}	8×10^{-8}	-0.0044
	0.01	0	1.2×10^{2}	8×10^{-7}	-0.014
	0.1	0	1.2×10^{2}	8×10^{-6}	-0.044
	1	0	1.2×10^{2}	8×10^{-5}	-0.14

Continued on next page

Burst Number	Window [s]	On Counts	Off Counts	α	Significance$_{LiMa}$ [σ]
	10	0	1.2×10^2	0.0008	-0.44
48	0.001	0	1.2×10^2	8×10^{-8}	-0.0044
	0.01	0	1.2×10^2	8×10^{-7}	-0.014
	0.1	0	1.2×10^2	8×10^{-6}	-0.044
	1	0	1.2×10^2	8×10^{-5}	-0.14
	10	0	1.2×10^2	0.0008	-0.44
49	0.001	0	1.2×10^2	8.8×10^{-8}	-0.0046
	0.01	0	1.2×10^2	8.8×10^{-7}	-0.015
	0.1	0	1.2×10^2	8.8×10^{-6}	-0.046
	1	0	1.2×10^2	8.8×10^{-5}	-0.15
	10	0	1.2×10^2	0.00088	-0.46
50	0.001	0	1.2×10^2	8.8×10^{-8}	-0.0046
	0.01	0	1.2×10^2	8.8×10^{-7}	-0.015
	0.1	0	1.2×10^2	8.8×10^{-6}	-0.046
	1	0	1.2×10^2	8.8×10^{-5}	-0.15
	10	1	1.2×10^2	0.00088	1.6
51	0.001	0	1.4×10^2	1×10^{-7}	-0.0055
	0.01	0	1.4×10^2	1×10^{-6}	-0.017
	0.1	0	1.4×10^2	1×10^{-5}	-0.055
	1	0	1.4×10^2	0.0001	-0.17
	10	0	1.4×10^2	0.001	-0.55
64	0.001	0	3×10^2	7.3×10^{-8}	-0.0067
	0.01	0	3×10^2	7.3×10^{-7}	-0.021
	0.1	0	3×10^2	7.3×10^{-6}	-0.067
	1	0	3×10^2	7.3×10^{-5}	-0.21
	10	1	3×10^2	0.00073	1.2
67	0.001	0	1.3×10^2	8.6×10^{-8}	-0.0047
	0.01	0	1.3×10^2	8.6×10^{-7}	-0.015
	0.1	0	1.3×10^2	8.6×10^{-6}	-0.047

Continued on next page

Burst Number	Window [s]	On Counts	Off Counts	α	Significance$_{LiMa}$ [σ]
	1	2	1.3×10^{2}	8.6×10^{-5}	4.1
	10	2	1.3×10^{2}	0.00086	2.8
68	0.001	0	1.2×10^{2}	8×10^{-8}	-0.0043
	0.01	0	1.2×10^{2}	8×10^{-7}	-0.014
	0.1	0	1.2×10^{2}	8×10^{-6}	-0.043
	1	0	1.2×10^{2}	8×10^{-5}	-0.14
	10	0	1.2×10^{2}	0.0008	-0.43
69	0.001	0	1.1×10^{2}	8×10^{-8}	-0.0042
	0.01	0	1.1×10^{2}	8×10^{-7}	-0.013
	0.1	0	1.1×10^{2}	8×10^{-6}	-0.042
	1	0	1.1×10^{2}	8×10^{-5}	-0.13
	10	0	1.1×10^{2}	0.0008	-0.42
70	0.001	0	1.1×10^{2}	8×10^{-8}	-0.0042
	0.01	0	1.1×10^{2}	8×10^{-7}	-0.013
	0.1	0	1.1×10^{2}	8×10^{-6}	-0.042
	1	0	1.1×10^{2}	8×10^{-5}	-0.13
	10	0	1.1×10^{2}	0.0008	-0.42
71	0.001	0	1.1×10^{2}	8×10^{-8}	-0.0042
	0.01	0	1.1×10^{2}	8×10^{-7}	-0.013
	0.1	0	1.1×10^{2}	8×10^{-6}	-0.042
	1	0	1.1×10^{2}	8×10^{-5}	-0.13
	10	0	1.1×10^{2}	0.0008	-0.42
72	0.001	0	1×10^{2}	9.2×10^{-8}	-0.0044
	0.01	0	1×10^{2}	9.2×10^{-7}	-0.014
	0.1	0	1×10^{2}	9.2×10^{-6}	-0.044
	1	0	1×10^{2}	9.2×10^{-5}	-0.14
	10	0	1×10^{2}	0.00092	-0.44
73	0.001	0	1.5×10^{2}	9.2×10^{-8}	-0.0052
	0.01	0	1.5×10^{2}	9.2×10^{-7}	-0.017

Continued on next page

Burst Number	**Window [s]**	**On Counts**	**Off Counts**	α	**Significance**$_{LiMa}$ [σ]
	0.1	0	1.5×10^{2}	9.2×10^{-6}	-0.052
	1	0	1.5×10^{2}	9.2×10^{-5}	-0.17
	10	0	1.5×10^{2}	0.00092	-0.52
Stacked	0.001	0	1.2×10^{4}	5.9×10^{-8}	-0.039
	0.01	0	1.2×10^{4}	5.9×10^{-7}	-0.12
	0.1	0	1.2×10^{4}	5.9×10^{-6}	-0.39
	1	2	1.2×10^{4}	5.9×10^{-5}	1.2
	10	9	1.2×10^{4}	5.9×10^{-4}	0.54

APPENDIX C

Run by Run Analysis

The individual analysis of runs is presented here in Figure C.1 through C.15 for the sources listed in Table 5.2. In each figure, the individual independent analysis of the run is presented and compared with a 3 σ significance (post-trials). In addition, the overall distribution of the significances for each of these individual sources is presented in a histogram. Finally, a cumulative significance is displayed using the average α value and the T.-P. Li et al. (1983) significance. For all sources, only one candidate run is identified and analyzed in more detail in Chapter 5.

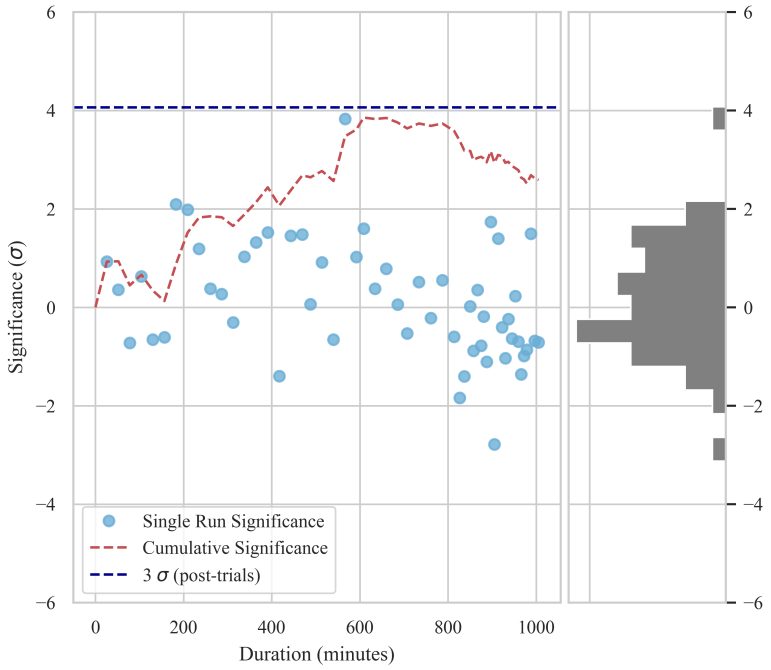

Figure C.1 Run by run analysis of significance of FRB 20121102A. Each blue point represents the T.-P. Li et al. (1983) significance for an individual run. The red dashed line shows the cumulative significance. The blue dashed lines indicate the post-trials 3σ confidence level for the search. In the right figure, the distribution of significances is presented in a histogram.

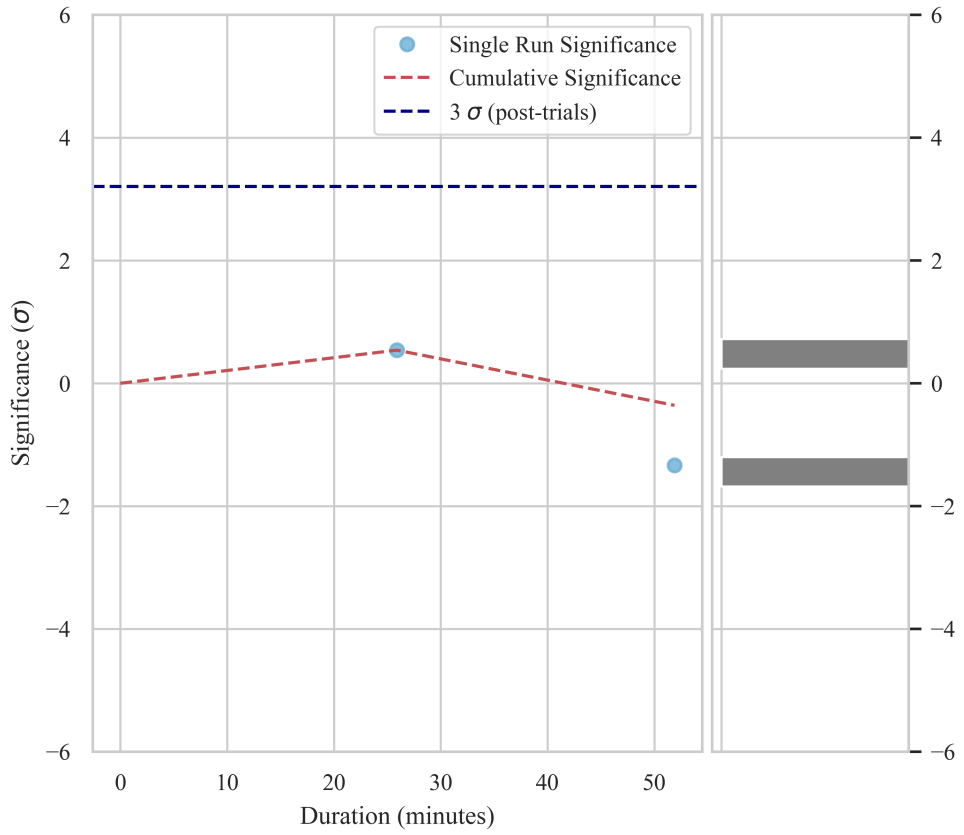

Figure C.2 Same as Figure C.1 for FRB 20180301A.

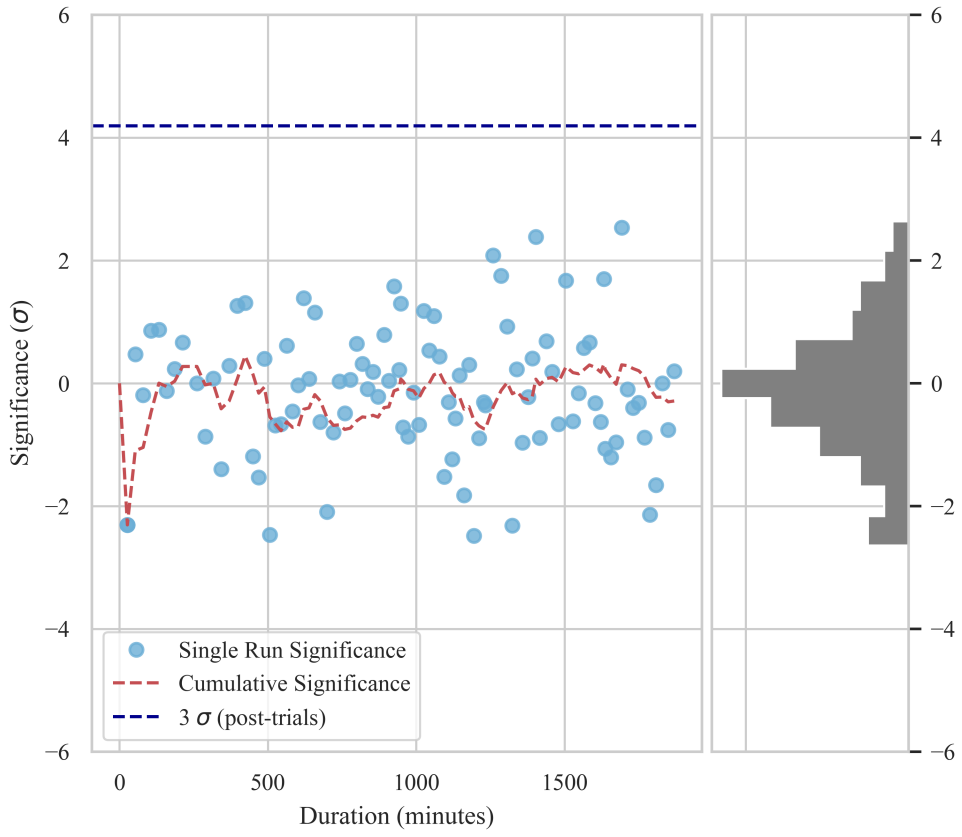

Figure C.3 Same as Figure C.1 for FRB 20180814A.

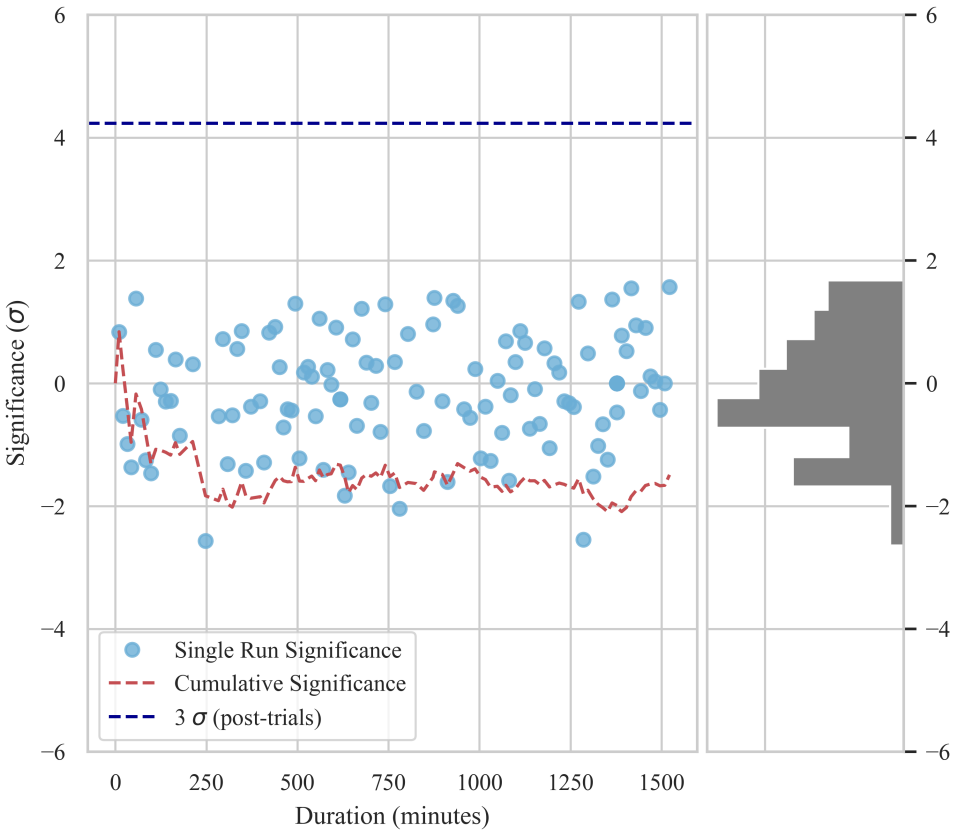

Figure C.4 Same as Figure C.1 for FRB 20180916B.

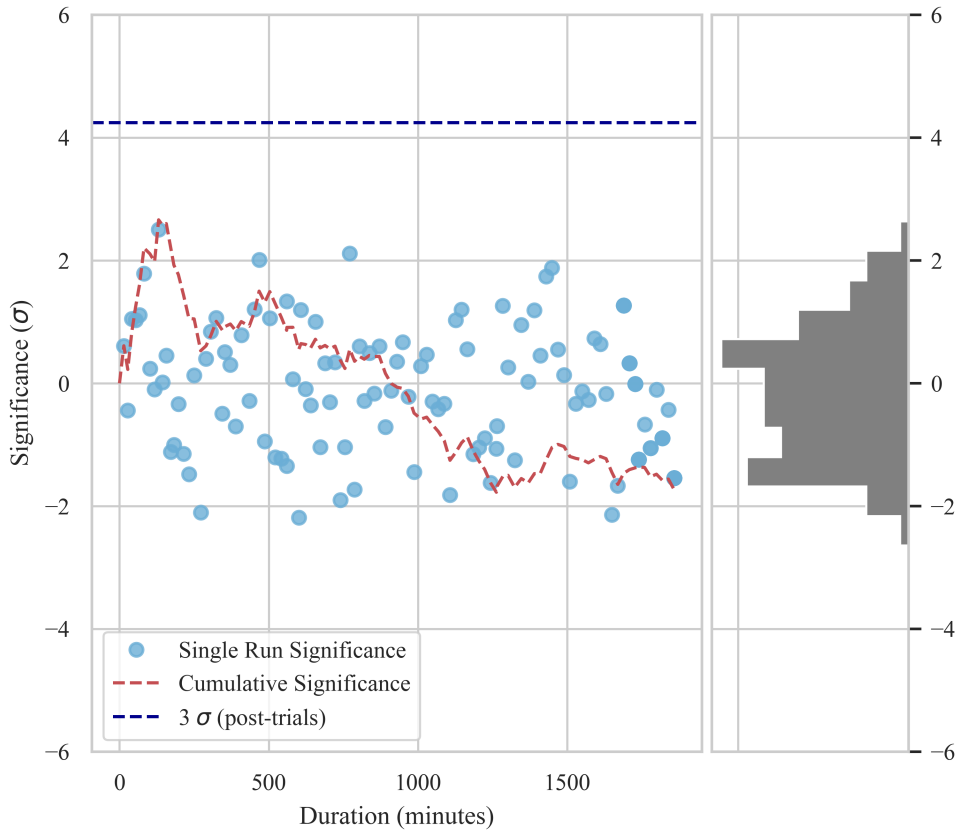

Figure C.5 Same as Figure C.1 for FRB 20181030A.

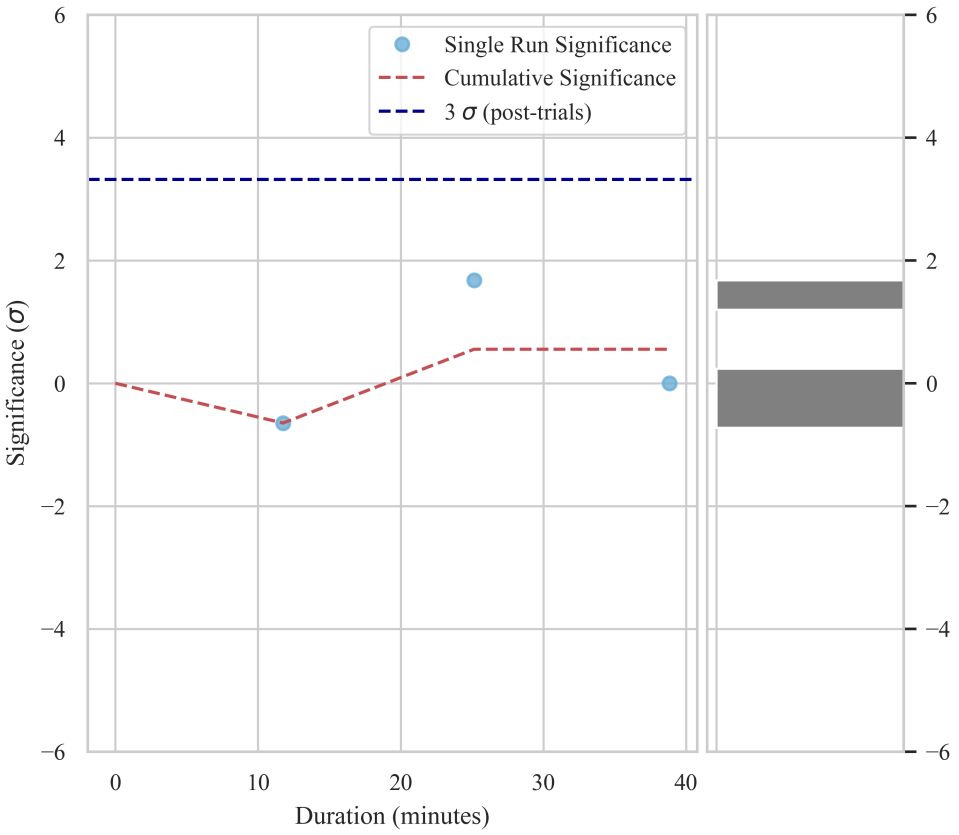

Figure C.6 Same as Figure C.1 for FRB 20181119A.

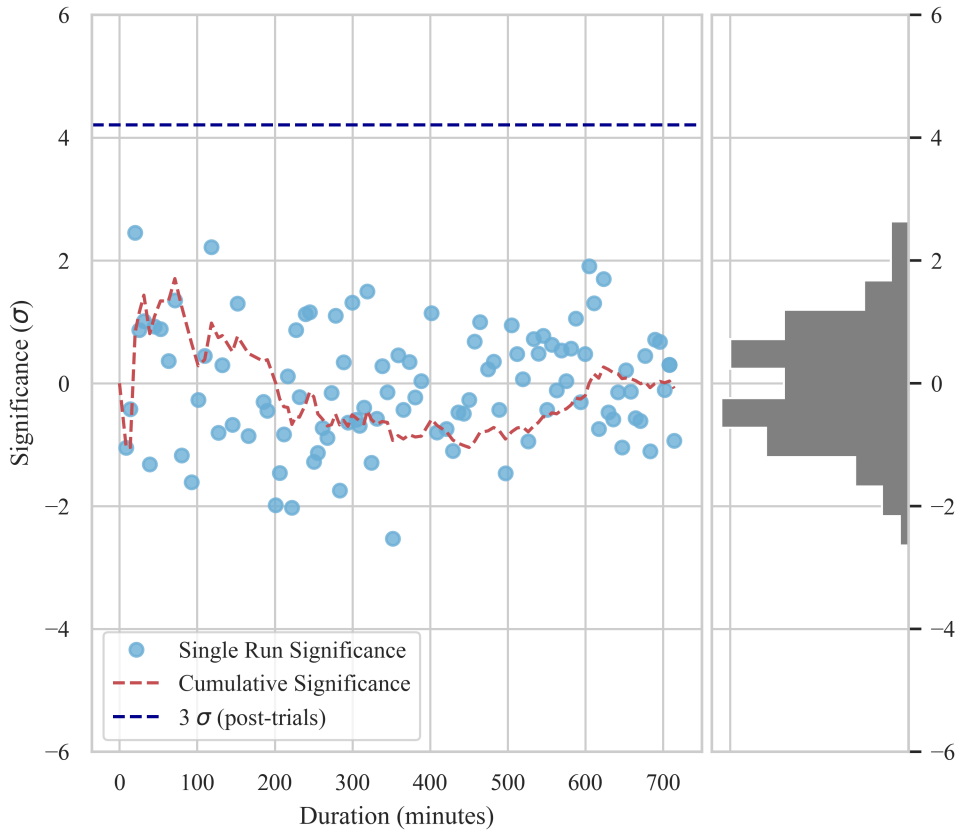

Figure C.7 Same as Figure C.1 for FRB 20190116B.

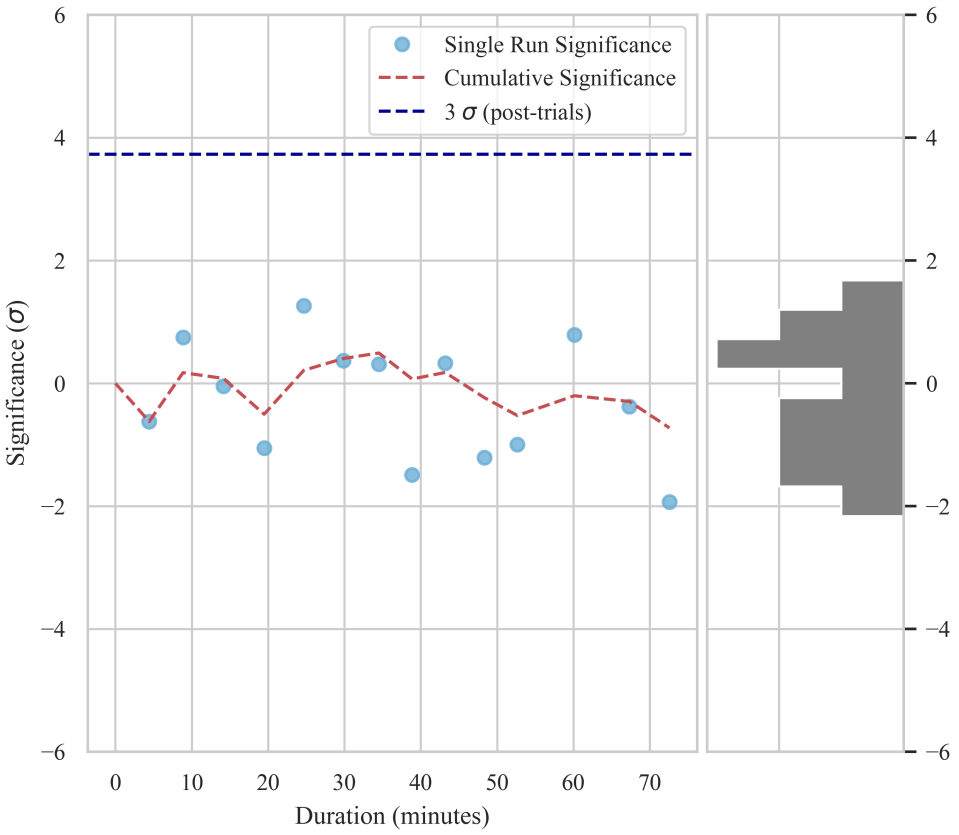

Figure C.8 Same as Figure C.1 for FRB 20190213A.

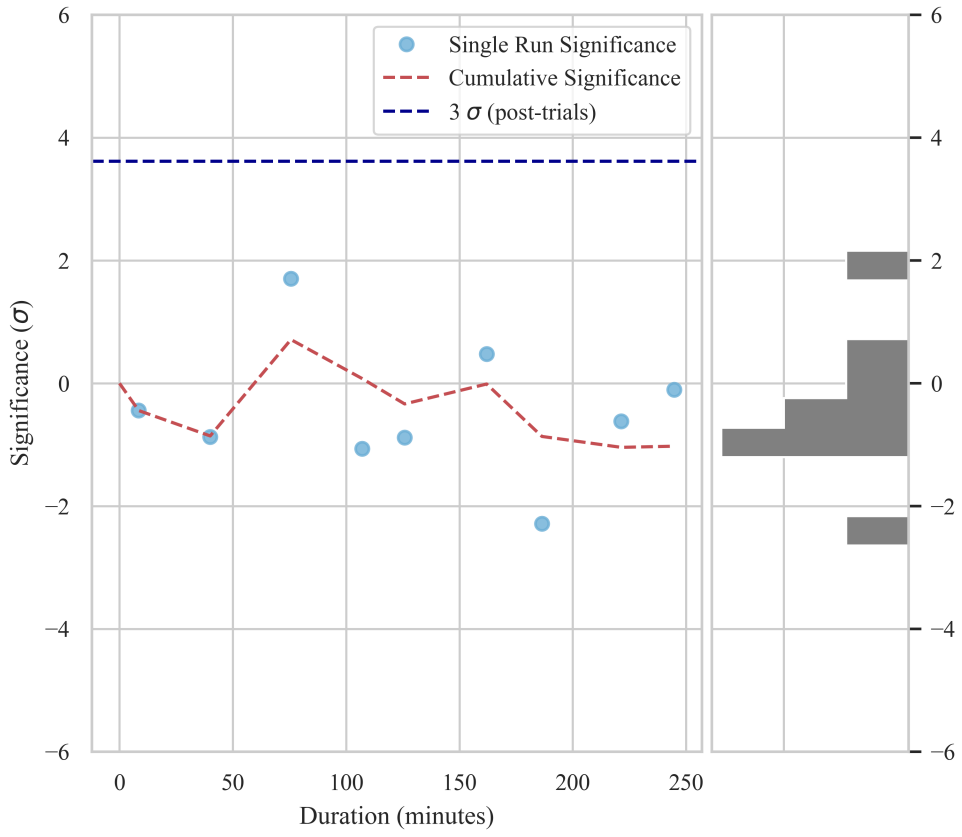

Figure C.9 Same as Figure C.1 for FRB 20190213B.

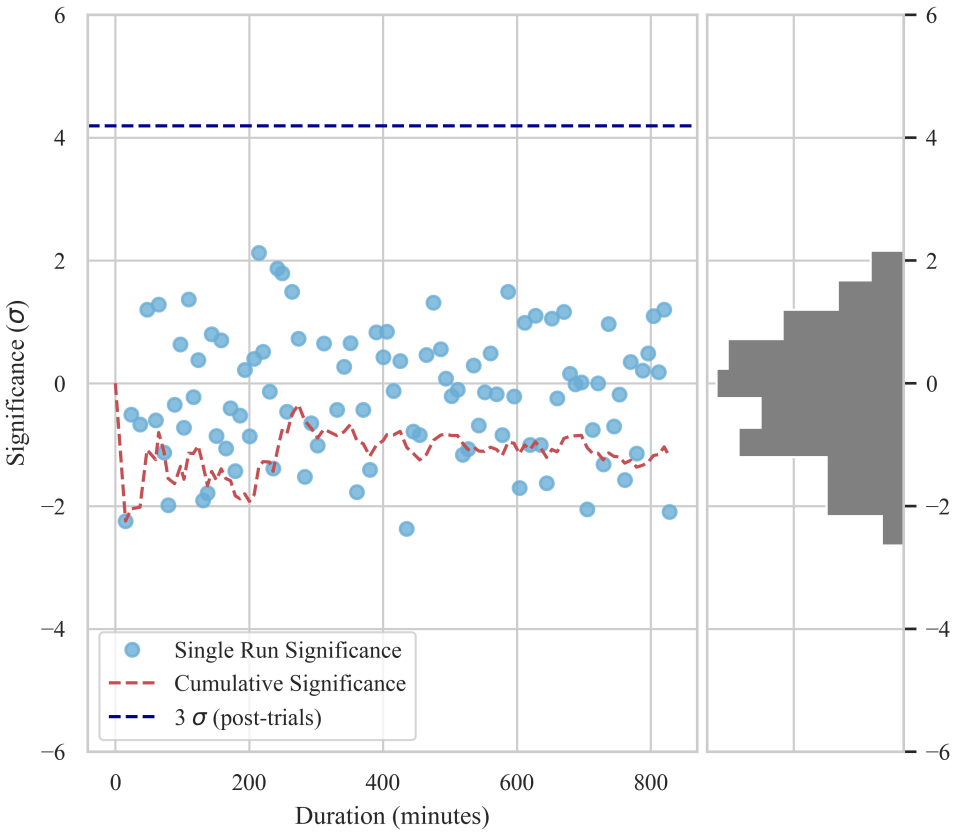

Figure C.10 Same as Figure C.1 for FRB 20190303A.

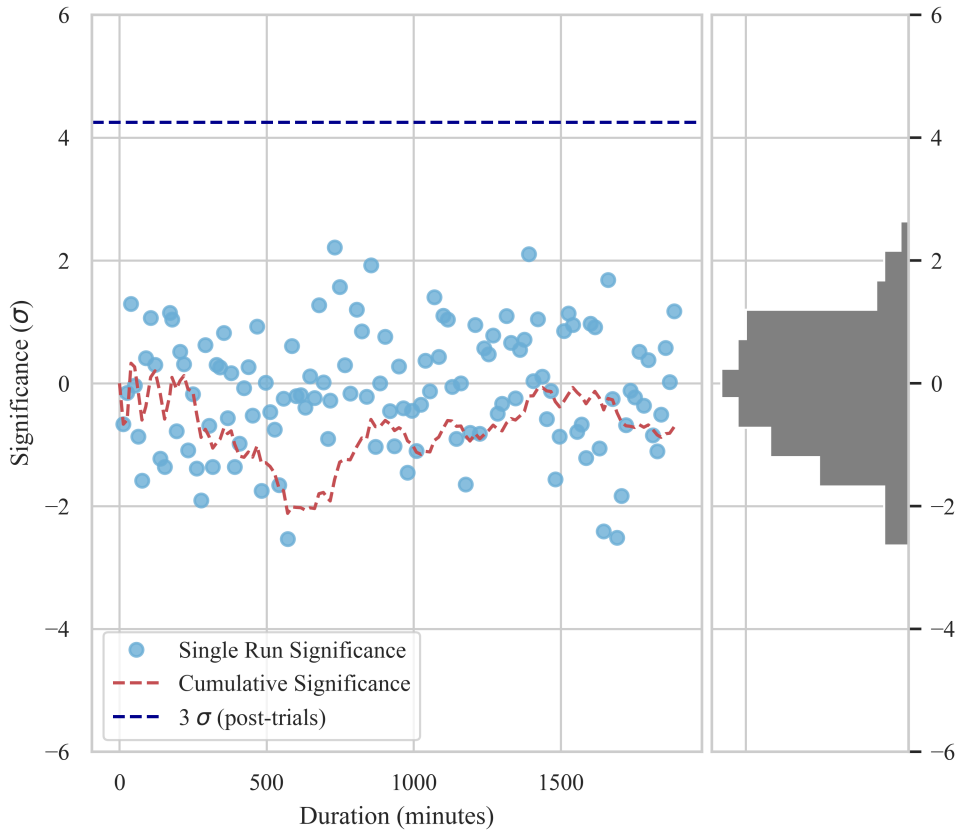

Figure C.11 Same as Figure C.1 for FRB 20200120E.

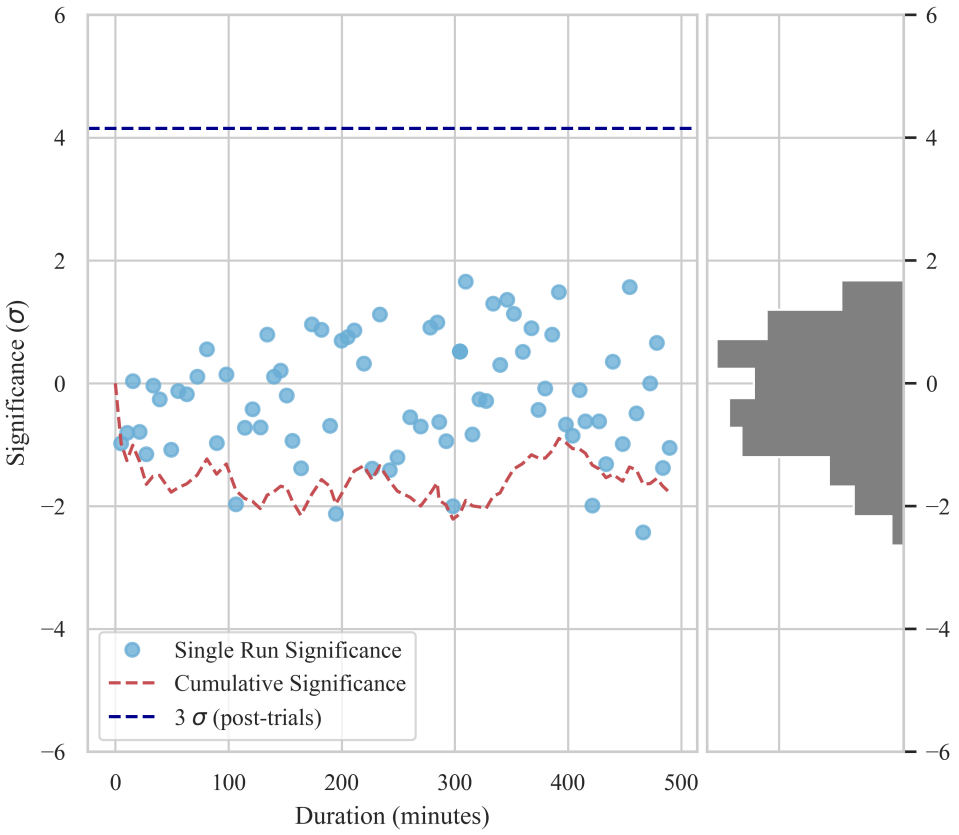

Figure C.12 Same as Figure C.1 for FRB 20201124A.

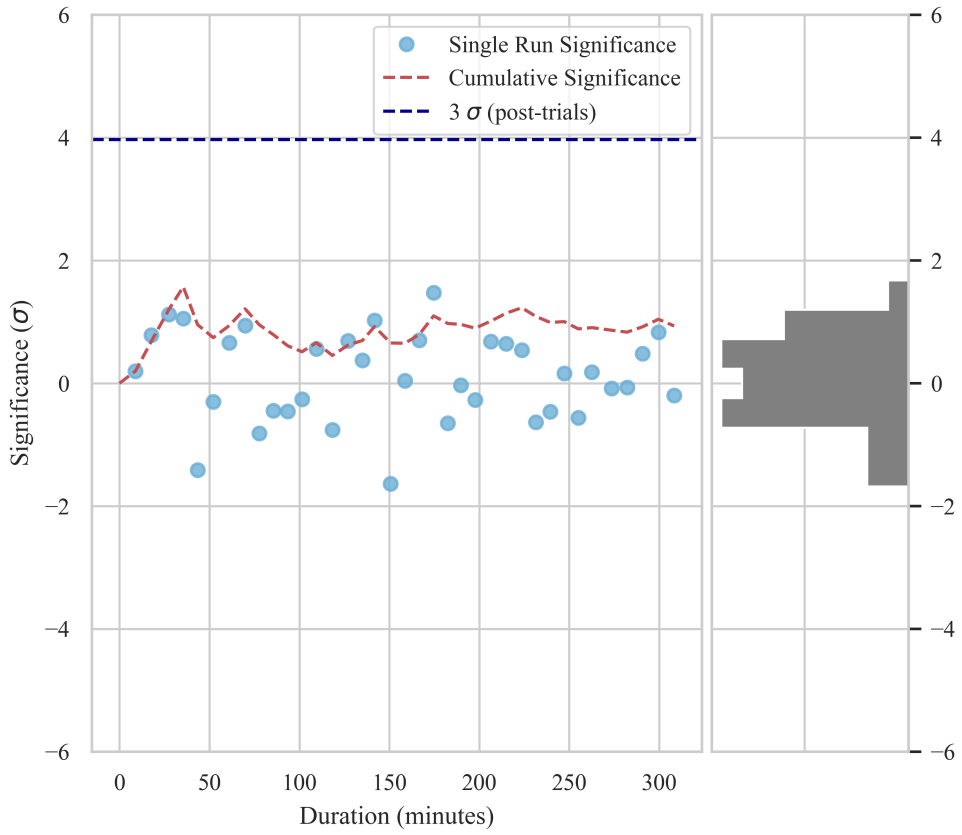

Figure C.13 Same as Figure C.1 for FRB 20220912a.

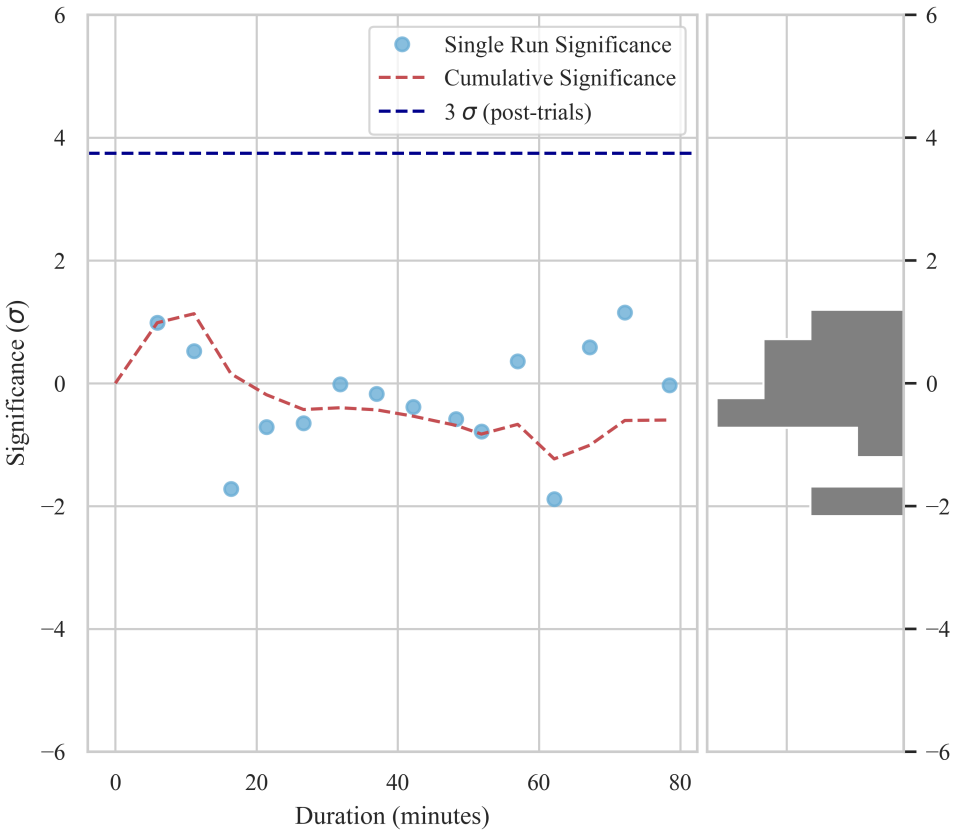

Figure C.14 Same as Figure C.1 for FRB 20240114A.

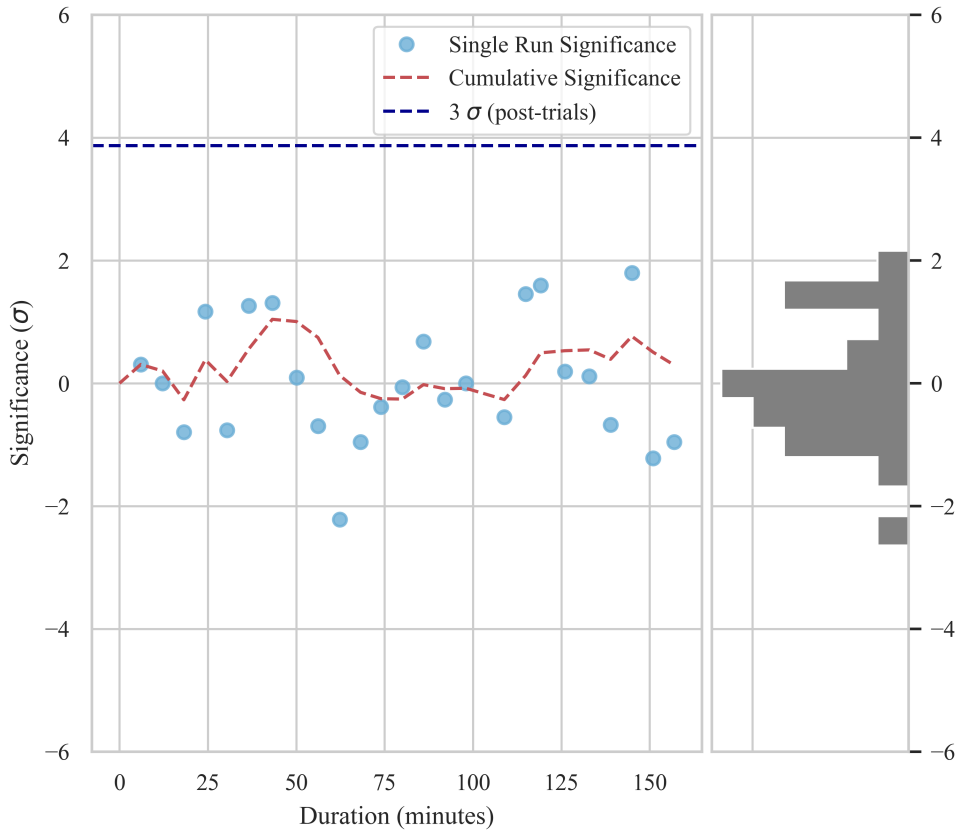

Figure C.15 Same as Figure C.1 for FRB 20240316A.

Bibliography

Aartsen, M. G., R. Abbasi, Y. Abdou, et al. (Aug. 2013). "Measurement of the cosmic ray energy spectrum with IceTop-73". In: *Physical Review D* 88. Publisher: APS ADS Bibcode: 2013PhRvD..88d2004A, p. 042004. ISSN: 1550-79980556-2821. DOI: 10.1103/PhysRevD.88.042004. URL: https://ui.adsabs.harvard.edu/abs/2013PhRvD..88d2004A (visited on 05/07/2025).

Aartsen, M. G., R. Abbasi, M. Ackermann, et al. (Dec. 2020). "Cosmic ray spectrum from 250 TeV to 10 PeV using IceTop". In: *Physical Review D* 102. Publisher: APS ADS Bibcode: 2020PhRvD.102l2001A, p. 122001. ISSN: 1550-79980556-2821. DOI: 10.1103/PhysRevD.102.122001. URL: https://ui.adsabs.harvard.edu/abs/2020PhRvD.102l2001A (visited on 05/07/2025).

Aartsen, M. G., M. Ackermann, J. Adams, et al. (Mar. 2017). "The IceCube Neutrino Observatory: instrumentation and online systems". In: *Journal of Instrumentation* 12. Publisher: IOP ADS Bibcode: 2017JInst..12P3012A, P03012. DOI: 10.1088/1748-0221/12/03/P03012. URL: https://ui.adsabs.harvard.edu/abs/2017JInst..12P3012A (visited on 05/21/2025).

Aartsen, M. G., M. Ackermann, J. Adams, et al. (Oct. 2019). "Cosmic ray spectrum and composition from PeV to EeV using 3 years of data from IceTop and IceCube". In: *Physical Review D* 100. Publisher: APS ADS Bibcode: 2019PhRvD.100h2002A, p. 082002. ISSN: 1550-79980556-2821. DOI: 10.1103/PhysRevD.100.082002. URL: https://ui.adsabs.harvard.edu/abs/2019PhRvD.100h2002A (visited on 05/07/2025).

Abbasi, R., M. Ackermann, J. Adams, et al. (Nov. 2023). "IceCat-1: The IceCube Event Catalog of Alert Tracks". In: *The Astrophysical Journal Supplement Series* 269. Publisher: IOP ADS Bibcode: 2023ApJS..269...25A, p. 25. ISSN: 0067-0049. DOI: 10.3847/1538-4365/acfa95. URL: https://ui.adsabs.harvard.edu/abs/2023ApJS..269...25A (visited on 05/19/2025).

Abbasi, R. U., M. Abe, T. Abu-Zayyad, et al. (Sept. 2018). "The Cosmic Ray Energy Spectrum between 2 PeV and 2 EeV Observed with the TALE Detector in Monocular Mode". In: *The Astrophysical Journal* 865. Publisher: IOP ADS Bibcode:

2018ApJ...865...74A, p. 74. ISSN: 0004-637X. DOI: 10.3847/1538-4357/aada05. URL: https://ui.adsabs.harvard.edu/abs/2018ApJ...865...74A (visited on 05/07/2025).

Abbott, Thomas and CHIME/FRB Collaboration (July 2024). "CHIME/FRB observation of a high activity state from a newly discovered repeating fast radio burst source FRB 20240316A". In: *The Astronomer's Telegram* 16734. ADS Bibcode: 2024ATel16734....1A, p. 1. URL: https://ui.adsabs.harvard.edu/abs/2024ATel16734....1A (visited on 07/05/2025).

Abbott, Thomas C., Andrew V. Zwaniga, Charanjot Brar, et al. (Jan. 2025). "frb-voe: A Real-time Virtual Observatory Event Alert Service for Fast Radio Bursts". In: *The Astronomical Journal* 169. Publisher: IOP ADS Bibcode: 2025AJ....169...39A, p. 39. ISSN: 0004-6256. DOI: 10.3847/1538-3881/ad9451. URL: https://ui.adsabs.harvard.edu/abs/2025AJ....169...39A (visited on 11/11/2025).

Abdalla, H., R. Adam, F. Aharonian, et al. (Nov. 2019). "A very-high-energy component deep in the γ-ray burst afterglow". In: *Nature* 575. ADS Bibcode: 2019Natur.575..464A, pp. 464–467. ISSN: 0028-0836. DOI: 10.1038/s41586-019-1743-9. URL: https://ui.adsabs.harvard.edu/abs/2019Natur.575..464A (visited on 06/25/2025).

Abdollahi, S., M. Ajello, L. Baldini, et al. (Apr. 2023). "The Fermi-LAT Lightcurve Repository". In: *The Astrophysical Journal Supplement Series* 265. Publisher: IOP ADS Bibcode: 2023ApJS..265...31A, p. 31. ISSN: 0067-0049. DOI: 10.3847/1538-4365/acbb6a. URL: https://ui.adsabs.harvard.edu/abs/2023ApJS..265...31A (visited on 07/10/2025).

Abdul Halim, A., P. Abreu, M. Aglietta, et al. (Nov. 2024). "Large-scale Cosmic-ray Anisotropies with 19 yr of Data from the Pierre Auger Observatory". In: *The Astrophysical Journal* 976. Publisher: IOP ADS Bibcode: 2024ApJ...976...48A, p. 48. ISSN: 0004-637X. DOI: 10.3847/1538-4357/ad843b. URL: https://ui.adsabs.harvard.edu/abs/2024ApJ...976...48A (visited on 05/21/2025).

Abe, H., K. Abe, S. Abe, et al. (Oct. 2023). "Observations of the Crab Nebula and Pulsar with the Large-sized Telescope Prototype of the Cherenkov Telescope Array". In: *The Astrophysical Journal* 956. Publisher: IOP ADS Bibcode: 2023ApJ...956...80A, p. 80. ISSN: 0004-637X. DOI: 10.3847/1538-4357/ace89d. URL: https://ui.adsabs.harvard.edu/abs/2023ApJ...956...80A (visited on 05/30/2025).

Abe, H., S. Abe, V. A. Acciari, et al. (Jan. 2024). "MAGIC detection of GRB 201216C at z = 1.1". In: *Monthly Notices of the Royal Astronomical Society* 527. Publisher: OUP ADS Bibcode: 2024MNRAS.527.5856A, pp. 5856–5867. ISSN: 0035-8711. DOI: 10.1093/mnras/stad2958. URL: https://ui.adsabs.harvard.edu/abs/2024MNRAS.527.5856A (visited on 07/03/2025).

Abe, K., S. Abe, A. Abhishek, et al. (Oct. 2024). "A detailed study of the very high-energy Crab pulsar emission with the LST-1". In: *Astronomy and Astrophysics* 690. Publisher: EDP ADS Bibcode: 2024A&A...690A.167A, A167. ISSN: 0004-6361. DOI: 10.1051/0004-6361/202450059. URL: https://ui.adsabs.harvard.edu/abs/2024A&A...690A.167A (visited on 07/01/2025).

Abe, K., S. Abe, A. Abhishek, et al. (June 2025). "Detection of the Geminga pulsar at energies down to 20 GeV with the LST-1 of CTAO". In: *Astronomy and Astrophysics* 698. Publisher: EDP ADS Bibcode: 2025A&A...698A.283A, A283. ISSN: 0004-6361. DOI: 10.1051/0004-6361/202554350. URL: https://ui.adsabs.harvard.edu/abs/2025A&A...698A.283A (visited on 07/01/2025).

Abeysekara, A. U., A. Albert, R. Alfaro, et al. (July 2023). "The High-Altitude Water Cherenkov (HAWC) observatory in México: The primary detector". In: *Nuclear Instruments and Methods in Physics Research A* 1052. Publisher: Elsevier ADS Bibcode: 2023NIMPA105268253A, p. 168253. ISSN: 0168-9002. DOI: 10.1016/j.nima.2023.168253. URL: https://ui.adsabs.harvard.edu/abs/2023NIMPA105268253A (visited on 06/20/2025).

Abeysekara, A. U., W. Benbow, R. Bird, et al. (Apr. 2018). "Multiwavelength Observations of the Blazar BL Lacertae: A New Fast TeV Gamma-Ray Flare". In: *The Astrophysical Journal* 856. Publisher: IOP ADS Bibcode: 2018ApJ...856...95A, p. 95. ISSN: 0004-637X. DOI: 10.3847/1538-4357/aab35c. URL: https://ui.adsabs.harvard.edu/abs/2018ApJ...856...95A (visited on 07/08/2025).

Abeysekara, A. U., W. Benbow, R. Bird, et al. (Feb. 2020). "The Great Markarian 421 Flare of 2010 February: Multiwavelength Variability and Correlation Studies". In: *The Astrophysical Journal* 890. Publisher: IOP ADS Bibcode: 2020ApJ...890...97A, p. 97. ISSN: 0004-637X. DOI: 10.3847/1538-4357/ab6612. URL: https://ui.adsabs.harvard.edu/abs/2020ApJ...890...97A (visited on 03/28/2025).

Abraham, J., P. Abreu, M. Aglietta, et al. (Aug. 2008). "Observation of the Suppression of the Flux of Cosmic Rays above 4×1019eV". In: *Physical Review Letters* 101. Publisher: APS ADS Bibcode: 2008PhRvL.101f1101A, p. 061101. ISSN: 0031-9007. DOI: 10.1103/PhysRevLett.101.061101. URL: https://ui.adsabs.harvard.edu/abs/2008PhRvL.101f1101A (visited on 05/07/2025).

Abraham, J., P. Abreu, M. Aglietta, et al. (Mar. 2010). "Measurement of the energy spectrum of cosmic rays above 1018 eV using the Pierre Auger Observatory". In: *Physics Letters B* 685. ADS Bibcode: 2010PhLB..685..239A, pp. 239–246. ISSN: 0370-2693. DOI: 10.1016/j.physletb.2010.02.013. URL: https://ui.adsabs.harvard.edu/abs/2010PhLB..685..239A (visited on 05/07/2025).

Abreu, P., M. Aglietta, J. M. Albury, et al. (Nov. 2021). "The energy spectrum of cosmic rays beyond the turn-down around 1017 eV as measured with the surface detector of the Pierre Auger Observatory". In: *European Physical Journal C* 81. Publisher: Springer ADS Bibcode: 2021EPJC...81..966A, p. 966. ISSN: 1434-6044. DOI: 10.1140/epjc/s10052-021-09700-w. URL: https://ui.adsabs.harvard.edu/abs/2021EPJC...81..966A (visited on 05/07/2025).

Acciari, V. A., S. Ansoldi, L. A. Antonelli, et al. (Nov. 2019). "Teraelectronvolt emission from the γ-ray burst GRB 190114C". en. In: *Nature* 575.7783. Publisher: Nature Publishing Group, pp. 455–458. ISSN: 1476-4687. DOI: 10.1038/s41586-019-1750-x. URL: https://www.nature.com/articles/s41586-019-1750-x (visited on 10/01/2024).

Acciari, V. A., S. Ansoldi, L. A. Antonelli, et al. (Feb. 2021). "MAGIC Observations of the Nearby Short Gamma-Ray Burst GRB 160821B". In: *The Astrophysical Journal* 908. Publisher: IOP ADS Bibcode: 2021ApJ...908...90A, p. 90. ISSN: 0004-637X. DOI: 10.3847/1538-4357/abd249. URL: https://ui.adsabs.harvard.edu/abs/2021ApJ...908...90A (visited on 07/03/2025).

Acero, Fabio, Juan Bernete, Noah Biederbeck, et al. (Feb. 2024). *Gammapy: Python toolbox for gamma-ray astronomy*. DOI: 10.5281/ZENODO.10726484. URL: https://zenodo.org/doi/10.5281/zenodo.10726484 (visited on 10/31/2024).

Acharyya, A., C. B. Adams, P. Bangale, et al. (Sept. 2024a). "Indirect search for dark matter with a combined analysis of dwarf spheroidal galaxies from VERITAS". In: *Physical Review D* 110. Publisher: APS ADS Bibcode: 2024PhRvD.110f3034A, p. 063034. ISSN: 1550-79980556-2821. DOI: 10.1103/PhysRevD.110.063034. URL: https://ui.adsabs.harvard.edu/abs/2024PhRvD.110f3034A (visited on 05/21/2025).

Acharyya, A., C. B. Adams, P. Bangale, et al. (Oct. 2024b). "Multiwavelength Investigation of γ-Ray Source MGRO J1908+06 Emission Using Fermi-LAT, VERITAS and HAWC". In: *The Astrophysical Journal* 974. Publisher: IOP ADS Bibcode: 2024ApJ...974...61A, p. 61. ISSN: 0004-637X. DOI: 10.3847/1538-4357/ad698d. URL: https://ui.adsabs.harvard.edu/abs/2024ApJ...974...61A (visited on 06/06/2025).

Adams, C. B., W. Benbow, A. Brill, et al. (Feb. 2022). "The throughput calibration of the VERITAS telescopes". In: *Astronomy and Astrophysics* 658. ADS Bibcode: 2022A&A...658A..83A, A83. ISSN: 0004-6361. DOI: 10.1051/0004-6361/202142275. URL: https://ui.adsabs.harvard.edu/abs/2022A&A...658A..83A (visited on 07/25/2023).

Adams, Colin B., Giovanni Ambrosi, Michelangelo Ambrosio, et al. (Jan. 2022). "Design and performance of the prototype Schwarzschild-Couder telescope camera". In: *Journal of Astronomical Telescopes, Instruments, and Systems* 8. ADS Bibcode:

2022JATIS...8a4007A, p. 014007. DOI: 10.1117/1.JATIS.8.1.014007. URL: https://ui.adsabs.harvard.edu/abs/2022JATIS...8a4007A (visited on 06/19/2025).

Aggarwal, Kshitij, Tamás Budavári, Adam T. Deller, et al. (Apr. 2021). "Probabilistic Association of Transients to their Hosts (PATH)". In: *The Astrophysical Journal* 911. Publisher: IOP ADS Bibcode: 2021ApJ...911...95A, p. 95. ISSN: 0004-637X. DOI: 10.3847/1538-4357/abe8d2. URL: https://ui.adsabs.harvard.edu/abs/2021ApJ...911...95A (visited on 10/31/2024).

Aharonian, F., A. G. Akhperjanian, A. R. Bazer-Bachi, et al. (Oct. 2006). "Observations of the Crab nebula with HESS". In: *Astronomy and Astrophysics* 457. ADS Bibcode: 2006A&A...457..899A, pp. 899–915. ISSN: 0004-6361. DOI: 10.1051/0004-6361:20065351. URL: https://ui.adsabs.harvard.edu/abs/2006A&A...457..899A (visited on 06/29/2025).

Aharonian, F., A. G. Akhperjanian, A. R. Bazer-Bachi, et al. (Aug. 2007). "An Exceptional Very High Energy Gamma-Ray Flare of PKS 2155-304". In: *The Astrophysical Journal* 664. Publisher: IOP ADS Bibcode: 2007ApJ...664L..71A, pp. L71–L74. ISSN: 0004-637X. DOI: 10.1086/520635. URL: https://ui.adsabs.harvard.edu/abs/2007ApJ...664L..71A (visited on 03/26/2025).

Aharonian, F., Q. An, Axikegu, et al. (Feb. 2021). "Observation of the Crab Nebula with LHAASO-KM2A - a performance study". In: *Chinese Physics C* 45. Publisher: IOP ADS Bibcode: 2021ChPhC..45b5002A, p. 025002. DOI: 10.1088/1674-1137/abd01b. URL: https://ui.adsabs.harvard.edu/abs/2021ChPhC..45b5002A (visited on 06/20/2025).

Aharonian, F., A. Archaryya, J. Aschersleben, et al. (July 2025). *H.E.S.S. programme searching for VHE gamma rays associated with FRBs*. ADS Bibcode: 2025arXiv250702143A. DOI: 10.48550/arXiv.2507.02143. URL: https://ui.adsabs.harvard.edu/abs/2025arXiv250702143A (visited on 07/09/2025).

Ahmad, Q. R., R. C. Allen, T. C. Andersen, et al. (July 2002). "Direct Evidence for Neutrino Flavor Transformation from Neutral-Current Interactions in the Sudbury Neutrino Observatory". In: *Physical Review Letters* 89. Publisher: APS ADS Bibcode: 2002PhRvL..89a1301A, p. 011301. ISSN: 0031-9007. DOI: 10.1103/PhysRevLett.89.011301. URL: https://ui.adsabs.harvard.edu/abs/2002PhRvL..89a1301A (visited on 05/21/2025).

Albert, A., R. Alfaro, H. Ashkar, et al. (Feb. 2019). *Science Case for a Wide Field-of-View Very-High-Energy Gamma-Ray Observatory in the Southern Hemisphere*. ADS Bibcode: 2019arXiv190208429A. DOI: 10.48550/arXiv.1902.08429. URL: https://ui.adsabs.harvard.edu/abs/2019arXiv190208429A (visited on 06/20/2025).

Albert, J., E. Aliu, H. Anderhub, et al. (Nov. 2007). "Variable Very High Energy γ-Ray Emission from Markarian 501". In: *The Astrophysical Journal* 669. Publisher: IOP ADS Bibcode: 2007ApJ...669..862A, pp. 862–883. ISSN: 0004-637X. DOI: 10.1086/521382. URL: https://ui.adsabs.harvard.edu/abs/2007ApJ...669..862A (visited on 03/28/2025).

Aleksić, J., S. Ansoldi, L. A. Antonelli, et al. (Nov. 2014). "Black hole lightning due to particle acceleration at subhorizon scales". In: *Science* 346. ADS Bibcode: 2014Sci...346.1080A, pp. 1080–1084. ISSN: 0036-8075. DOI: 10.1126/science.1256183. URL: https://ui.adsabs.harvard.edu/abs/2014Sci...346.1080A (visited on 05/22/2025).

Aleksić, J., S. Ansoldi, L. A. Antonelli, et al. (Jan. 2016). "The major upgrade of the MAGIC telescopes, Part II: A performance study using observations of the Crab Nebula". In: *Astroparticle Physics* 72. ADS Bibcode: 2016APh....72...76A, pp. 76–94. ISSN: 0927-6505. DOI: 10.1016/j.astropartphys.2015.02.005. URL: https://ui.adsabs.harvard.edu/abs/2016APh....72...76A (visited on 06/29/2025).

Aleksić, J., L. A. Antonelli, P. Antoranz, et al. (Mar. 2011). "MAGIC Discovery of Very High Energy Emission from the FSRQ PKS 1222+21". In: *The Astrophysical Journal* 730. Publisher: IOP ADS Bibcode: 2011ApJ...730L...8A, p. L8. ISSN: 0004-637X. DOI: 10.1088/2041-8205/730/1/L8. URL: https://ui.adsabs.harvard.edu/abs/2011ApJ...730L...8A (visited on 03/28/2025).

Alfaro, R., C. Alvarez, J. D. Álvarez, et al. (Dec. 2017). "All-particle cosmic ray energy spectrum measured by the HAWC experiment from 10 to 500 TeV". In: *Physical Review D* 96. Publisher: APS ADS Bibcode: 2017PhRvD..96l2001A, p. 122001. ISSN: 1550-79980556-2821. DOI: 10.1103/PhysRevD.96.122001. URL: https://ui.adsabs.harvard.edu/abs/2017PhRvD..96l2001A (visited on 05/07/2025).

Aliu, E., S. Archambault, T. Arlen, et al. (Dec. 2014). "Investigating Broadband Variability of the TeV Blazar 1ES 1959+650". In: *The Astrophysical Journal* 797. Publisher: IOP ADS Bibcode: 2014ApJ...797...89A, p. 89. ISSN: 0004-637X. DOI: 10.1088/0004-637X/797/2/89. URL: https://ui.adsabs.harvard.edu/abs/2014ApJ...797...89A (visited on 03/28/2025).

Anderson, Carl D. (Mar. 1933). "The Positive Electron". In: *Physical Review* 43. Publisher: APS ADS Bibcode: 1933PhRv...43..491A, pp. 491–494. ISSN: 1536-6065. DOI: 10.1103/PhysRev.43.491. URL: https://ui.adsabs.harvard.edu/abs/1933PhRv...43..491A (visited on 05/21/2025).

Andrew, Shion and Chime/Frb Collaboration (Mar. 2025). "The sub-arcsecond localization of FRB 20250316A using CHIME/FRB Outriggers coincides with reported X-ray counterparts". In: *The Astronomer's Telegram* 17114. ADS Bibcode: 2025ATel17114....1A, p. 1.

URL: https://ui.adsabs.harvard.edu/abs/2025ATel17114....1A (visited on 06/17/2025).

Angüner, E. O. (May 2023). *Exploring the high energy frontiers of the Milky Way with ground-based gamma-ray astronomy: PeVatrons and the quest for the origin of Galactic cosmic-rays*. ADS Bibcode: 2023arXiv230512729A. DOI: 10.48550/arXiv.2305.12729. URL: https://ui.adsabs.harvard.edu/abs/2023arXiv230512729A (visited on 05/12/2025).

Ansoldi, S., L. A. Antonelli, P. Antoranz, et al. (Jan. 2016). "Teraelectronvolt pulsed emission from the Crab Pulsar detected by MAGIC". In: *Astronomy and Astrophysics* 585. ADS Bibcode: 2016A&A...585A.133A, A133. ISSN: 0004-6361. DOI: 10.1051/0004-6361/201526853. URL: https://ui.adsabs.harvard.edu/abs/2016A&A...585A.133A (visited on 07/01/2025).

Antoni, T., W. D. Apel, A. F. Badea, et al. (Sept. 2005). "KASCADE measurements of energy spectra for elemental groups of cosmic rays: Results and open problems". In: *Astroparticle Physics* 24. ADS Bibcode: 2005APh....24....1A, pp. 1–25. ISSN: 0927-6505. DOI: 10.1016/j.astropartphys.2005.04.001. URL: https://ui.adsabs.harvard.edu/abs/2005APh....24....1A (visited on 05/07/2025).

Apanasenko, A. V., V. A. Sukhadolskaya, V. A. Derbina, et al. (Oct. 2001). "Composition and energy spectra of cosmic-ray primaries in the energy range 10 13-10 15 eV/particle observed by Japanese-Russian joint balloon experiment". In: *Astroparticle Physics* 16. ADS Bibcode: 2001APh....16...13A, pp. 13–46. ISSN: 0927-6505. DOI: 10.1016/S0927-6505(00)00163-8. URL: https://ui.adsabs.harvard.edu/abs/2001APh...16...13A (visited on 05/07/2025).

Apel, W. D., J. C. Arteaga-Velázquez, K. Bekk, et al. (Oct. 2011). "Kneelike Structure in the Spectrum of the Heavy Component of Cosmic Rays Observed with KASCADE-Grande". In: *Physical Review Letters* 107. Publisher: APS ADS Bibcode: 2011PhRvL.107q1104A, p. 171104. ISSN: 0031-9007. DOI: 10.1103/PhysRevLett.107.171104. URL: https://ui.adsabs.harvard.edu/abs/2011PhRvL.107q1104A (visited on 05/07/2025).

Apel, W. D., J. C. Arteaga-Velàzquez, K. Bekk, et al. (Apr. 2013). "Ankle-like feature in the energy spectrum of light elements of cosmic rays observed with KASCADE-Grande". In: *Physical Review D* 87. Publisher: APS ADS Bibcode: 2013PhRvD..87h1101A, p. 081101. ISSN: 1550-79980556-2821. DOI: 10.1103/PhysRevD.87.081101. URL: https://ui.adsabs.harvard.edu/abs/2013PhRvD..87h1101A (visited on 05/07/2025).

Archambault, S., M. Beilicke, W. Benbow, et al. (Dec. 2013). "VERITAS Observations of the Microquasar Cygnus X-3". In: *The Astrophysical Journal* 779. Publisher: IOP ADS

Bibcode: 2013ApJ...779..150A, p. 150. ISSN: 0004-637X. DOI: 10.1088/0004-637X/779/2/150. URL: https://ui.adsabs.harvard.edu/abs/2013ApJ...779..150A (visited on 07/18/2024).

Archambault, S. and VERITAS Collaboration (July 2017). "Search for Primordial Black Hole Evaporation with VERITAS". In: vol. 301. ADS Bibcode: 2017ICRC...35..691A. eprint: arXiv:1709.00307, p. 691. DOI: 10.22323/1.301.0691. URL: https://ui.adsabs.harvard.edu/abs/2017ICRC...35..691A (visited on 06/30/2025).

Arlen, T., T. Aune, M. Beilicke, et al. (Jan. 2013). "Rapid TeV Gamma-Ray Flaring of BL Lacertae". In: *The Astrophysical Journal* 762. Publisher: IOP ADS Bibcode: 2013ApJ...762...92A, p. 92. ISSN: 0004-637X. DOI: 10.1088/0004-637X/762/2/92. URL: https://ui.adsabs.harvard.edu/abs/2013ApJ...762...92A (visited on 03/28/2025).

Arteaga-Velázquez, C. J., D. Rivera-Rangel, W. D. Apel, et al. (July 2017). "Measurements of the muon content of EAS in KASCADE-Grande compared with SIBYLL 2.3 predictions". In: *International Cosmic Ray Conference*. Vol. 301. ADS Bibcode: 2017ICRC...35..316A, p. 316. DOI: 10.22323/1.301.0316. URL: https://ui.adsabs.harvard.edu/abs/2017ICRC...35..316A (visited on 05/07/2025).

Astapov, I. I., P. A. Bezyazeekov, M. Blank, et al. (Apr. 2022). "Cosmic-Ray Research at the TAIGA Astrophysical Facility: Results and Plans". In: *Soviet Journal of Experimental and Theoretical Physics* 134. Publisher: Springer ADS Bibcode: 2022JETP..134..469A, pp. 469–478. ISSN: 1063-7761. DOI: 10.1134/S1063776122040136. URL: https://ui.adsabs.harvard.edu/abs/2022JETP..134..469A (visited on 05/07/2025).

Astropy Collaboration, A. M. Price-Whelan, B. M. Sipőcz, et al. (Sept. 2018). "The Astropy Project: Building an Open-science Project and Status of the v2.0 Core Package". In: *The Astronomical Journal* 156. Publisher: IOP ADS Bibcode: 2018AJ....156..123A, p. 123. ISSN: 0004-6256. DOI: 10.3847/1538-3881/aabc4f. URL: https://ui.adsabs.harvard.edu/abs/2018AJ....156..123A (visited on 07/06/2025).

Astropy Collaboration, Adrian M. Price-Whelan, Pey Lian Lim, et al. (Aug. 2022). "The Astropy Project: Sustaining and Growing a Community-oriented Open-source Project and the Latest Major Release (v5.0) of the Core Package". In: *The Astrophysical Journal* 935. Publisher: IOP ADS Bibcode: 2022ApJ...935..167A, p. 167. ISSN: 0004-637X. DOI: 10.3847/1538-4357/ac7c74. URL: https://ui.adsabs.harvard.edu/abs/2022ApJ...935..167A (visited on 07/06/2025).

Astropy Collaboration, Thomas P. Robitaille, Erik J. Tollerud, et al. (Oct. 2013). "Astropy: A community Python package for astronomy". In: *Astronomy and Astrophysics* 558. ADS Bibcode: 2013A&A...558A..33A, A33. ISSN: 0004-6361. DOI: 10.1051/0004-6361/

201322068. URL: https://ui.adsabs.harvard.edu/abs/2013A&A...558A..33A (visited on 07/06/2025).

Atwood, W. B., A. A. Abdo, M. Ackermann, et al. (June 2009). "The Large Area Telescope on the Fermi Gamma-Ray Space Telescope Mission". In: *The Astrophysical Journal* 697. Publisher: IOP ADS Bibcode: 2009ApJ...697.1071A, pp. 1071–1102. ISSN: 0004-637X. DOI: 10.1088/0004-637X/697/2/1071. URL: https://ui.adsabs.harvard.edu/abs/2009ApJ...697.1071A (visited on 06/20/2025).

Ave, M., J. Knapp, J. Lloyd-Evans, et al. (Apr. 2003). "The energy spectrum of cosmic rays in the range 3×1017-4×1018 eV as measured with the Haverah Park array". In: *Astroparticle Physics* 19. ADS Bibcode: 2003APh....19...47A, pp. 47–60. ISSN: 0927-6505. DOI: 10.1016/S0927-6505(02)00188-3. URL: https://ui.adsabs.harvard.edu/abs/2003APh....19...47A (visited on 05/07/2025).

Axford, W. I., E. Leer, and G. Skadron (Jan. 1977). "The Acceleration of Cosmic Rays by Shock Waves". In: *International Cosmic Ray Conference*. Vol. 11. ADS Bibcode: 1977ICRC...11..132A, p. 132. URL: https://ui.adsabs.harvard.edu/abs/1977ICRC...11..132A (visited on 05/08/2025).

Batković, Ivana, Alessandro De Angelis, Michele Doro, et al. (June 2021). "Axion-Like Particle Searches with IACTs". In: *Universe* 7. ADS Bibcode: 2021Univ....7..185B, p. 185. DOI: 10.3390/universe7060185. URL: https://ui.adsabs.harvard.edu/abs/2021Univ....7..185B (visited on 05/21/2025).

Batten, Adam (May 2019). "Fruitbat: A Python Package for Estimating Redshifts of Fast Radio Bursts". In: *The Journal of Open Source Software* 4. ADS Bibcode: 2019JOSS....4.1399B, p. 1399. DOI: 10.21105/joss.01399. URL: https://ui.adsabs.harvard.edu/abs/2019JOSS....4.1399B (visited on 11/13/2024).

Bell, A. R. (Jan. 1978). "The acceleration of cosmic rays in shock fronts - I." In: *Monthly Notices of the Royal Astronomical Society* 182. Publisher: OUP ADS Bibcode: 1978MNRAS.182..147B, pp. 147–156. ISSN: 0035-8711. DOI: 10.1093/mnras/182.2.147. URL: https://ui.adsabs.harvard.edu/abs/1978MNRAS.182..147B (visited on 05/08/2025).

Beniamini, Paz, Zorawar Wadiasingh, Aaron Trigg, et al. (Feb. 2025). "Extragalactic Magnetar Giant Flares: Population Implications, Rates, and Prospects for Gamma-Rays, Gravitational Waves, and Neutrinos". In: *The Astrophysical Journal* 980. Publisher: IOP ADS Bibcode: 2025ApJ...980..211B, p. 211. ISSN: 0004-637X. DOI: 10.3847/1538-4357/ada947. URL: https://ui.adsabs.harvard.edu/abs/2025ApJ...980..211B (visited on 07/01/2025).

Bethe, H. and W. Heitler (Aug. 1934). "On the Stopping of Fast Particles and on the Creation of Positive Electrons". In: *Proceedings of the Royal Society of London Series A* 146.

ADS Bibcode: 1934RSPSA.146...83B, pp. 83–112. ISSN: 0080-46301364-5021. DOI: 10.1098/rspa.1934.0140. URL: https://ui.adsabs.harvard.edu/abs/1934RSPSA.146...83B (visited on 07/12/2025).

Bhandari, Shivani, Kasper E. Heintz, Kshitij Aggarwal, et al. (Feb. 2022). "Characterizing the Fast Radio Burst Host Galaxy Population and its Connection to Transients in the Local and Extragalactic Universe". In: *The Astronomical Journal* 163. Publisher: IOP ADS Bibcode: 2022AJ....163...69B, p. 69. ISSN: 0004-6256. DOI: 10.3847/1538-3881/ac3aec. URL: https://ui.adsabs.harvard.edu/abs/2022AJ...163...69B (visited on 06/14/2025).

Bhardwaj, M., B. M. Gaensler, V. M. Kaspi, et al. (Apr. 2021a). "A Nearby Repeating Fast Radio Burst in the Direction of M81". In: *The Astrophysical Journal* 910. Publisher: IOP ADS Bibcode: 2021ApJ...910L..18B, p. L18. ISSN: 0004-637X. DOI: 10.3847/2041-8213/abeaa6. URL: https://ui.adsabs.harvard.edu/abs/2021ApJ...910L..18B (visited on 07/05/2025).

Bhardwaj, M., A. Yu. Kirichenko, D. Michilli, et al. (Oct. 2021b). "A Local Universe Host for the Repeating Fast Radio Burst FRB 20181030A". In: *The Astrophysical Journal* 919. Publisher: IOP ADS Bibcode: 2021ApJ...919L..24B, p. L24. ISSN: 0004-637X. DOI: 10.3847/2041-8213/ac223b. URL: https://ui.adsabs.harvard.edu/abs/2021ApJ...919L..24B (visited on 06/14/2025).

Bhardwaj, Mohit, Aida Kirichenko, and Armando Gil de Paz (May 2024). "A redshift for the host galaxy of FRB 20240114A". In: *The Astronomer's Telegram* 16613. ADS Bibcode: 2024ATel16613....1B, p. 1. URL: https://ui.adsabs.harvard.edu/abs/2024ATel16613....1B (visited on 07/05/2025).

Bird, D. J., S. C. Corbato, H. Y. Dai, et al. (Mar. 1994). "The Cosmic-Ray Energy Spectrum Observed by the Fly's Eye". In: *The Astrophysical Journal* 424. Publisher: IOP ADS Bibcode: 1994ApJ...424..491B, p. 491. ISSN: 0004-637X. DOI: 10.1086/173906. URL: https://ui.adsabs.harvard.edu/abs/1994ApJ...424..491B (visited on 05/07/2025).

Blanch, Oscar (Dec. 2020). "GRB 201216C: MAGIC detection in very high energy gamma rays". In: *The Astronomer's Telegram* 14275. ADS Bibcode: 2020ATel14275....1B, p. 1. URL: https://ui.adsabs.harvard.edu/abs/2020ATel14275....1B (visited on 11/05/2024).

Blandford, R. D. and J. P. Ostriker (Apr. 1978). "Particle acceleration by astrophysical shocks." In: *The Astrophysical Journal* 221. Publisher: IOP ADS Bibcode: 1978ApJ...221L..29B, pp. L29–L32. ISSN: 0004-637X. DOI: 10.1086/182658. URL: https://ui.adsabs.harvard.edu/abs/1978ApJ...221L..29B (visited on 05/08/2025).

Blasi, Pasquale (Nov. 2013). "The origin of galactic cosmic rays". In: *Astronomy and Astrophysics Review* 21. Publisher: Springer ADS Bibcode: 2013A&ARv..21...70B, p. 70. ISSN: 0935-4956. DOI: 10.1007/s00159-013-0070-7. URL: https://ui.adsabs.harvard.edu/abs/2013A&ARv..21...70B (visited on 05/12/2025).

Bochenek, C. D., V. Ravi, K. V. Belov, et al. (Nov. 2020). "A fast radio burst associated with a Galactic magnetar". In: *Nature* 587. ADS Bibcode: 2020Natur.587...59B, pp. 59–62. ISSN: 0028-0836. DOI: 10.1038/s41586-020-2872-x. URL: https://ui.adsabs.harvard.edu/abs/2020Natur.587...59B (visited on 07/03/2025).

Böttcher, Markus (Jan. 2019). "Progress in Multi-Wavelength and Multi-Messenger Observations of Blazars and Theoretical Challenges". In: *Galaxies* 7. ADS Bibcode: 2019Galax...7...20B, p. 20. DOI: 10.3390/galaxies7010020. URL: https://ui.adsabs.harvard.edu/abs/2019Galax...7...20B (visited on 07/01/2025).

Buckley, James and APT Team (Apr. 2022). "The Advanced Particle-astrophysics Telescope (APT)". In: *International Cosmic Ray Conference*. Vol. 19. ADS Bibcode: 2022HEAD...1940404B. ICRC, p. 404.04. URL: https://ui.adsabs.harvard.edu/abs/2022HEAD...1940404B (visited on 06/20/2025).

Cao, Zhen, F. Aharonian, Q. An, et al. (Nov. 2023). "Very high-energy gamma-ray emission beyond 10 TeV from GRB 221009A". In: *Science Advances* 9. ADS Bibcode: 2023SciA....9J2778C, eadj2778. DOI: 10.1126/sciadv.adj2778. URL: https://ui.adsabs.harvard.edu/abs/2023SciA....9J2778C (visited on 06/25/2025).

Carlson, J. F. and J. R. Oppenheimer (Feb. 1937). "On Multiplicative Showers". In: *Physical Review* 51.4. Publisher: American Physical Society, pp. 220–231. DOI: 10.1103/PhysRev.51.220. URL: https://link.aps.org/doi/10.1103/PhysRev.51.220 (visited on 06/25/2025).

Cash, W. (Mar. 1979). "Parameter estimation in astronomy through application of the likelihood ratio." In: *The Astrophysical Journal* 228. Publisher: IOP ADS Bibcode: 1979ApJ...228..939C, pp. 939–947. ISSN: 0004-637X. DOI: 10.1086/156922. URL: https://ui.adsabs.harvard.edu/abs/1979ApJ...228..939C (visited on 07/17/2024).

Cerruti, Matteo (Oct. 2020). "Leptonic and Hadronic Radiative Processes in Supermassive-Black-Hole Jets". In: *Galaxies* 8. ADS Bibcode: 2020Galax...8...72C, p. 72. DOI: 10.3390/galaxies8040072. URL: https://ui.adsabs.harvard.edu/abs/2020Galax...8...72C (visited on 07/01/2025).

Chatterjee, S., C. J. Law, R. S. Wharton, et al. (Jan. 2017). "A direct localization of a fast radio burst and its host". In: *Nature* 541. ADS Bibcode: 2017Natur.541...58C, pp. 58–61. ISSN: 0028-0836. DOI: 10.1038/nature20797. URL: https://ui.adsabs.harvard.edu/abs/2017Natur.541...58C (visited on 06/13/2025).

Cherenkov Telescope Array Consortium, B. S. Acharya, I. Agudo, et al. (Mar. 2019). *Science with the Cherenkov Telescope Array*. Publication Title: Science with the Cherenkov Telescope Array ADS Bibcode: 2019scta.book.....C. DOI: 10.1142/10986. URL: https://ui.adsabs.harvard.edu/abs/2019scta.book.....C (visited on 07/10/2025).

Chilingarian, A., G. Gharagyozyan, S. Ghazaryan, et al. (Sept. 2007). "Study of extensive air showers and primary energy spectra by MAKET-ANI detector on mountain Aragats". In: *Astroparticle Physics* 28. ADS Bibcode: 2007APh....28...58C, pp. 58–71. ISSN: 0927-6505. DOI: 10.1016/j.astropartphys.2007.04.005. URL: https://ui.adsabs.harvard.edu/abs/2007APh....28...58C (visited on 05/07/2025).

CHIME Collaboration, Mandana Amiri, Kevin Bandura, et al. (Aug. 2022). "An Overview of CHIME, the Canadian Hydrogen Intensity Mapping Experiment". In: *The Astrophysical Journal Supplement Series* 261. Publisher: IOP ADS Bibcode: 2022ApJS..261...29C, p. 29. ISSN: 0067-0049. DOI: 10.3847/1538-4365/ac6fd9. URL: https://ui.adsabs.harvard.edu/abs/2022ApJS..261...29C (visited on 07/04/2025).

CHIME/FRB Collaboration, Thomas C. Abbott, Daniel Amouyal, et al. (June 2025). *FRB 20250316A: A Brilliant and Nearby One-Off Fast Radio Burst Localized to 13 parsec Precision*. ADS Bibcode: 2025arXiv250619006F. DOI: 10.48550/arXiv.2506.19006. URL: https://ui.adsabs.harvard.edu/abs/2025arXiv250619006F (visited on 07/05/2025).

CHIME/FRB Collaboration, M. Amiri, B. C. Andersen, et al. (June 2020a). "Periodic activity from a fast radio burst source". In: *Nature* 582. ADS Bibcode: 2020Natur.582..351C, pp. 351–355. ISSN: 0028-0836. DOI: 10.1038/s41586-020-2398-2. URL: https://ui.adsabs.harvard.edu/abs/2020Natur.582..351C (visited on 06/14/2025).

CHIME/FRB Collaboration, M. Amiri, K. Bandura, et al. (Jan. 2019a). "A second source of repeating fast radio bursts". In: *Nature* 566. ADS Bibcode: 2019Natur.566..235C, pp. 235–238. ISSN: 0028-0836. DOI: 10.1038/s41586-018-0864-x. URL: https://ui.adsabs.harvard.edu/abs/2019Natur.566..235C (visited on 06/14/2025).

CHIME/FRB Collaboration, Mandana Amiri, Bridget C. Andersen, et al. (Dec. 2021). "The First CHIME/FRB Fast Radio Burst Catalog". In: *The Astrophysical Journal Supplement Series* 257. Publisher: IOP ADS Bibcode: 2021ApJS..257...59C, p. 59. ISSN: 0067-0049. DOI: 10.3847/1538-4365/ac33ab. URL: https://ui.adsabs.harvard.edu/abs/2021ApJS..257...59C (visited on 07/05/2025).

CHIME/FRB Collaboration, Mandana Amiri, Bridget C. Andersen, et al. (July 2024). "Updating the First CHIME/FRB Catalog of Fast Radio Bursts with Baseband Data". In: *The Astrophysical Journal* 969. Publisher: IOP ADS Bibcode: 2024ApJ...969..145C, p. 145. ISSN: 0004-637X. DOI: 10.3847/1538-4357/ad464b. URL: https://ui.adsabs.harvard.edu/abs/2024ApJ...969..145C (visited on 06/14/2025).

CHIME/FRB Collaboration, B. C. Andersen, K. Bandura, et al. (Nov. 2019b). "CHIME/FRB Discovery of Eight New Repeating Fast Radio Burst Sources". In: *The Astrophysical Journal* 885. Publisher: IOP ADS Bibcode: 2019ApJ...885L..24C, p. L24. ISSN: 0004-637X. DOI: 10.3847/2041-8213/ab4a80. URL: https://ui.adsabs.harvard.edu/abs/2019ApJ...885L..24C (visited on 06/14/2025).

CHIME/FRB Collaboration, B. C. Andersen, K. M. Bandura, et al. (Nov. 2020b). "A bright millisecond-duration radio burst from a Galactic magnetar". In: *Nature* 587. ADS Bibcode: 2020Natur.587...54C, pp. 54–58. ISSN: 0028-0836. DOI: 10.1038/s41586-020-2863-y. URL: https://ui.adsabs.harvard.edu/abs/2020Natur.587...54C (visited on 07/05/2025).

Chime/Frb Collabortion (Mar. 2021). "Recent high activity from a repeating Fast Radio Burst discovered by CHIME/FRB". In: *The Astronomer's Telegram* 14497. ADS Bibcode: 2021ATel14497....1C, p. 1. URL: https://ui.adsabs.harvard.edu/abs/2021ATel14497....1C (visited on 07/06/2025).

Christiansen, J. and VERITAS Collaboration (July 2017). "Characterization of a Maximum Likelihood Gamma-Ray Reconstruction Algorithm for VERITAS". In: vol. 301. ADS Bibcode: 2017ICRC...35..789C. eprint: arXiv:1708.05684, p. 789. DOI: 10.22323/1.301.0789. URL: https://ui.adsabs.harvard.edu/abs/2017ICRC...35..789C (visited on 06/29/2025).

Cogan, P. (Jan. 2008). *VEGAS, the VERITAS Gamma-ray Analysis Suite*. Conference Name: International Cosmic Ray Conference Volume: 3 ADS Bibcode: 2008ICRC....3.1385C. eprint: arXiv:0709.4233. DOI: 10.48550/arXiv.0709.4233. URL: https://ui.adsabs.harvard.edu/abs/2008ICRC....3.1385C (visited on 06/29/2025).

Collaboration, Amy Furniss VERITAS (Oct. 2024). "VERITAS Detection of Gamma-ray Flaring Activity from BL Lacertae". In: *The Astronomer's Telegram* 16854. ADS Bibcode: 2024ATel16854....1C, p. 1. URL: https://ui.adsabs.harvard.edu/abs/2024ATel16854....1C (visited on 05/30/2025).

Collaboration, MAGIC, J. Aleksić, S. Ansoldi, et al. (Mar. 2015). "Measurement of the Crab Nebula spectrum over three decades in energy with the MAGIC telescopes". In: *Journal of High Energy Astrophysics* 5-6. arXiv:1406.6892 [astro-ph], pp. 30–38. ISSN: 22144048. DOI: 10.1016/j.jheap.2015.01.002. URL: http://arxiv.org/abs/1406.6892 (visited on 02/11/2025).

Compton, Arthur H. (May 1923). "A Quantum Theory of the Scattering of X-rays by Light Elements". In: *Physical Review* 21.5. Publisher: American Physical Society, pp. 483–502. DOI: 10.1103/PhysRev.21.483. URL: https://link.aps.org/doi/10.1103/PhysRev.21.483 (visited on 05/17/2025).

Condon, James J. and Scott M. Ransom (Jan. 2016). *Essential Radio Astronomy*. Publication Title: Essential Radio Astronomy ADS Bibcode: 2016era..book.....C. URL: https://ui.adsabs.harvard.edu/abs/2016era..book.....C (visited on 05/14/2025).

Cortina, Juan and CTAO LST Collaboration (Dec. 2023). "First detection of VHE gamma-ray emission from FSRQ OP 313 with LST-1". In: *The Astronomer's Telegram* 16381. ADS Bibcode: 2023ATel16381....1C, p. 1. URL: https://ui.adsabs.harvard.edu/abs/2023ATel16381....1C (visited on 05/08/2025).

Cristofari, Pierre (Aug. 2021). "The Hunt for Pevatrons: The Case of Supernova Remnants". In: *Universe* 7. ADS Bibcode: 2021Univ....7..324C, p. 324. DOI: 10.3390/universe7090324. URL: https://ui.adsabs.harvard.edu/abs/2021Univ...7..324C (visited on 05/21/2025).

Cruces, M., L. G. Spitler, P. Scholz, et al. (Jan. 2021). "Repeating behaviour of FRB 121102: periodicity, waiting times, and energy distribution". In: *Monthly Notices of the Royal Astronomical Society* 500. Publisher: OUP ADS Bibcode: 2021MNRAS.500..448C, pp. 448–463. ISSN: 0035-8711. DOI: 10.1093/mnras/staa3223. URL: https://ui.adsabs.harvard.edu/abs/2021MNRAS.500..448C (visited on 12/15/2025).

Cummmings, J. R., S. D. Barthelmy, M. M. Chester, et al. (July 2014). "Newly discovered SGR 1935+2154: Swift observations". In: *The Astronomer's Telegram* 6294. ADS Bibcode: 2014ATel.6294....1C, p. 1. URL: https://ui.adsabs.harvard.edu/abs/2014ATel.6294....1C (visited on 06/23/2025).

Curtin, Alice P. and CHIME/FRB Collaboration (Aug. 2024). "CHIME/FRB Updated Position for Repeating Source FRB 20240316A". In: *The Astronomer's Telegram* 16780. ADS Bibcode: 2024ATel16780....1C, p. 1. URL: https://ui.adsabs.harvard.edu/abs/2024ATel16780....1C (visited on 06/17/2025).

Davies, John M. and Eugene S. Cotton (Apr. 1957). "Design of the quartermaster solar furnace". In: *Solar Energy* 1.2, pp. 16–22. ISSN: 0038-092X. DOI: 10.1016/0038-092X(57)90116-0. URL: https://www.sciencedirect.com/science/article/pii/0038092X57901160 (visited on 07/11/2025).

Derbina, V. A., V. I. Galkin, M. Hareyama, et al. (July 2005). "Cosmic-Ray Spectra and Composition in the Energy Range of 10-1000 TeV per Particle Obtained by the RUNJOB Experiment". In: *The Astrophysical Journal* 628. Publisher: IOP ADS Bibcode: 2005ApJ...628L..41D, pp. L41–L44. ISSN: 0004-637X. DOI: 10.1086/432715. URL: https://ui.adsabs.harvard.edu/abs/2005ApJ...628L..41D (visited on 05/07/2025).

DuPlain, Ron, Scott Ransom, Paul Demorest, et al. (Aug. 2008). "Launching GUPPI: the Green Bank Ultimate Pulsar Processing Instrument". In: vol. 7019. ADS Bibcode:

2008SPIE.7019E..1DD, p. 70191D. DOI: 10.1117/12.790003. URL: https://ui.adsabs.harvard.edu/abs/2008SPIE.7019E..1DD (visited on 07/04/2025).

EAS-Top Collaboration, M. Aglietta, B. Alessandro, et al. (Jan. 1999). "The EAS size spectrum and the cosmic ray energy spectrum in the region 10^15-10^16 eV". In: *Astroparticle Physics* 10. ADS Bibcode: 1999APh....10....1E, pp. 1–9. ISSN: 0927-6505. DOI: 10.1016/S0927-6505(98)00035-8. URL: https://ui.adsabs.harvard.edu/abs/1999APh....10....1E (visited on 05/07/2025).

Emmanoulopoulos, D., I. M. McHardy, and I. E. Papadakis (Aug. 2013). "Generating artificial light curves: revisited and updated". In: *Monthly Notices of the Royal Astronomical Society* 433. Publisher: OUP ADS Bibcode: 2013MNRAS.433..907E, pp. 907–927. ISSN: 0035-8711. DOI: 10.1093/mnras/stt764. URL: https://ui.adsabs.harvard.edu/abs/2013MNRAS.433..907E (visited on 06/30/2025).

Engel, Ralph, Dieter Heck, and Tanguy Pierog (Nov. 2011). "Extensive Air Showers and Hadronic Interactions at High Energy". In: *Annual Review of Nuclear and Particle Science* 61. ADS Bibcode: 2011ARNPS..61..467E, pp. 467–489. ISSN: 0163-8998. DOI: 10.1146/annurev.nucl.012809.104544. URL: https://ui.adsabs.harvard.edu/abs/2011ARNPS..61..467E (visited on 07/12/2025).

Event Horizon Telescope Collaboration, Kazunori Akiyama, Antxon Alberdi, et al. (Apr. 2019). "First M87 Event Horizon Telescope Results. I. The Shadow of the Supermassive Black Hole". In: *The Astrophysical Journal* 875. Publisher: IOP ADS Bibcode: 2019ApJ...875L...1E, p. L1. ISSN: 0004-637X. DOI: 10.3847/2041-8213/ab0ec7. URL: https://ui.adsabs.harvard.edu/abs/2019ApJ...875L...1E (visited on 07/01/2025).

Feldman, Gary J. and Robert D. Cousins (Apr. 1998). "Unified approach to the classical statistical analysis of small signals". In: *Physical Review D* 57. Publisher: APS ADS Bibcode: 1998PhRvD..57.3873F, pp. 3873–3889. ISSN: 1550-79980556-2821. DOI: 10.1103/PhysRevD.57.3873. URL: https://ui.adsabs.harvard.edu/abs/1998PhRvD..57.3873F (visited on 07/08/2025).

Fenu, F. and Pierre Auger Collaboration (July 2017). "The cosmic ray energy spectrum measured using the Pierre Auger Observatory". In: vol. 301. ADS Bibcode: 2017ICRC...35..486F, p. 486. DOI: 10.22323/1.301.0486. URL: https://ui.adsabs.harvard.edu/abs/2017ICRC...35..486F (visited on 05/07/2025).

Fermi, Enrico (Apr. 1949). "On the Origin of the Cosmic Radiation". In: *Physical Review* 75. Publisher: APS ADS Bibcode: 1949PhRv...75.1169F, pp. 1169–1174. ISSN: 1536-6065. DOI: 10.1103/PhysRev.75.1169. URL: https://ui.adsabs.harvard.edu/abs/1949PhRv...75.1169F (visited on 05/06/2025).

Fermi-LAT Collaboration (Nov. 2021). *Fermi-LAT Cicerone*. URL: https://fermi.gsfc.nasa.gov/ssc/data/analysis/documentation/Cicerone/Cicerone_Introduction/LAT_overview.html (visited on 05/13/2025).

Fermi-LAT Collaboration, M. Ajello, W. B. Atwood, et al. (Apr. 2021). "High-energy emission from a magnetar giant flare in the Sculptor galaxy". In: *Nature Astronomy* 5. ADS Bibcode: 2021NatAs...5..385F, pp. 385–391. ISSN: 2397-3366. DOI: 10.1038/s41550-020-01287-8. URL: https://ui.adsabs.harvard.edu/abs/2021NatAs...5..385F (visited on 07/01/2025).

Fong, Wen-fai, Yuxin Dong, Joel Leja, et al. (Oct. 2021). "Chronicling the Host Galaxy Properties of the Remarkable Repeating FRB 20201124A". In: *The Astrophysical Journal* 919. Publisher: IOP ADS Bibcode: 2021ApJ...919L..23F, p. L23. ISSN: 0004-637X. DOI: 10.3847/2041-8213/ac242b. URL: https://ui.adsabs.harvard.edu/abs/2021ApJ...919L..23F (visited on 06/17/2025).

Fonseca, E., B. C. Andersen, M. Bhardwaj, et al. (Mar. 2020). "Nine New Repeating Fast Radio Burst Sources from CHIME/FRB". In: *The Astrophysical Journal* 891. Publisher: IOP ADS Bibcode: 2020ApJ...891L...6F, p. L6. ISSN: 0004-637X. DOI: 10.3847/2041-8213/ab7208. URL: https://ui.adsabs.harvard.edu/abs/2020ApJ...891L...6F (visited on 06/17/2025).

Frank, I. M. and I. E. Tamm (1937). "Coherent visible radiation of fast electrons passing through matter". In: *Compt. Rend. Acad. Sci. URSS* 14.3. Ed. by V. L. Ginzburg, B. M. Bolotovsky, and I. M. Dremin, pp. 109–114. DOI: 10.3367/UFNr.0093.196710o.0388.

Freedman, Wendy L., Shaun M. Hughes, Barry F. Madore, et al. (June 1994). "The Hubble Space Telescope Extragalactic Distance Scale Key Project. I. The Discovery of Cepheids and a New Distance to M81". In: *The Astrophysical Journal* 427. Publisher: IOP ADS Bibcode: 1994ApJ...427..628F, p. 628. ISSN: 0004-637X. DOI: 10.1086/174172. URL: https://ui.adsabs.harvard.edu/abs/1994ApJ...427..628F (visited on 07/09/2025).

Gabici, Stefano, Carmelo Evoli, Daniele Gaggero, et al. (Jan. 2019). "The origin of Galactic cosmic rays: Challenges to the standard paradigm". In: *International Journal of Modern Physics D* 28. ADS Bibcode: 2019IJMPD..2830022G, pp. 1930022–339. ISSN: 0218-2718. DOI: 10.1142/S0218271819300222. URL: https://ui.adsabs.harvard.edu/abs/2019IJMPD..2830022G (visited on 05/21/2025).

Gaidos, J. A., C. W. Akerlof, S. Biller, et al. (Sept. 1996). "Extremely rapid bursts of TeV photons from the active galaxy Markarian 421". In: *Nature* 383. ADS Bibcode: 1996Natur.383..319G, pp. 319–320. ISSN: 0028-0836. DOI: 10.1038/383319a0. URL:

https://ui.adsabs.harvard.edu/abs/1996Natur.383..319G (visited on 03/28/2025).

Garyaka, A. P., R. M. Martirosov, S. V. Ter-Antonyan, et al. (Nov. 2008). "An all-particle primary energy spectrum in the 3 200 PeV energy range". In: *Journal of Physics G Nuclear Physics* 35. Publisher: IOP ADS Bibcode: 2008JPhG...35k5201G, p. 115201. ISSN: 0954-3899. DOI: 10.1088/0954-3899/35/11/115201. URL: https://ui.adsabs.harvard.edu/abs/2008JPhG...35k5201G (visited on 05/07/2025).

GBT Support Staff (June 2025). *Proposer's Guide for the Green Bank Telescope*. URL: https://www.gb.nrao.edu/scienceDocs/GBTpg.pdf.

Grebenyuk, V., D. Karmanov, I. Kovalev, et al. (Dec. 2019). "Energy spectra of abundant cosmic-ray nuclei in the NUCLEON experiment". In: *Advances in Space Research* 64. ADS Bibcode: 2019AdSpR..64.2546G, pp. 2546–2558. ISSN: 0273-1177. DOI: 10.1016/j.asr.2019.10.004. URL: https://ui.adsabs.harvard.edu/abs/2019AdSpR..64.2546G (visited on 05/07/2025).

Gupta, S. P., U. S. Pandey, K. Singh, et al. (Jan. 2012). "Optical intra-day variability timescales and black hole mass of the blazars". In: *New Astronomy* 17. ADS Bibcode: 2012NewA...17....8G, pp. 8–17. ISSN: 1384-1076. DOI: 10.1016/j.newast.2011.05.005. URL: https://ui.adsabs.harvard.edu/abs/2012NewA...17....8G (visited on 07/10/2025).

Hanna, D., A. McCann, M. McCutcheon, et al. (Jan. 2010). "An LED-based flasher system for VERITAS". In: *Nuclear Instruments and Methods in Physics Research A* 612. ADS Bibcode: 2010NIMPA.612..278H, pp. 278–287. ISSN: 0168-9002. DOI: 10.1016/j.nima.2009.10.107. URL: https://ui.adsabs.harvard.edu/abs/2010NIMPA.612..278H (visited on 06/29/2025).

Heck, D., J. Knapp, J. N. Capdevielle, et al. (Feb. 1998). *CORSIKA: a Monte Carlo code to simulate extensive air showers.* Publication Title: CORSIKA: a Monte Carlo code to simulate extensive air showers ADS Bibcode: 1998cmcc.book.....H. URL: https://ui.adsabs.harvard.edu/abs/1998cmcc.book.....H (visited on 05/13/2025).

Heck, Dieter, Tanguy Pierog, and Johannes Knapp (Feb. 2012). "CORSIKA: An Air Shower Simulation Program". In: *Astrophysics Source Code Library*. ADS Bibcode: 2012ascl.soft02006H, ascl:1202.006. URL: https://ui.adsabs.harvard.edu/abs/2012ascl.soft02006H (visited on 06/29/2025).

Heitler, W. (1944). *The Quantum Theory Of Radiation Ed. 2*. eng. URL: http://archive.org/details/in.ernet.dli.2015.37198 (visited on 06/25/2025).

Herrmann, Wolfgang (Apr. 2021). "Extremely bright pulse from FRB20201124A observed with the 25-m Stockert Radio Telescope". In: *The Astronomer's Telegram* 14556. ADS

Bibcode: 2021ATel14556....1H, p. 1. URL: https://ui.adsabs.harvard.edu/abs/2021ATel14556....1H (visited on 07/06/2025).

Hervet, O., C. Boisson, and H. Sol (July 2016). "An innovative blazar classification based on radio jet kinematics". In: *Astronomy and Astrophysics* 592. Publisher: EDP ADS Bibcode: 2016A&A...592A..22H, A22. ISSN: 0004-6361. DOI: 10.1051/0004-6361/201628117. URL: https://ui.adsabs.harvard.edu/abs/2016A&A...592A..22H (visited on 07/10/2025).

Hess, Victor (July 2018). *On the Observations of the Penetrating Radiation during Seven Balloon Flights*. ADS Bibcode: 2018arXiv180802927H. DOI: 10.48550/arXiv.1808.02927. URL: https://ui.adsabs.harvard.edu/abs/2018arXiv180802927H (visited on 05/09/2025).

Hess, Victor F. (1912). "Über Beobachtungen der durchdringenden Strahlung bei sieben Freiballonfahrten". In: *Physik Zeitchr* 13, pp. 1084–1091.

Hillas, A. M. (Aug. 1985). "Cerenkov Light Images of EAS Produced by Primary Gamma Rays and by Nuclei". In: *International Cosmic Ray Conference*. Vol. 3. ADS Bibcode: 1985ICRC....3..445H, p. 445. URL: https://ui.adsabs.harvard.edu/abs/1985ICRC....3..445H (visited on 04/09/2025).

Hinton, J. A. and W. Hofmann (Sept. 2009). "Teraelectronvolt Astronomy". In: *Annual Review of Astronomy and Astrophysics* 47. ADS Bibcode: 2009ARA&A..47..523H, pp. 523–565. ISSN: 0066-4146. DOI: 10.1146/annurev-astro-082708-101816. URL: https://ui.adsabs.harvard.edu/abs/2009ARA&A..47..523H (visited on 06/20/2025).

Holder, Jamie (Oct. 2015). *Atmospheric Cherenkov Gamma-ray Telescopes*. ADS Bibcode: 2015arXiv151005675H. DOI: 10.48550/arXiv.1510.05675. URL: https://ui.adsabs.harvard.edu/abs/2015arXiv151005675H (visited on 06/02/2025).

Huentemeyer, Petra, Segev BenZvi, Brenda Dingus, et al. (Sept. 2019). *The Southern Wide-Field Gamma-Ray Observatory (SWGO): A Next-Generation Ground-Based Survey Instrument*. Conference Name: Bulletin of the American Astronomical Society Volume: 51 ADS Bibcode: 2019BAAS...51g.109H. eprint: arXiv:1907.07737. DOI: 10.48550/arXiv.1907.07737. URL: https://ui.adsabs.harvard.edu/abs/2019BAAS...51g.109H (visited on 06/20/2025).

IceCube Collaboration, M. G. Aartsen, M. Ackermann, et al. (July 2018). "Neutrino emission from the direction of the blazar TXS 0506+056 prior to the IceCube-170922A alert". In: *Science* 361. ADS Bibcode: 2018Sci...361..147I, pp. 147–151. ISSN: 0036-8075. DOI: 10.1126/science.aat2890. URL: https://ui.adsabs.harvard.edu/abs/2018Sci...361..147I (visited on 05/21/2025).

IceCube Collaboration, R. Abbasi, M. Ackermann, et al. (Nov. 2022). "Evidence for neutrino emission from the nearby active galaxy NGC 1068". In: *Science* 378. ADS Bibcode: 2022Sci...378..538I, pp. 538–543. ISSN: 0036-8075. DOI: 10.1126/science.abg3395. URL: https://ui.adsabs.harvard.edu/abs/2022Sci...378..538I (visited on 05/21/2025).

Icecube Collaboration, R. Abbasi, M. Ackermann, et al. (June 2023). "Observation of high-energy neutrinos from the Galactic plane". In: *Science* 380. ADS Bibcode: 2023Sci...380.1338I, pp. 1338–1343. ISSN: 0036-8075. DOI: 10.1126/science.adc9818. URL: https://ui.adsabs.harvard.edu/abs/2023Sci...380.1338I (visited on 05/21/2025).

Ito, N., S. Kawakami, Y. Hayashi, et al. (Jan. 1997). "The Energy Spectrum and Chemical Composition of Primary Cosmic Rays above 100 TeV Derived from Size Spectrum at Mt. Norikura". In: *International Cosmic Ray Conference*. Vol. 4. ADS Bibcode: 1997ICRC....4..117I, p. 117. URL: https://ui.adsabs.harvard.edu/abs/1997ICRC....4..117I (visited on 05/07/2025).

Ivanenko, I. P., V. Ya. Shestoperov, L. O. Chikova, et al. (Jan. 1993). "Energy Spectra of Cosmic Rays above 2 TeV as Measured by the 'SOKOL' Apparatus". In: *International Cosmic Ray Conference*. Vol. 2. ADS Bibcode: 1993ICRC....2...17I, p. 17. URL: https://ui.adsabs.harvard.edu/abs/1993ICRC....2...17I (visited on 05/07/2025).

Ivanov, A. A., S. P. Knurenko, and I. Ye Sleptsov (June 2009). "Measuring extensive air showers with Cherenkov light detectors of the Yakutsk array: the energy spectrum of cosmic rays". In: *New Journal of Physics* 11. Publisher: IOP ADS Bibcode: 2009NJPh...11f5008I, p. 065008. ISSN: 1367-2630. DOI: 10.1088/1367-2630/11/6/065008. URL: https://ui.adsabs.harvard.edu/abs/2009NJPh...11f5008I (visited on 05/07/2025).

Ivanov, D. (July 2015). "TA Spectrum Summary". In: *International Cosmic Ray Conference*. Vol. 34. ADS Bibcode: 2015ICRC...34..349I, p. 349. DOI: 10.22323/1.236.0349. URL: https://ui.adsabs.harvard.edu/abs/2015ICRC...34..349I (visited on 05/07/2025).

Jackson, John David (July 1998). *Classical Electrodynamics*. 3rd. Wiley-VCH. ISBN: 0-471-30932-X.

Josephy, A., P. Chawla, E. Fonseca, et al. (Sept. 2019). "CHIME/FRB Detection of the Original Repeating Fast Radio Burst Source FRB 121102". In: *The Astrophysical Journal* 882. Publisher: IOP ADS Bibcode: 2019ApJ...882L..18J, p. L18. ISSN: 0004-637X. DOI: 10.3847/2041-8213/ab2c00. URL: https://ui.adsabs.harvard.edu/abs/2019ApJ...882L..18J (visited on 12/15/2025).

Karachentsev, I. D., A. E. Dolphin, D. Geisler, et al. (Jan. 2002). "The M 81 group of galaxies: New distances, kinematics and structure". In: *Astronomy and Astrophysics* 383. ADS Bibcode: 2002A&A...383..125K, pp. 125–136. ISSN: 0004-6361. DOI: 10.1051/0004-6361:20011741. URL: https://ui.adsabs.harvard.edu/abs/2002A&A...383..125K (visited on 07/05/2025).

KASCADE-Grande Collaboration, : W. D. Apel, et al. (June 2009). *Cosmic Ray Measurements with the KASCADE-Grande Experiment*. ADS Bibcode: 2009arXiv0906.4007K. DOI: 10.48550/arXiv.0906.4007. URL: https://ui.adsabs.harvard.edu/abs/2009arXiv0906.4007K (visited on 05/07/2025).

Kieda, D. B. (Jan. 2013). *The Gamma Ray Detection Sensitivity of the Upgraded VERITAS Observatory*. Conference Name: International Cosmic Ray Conference Volume: 33 ADS Bibcode: 2013ICRC...33.1124K. eprint: arXiv:1308.4849. DOI: 10.48550/arXiv.1308.4849. URL: https://ui.adsabs.harvard.edu/abs/2013ICRC...33.1124K (visited on 05/30/2025).

Kieda, David (Jan. 2011). "Status of the VERITAS Upgrade". In: *International Cosmic Ray Conference*. Vol. 9. ADS Bibcode: 2011ICRC....9...14K. eprint: arXiv:1110.4360, p. 14. DOI: 10.7529/ICRC2011/V09/0343. URL: https://ui.adsabs.harvard.edu/abs/2011ICRC....9...14K (visited on 05/30/2025).

Kifune, T. (Dec. 1996). "Ground-based gamma-ray astronomy: general remarks." In: *Nuovo Cimento C Geophysics Space Physics C* 19C. ADS Bibcode: 1996NCimC..19..953K, pp. 953–957. ISSN: 0390-5551. DOI: 10.1007/BF02508136. URL: https://ui.adsabs.harvard.edu/abs/1996NCimC..19..953K (visited on 05/09/2025).

Kilpatrick, C. D., W. Fong, J. X. Prochaska, et al. (Apr. 2021). "A redshift for the putative host galaxy of FRB20201124A". In: *The Astronomer's Telegram* 14516. ADS Bibcode: 2021ATel14516....1K, p. 1. URL: https://ui.adsabs.harvard.edu/abs/2021ATel14516....1K (visited on 07/06/2025).

Kirsten, F., B. Marcote, K. Nimmo, et al. (Feb. 2022). "A repeating fast radio burst source in a globular cluster". In: *Nature* 602. ADS Bibcode: 2022Natur.602..585K, pp. 585–589. ISSN: 0028-0836. DOI: 10.1038/s41586-021-04354-w. URL: https://ui.adsabs.harvard.edu/abs/2022Natur.602..585K (visited on 07/05/2025).

KM3NeT Collaboration, S. Aiello, A. Albert, et al. (Sept. 2024). "Astronomy potential of KM3NeT/ARCA". In: *European Physical Journal C* 84. Publisher: Springer ADS Bibcode: 2024EPJC...84..885K, p. 885. ISSN: 1434-6044. DOI: 10.1140/epjc/s10052-024-13137-2. URL: https://ui.adsabs.harvard.edu/abs/2024EPJC...84..885K (visited on 05/21/2025).

Knoetig, Max L. (Aug. 2014). "Signal Discovery, Limits, and Uncertainties with Sparse On/Off Measurements: An Objective Bayesian Analysis". In: *The Astrophysical Journal*

790. Publisher: IOP ADS Bibcode: 2014ApJ...790..106K, p. 106. ISSN: 0004-637X. DOI: 10.1088/0004-637X/790/2/106. URL: https://ui.adsabs.harvard.edu/abs/2014ApJ...790..106K (visited on 06/30/2025).

Krause, Maria (Jan. 2017). "High-sensitivity analysis of the Cygnus region observed with VERITAS". ADS Bibcode: 2017PhDT.....452K. Ph.D. thesis. URL: https://ui.adsabs.harvard.edu/abs/2017PhDT.....452K (visited on 06/29/2025).

Krennrich, F., G. Blaylock, S. M. Bradbury, et al. (Mar. 2007). "Status report from VERITAS". In: vol. 60. ADS Bibcode: 2007JPhCS..60...34K. IOP, pp. 34–39. DOI: 10.1088/1742-6596/60/1/006. URL: https://ui.adsabs.harvard.edu/abs/2007JPhCS..60...34K (visited on 06/20/2025).

Krymskii, G. F. (June 1977). "A regular mechanism for the acceleration of charged particles on the front of a shock wave". In: *Soviet Physics Doklady* 22. ADS Bibcode: 1977SPhD...22..327K, p. 327. URL: https://ui.adsabs.harvard.edu/abs/1977SPhD...22..327K (visited on 05/08/2025).

Kumar, Pravir, R. M. Shannon, V. Moss, et al. (Apr. 2021). "ASKAP detection of a repeat burst from the FRB 20201124A source". In: *The Astronomer's Telegram* 14502. ADS Bibcode: 2021ATel14502....1K, p. 1. URL: https://ui.adsabs.harvard.edu/abs/2021ATel14502....1K (visited on 07/06/2025).

Law, Casey, Shriharsh Tendulkar, Tracy Clarke, et al. (Apr. 2021). "VLA/realfast localization and deep imaging of FRB 20201124A". In: *The Astronomer's Telegram* 14526. ADS Bibcode: 2021ATel14526....1L, p. 1. URL: https://ui.adsabs.harvard.edu/abs/2021ATel14526....1L (visited on 07/06/2025).

Lenain, J. -P. (Jan. 2018). "FLaapLUC: A pipeline for the generation of prompt alerts on transient Fermi-LAT γ-ray sources". In: *Astronomy and Computing* 22. ADS Bibcode: 2018A&C....22....9L, pp. 9–15. ISSN: 2213-1337. DOI: 10.1016/j.ascom.2017.11.002. URL: https://ui.adsabs.harvard.edu/abs/2018A&C....22....9L (visited on 05/30/2025).

LHAASO Collaboration, Z. Cao, F. Aharonian, et al. (June 2023). "A tera-electron volt afterglow from a narrow jet in an extremely bright gamma-ray burst." In: *Science* 380. ADS Bibcode: 2023Sci...380.1390L, pp. 1390–1396. ISSN: 0036-8075. DOI: 10.1126/science.adg9328. URL: https://ui.adsabs.harvard.edu/abs/2023Sci...380.1390L (visited on 06/25/2025).

LHCb collaboration (Apr. 2025). *Technology developments for LHCb Upgrade II*. ADS Bibcode: 2025arXiv250403088L. DOI: 10.48550/arXiv.2504.03088. URL: https://ui.adsabs.harvard.edu/abs/2025arXiv250403088L (visited on 05/21/2025).

Li, C. K., L. Lin, S. L. Xiong, et al. (Apr. 2021). "HXMT identification of a non-thermal X-ray burst from SGR J1935+2154 and with FRB 200428". In: *Nature Astronomy* 5. ADS

Bibcode: 2021NatAs...5..378L, pp. 378–384. ISSN: 2397-3366. DOI: 10.1038/s41550-021-01302-6. URL: https://ui.adsabs.harvard.edu/abs/2021NatAs...5..378L (visited on 07/03/2025).

Li, T.-P. and Y.-Q. Ma (Sept. 1983). "Analysis methods for results in gamma-ray astronomy." In: *The Astrophysical Journal* 272. Publisher: IOP ADS Bibcode: 1983ApJ...272..317L, pp. 317–324. ISSN: 0004-637X. DOI: 10.1086/161295. URL: https://ui.adsabs.harvard.edu/abs/1983ApJ...272..317L (visited on 10/31/2025).

Lin, Tony Tsen-Yuan (Mar. 2020). "Measurement of the Bethe-Heitler Cross Section in the TeV Regime and Search for Lorentz Invariance Violation with VERITAS". en. In: *McGill University*.

Longair, Malcolm S. (2011). *High Energy Astrophysics*. 3rd ed. Cambridge: Cambridge University Press. ISBN: 978-0-521-75618-1. DOI: 10.1017/CBO9780511778346. URL: https://www.cambridge.org/core/books/high-energy-astrophysics/CF25E2E5FC0EDFC51FCD7846A262C0AE (visited on 04/09/2025).

Luo, R., B. J. Wang, Y. P. Men, et al. (Oct. 2020). "Diverse polarization angle swings from a repeating fast radio burst source". In: *Nature* 586. ADS Bibcode: 2020Natur.586..693L, pp. 693–696. ISSN: 0028-0836. DOI: 10.1038/s41586-020-2827-2. URL: https://ui.adsabs.harvard.edu/abs/2020Natur.586..693L (visited on 06/14/2025).

MAGIC Collaboration, V. A. Acciari, S. Ansoldi, et al. (Mar. 2019). "A fast, very-high-energy γ-ray flare from BL Lacertae during a period of multi-wavelength activity in June 2015". In: *Astronomy and Astrophysics* 623. Publisher: EDP ADS Bibcode: 2019A&A...623A.175M, A175. ISSN: 0004-6361. DOI: 10.1051/0004-6361/201834010. URL: https://ui.adsabs.harvard.edu/abs/2019A&A...623A.175M (visited on 07/10/2025).

MAGIC Collaboration, V. A. Acciari, S. Ansoldi, et al. (Nov. 2020). "Detection of the Geminga pulsar with MAGIC hints at a power-law tail emission beyond 15 GeV". In: *Astronomy and Astrophysics* 643. ADS Bibcode: 2020A&A...643L..14M, p. L14. ISSN: 0004-6361. DOI: 10.1051/0004-6361/202039131. URL: https://ui.adsabs.harvard.edu/abs/2020A&A...643L..14M (visited on 07/01/2025).

Maier, G., V. A. Acciari, R. Amini, et al. (Jan. 2008). *VERITAS: Status and Latest Results*. Conference Name: International Cosmic Ray Conference Volume: 3 ADS Bibcode: 2008ICRC....3.1457M. eprint: arXiv:0709.3654. DOI: 10.48550/arXiv.0709.3654. URL: https://ui.adsabs.harvard.edu/abs/2008ICRC....3.1457M (visited on 05/30/2025).

Maier, G. and J. Holder (July 2017). "Eventdisplay: An Analysis and Reconstruction Package for Ground-based Gamma-ray Astronomy". In: *International Cosmic Ray Confer-*

ence. Vol. 301. ADS Bibcode: 2017ICRC...35..747M. eprint: arXiv:1708.04048, p. 747. DOI: 10.22323/1.301.0747. URL: https://ui.adsabs.harvard.edu/abs/2017ICRC...35..747M (visited on 06/29/2025).

Marcote, B., K. Nimmo, J. W. T. Hessels, et al. (Jan. 2020). "A repeating fast radio burst source localized to a nearby spiral galaxy". In: *Nature* 577. ADS Bibcode: 2020Natur.577..190M, pp. 190–194. ISSN: 0028-0836. DOI: 10.1038/s41586-019-1866-z. URL: https://ui.adsabs.harvard.edu/abs/2020Natur.577..190M (visited on 06/14/2025).

Margalit, Ben, Paz Beniamini, Navin Sridhar, et al. (Aug. 2020). "Implications of a Fast Radio Burst from a Galactic Magnetar". In: *The Astrophysical Journal* 899. Publisher: IOP ADS Bibcode: 2020ApJ...899L..27M, p. L27. ISSN: 0004-637X. DOI: 10.3847/2041-8213/abac57. URL: https://ui.adsabs.harvard.edu/abs/2020ApJ...899L..27M (visited on 07/05/2025).

Maurin, David, Markus Ahlers, Hans Dembinski, et al. (Oct. 2023). "A cosmic-ray database update: CRDB v4.1". In: *European Physical Journal C* 83. Publisher: Springer ADS Bibcode: 2023EPJC...83..971M, p. 971. ISSN: 1434-6044. DOI: 10.1140/epjc/s10052-023-12092-8. URL: https://ui.adsabs.harvard.edu/abs/2023EPJC...83..971M (visited on 05/07/2025).

McHardy, I. M., E. Koerding, C. Knigge, et al. (Dec. 2006). "Active galactic nuclei as scaled-up Galactic black holes". In: *Nature* 444. ADS Bibcode: 2006Natur.444..730M, pp. 730–732. ISSN: 0028-0836. DOI: 10.1038/nature05389. URL: https://ui.adsabs.harvard.edu/abs/2006Natur.444..730M (visited on 06/30/2025).

McKinven, Ryan and Chime/Frb Collaboration (Oct. 2022). "Nine Bursts in Three Days from a Newly Discovered Repeating Source of Fast Radio Bursts". In: *The Astronomer's Telegram* 15679. ADS Bibcode: 2022ATel15679....1M, p. 1. URL: https://ui.adsabs.harvard.edu/abs/2022ATel15679....1M (visited on 07/05/2025).

Mereghetti, S., V. Savchenko, C. Ferrigno, et al. (Aug. 2020). "INTEGRAL Discovery of a Burst with Associated Radio Emission from the Magnetar SGR 1935+2154". In: *The Astrophysical Journal* 898. Publisher: IOP ADS Bibcode: 2020ApJ...898L..29M, p. L29. ISSN: 0004-637X. DOI: 10.3847/2041-8213/aba2cf. URL: https://ui.adsabs.harvard.edu/abs/2020ApJ...898L..29M (visited on 07/03/2025).

Michilli, Daniele, Mohit Bhardwaj, Charanjot Brar, et al. (June 2023). "Subarcminute Localization of 13 Repeating Fast Radio Bursts Detected by CHIME/FRB". In: *The Astrophysical Journal* 950. Publisher: IOP ADS Bibcode: 2023ApJ...950..134M, p. 134. ISSN: 0004-637X. DOI: 10.3847/1538-4357/accf89. URL: https://ui.adsabs.harvard.edu/abs/2023ApJ...950..134M (visited on 06/14/2025).

Miller, J. S., H. B. French, and S. A. Hawley (Jan. 1978). "The spectrum and magnitude of the galaxy associated with BL Lacertae." In: *The Astrophysical Journal* 219. Publisher: IOP ADS Bibcode: 1978ApJ...219L..85M, pp. L85–L87. ISSN: 0004-637X. DOI: 10.1086/182612. URL: https://ui.adsabs.harvard.edu/abs/1978ApJ...219L..85M (visited on 07/10/2025).

Moiseev, A. A., R. C. Hartman, T. E. Johnson, et al. (Jan. 2005). "Design and Characteristics of the Anticoincidence Detector for the GLAST Large Area Telescope". In: *International Cosmic Ray Conference*. Vol. 5. ADS Bibcode: 2005ICRC....5..419M, p. 419. URL: https://ui.adsabs.harvard.edu/abs/2005ICRC....5..419M (visited on 06/20/2025).

Morales-Soto, J. A., J. C. Arteaga-Velázquez, Hawc, et al. (Mar. 2022). "The all-particle cosmic ray energy spectrum measured with HAWC". In: ADS Bibcode: 2022icrc.confE.330M. eprint: arXiv:2108.04748, p. 330. DOI: 10.22323/1.395.0330. URL: https://ui.adsabs.harvard.edu/abs/2022icrc.confE.330M (visited on 05/07/2025).

Murase, Kohta, Kazumi Kashiyama, and Peter Mészáros (Sept. 2016). "A burst in a wind bubble and the impact on baryonic ejecta: high-energy gamma-ray flashes and afterglows from fast radio bursts and pulsar-driven supernova remnants". In: *Monthly Notices of the Royal Astronomical Society* 461. Publisher: OUP ADS Bibcode: 2016MNRAS.461.1498M, pp. 1498–1511. ISSN: 0035-8711. DOI: 10.1093/mnras/stw1328. URL: https://ui.adsabs.harvard.edu/abs/2016MNRAS.461.1498M (visited on 07/09/2025).

— (May 2017). "Erratum: A burst in a wind bubble and the impact on baryonic ejecta: high-energy gamma-ray flashes and afterglows from fast radio bursts and pulsar-driven supernova remnants". In: *Monthly Notices of the Royal Astronomical Society* 467. Publisher: OUP ADS Bibcode: 2017MNRAS.467.3542M, pp. 3542–3543. ISSN: 0035-8711. DOI: 10.1093/mnras/stx310. URL: https://ui.adsabs.harvard.edu/abs/2017MNRAS.467.3542M (visited on 07/09/2025).

Neshpor, Yu. I., N. N. Chalenko, A. A. Stepanian, et al. (Apr. 2001). "BL Lac: A New Ultrahigh-Energy Gamma-Ray Source". In: *Astronomy Reports* 45. Publisher: Springer ADS Bibcode: 2001ARep...45..249N, pp. 249–254. ISSN: 1063-7729. DOI: 10.1134/1.1361316. URL: https://ui.adsabs.harvard.edu/abs/2001ARep...45..249N (visited on 07/10/2025).

Ng, Mason and CHIME/FRB Collaboration (Mar. 2025). "Discovery of FRB 20250316A, a bright fast radio burst in the direction of the nearby galaxy NGC 4141". In: *The Astronomer's Telegram* 17081. ADS Bibcode: 2025ATel17081....1N, p. 1. URL: https://ui.adsabs.harvard.edu/abs/2025ATel17081....1N (visited on 07/05/2025).

Nigro, C., J. Sitarek, P. Gliwny, et al. (Apr. 2022). "agnpy: An open-source python package modelling the radiative processes of jetted active galactic nuclei". In: *Astronomy and Astrophysics* 660. ADS Bibcode: 2022A&A...660A..18N, A18. ISSN: 0004-6361. DOI: 10.1051/0004-6361/202142000. URL: https://ui.adsabs.harvard.edu/abs/2022A&A...660A..18N (visited on 06/25/2025).

Nigro, Cosimo, Tarek Hassan, and Laura Olivera-Nieto (Oct. 2021). "Evolution of Data Formats in Very-High-Energy Gamma-Ray Astronomy". In: *Universe* 7.10. Number: 10 Publisher: Multidisciplinary Digital Publishing Institute, p. 374. ISSN: 2218-1997. DOI: 10.3390/universe7100374. URL: https://www.mdpi.com/2218-1997/7/10/374 (visited on 02/10/2025).

Noda, Koji and Robert Daniel Parsons (Jan. 2022). "Gamma-Ray Bursts at TeV Energies: Observational Status". In: *Galaxies* 10. ADS Bibcode: 2022Galax..10....7N, p. 7. DOI: 10.3390/galaxies10010007. URL: https://ui.adsabs.harvard.edu/abs/2022Galax..10....7N (visited on 07/03/2025).

Nozaki, Seiya, Katsuaki Asano, Juan Escudero, et al. (Sept. 2023). *LST-1 observations of an enormous flare of BL Lacertae in 2021*. ADS Bibcode: 2023arXiv230909715N. DOI: 10.48550/arXiv.2309.09715. URL: https://ui.adsabs.harvard.edu/abs/2023arXiv230909715N (visited on 07/10/2025).

Pandey, A. and C. S. Stalin (Dec. 2022). "Detection of minute-timescale γ-ray variability in BL Lacertae by Fermi-LAT". In: *Astronomy and Astrophysics* 668. ADS Bibcode: 2022A&A...668A.152P, A152. ISSN: 0004-6361. DOI: 10.1051/0004-6361/202244648. URL: https://ui.adsabs.harvard.edu/abs/2022A&A...668A.152P (visited on 07/11/2025).

Park, N. and VERITAS Collaboration (July 2015). "Performance of the VERITAS experiment". In: *International Cosmic Ray Conference*. Vol. 34. ADS Bibcode: 2015ICRC...34..771P. eprint: arXiv:1508.07070: ICRC, p. 771. DOI: 10.22323/1.236.0771. URL: https://ui.adsabs.harvard.edu/abs/2015ICRC...34..771P (visited on 06/20/2025).

Parker, E. N. (Dec. 1957). "Sweet's Mechanism for Merging Magnetic Fields in Conducting Fluids". In: *Journal of Geophysical Research* 62. ADS Bibcode: 1957JGR....62..509P, pp. 509–520. ISSN: 0148-0227. DOI: 10.1029/JZ062i004p00509. URL: https://ui.adsabs.harvard.edu/abs/1957JGR....62..509P (visited on 05/15/2025).

Parsons, R. D. and J. A. Hinton (Apr. 2014). "A Monte Carlo template based analysis for air-Cherenkov arrays". In: *Astroparticle Physics* 56. ADS Bibcode: 2014APh....56...26P, pp. 26–34. ISSN: 0927-6505. DOI: 10.1016/j.astropartphys.2014.03.002. URL: https://ui.adsabs.harvard.edu/abs/2014APh....56...26P (visited on 06/29/2025).

Particle Data Group, R L Workman, V D Burkert, et al. (Aug. 2022). "Review of Particle Physics". In: *Progress of Theoretical and Experimental Physics* 2022.8, p. 083C01. ISSN: 2050-3911. DOI: 10.1093/ptep/ptac097. URL: https://doi.org/10.1093/ptep/ptac097 (visited on 05/12/2025).

Patel, Anirudh, Brian D. Metzger, Jakub Cehula, et al. (May 2025). "Direct Evidence for r-process Nucleosynthesis in Delayed MeV Emission from the SGR 1806–20 Magnetar Giant Flare". In: *The Astrophysical Journal* 984. Publisher: IOP ADS Bibcode: 2025ApJ...984L..29P, p. L29. ISSN: 0004-637X. DOI: 10.3847/2041-8213/adc9b0. URL: https://ui.adsabs.harvard.edu/abs/2025ApJ...984L..29P (visited on 05/21/2025).

Pearlman, Aaron B., Paul Scholz, Suryarao Bethapudi, et al. (Jan. 2025). "Multiwavelength constraints on the origin of a nearby repeating fast radio burst source in a globular cluster". In: *Nature Astronomy* 9. ADS Bibcode: 2025NatAs...9..111P, pp. 111–127. ISSN: 2397-3366. DOI: 10.1038/s41550-024-02386-6. URL: https://ui.adsabs.harvard.edu/abs/2025NatAs...9..111P (visited on 11/11/2025).

Pedregosa, Fabian, Gaël Varoquaux, Alexandre Gramfort, et al. (Oct. 2011). "Scikit-learn: Machine Learning in Python". In: *Journal of Machine Learning Research* 12. ADS Bibcode: 2011JMLR...12.2825P, pp. 2825–2830. DOI: 10.48550/arXiv.1201.0490. URL: https://ui.adsabs.harvard.edu/abs/2011JMLR...12.2825P (visited on 10/31/2024).

Petschek, H. E. (Jan. 1964). "Magnetic Field Annihilation". In: *NASA Special Publication*. Vol. 50. ADS Bibcode: 1964NASSP..50..425P, p. 425. URL: https://ui.adsabs.harvard.edu/abs/1964NASSP..50..425P (visited on 05/15/2025).

Piro, L., G. Bruni, E. Troja, et al. (Dec. 2021). "The fast radio burst FRB 20201124A in a star-forming region: Constraints to the progenitor and multiwavelength counterparts". In: *Astronomy and Astrophysics* 656. ADS Bibcode: 2021A&A...656L..15P, p. L15. ISSN: 0004-6361. DOI: 10.1051/0004-6361/202141903. URL: https://ui.adsabs.harvard.edu/abs/2021A&A...656L..15P (visited on 07/05/2025).

Pleunis, Ziggy, Deborah C. Good, Victoria M. Kaspi, et al. (Dec. 2021). "Fast Radio Burst Morphology in the First CHIME/FRB Catalog". In: *The Astrophysical Journal* 923. Publisher: IOP ADS Bibcode: 2021ApJ...923....1P, p. 1. ISSN: 0004-637X. DOI: 10.3847/1538-4357/ac33ac. URL: https://ui.adsabs.harvard.edu/abs/2021ApJ...923....1P (visited on 10/31/2024).

Price, D. C., G. Foster, M. Geyer, et al. (July 2019). "A fast radio burst with frequency-dependent polarization detected during Breakthrough Listen observations". In: *Monthly Notices of the Royal Astronomical Society* 486. Publisher: OUP ADS Bibcode: 2019MNRAS.486.3636P, pp. 3636–3646. ISSN: 0035-8711. DOI: 10.1093/mnras/

stz958. URL: https://ui.adsabs.harvard.edu/abs/2019MNRAS.486.3636P (visited on 06/13/2025).

Price, Danny C., Vishal Gajjar, Aman Dhar, et al. (Mar. 2018). "Detection of a new fast radio burst during Breakthrough Listen observations". In: *The Astronomer's Telegram* 11376. ADS Bibcode: 2018ATel11376....1P, p. 1. URL: https://ui.adsabs.harvard.edu/abs/2018ATel11376....1P (visited on 06/13/2025).

Principe, G., M. Negro N. Di Lalla, N. Omodei, et al. (Apr. 2024). "FRB 20240114A: No counterpart candidate in Fermi-LAT observations". In: *The Astronomer's Telegram* 16602. ADS Bibcode: 2024ATel16602....1P, p. 1. URL: https://ui.adsabs.harvard.edu/abs/2024ATel16602....1P (visited on 07/03/2025).

Principe, G., L. Di Venere, M. Negro, et al. (July 2023). "Hunting for gamma-ray emission from fast radio bursts". In: *Astronomy and Astrophysics* 675. Publisher: EDP ADS Bibcode: 2023A&A...675A..99P, A99. ISSN: 0004-6361. DOI: 10.1051/0004-6361/202346492. URL: https://ui.adsabs.harvard.edu/abs/2023A&A...675A..99P (visited on 07/03/2025).

Prosin, V. V., S. F. Berezhnev, N. M. Budnev, et al. (Aug. 2014). "Tunka-133: Results of 3 year operation". In: *Nuclear Instruments and Methods in Physics Research A* 756. ADS Bibcode: 2014NIMPA.756...94P, pp. 94–101. ISSN: 0168-9002. DOI: 10.1016/j.nima.2013.09.018. URL: https://ui.adsabs.harvard.edu/abs/2014NIMPA.756...94P (visited on 05/07/2025).

Qu, Yuanhong and Bing Zhang (Mar. 2022). "Neutrino emission from fast radio burst-emitting magnetars". In: *Monthly Notices of the Royal Astronomical Society* 511. Publisher: OUP ADS Bibcode: 2022MNRAS.511..972Q, pp. 972–979. ISSN: 0035-8711. DOI: 10.1093/mnras/stac117. URL: https://ui.adsabs.harvard.edu/abs/2022MNRAS.511..972Q (visited on 06/23/2025).

Ravi, Vikram, Morgan Catha, Ge Chen, et al. (May 2023). "Deep Synoptic Array Science: Discovery of the Host Galaxy of FRB 20220912A". In: *The Astrophysical Journal* 949. Publisher: IOP ADS Bibcode: 2023ApJ...949L...3R, p. L3. ISSN: 0004-637X. DOI: 10.3847/2041-8213/acc4b6. URL: https://ui.adsabs.harvard.edu/abs/2023ApJ...949L...3R (visited on 06/17/2025).

Rawlins, K. and IceCube Collaboration (July 2015). "Latest Results on Cosmic Ray Spectrum and Composition from Three Years of IceTop and IceCube". In: vol. 34. ADS Bibcode: 2015ICRC...34..334R, p. 334. DOI: 10.22323/1.236.0334. URL: https://ui.adsabs.harvard.edu/abs/2015ICRC...34..334R (visited on 05/07/2025).

Rhodes, Brandon Craig (Dec. 2011). "PyEphem: Astronomical Ephemeris for Python". In: *Astrophysics Source Code Library*. ADS Bibcode: 2011ascl.soft12014R, ascl:1112.014. URL:

https://ui.adsabs.harvard.edu/abs/2011ascl.soft12014R (visited on 07/09/2025).

Richard Fitzpatrick (June 2014). *Classical Electromagnetism*. URL: https://farside.ph.utexas.edu/teaching/jk1/Electromagnetism/Electromagnetism.html (visited on 07/12/2025).

Ridnaia, A., D. Svinkin, D. Frederiks, et al. (Apr. 2021). "A peculiar hard X-ray counterpart of a Galactic fast radio burst". In: *Nature Astronomy* 5. ADS Bibcode: 2021NatAs...5..372R, pp. 372–377. ISSN: 2397-3366. DOI: 10.1038/s41550-020-01265-0. URL: https://ui.adsabs.harvard.edu/abs/2021NatAs...5..372R (visited on 07/03/2025).

Righi, C., F. Tavecchio, and D. Guetta (Feb. 2017). "High-energy emitting BL Lacs and high-energy neutrinos. Prospects for the direct association with IceCube and KM3NeT". In: *Astronomy and Astrophysics* 598. ADS Bibcode: 2017A&A...598A..36R, A36. ISSN: 0004-6361. DOI: 10.1051/0004-6361/201629412. URL: https://ui.adsabs.harvard.edu/abs/2017A&A...598A..36R (visited on 06/23/2025).

Rolke, Wolfgang A. and Angel M. López (Feb. 2001). "Confidence intervals and upper bounds for small signals in the presence of background noise". In: *Nuclear Instruments and Methods in Physics Research A* 458. ADS Bibcode: 2001NIMPA.458..745R, pp. 745–758. ISSN: 0168-9002. DOI: 10.1016/S0168-9002(00)00935-9. URL: https://ui.adsabs.harvard.edu/abs/2001NIMPA.458..745R (visited on 11/07/2024).

Rybicki, George B. and Alan P. Lightman (Jan. 1979). *Radiative processes in astrophysics*. Publication Title: A Wiley-Interscience Publication ADS Bibcode: 1979rpa..book.....R. URL: https://ui.adsabs.harvard.edu/abs/1979rpa..book.....R (visited on 05/13/2025).

Scargle, Jeffrey D. (Sept. 1998). "Studies in Astronomical Time Series Analysis. V. Bayesian Blocks, a New Method to Analyze Structure in Photon Counting Data". In: *The Astrophysical Journal* 504. Publisher: IOP ADS Bibcode: 1998ApJ...504..405S, pp. 405–418. ISSN: 0004-637X. DOI: 10.1086/306064. URL: https://ui.adsabs.harvard.edu/abs/1998ApJ...504..405S (visited on 03/26/2025).

Scargle, Jeffrey D., Jay P. Norris, Brad Jackson, et al. (Feb. 2013). "Studies in Astronomical Time Series Analysis. VI. Bayesian Block Representations". In: *The Astrophysical Journal* 764. Publisher: IOP ADS Bibcode: 2013ApJ...764..167S, p. 167. ISSN: 0004-637X. DOI: 10.1088/0004-637X/764/2/167. URL: https://ui.adsabs.harvard.edu/abs/2013ApJ...764..167S (visited on 03/26/2025).

Schmidt, Fabian and Johannes Knapp (2005). *CORSIKA Shower Images*. URL: https://www-zeuthen.desy.de/~jknapp/fs/showerimages.html.

Schoo, S., W. D. Apel, J. C. Arteaga-Velázquez, et al. (July 2015). "The energy spectrum of cosmic rays in the range from 10^{14} to 10^{18}eV". In: vol. 34. ADS Bibcode: 2015ICRC...34..263S, p. 263. DOI: 10.22323/1.236.0263. URL: https://ui.adsabs.harvard.edu/abs/2015ICRC...34..263S (visited on 05/07/2025).

Shin, Kaitlyn and CHIME/FRB Collaboration (Jan. 2024). "CHIME/FRB discovery of a new repeating fast radio burst source FRB 20240114A". In: *The Astronomer's Telegram* 16420. ADS Bibcode: 2024ATel16420....1S, p. 1. URL: https://ui.adsabs.harvard.edu/abs/2024ATel16420....1S (visited on 07/05/2025).

Spitler, L. G., P. Scholz, J. W. T. Hessels, et al. (Mar. 2016). "A repeating fast radio burst". In: *Nature* 531. ADS Bibcode: 2016Natur.531..202S, pp. 202–205. ISSN: 0028-0836. DOI: 10.1038/nature17168. URL: https://ui.adsabs.harvard.edu/abs/2016Natur.531..202S (visited on 06/13/2025).

Spitler, Laura and Henning Hilmarsson (Apr. 2021). "Radio observations of FRB20201124a at 4-8 GHz with the 100-m Effelsberg Radio Telescope". In: *The Astronomer's Telegram* 14537. ADS Bibcode: 2021ATel14537....1S, p. 1. URL: https://ui.adsabs.harvard.edu/abs/2021ATel14537....1S (visited on 07/06/2025).

Stamatikos, M., D. Malesani, K. L. Page, et al. (Jan. 2014). "GRB 140705A: Swift detection of a short burst." In: *GRB Coordinates Network* 16520. ADS Bibcode: 2014GCN.16520....1S, p. 1. URL: https://ui.adsabs.harvard.edu/abs/2014GCN.16520....1S (visited on 07/05/2025).

Sun, H., H. Q. Cheng, D. Y. Li, et al. (Mar. 2025). "FRB 20250316A: detection of a candidate associated X-ray source EP J120944.2+585060 by Einstein Probe". In: *The Astronomer's Telegram* 17100. ADS Bibcode: 2025ATel17100....1S, p. 1. URL: https://ui.adsabs.harvard.edu/abs/2025ATel17100....1S (visited on 07/05/2025).

Sweet, P. A. (Jan. 1958). "The Neutral Point Theory of Solar Flares". In: vol. 6. ADS Bibcode: 1958IAUS....6..123S, p. 123. URL: https://ui.adsabs.harvard.edu/abs/1958IAUS....6..123S (visited on 05/15/2025).

Swordy, S. P. and D. B. Kieda (May 2000). "Elemental composition of cosmic rays near the knee by multiparameter measurements of air showers". In: *Astroparticle Physics* 13. ADS Bibcode: 2000APh....13..137S, pp. 137–150. ISSN: 0927-6505. DOI: 10.1016/S0927-6505(99)00117-6. URL: https://ui.adsabs.harvard.edu/abs/2000APh....13..137S (visited on 05/07/2025).

Takahashi, Yoshiyuki (Jan. 1998). "Elemental Abundance of High Energy Cosmic Rays". In: *Nuclear Physics B Proceedings Supplements* 60. ADS Bibcode: 1998NuPhS..60...83T, pp. 83–92. ISSN: 0920-5632. DOI: 10.1016/S0920-5632(97)00503-3. URL: https://ui.adsabs.harvard.edu/abs/1998NuPhS..60...83T (visited on 05/07/2025).

Takeda, M., N. Sakaki, K. Honda, et al. (July 2003). "Energy determination in the Akeno Giant Air Shower Array experiment". In: *Astroparticle Physics* 19. ADS Bibcode: 2003APh....19..447T, pp. 447–462. ISSN: 0927-6505. DOI: 10.1016/S0927-6505(02)00243-8. URL: https://ui.adsabs.harvard.edu/abs/2003APh....19..447T (visited on 05/07/2025).

Taylor, J. H. and J. M. Weisberg (Feb. 1982). "A new test of general relativity - Gravitational radiation and the binary pulsar PSR 1913+16". In: *The Astrophysical Journal* 253. Publisher: IOP ADS Bibcode: 1982ApJ...253..908T, pp. 908–920. ISSN: 0004-637X. DOI: 10.1086/159690. URL: https://ui.adsabs.harvard.edu/abs/1982ApJ...253..908T (visited on 05/21/2025).

Telescope Array Collaboration, R. U. Abbasi, M. G. Allen, et al. (Nov. 2023). "An extremely energetic cosmic ray observed by a surface detector array". In: *Science* 382. ADS Bibcode: 2023Sci...382..903T, pp. 903–907. ISSN: 0036-8075. DOI: 10.1126/science.abo5095. URL: https://ui.adsabs.harvard.edu/abs/2023Sci...382..903T (visited on 05/21/2025).

Tendulkar, S. P., C. G. Bassa, J. M. Cordes, et al. (Jan. 2017). "The Host Galaxy and Redshift of the Repeating Fast Radio Burst FRB 121102". In: *The Astrophysical Journal* 834. Publisher: IOP ADS Bibcode: 2017ApJ...834L...7T, p. L7. ISSN: 0004-637X. DOI: 10.3847/2041-8213/834/2/L7. URL: https://ui.adsabs.harvard.edu/abs/2017ApJ...834L...7T (visited on 06/13/2025).

Ter-Antonyan, Samvel (June 2014). "Sharp knee phenomenon of primary cosmic ray energy spectrum". In: *Physical Review D* 89. Publisher: APS ADS Bibcode: 2014PhRvD..89l3003T, p. 123003. ISSN: 1550-79980556-2821. DOI: 10.1103/PhysRevD.89.123003. URL: https://ui.adsabs.harvard.edu/abs/2014PhRvD..89l3003T (visited on 05/07/2025).

The Pierre Auger Collaboration, A. Aab, P. Abreu, et al. (Sept. 2015). *The Pierre Auger Observatory: Contributions to the 34th International Cosmic Ray Conference (ICRC 2015)*. ADS Bibcode: 2015arXiv150903732T. DOI: 10.48550/arXiv.1509.03732. URL: https://ui.adsabs.harvard.edu/abs/2015arXiv150903732T (visited on 05/07/2025).

Tian, Jun, Ines Pastor-Marazuela, Ben Stappers, et al. (Feb. 2024). "Detection and localisation of the highly active FRB 20240114A by MeerKAT". In: *The Astronomer's Telegram* 16446. ADS Bibcode: 2024ATel16446....1T, p. 1. URL: https://ui.adsabs.harvard.edu/abs/2024ATel16446....1T (visited on 07/05/2025).

VanderPlas, Jake (Sept. 2012). *Dynamic Programming in Python: Bayesian Blocks — Pythonic Perambulations*. URL: https://jakevdp.github.io/blog/2012/09/12/dynamic-programming-in-python/ (visited on 07/01/2025).

VERITAS Collaboration, E. Aliu, T. Arlen, et al. (Oct. 2011). "Detection of Pulsed Gamma Rays Above 100 GeV from the Crab Pulsar". In: *Science* 334. ADS Bibcode: 2011Sci...334...69V, p. 69. ISSN: 0036-8075. DOI: 10.1126/science.1208192. URL: https://ui.adsabs.harvard.edu/abs/2011Sci...334...69V (visited on 07/01/2025).

Vianello, Giacomo (May 2018). "The Significance of an Excess in a Counting Experiment: Assessing the Impact of Systematic Uncertainties and the Case with a Gaussian Background". en. In: *The Astrophysical Journal Supplement Series* 236.1, p. 17. ISSN: 0067-0049. DOI: 10.3847/1538-4365/aab780. URL: https://ui.adsabs.harvard.edu/abs/2018ApJS..236...17V/abstract (visited on 07/17/2024).

Wagner, S. J. and A. Witzel (Jan. 1995). "Intraday Variability In Quasars and BL Lac Objects". In: *Annual Review of Astronomy and Astrophysics* 33. ADS Bibcode: 1995ARA&A..33..163W, pp. 163–198. ISSN: 0066-4146. DOI: 10.1146/annurev.aa.33.090195.001115. URL: https://ui.adsabs.harvard.edu/abs/1995ARA&A..33..163W (visited on 07/01/2025).

Wakely, S. P. and D. Horan (Jan. 2008). "TeVCat: An online catalog for Very High Energy Gamma-Ray Astronomy". In: vol. 3. ADS Bibcode: 2008ICRC....3.1341W, pp. 1341–1344. URL: https://ui.adsabs.harvard.edu/abs/2008ICRC....3.1341W (visited on 09/19/2025).

Weekes, T. C., M. F. Cawley, D. J. Fegan, et al. (July 1989). "Observation of TeV Gamma Rays from the Crab Nebula Using the Atmospheric Cerenkov Imaging Technique". In: *The Astrophysical Journal* 342. Publisher: IOP ADS Bibcode: 1989ApJ...342..379W, p. 379. ISSN: 0004-637X. DOI: 10.1086/167599. URL: https://ui.adsabs.harvard.edu/abs/1989ApJ...342..379W (visited on 06/20/2025).

Weinstein, A. (Jan. 2008). *The VERITAS Trigger System*. Conference Name: International Cosmic Ray Conference Volume: 3 ADS Bibcode: 2008ICRC....3.1539W. eprint: arXiv:0709.4438. DOI: 10.48550/arXiv.0709.4438. URL: https://ui.adsabs.harvard.edu/abs/2008ICRC....3.1539W (visited on 06/28/2025).

Wharton, Robert, Suryarao Bethapudi, Viswesh Marthi, et al. (Apr. 2021). "uGMRT localization of FRB20201124A". In: *The Astronomer's Telegram* 14538. ADS Bibcode: 2021ATel14538....1W, p. 1. URL: https://ui.adsabs.harvard.edu/abs/2021ATel14538....1W (visited on 07/06/2025).

Xiang, Guangman, Min Zha, Zhiguo Yao, et al. (Oct. 2024). "LHAASO detects rapid variability of the TeV Gamma-ray Activity of BL Lacertae". In: *The Astronomer's Telegram* 16850. ADS Bibcode: 2024ATel16850....1X, p. 1. URL: https://ui.adsabs.harvard.edu/abs/2024ATel16850....1X (visited on 05/30/2025).

Xing, Yi, Wenfei Yu, Zhen Yan, et al. (Nov. 2024). *Flaring gamma-ray emission coincident with a hyperactive fast radio burst source*. ADS Bibcode: 2024arXiv241106996X. DOI: 10.48550/arXiv.2411.06996. URL: https://ui.adsabs.harvard.edu/abs/2024arXiv241106996X (visited on 07/03/2025).

Xu, Heng, Jiarui Niu, Kejia Lee, et al. (Apr. 2021). "FAST detection and localization of FRB20201124A". In: *The Astronomer's Telegram* 14518. ADS Bibcode: 2021ATel14518....1X, p. 1. URL: https://ui.adsabs.harvard.edu/abs/2021ATel14518....1X (visited on 07/06/2025).

Yao, J. M., R. N. Manchester, and N. Wang (Jan. 2017). "A New Electron-density Model for Estimation of Pulsar and FRB Distances". In: *The Astrophysical Journal* 835. Publisher: IOP ADS Bibcode: 2017ApJ...835...29Y, p. 29. ISSN: 0004-637X. DOI: 10.3847/1538-4357/835/1/29. URL: https://ui.adsabs.harvard.edu/abs/2017ApJ...835...29Y (visited on 07/09/2025).

Younes, George, Chryssa Kouveliotou, Amruta Jaodand, et al. (Oct. 2017). "X-Ray and Radio Observations of the Magnetar SGR J1935+2154 during Its 2014, 2015, and 2016 Outbursts". In: *The Astrophysical Journal* 847. Publisher: IOP ADS Bibcode: 2017ApJ...847...85Y, p. 85. ISSN: 0004-637X. DOI: 10.3847/1538-4357/aa899a. URL: https://ui.adsabs.harvard.edu/abs/2017ApJ...847...85Y (visited on 07/05/2025).

Zhang, Junshuo, Qin Wu, Shuo Cao, et al. (Mar. 2024). "Detection of hyper-activity of FRB 20240114A with FAST". In: *The Astronomer's Telegram* 16505. ADS Bibcode: 2024ATel16505....1Z, p. 1. URL: https://ui.adsabs.harvard.edu/abs/2024ATel16505....1Z (visited on 07/05/2025).

Zhang, Zhipeng, Ruizhi Yang, Shoushan Zhang, et al. (Mar. 2025). "Layout optimization and performance analysis of large array of imaging atmospheric Cherenkov telescopes". In: *Chinese Physics C* 49. Publisher: IOP ADS Bibcode: 2025ChPhC..49c5001Z, p. 035001. DOI: 10.1088/1674-1137/ad8e3f. URL: https://ui.adsabs.harvard.edu/abs/2025ChPhC..49c5001Z (visited on 07/10/2025).

Zitzer, Benjamin and VERITAS Collaboration (Jan. 2013). *Lorentz Invariance Violation Limits from the Crab Pulsar using VERITAS*. Conference Name: International Cosmic Ray Conference Volume: 33 ADS Bibcode: 2013ICRC...33.2768Z. eprint: arXiv:1307.8382. DOI: 10.48550/arXiv.1307.8382. URL: https://ui.adsabs.harvard.edu/abs/2013ICRC...33.2768Z (visited on 05/21/2025).

Zyl, P. V. van, G. La Mura, and Denis Bernard (Oct. 2024). "Fermi-LAT detection of enhanced gamma-ray activity from the blazar BL Lacertae". In: *The Astronomer's Telegram* 16849. ADS Bibcode: 2024ATel16849....1V, p. 1. URL: https://ui.adsabs.harvard.edu/abs/2024ATel16849....1V (visited on 05/30/2025).

Glossary

AGN Active Galactic Nuclei. 2, 12, 13, 15

ATel Astronomer's Telegram. 96

BDT Boosted Decision Tree. 52

CFD Constant Fraction Discriminator. 42, 44, 45

CHIME Canadian Hydrogen Intensity Mapping Experiment. 90–94, 97–99, 101, 104, 111, 112, 134

CTAO Cherenkov Telescope Array Observatory. 36, 135

DM Dispersion Measure. 93, 95, 97, 98

ECM Enhanced Current Monitor. xviii, 133

ED EventDisplay. 46, 52

FoV Field of View. 54–57

FRB A fast radio burst (FRB) is a millisecond duration burst of radio waves whose origins currently remain unknown.. xi, xvi, 9, 46, 62, 89–102, 104, 107, 110, 111, 113, 118, 131, 132, 134, 137

FSRQ Flat Spectrum Radio Quasar. 13

GBT Robert C. Byrd Green Bank Telescope . 92, 104

GPC Gaussian process classifiers. 112

GRB Gamma-ray Burst. 85, 86

GRB Gamma-ray Burst. 13, 15, 83

H.E.S.S. High Energy Stereoscopic System. 49

HBL High frequency peaked BL Lac. 12, 14

IACT Imaging Atmospheric Cherenkov Telescope. 36, 37, 41, 60, 63, 66, 80, 85, 132, 135

IACT Imaging Atmospheric Cherenkov Telescopes are a type of ground based gamma-ray telescope and include observatories like VERITAS, CTAO, and MAGIC.. 35, 54, 55, 134

IBL Intermediate frequency peaked BL Lac. 12

IRF Image Response Function. xvi, 58, 60, 62–64, 101, 124

ITM Image Template Method. 49

LBL Low frequency peaked BL Lac. 12

MSCL Mean Scaled Length. 48

MSCW Mean Scaled Width. 48

NSB Night Sky Background. 44, 45, 123

PRS Persistent Radio Source. 96

pSCT prototype Schwarzschild-Couder Telescope. 133, 134

PSF Point Spread Function. 49, 50, 60

PWN Pulsar Wind Nebula. 13

SED Spectral energy distribution. 25, 27

SNR A supernova remanent (SNR) is the nebular structure surrounding the compact object left after a supernova.. 2, 14

SSC Synchrotron self-Compton . 26, 27, 29

TNS Transient Name Server. 90

TOO Target of Opportunity. xvii

UHE Ultra high energy; used to refer to the study of astrophysical photons >100 TeV.. 12

V2DL3 VERITAS to data level three.. xvii

VBF VERITAS Bank Format, the storage format for all raw VERITAS gamma-ray data. 42, 46

VEGAS VERITAS Gamma-ray Analysis Suite. xvii, 46, 49, 51, 52, 66–68, 101

VERITAS Very Energetic Radiation Imaging Telescope Array System. xi, xii, xv–xviii, 9, 11, 16, 28, 35–37, 42, 44–46, 49, 51–53, 55, 56, 58, 60–65, 77, 83, 85, 89–96, 98, 99, 101, 104, 107–109, 111–113, 115, 118–122, 124, 125, 128, 132–134, 137

VHE Very high energy; used to refer to the study of astrophysical photons from ∼100 GeV to ∼100 TeV.. 10–12, 14, 25, 62, 80, 81, 83–86, 93, 103, 118, 120, 121, 130–132, 134, 135

VLA Very Large Array. 96

WIMP Weakly interacting massive particles are a class of models of particle dark matter.. 2, 8